Coherent photons

from a solid-state artificial atom

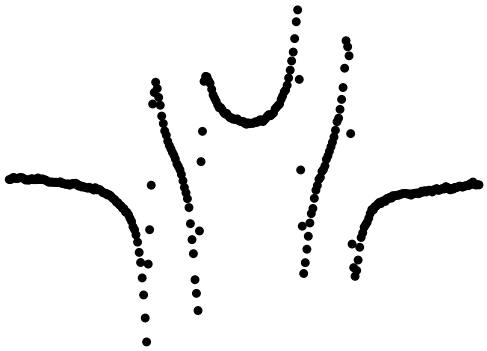

Clemens Matthiesen

St John's College

Department of Physics

University of Cambridge

This dissertation is submitted for the degree of

Doctor of Philosophy

May 2013

This dissertation is the result of my own work and includes nothing which is the outcome of work done in collaboration except where specifically indicated in the text.

This dissertation does not exceed the word limit of 60000 words.

Meinen Eltern.

Acknowledgements

I have left the acknowledgements to be written last, after finishing the 'serious' parts of this thesis. After all, it should be the easiest bit. So I thought, but it turns out it is quite difficult to summarise four years of work (and life) on one page. I had the pleasure of working with many fantastic colleagues and they have contributed greatly to the results presented later on, in teaching, training, discussing (more passionately since the arrival of Claire) and working together.

First, I should and want to thank my supervisor Mete Atatüre for his academic guidance throughout the years, while giving me the freedom to pursue interesting (at least initially) side projects. He has been increasingly busy, but his door is still always open (quite literally) and he somehow always manages to find the right words to motivate.

I am very grateful to the super-postdoc Nick (now super-group leader I expect) who taught me optics, research practices and the lab techniques when I was in my first year. I hope Eleni is doing well! I have fond memories of working with Chaoyang in my first year (I had real difficulties following your labwork in the first few months!). Visiting him, now that he is a senior academic, and his group (Yu-Ming, Yu He and Yu-Jia) in Hefei was a real pleasure.

Tina was around when I pressed first buttons in the lab (x up and down, y up and down, NOT z) and her presence has been a constant in the group. Seeing some parts of California with her, on the pretext of going to 'the-world's-leading-something-optics-something-conference' was really fun (I mean Photonic West.). I also want to thank Peter Humphreys for his valuable work on the Michelson interferometer during his Part III project.

The last two years have seen a renewed QD team: one-by-one Claire,

Jack, Megan, Carsten and Rob joined and brought with them fresh ideas and a solid theoretical background. The working atmosphere in both the lab and the Room 935A (coincidence? I think not) has always been relaxed and driven at the same time, and I feel very much at home there. I am also very grateful to Carsten, Jack and Rob for proof-reading this thesis, and picking up on the occasional factual error as well.

The friendly, outgoing and fun nature of the whole AMOP-MESS (QINM now?) group has made the past years into a very enjoyable experience and I thank members here if I haven't mentioned them earlier: Yong, Yuri, Josh (who should get a master in labview with his PhD), Ben, the NV team(s) of Helena, Dhiren, and recently Lina and David. Paul filled the role of experienced post-doc very well, and I was able to learn a lot from him, when I was meant to teach our lab techniques. The one year he spent with us was a fruitful one and I hope we keep up the communication. Zhenyong Li brought a different set of skills to the lab during his stay and I hope his research is benefiting from the new experiences.

Jeroen Elzerman and Andrew Ferguson kindly agreed to examine my thesis work and conduct the viva, and I am grateful for their thorough reading and insightful questions and comments.

I am very much looking forward to get back to the lab and work with my teammates on the exciting projects planned for the future. Thanks to Prof. Richard Phillips's continued support of my JRF applications, Prof. Skolnick's multiple reference letters and Mete's willingness to keep me, I will be able to spend another few years in Cambridge. I have also enjoyed enlightening physics discussions with Prof. Phillips.

Finally, I cannot be grateful enough to Kelly. After nearly three years of being in Cambridge together I still don't know she manages to balances the long working hours with everything else so well.

Summary

Single spins confined in semiconductor quantum dots - artificial atoms in the solid-state - are attractive candidates for quantum mechanical bits, the fundamental units and building blocks of a quantum computer. The ability to address quantum dot spins optically allows us to initialise and manipulate the state of the quantum bit. Gaining information on the qubit, for example by reading out its state, not only requires state-selective optical excitation, but also access to the single photons scattered in response by the quantum dot. Further, for a distributed computer architecture where nodes of few quantum bits are interlinked via optical communication channels photonic quantum bits are required to faithfully transmit the quantum information.

In this thesis we advocate resonant excitation of quantum dot transitions and collection of the resonance fluorescence to address two outstanding challenges: generating dephasing-free single photons for use as flying quantum bits and single-shot spin readout. To this end we investigate the spectral and first-order coherence properties of quantum dot resonance fluorescence. In particular, we directly observe highly coherent scattering in the low Rabi frequency limit which has remained unexplored for solid-state single photon emitters so far. At the same time, interactions with the semiconductor environment are revealed and quantified through their optical signatures: exciton-phonon coupling, nuclear spin dynamics and local electric field fluctuations signal a departure from the ideal atom-like behaviour.

Taking advantage of the laser-like coherence of single phase-locked quantum dot photons in the Heitler regime, we demonstrate near-ideal two-photon quantum interference. This benchmark measurement is a precursor for the photonic entanglement of distant quantum dot spins in a quantum optical network, and the results here predict a high fidelity operation.

Finally, moving to tunnel-coupled quantum dot molecules we show that the overlap of carrier wave functions in two closely spaced quantum dots forms new spin-selective optical transitions not available in single quantum dots. Then, the presence or absence of scattered photons reveals the electron spin. Intermittency in the quantum dot resonance fluorescence allowed us, for the first time, to observe spin quantum jumps in real-time.

Both achievements - highly coherent photons and spin readout - provide the missing link to attempt creation of a small-scale quantum network now.

Contents

Chapter 1

Introduction

The last two decades have seen a tremendous interest in the emerging field of quantum information technology. The promise of quantum information processing is an exponential speed-up of a range of computational problems whose calculation is not feasible with current technology. In the pursuit of control of materials at the fundamental - quantum - level, this research has already developed a rich toolbox of techniques that enabled advances in metrology and sensing applications, and is driving progress in understanding and designing materials at the nanoscale.

Binary logic, the basis of classical computers, despite its obvious successes, is not very good at dealing with complex system problems, e.g. many-body simulations. In these problems the number of computational steps scales exponentially with the number of elements, such that any simulation becomes rapidly intractable. Protein folding provides an example of such a complex system where understanding the spatial configurations is also key to understanding diseases like Alzheimer's. As another example, quantum mechanical processes themselves cannot be efficiently modelled with classical computers as there is no classical equivalent for most quantum effects. The solution is a computer that does not operate on classical physics, but on the basis of quantum mechanics, where entanglement of different quantum bits is exploited for massive parallel computing. At this stage research evolves from obtaining information about physical systems to an approach where "information is physical"[1] and constitutes a part of a

complex system.

Today's paradigm of a quantum computer, dubbed the "Quantum Internet" [2], is a network consisting of nodes of one to a few *stationary quantum bits*, such as single atoms, solid-state impurities, electron or hole spins connected via *flying quantum bits*, such as single photons. Quantum information processing based on solid-state spins was kick-started by a proposal by Loss and DiVincenzo less than 15 years ago [3]. The requirements for a realisation are summarised in what are known as the 7 DiVincenzo criteria [4]. Starting with a physical representation of a quantum bit, control over individual quantum bits, pairs of quantum bits and the exchange of information between separate quantum bits form the ingredients necessary to perform arbitrary operations and algorithms.
Getting to the stage of a working prototype of a quantum computer is a huge technical challenge, and at the present time many research groups, academic, governmental and commercial alike, are exploring a number of physical systems that can form the building blocks.
This thesis is concerned with small parts of this huge challenge for one particular physical system: optically active semiconductor quantum dots. We loosely summarise the aims of this particular work as follows. The generation of *clean* photons from a semiconductor quantum dot. Of course, *clean* is not a proper scientific term, but purposely chosen, as the requirements on photons change with the respective goals. For the greatest part of this thesis we are concerned with generating photons of high coherence, with as little dephasing as possible. However, in applications such as spin readout, scattering rates and the need for recycling transitions take precedence.
Phrased differently, in this thesis we discuss resonant generation of single photons from single quantum dots and tunnel-coupled quantum dot molecules in the context of quantum information processing.

In the introduction we cover the basics of what quantum dots (QDs) are and give a brief overview on different types of QDs and their properties. We will put this work in a wider context by presenting the main motivation, quantum information processing, and review the standard criteria required for a physical realisation of a

quantum bit and the transfer of quantum mechanical information via flying quantum bits. Chapter 2 provides the theoretical background for the thesis. It covers light-matter interaction for the simplest case of a two-level system. This forms the theoretical basis to calculate the properties of resonance fluorescence and links to the standard techniques of quantum optical interferometry, namely the first- and second-order correlation functions. Chapter 3 introduces the experimental system and lab techniques, from sample processing to resonant spectroscopy. Applying these techniques, Chapter 4 translates the resonance fluorescence theory from Chapter 2 into experiments, highlighting the near-ideal behaviour of QD optical transitions in the low power limit of resonant excitation. This includes the direct observation of highly coherent scattering, which has remained largely unexplored for solid-state single photon emitters. Deviations from this ideal behaviour are explored in the second half of the chapter, where we reveal signatures of exciton-phonon coupling, effects of nuclear spin dynamics, and spectral wandering in the statistical properties of resonance fluorescence. Chapter 5 investigates properties of optically induced electric fields in our QD device structure. Chapter 6 demonstrates the potential of shaped single coherent photons for quantum interference applications, exemplified in two-photon interference measurements in a Hong-Ou-Mandel interferometer. Chapter 7 illustrates single-shot spin readout in a vertically stacked tunnel-coupled quantum dot molecule. Finally, conclusions and a very brief outlook on further experimental work are given in Chapter 8.

1.1 Quantum Information Processing

Quantum computing proposes to make use of intrinsically quantum mechanical features such as superposition of states and entanglement. Whereas classical bits take only the values `0` or `1`, the state of a quantum bit, or short *qubit*, is given by a linear superposition of its two basis states $|\psi\rangle = c_0|0\rangle + c_1|1\rangle$, where the coefficients are in general complex. It has been shown that some problems can be solved more 'efficiently' using qubits, most notably Shor's algorithm to factoring high digit numbers [5]. In addition to these improvements on classical computing, new, entirely quantum mechanical concepts can be realised, with quantum cryptography and quantum key distribution as the high profile applications which are

already commercially available

1.1.1 DiVincenzo's 5 + 2 and quantum optical networks

A set of requirements a physical qubit needs to fulfill has been formulated by DiVincenzo and co-workers in 2000 [4] which quickly became the Commandments of quantum computing. We quote them here directly:

1. *A scalable physical system with well characterised qubits.* What are the qubit basis states and how are they coupled? What other states or interactions may play a role? The scalability requirement is more involved; we need not only consider qubit-qubit coupling, but also the physical resources involved.

2. *The ability to initialise the state of the qubits to a simple fiducial state, such as* $|000\ldots\rangle$. We need to set the exact state (phase and amplitude) of the system before any operations are performed.

3. *Long relevant decoherence times, much longer than the gate operation time.* In short, a quantum state loses memory of its phase (dephasing) and amplitude (relaxation) after some time and any operation on a state that is no longer well defined is meaningless. Mechanisms for error correction exist, see for instance Ref. [6] and the standard estimate is that the decoherence time needs to be larger than the gate operation by a factor of $10^4 - 10^5$.

4. *A set of universal quantum gates.* Any operation can then be broken down into a number of gate operations. For a single qubit this translates to having full control over amplitude and phase of the qubit. Conceptually, the qubit state is visualised as a point on the surface of a sphere (*Bloch sphere*) and experimentally we need to be able to reach any point on the surface.

5. *A qubit-specific measurement capability* to read out the results of a set of operations.

The starting point to any physical implementation is to identify a two-level system that serves as qubit. Two-level systems or quasi-two-level systems can be found in many areas of physics, so there is a wealth of qubit candidates. A number of these are presented in Ref. [7], or more recently in Ref. [8]. Electron or hole spins in quantum dots are attractive candidates as they can be controllably introduced, spin states can be manipulated optically, and/or using external electric and magnetic fields. Equally important, research suggests very long decoherence times. We will elaborate on the performance of spins in QDs in the context of these requirements in section 1.4.
The last two requirements are slightly separate from the previous ones; they are concerned with communicating quantum information between separate qubits and over macroscopic distances.

6. *The ability to interconvert stationary and flying qubits.* This translates to creating entanglement between the stationary qubit, e.g. the QD spin, and a photon.

7. *The ability faithfully to transmit flying qubits between specified locations*, which requires a communication channel.

Requirements 6 and 7 lead to the vision of a quantum optical network we mentioned earlier - the Quantum Internet. Figure 1.1 from Ref. [2] shows a graphical representation of the concept. Theoretical proposals based on this idea are already well-developed.

1.2 Semiconductor quantum dots

In general, QDs (sometimes called quantum boxes) refer to semiconductor structures that confine electrons (or holes) in nanoscale potentials in all three spatial dimensions. As such they show many properties known from atoms: The three-dimensional quantum confinement gives rise to a δ-function-like density of states (i.e. discrete energy levels) and a shell structure is observed when electrons are added one by one [9; 10; 11]. Single quantum dots have been termed 'artificial atoms' for these reasons. Semiconductor quantum dots have been the subject of

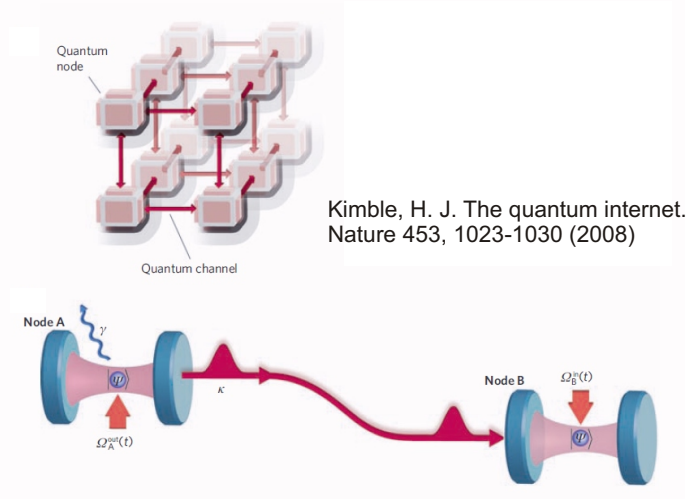

Figure 1.1: Illustration of the quantum internet as a network of nodes connected by non-classical communication channels (top) and the transfer of quantum information between two qubits in cavities. Reproduced from Ref. [2].

much research during the past 20 years. First proposed by Arakawa and Sakaki in 1982 as highly efficient and temperature-independent emitters in the active areas of semiconductor diode lasers [12], they are now used in a number of research areas.

Realisation of these structures was made possible following the advances in fabrication techniques such as molecular beam epitaxy or metalorganic chemical vapour deposition [13] that allow layer by layer growth of semiconductors while controlling the composition of each layer.

There are two main techniques for creating quantum dots: self-assembly and electrical definition. Both types of dots are commonly used in experiments aiming to control quantum properties like the electron spin and will be briefly introduced:

- Electrically defined QDs: metallic surface gates above a two-dimensional electron gas at an interface, typically GaAs/AlGaAs, can be used to deplete the electron gas below them, isolating small islands of electrons from the electron gas. The small size of the islands leads to quantisation in the remaining two dimensions. These electrically defined dots are also called *lateral* QDs and the strength and shape of their confining potential can be

conveniently modified by changing the gate voltage, allowing an all-electric approach to spin control. In such a way tunnel-coupled double and triple QD structures have been realised [14].

- *Self-assembled* dots: the quantum dots used in this study were grown in *Stranski-Krastanov* mode[1] [17]. Layered semiconductor structures are created using molecular beam epitaxy. A higher bandgap substrate layer, typically GaAs, is grown, followed by $\sim$ two monolayers of a lower bandgap material, InAs in our case. This is called the wetting layer. As a consequence of local strain fields due to the mismatch of lattice constants between two layers islands form in the wetting layer at a critical thickness. The growth conditions determine size and shape of these islands, hence the confinement energy. Self-assembled QDs are usually lens-shaped with a diameter of a couple of tens of nanometres and a stronger confinement in growth (z-) direction (few nm). The wetting layer containing the QDs is overgrown with GaAs, in some cases only partially, such that the QD height can be controlled in an additional annealing step. When another InAs wetting layer is added 10-20 nm above the previous, QDs nucleate preferentially on top of QDs in the first layer, thus vertically coupled QD molecules are created. Gating the sample allows control over the number of charges resident in the QD. For an introduction and a review of QD growth see for instance Ref. [18].

1.2.1 Quantum information, metrology and mesoscopic physics

QDs provide optically addressable two-level systems in the the solid state with good optical properties. Excited state lifetimes on the order of one nanosecond promise high single photon emission rates. This makes QDs attractive for quantum key distribution. Electrically driven single photon sources have been

[1] There are other important self-assembly mechanisms that lead to creation of quantum dots, such as precipitation of colloidal QDs (e.g. CdTe and CdSe) in solution[15], or QDs formed as interface fluctuations in a quantum well [16]. For the purpose of spin control the electrically defined QDs and Stranski-Krastanov QDs offer the most desirable properties and are used in current research.

developed [19] and tested in laboratories [20].
The confinement of single spin carriers provides partial protection from the solid-state environmental effects that rapidly dephase and relax any unprotected initially well-defined states. Spin manipulation, taking advantage of the optically excited states, allows gate operation times of picoseconds [21; 22] which is considerably faster than using electric fields or microwave excitation.
Spins and charges in quantum dots are not completely isolated, however, and the question of how atom-like these artificial atoms really are is an important one to answer. What role does the semiconductor environment play? Bound electron-hole pairs in QDs, excitons, still interact with the lattice phonons, electron and exciton spins experience the dynamics of the nuclear spin bath via the hyperfine interaction. QD transition energies are sensitive to electric field fluctuations in the environment, dynamics of nearby charge traps or neighbouring QDs. These effects pose challenges to quantum information applications, where unwanted interaction should be kept to a minimum, but open up other opportunities.
The sensitivity to environmental effects can be exploited for metrology applications. This has been spectacularly demonstrated for magnetometry with the nitrogen vacancy centre in diamond [23]. For QDs, electrometry has been proposed and demonstrated [24]. At the same time, optical thermometers based on colloidal QDs are advocated in biological sciences (see for example Ref. [25]).
The environmental effects on the QD optical properties are topic of section 4.2 in Chapter 4, and Chapter 5 contains an application of QD electrometry.// Next we look at the QD energy level structure in more detail.

1.3 QD level structures

This section contains a brief discussion of the level structure for the neutral and the negatively charged QD ground states. The effects of external electric and magnetic fields of the levels are touched upon, and we introduce some interactions with the solid-state environment. These will be picked up again at the appropriate places in the experimental chapters.

1.3.1 Exciton fine structure

We are working with QDs which are either empty or single electron charged in their ground state. The excited states, accessible via absorption of a photon, are then the neutral exciton (a single electron-hole pair) and the negatively charged exciton (called trion), respectively. The heavy- and light-hole bands are strongly separated in quantum confinement, so that holes in the QD are to a good approximation heavy-holes with total angular momentum $J_{\mathrm{hh}} = 3/2$[1]. The energy and fine structure of the optical transitions are governed by Coulomb interactions which we separate into direct Coulomb interaction and exchange interaction.
Direct Coulomb interactions for two particles a and b are, in general, given by

$$V_{\mathrm{Coulomb}} = \int\int d\mathbf{r}d\mathbf{r}' \left|\mathbf{r}-\mathbf{r}'\right|^{-1} \phi^a(\mathbf{r})^* \phi^b(\mathbf{r}')^* \phi^a(\mathbf{r}) \phi^b(\mathbf{r}'), \tag{1.1}$$

where the $\phi^i(\mathbf{x})$ are the orthonormal wavefunctions of particles i (electron e or hole h) at location $\mathbf{x}$. Exchange interaction

$$V_{\mathrm{exchange}} = \int\int d\mathbf{r}d\mathbf{r}' \left|\mathbf{r}-\mathbf{r}'\right|^{-1} \phi^a(\mathbf{r})^* \phi^b(\mathbf{r}')^* \phi^a(\mathbf{r}') \phi^b(\mathbf{r}) \tag{1.2}$$

has consequences for the fine structure of the neutral exciton. Neglecting exchange, there are four degenerate neutral exciton states at zero magnetic field: $\uparrow\Downarrow$, $\downarrow\Uparrow$, $\uparrow\Uparrow$ and $\downarrow\Downarrow$, where single-lined arrows denote electron spin projection and double-lined arrows the heavy hole projections. Creation and recombination of $\uparrow\Downarrow$, $\downarrow\Uparrow$ excitons is allowed by electric dipole selection rules and hence they are 'bright', while the $\uparrow\Uparrow$ and $\downarrow\Downarrow$ excitons are forbidden and 'dark'. Electron-hole exchange gives rise to three terms [28]: The isotropic exchange splits dark and bright excitons by an energy δ_0. The anisotropic exchange δ_1 hybridises the two bright excitons in the absence of magnetic field into orthogonal, linear superpositions $\uparrow\Downarrow \pm \downarrow\Uparrow$ [29]. Their splitting is known as XY-splitting. The dark excitons are split by δ_2. Anisotropic electron-hole exchange vanishes for QDs with cir-

[1] The approximation of holes in QDs as pure heavy-holes is a valid approximation in many cases, but QDs do exhibit a small degree of mixing with the light-holes states $\Uparrow_{+1/2}$ and $\Downarrow_{-1/2}$. For single QDs a spread of admixtures has been observed; for our single QD samples the admixture is typically of a few percent [26]. In coupled QDs heavy-light hole mixing can be enhanced through an offset of the vertically stacked QDs relative to each other [27].

cular symmetry, but we observe it for all QDs in our sample. The exchange Hamiltonian for basis states $\uparrow\Downarrow$, $\downarrow\Uparrow$, $\uparrow\Uparrow$, $\downarrow\Downarrow$ is [28]

$$H_{\text{exchange}} = \frac{1}{2}\begin{pmatrix} \delta_0 & \delta_1 & 0 & 0 \\ \delta_1 & \delta_0 & 0 & 0 \\ 0 & 0 & -\delta_0 & \delta_2 \\ 0 & 0 & \delta_2 & -\delta_0 \end{pmatrix}. \tag{1.3}$$

1.3.2 The nuclear Overhauser field

We have to keep in mind that, while QDs are termed artificial atoms and show some atomic-like properties, charges are confined in a mesoscopic environment and interactions with the solid-state matrix can give rise to very 'un-atomic' effects.

A self-assembled In/GaAs quantum dot consists of $N \sim 10^5$ atoms and each one of them has a nuclear spin (spin 3/2 for Ga and As and 9/2 for In). A single electron or hole spin confined in the QD interacts with the nuclear spins through the hyperfine interaction. For electrons the dominant term of this interaction [30] is the Fermi contact interaction[1]

$$H_{HF} = \sum_k A_k \hat{\mathbf{S}} \cdot \hat{\mathbf{I}}_\mathbf{k} \delta\left(\mathbf{r} - \mathbf{R}_k\right), \tag{1.4}$$

where $\mathbf{R}_k$ gives the position of the kth nucleus with spin $\hat{\mathbf{I}}_\mathbf{k}$, $\mathbf{r}$ the position of the electron with spin $\hat{\mathbf{S}}$, and the hyperfine coupling constant A reflects the spatial dependence of the electron wave function in the QD. The effect of nuclear spins is commonly described as an effective magnetic field $\mathbf{B_N}$ acting on the electron. The magnitude of this field, named *Overhauser* field, is then given as

$$\mathbf{B_N} = \frac{\sum_k A_k \hat{\mathbf{I}}_\mathbf{k}}{g\mu_B}. \tag{1.5}$$

The Overhauser field effect can be understood as the electron spin precessing in a time-varying magnetic field, where the field strength and direction at any time is

[1] We note that other terms, such as dipole and quadrupole interaction play a role too, see for instance Refs. [31; 32].

given by the sum of all nuclear spins vectors. If there is no preferential alignment of the nuclear spins, for instance in the absence of an external magnetic field, then the individual spins are randomly oriented. This gives rise to a spherical symmetry of the Overhauser field distribution. While the mean of the Overhauser field is zero, the most likely configuration has a finite field strength.
The Overhauser field evolves on timescales of microseconds [33] while remaining frozen on shorter timescales. Its root-mean-square magnitude can be estimated from the number of nuclear spins and is typically on the order of a few tens of millitesla [34].
Eq. (1.4) includes electron-nuclear spin flip-flop terms, and hyperfine interaction is the dominant source of spin relaxation at low magnetic fields. This relaxation is due to direct coupling between the ground states. At finite fields the incommensurate splitting of the QD ground state compared to the nuclear spin splitting renders spin relaxation due to the flip-flop terms inefficient. However, electric-dipole forbidden transitions can be enabled by concomitant nuclear spin flips. Research into this link between electron spin and nuclear polarisation has revealed interesting physics [35; 36] and partial control of the nuclear spins has been demonstrated [37; 38; 39; 40]. A controllable nuclear field can be employed as resource in quantum control [41].
The influence of the nuclear spin bath on QD emission spectra will be discussed in Chapter 4, section 4.2.3.

1.3.3 Trion levels under magnetic and electric fields

Zeeman shifts. So far research into electron or hole spins in optically active QDs has focussed mostly on single spins as qubits. Experimental studies into other approaches, such as using two spins, have only emerged recently [42; 43; 44]. Our approach also concentrates on a single spin. Under magnetic field the degeneracies of the single electron ground states and the excited trion states are lifted according to the electron (g_e) and hole (g_h) g-factors:

$$H_{\text{Zeeman}} = -\mu_B \left(g_{e,z} \mathbf{S_{e,z}} - \frac{g_{h,z}}{3} \mathbf{J_{e,z}} \right) \mathbf{B_z},$$

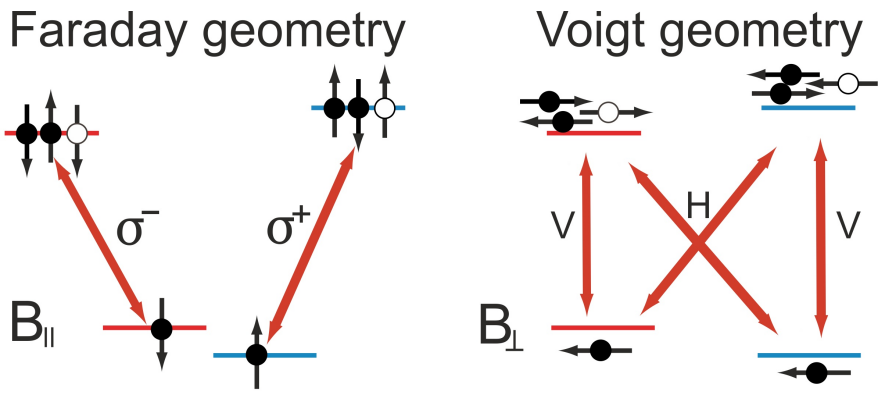

Figure 1.2: Selection rules for Faraday and Voigt geometry under magnetic field. The spin and charge states for each level are given: arrows denote spin projection for electrons (filled circles) and holes (empty circles). In the excited states the two electrons form a spin singlet, so that the total spin is determined by the hole spin projection.

where μ_B is the Bohr magneton and we have chosen the magnetic field to be in the z-direction and neglected the diamagnetic shift, which adds a quadratic dependence on the magnetic field [45]. Two geometries are being explored in experiments: in Faraday geometry the magnetic field is parallel to the sample growth axis and coincides with the direction of optical axis. In Voigt geometry the magnetic field is perpendicular to the growth and optical axis. Selection rules differ for these two geometries. We show the level structure and selection rules for the trion transitions in Fig. 1.2.

Faraday geometry is used in Chapter 5. The solid-state environment (see previous section) relaxes the selection rules, so that there is a small probability of relaxation into the opposite ground state when cycling one of the allowed transitions (branching ration $\sim$ 200:1). The ground states are very weakly coupled, leading to a finite spin-flip rate (see 1.3).

Stark shifts Excitons in QDs have a large permanent electron dipole moment, as the electron and hole are physically separated by a $\sim$ nanometre distance [46]. Due to the local confinement in the low bandgap QD, the exciton energy can be tuned over many times its radiative linewidth by external electric fields without ionising. The energetic shift of QD photoluminescence as a function of applied

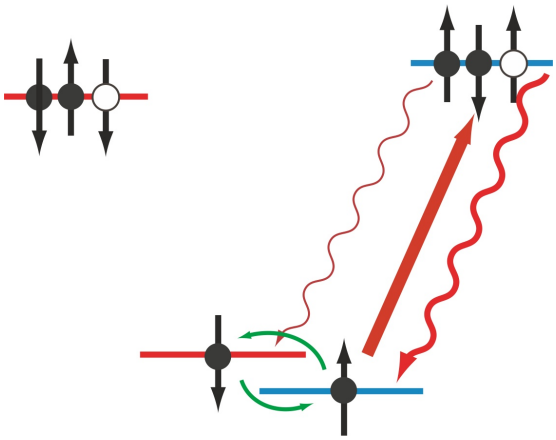

Figure 1.3: Relaxation of selection rules in the trion transition as a result of interactions with the environment.

vertical field F is dominated by the change of the exciton energy and contains both linear and quadratic terms:

$$\Delta E_{\text{exciton}} = -\mu F_{\text{applied}} + \alpha F^2_{\text{applied}} \,, \tag{1.6}$$

where μ is the permanent dipole and α the polarisability. In our structures the Stark shift is entirely linear to a good approximation; the quadratic term has been observed for larger applied fields in different QD device structures [46; 47].

1.4 Coherent control of single spins: state of research

Here, we summarise the current state of research into coherent control of spins in QDs. It will become obvious that not all DiVincenzo criteria can be realised to equal extents in single QDs and how coupled QDs, quantum dots molecules (QDMs), offer a natural extension that allows spin state readout.
A complete quantum operation on a single qubit can be separated into three parts: state preparation/initialisation, coherent manipulation and state readout at the end. From the DiVincenzo criteria we pick the three requirements relating to spin control and the requirement on coherence times. We give an overview

of recent progress in these areas, focussing mostly on optically active QDs. The numbering below follows the DiVincenzo criteria introduced earlier, so, having chosen spin up and down as basis states, we start with number two:

2. **State initialisation** was first demonstrated in 2006 [48]. It relies on the state mixing in Faraday geometry described above (see Fig. 1.3). A spin-flip Raman transition occurs after cycling a trion transition for a few μs, and provided that spin relaxation is much slower than this optical 'spin pumping', the spin state is initialised. Transferring this protocol into Voigt geometry, optical spin pumping initialises the spin within a few ns [49] . This is possible as the excited trion state is coupled equally to both single electron spin ground states. However, initialisation fidelities can suffer from detuned pumping via the other excited state (cf. Fig. 1.2). Similar optical pumping has also been observed for single holes [50].

3. Much effort has also been put into determining spin **coherence** times (the dephasing time T_2) and prolonging it. We distinguish here between the inhomogeneous dephasing time $T_2^\star$ which is derived from a time-averaged measurement and equivalent to an ensemble dephasing time, and the homogeneous dephasing time T_2 which would be measured for a single spin in a single measurement. The inhomogenous dephasing time $T_2^\star$ of the electron spin is consistently found to be on the order of 1 ns, limited by averaging over the different Overhauser field configurations for individual measurements [39; 51; 52; 53]. However, the Overhauser field is fluctuating slowly ($\sim$ μs or slower [33]), so we should expect homogeneous T_2 times in the microsecond range as well. Optical spin-echo of a single spin [52] and manipulation of a spin ensemble subset [54] do indeed recover $T_2 \sim$ few μs.
Use of dynamic decoupling techniques has resulted in a tremendous improvement of these numbers for electrically defined QDs, reaching dephasing times in excess of 100 μs [55]. In parallel, research efforts directed at influencing the nuclear spin bath and quieting down the fluctuations have shown some success [37], and coherent population trapping measurements suggest an improved inhomogeneous dephasing time of a few microseconds. Further, qubits encoded in the two-electron singlet-triplet basis can be en-

gineered to be insensitive to environmental fluctuations and the inhomogeneous dephasing time is in on the order of 100 ns, or longer [44].
Finally, much attention has also been paid to hole spin qubits due to their reduced Fermi contact hyperfine interaction. Inhomogeneous dephasing times in the range of 2 to 20 ns have been reported [43; 56; 57], and $T_2 \sim 1$ μs with a a Hahn spin-echo [56].
With ps manipulation capabilities, these coherence times would be sufficient for $10^4 - 10^5$ operations, i.e. error correction. We note, that each optical operation may still induce some decoherence, however, so it remains to be seen what the performance in actual applications will be like.

4. The requirement of a universal **set of quantum gates** is experimentally equivalent to having full control over the Bloch sphere for a single qubit. In order to reach any point on the Bloch sphere rotations about two axes are necessary. Typically one rotation axis can be associated with controlling the amplitude of the qubit (rotations in $zx-$ or $zy-$plane) at a fixed phase, the other rotation sets the phase of the qubit (xy-plane). Much progress has been made in coherent optical control of electron spins. Complete control has been achieved for single spins [22; 58] and an ensemble subset [59]. Press *et al.* [22] and Kim *et al.* [58] operate in Voigt geometry, where the electron ground states can be coupled using two-photon Raman transitions, cf. Fig. 1.2. Rabi oscillations between $\uparrow$ and $\downarrow$ are observed, demonstrating control over the qubit amplitude. Fast Larmor precession in a high magnetic field provides the second rotation for Press *et al.* as is evidenced by Ramsey interference. In [58] the free Larmor precession is complimented by geometric phases that can be imparted to one spin component of a coherent superposition of $\uparrow$ and $\downarrow$. This adds control to the otherwise free precession about the magnetic field.
The same level of control has been demonstrated for single hole spins in a QD [43; 56; 57]. Further, research conducted in the United States's Naval Research Laboratory could extend the control scheme to two independent spins (both electrons and holes) in tunnel-coupled QD molecules. Employing exchange interaction between the spins and geometric phase gates

allowed the implementation of two-qubit rotations - the first demonstration of both single- and two-qubit control for QDs [42; 43].
With regard to electrically defined QDs, rotations of 2-electron qubits in electrically defined double QDs have been achieved via control of the exchange interaction [51] and more recently by creating a magnetic field gradient across the QDM [38]. The combination of the rotations enable full control over the Bloch sphere.
In Faraday geometry spin rotations have been performed using microwaves [60]. While operation in Voigt geometry allows completion of a gate operation in a few tens of ps [22], the need to rely on microwave rotations have limited spin manipulation in Faraday geometry to $\sim$ 100 ns.

5. Spin **readout** has mostly relied on averaging the results of many ($> 10^4$) measurements to obtain reliable results. Attempting to directly measure the population of a spin state in Voigt geometry leads to spin shelving within a few optical cycles, so that only 1-2 photons are scattered in each readout attempt. Standard photon collection and detection efficiencies are around 0.1-1% [53; 61], requiring $\sim 10^4$ attempts to distinguish between spin up and down states. The collection and detection rates are mostly limited by the photon extraction from the high-index semiconductor into free space. Research to remedy this problem is progressing well though, with reports of 70 % sample outcoupling efficiencies in specialised sample designs [62]. Single-shot readout in Faraday geometry is less hopeless; the reduced back-action of the readout laser causes spin shelving in ~ 1 μs [26] here and state-of-the-art collection efficiencies should allow single-shot readout now. Non-destructive readout techniques, such as Faraday rotation [63] and Kerr rotation [64] have been successfully applied to determine the spin state of a single electron, but require integration over many milliseconds.
The first successful attempt at single-shot spin readout is detailed in Chapter 7 of this thesis. We use a QD molecule consisting of two vertically coupled QDs where a transition to a molecular excited state is spin-sensitive and recycling.

6. **Spin-photon entanglement:** The sixth of the Divincenzo criteria was

demonstrated independently by three groups recently [53; 65; 66]. They employ a single electron spin in a single QD in Voigt geometry. As each excited state forms a Λ-system with the two ground states the polarisation (and frequency) of a single scattered photon is entangled with the state of the QD electron spin. Measurements of spin-photon correlations in two independent bases were then used to prove the entanglement.

Chapter 2

Light-matter interaction of two levels: resonance fluorescence

In this chapter we recap the near-resonant light-matter interaction of a simple two-level system. This is a standard topic in quantum optics textbooks and as such it would be pointless to provide a comprehensive treatment here. However, Chapter 4 and, to some extent, Chapter 6 are concerned with determining the extent to which optical QD transitions confirm with the predictions for ideal two-level systems. So we give here a summary of theoretical background and sketch out derivations of resonance fluorescence properties. Important reference for this chapter are Loudon's *The Quantum Theory of Light* [67], chapters 2, 7.9 and 8 in particular, *Quantum Optics* by Scully and Zubairy [68], chapters 5 and 10, and *Elements of Quantum Optics* by Meystre and Sargent [69], chapters 4 and 16.

The aim of this chapter is to sketch out how we can derive the properties of the emission from a resonantly driven two-level system. The resonance fluorescence is defined by its spectral and statistical properties, which can be calculated - and measured - through field- and intensity-correlation functions. The resonance fluorescence spectrum, first derived by Mollow in 1969 [70], can be found with a fully quantum mechanical treatment, i.e. with both quantised fields and a quantised emitter, see Ref. [71] for example. A semi-classical approach, where the optical field is classical, gives the same results though, and for simplicity this

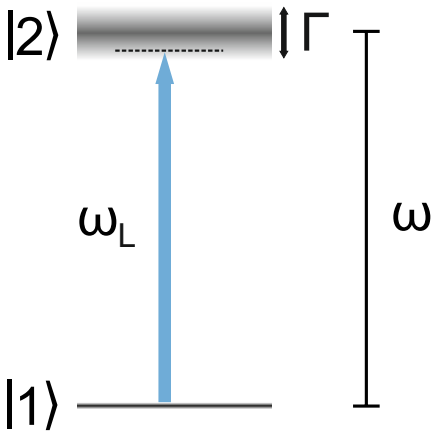

Figure 2.1: Sketch of two-level system and optical field. The ground ($|1\rangle$) and excited ($|2\rangle$) states are coupled by a monochromatic field of energy $\hbar\omega_{\mathrm{L}}$ which is close to the energy difference for the two levels. Spontaneous emission broadens state $|2\rangle$ and its population relaxes with rate Γ.

approach will be followed. Details of the calculation can also be found in Ref. [72], a subsequent paper by Mollow. The optical Bloch equations obtained this way not only reveal the steady-state behaviour of populations and coherences of the two-level-system for near-resonant driving frequencies, but solving the density matrix equation of motion is also key to obtaining the first-order correlation function, and hence the spectrum of the scattered light (the resonance fluorescence). The intensity correlation function can be derived in a similar fashion.

2.1 Optical Bloch equations and the density matrix

The premise. First we introduce the parameters of the two-level system and the light field. Figure 2.1 shows a sketch of the energy levels. Ground and excited states, denoted $|1\rangle$ and $|2\rangle$, are separated by an energy $\hbar\omega$. For a QD neutral exciton transition the ground state would correspond to the crystal ground state, while the excited state is a single exciton. In the sketch the excited state is broadened due to spontaneous radiative relaxation to the ground state, and the width Γ indicates the decay rate. In the absence of other interactions, this

decay rate is given by the inverse excited state lifetime which we denote T_1. This timescale governs the decay of excited state population, but also the decay of the QD polarisation. To account for additional dephasing processes of the polarisation we introduce the dephasing time T_2 here. We distinguish between radiative dephasing and any additional pure dephasing, quantified by γ_p:

$$\frac{1}{T_2} = \frac{1}{2T_1} + \gamma_\mathrm{p}. \tag{2.1}$$

The optical field is a single monochromatic mode of frequency $\omega_\mathrm{L} = \omega + \Delta$, where Δ is the detuning from the QD resonance. The QD-field interaction is conveniently described using the QD density matrix:

$$\begin{aligned}\rho &= |\Psi\rangle\langle\Psi| \\ &= \left(c_1(t)|1\rangle + c_2(t)|2\rangle\right)\left(c_1^\star(t)\langle 1| + c_2^\star(t)\langle 2|\right) \\ &= |c_1|^2|1\rangle\langle 1| + c_1c_2^\star|1\rangle\langle 2| + c_2c_1^\star|2\rangle\langle 1| + |c_2|^2|2\rangle\langle 2|\end{aligned} \tag{2.2}$$

where the QD state $|\Psi\rangle$ is a linear superposition of its two basis states, with time-dependent coefficients $c_i(t)$. The density matrix elements ρ_{ij} are obtained as

$$\rho_{ij} = \langle i|\rho|j\rangle. \tag{2.3}$$

The diagonal elements give the populations and satisfy $\rho_{11} + \rho_{22} = 1$. The off-diagonal elements $\rho_{12} = \rho_{21}^\star$ are related to the QD polarisation and called the 'coherences'.

Optical Bloch equations. The evolution of the density matrix elements for the QD-light interaction is described by the equation of motion

$$\dot{\rho} = -\frac{i}{\hbar}[\mathcal{H}_\mathrm{int}, \rho] - \frac{1}{2}(\gamma\rho + \rho\gamma). \tag{2.4}$$

Here the first term describes the QD-field interaction and the second term adds population relaxation. The interaction Hamiltonian contains the electric dipole

interaction with the radiation field and we give it in the interaction picture here:

$$\mathcal{H}_{\text{int}} = -\hbar\Omega U_0^\dagger(t)\left(e^{-i\phi}|2\rangle\langle 1| + e^{i\phi}|1\rangle\langle 2|\right)U_0(t)\cos\omega_{\text{L}}t\,. \tag{2.5}$$

The radiation field drives transitions between the QD ground and excited states and the Rabi frequency Ω describes the rate. It is linked to the amplitude of the radiation field $\mathcal{E}$ and the dipole matrix element $\mathbf{D_{12}} = \langle 1|x|2\rangle$ (here for a field polarised along x) as

$$\Omega = \frac{|\mathbf{D_{12}}|\,\mathcal{E}}{\hbar}.$$

With interaction operator $U_0(t) = e^{-i\omega_2 t}|2\rangle\langle 2| + e^{-i\omega_1 t}|1\rangle\langle 1|$, where $\hbar\omega_{1,2}$ correspond to the energies of ground and excited states, and $\omega = \omega_2 - \omega_1$ the interaction Hamiltonian becomes

$$\mathcal{H}_{\text{int}} = -\frac{\hbar\Omega}{2}\left(e^{i\omega t - i\phi}|2\rangle\langle 1| + e^{-i\omega t + i\phi}|1\rangle\langle 2|\right)\left(e^{i\omega_{\text{L}}t} + e^{-i\omega_{\text{L}}t}\right)\,. \tag{2.6}$$

Multiplication of the two brackets on the right-hand side yields four terms, two of which oscillate at the difference frequency $\pm(\omega - \omega_{\text{L}})$, and two oscillating at the sum frequency $\pm(\omega + \omega_{\text{L}})$. Discarding of the latter two in the rotating wave approximation and writing the difference frequency as Δ we arrive at the final interaction picture Hamiltonian:

$$\mathcal{H}_{\text{int}} = -\frac{\hbar\Omega}{2}\left(e^{-i\phi}|2\rangle\langle 1|\,e^{i\Delta t} + e^{i\phi}|1\rangle\langle 2|\,e^{-i\Delta t}\right)\,. \tag{2.7}$$

For the relaxation terms in Eq. (2.4) we assume for now just the excited state lifetime T_1. The matrix $\gamma\rho + \rho\gamma$ then becomes

$$\gamma\rho + \rho\gamma = \begin{pmatrix} 0 & \frac{\rho_{12}}{T_1} \\ \frac{\rho_{21}}{T_1} & \frac{2\rho_{22}}{T_1} \end{pmatrix}. \tag{2.8}$$

Using Eq. 2.7 and Eq. 2.8 in Eq. 2.4 we evaluate the density matrix elements' equation of motion:

$$\dot{\rho_{12}} = i\frac{\Omega}{2}e^{-i\Delta t}\left(\rho_{22} - \rho_{11}\right) - \frac{\rho_{12}}{2T_1} \tag{2.9}$$

$$\dot{\rho_{22}} = i\frac{\Omega}{2}\left(e^{i\Delta t}\rho_{12} - e^{-i\Delta t}\rho_{21}\right) - \frac{\rho_{22}}{T_1} \tag{2.10}$$

With the substitution $\tilde{\rho_{12}} = e^{i\Delta t}\rho_{12}$ we can take out the oscillating factors. Further, we include pure dephasing processes phenomenologically by replacing $2T_1$ in Eq. (2.9) with T_2. Then the equations of motion are equivalent to the Bloch equations derived for nuclear magnetic resonance of spin 1/2 systems [73] and hence called the *optical Bloch equations*:

$$\dot{\tilde{\rho_{12}}} = i\frac{\Omega}{2}\left(\tilde{\rho_{22}} - \tilde{\rho_{11}}\right) - \tilde{\rho_{12}}\left(\frac{1}{T_2} - i\Delta\right) \tag{2.11}$$

$$\dot{\tilde{\rho_{22}}} = i\frac{\Omega}{2}\left(\tilde{\rho_{12}} - \tilde{\rho_{21}}\right) - \frac{\tilde{\rho_{22}}}{T_1}. \tag{2.12}$$

Steady-state solutions. To relate the Bloch equations to measurable quantities we have to link the electric field operators for QD emission to the density matrix elements. To this end we introduce the transition operators first.

$$\sigma_- = |1\rangle\langle 2| \tag{2.13}$$

$$\sigma_+ = |2\rangle\langle 1| \tag{2.14}$$

The time dependence of their expectation value follows

$$\langle\sigma_-(t)\rangle = \tilde{\rho_{21}}e^{-i\omega_L t}\,. \tag{2.15}$$

The positive frequency part of the electric field operator is proportional to the lowering operator and defined as

$$\mathbf{E}^+\left(\mathbf{r},\hat{t}\right) = \frac{e\omega^2\mathbf{e_{sc}}\cdot\mathbf{D_{12}}}{4\pi\epsilon_0 c^2 r}\sigma_-\left(\hat{t}\right)\,. \tag{2.16}$$

$\hat{t}$ is the retarded time and $\mathbf{e_{sc}}$ the polarisation vector of the scattered field. Measuring the intensity of the scattered light is proportional to the single-time first-order correlation time of the field:

$$I \propto \int_0^T \mathrm{d}t \left\langle E^- \left(\hat{t}\right) E^+ \left(\hat{t}\right)\right\rangle \propto \int_0^T \mathrm{d}t \left\langle \sigma_+ \left(\hat{t}\right) \sigma_- \left(\hat{t}\right)\right\rangle . \tag{2.17}$$

With

$$\begin{aligned} \sigma_+ \left(\hat{t}\right) \sigma_- \left(\hat{t}\right) &= |2\rangle \langle 2| , \\ \left\langle \sigma_+ \left(\hat{t}\right) \sigma_- \left(\hat{t}\right)\right\rangle &= \tilde{\rho_{22}} \end{aligned} \tag{2.18}$$

we find that the intensity is proportional to the steady-state excited state population $\tilde{\rho_{22}}\left(t \to \infty\right) = \rho_{22,ss}^{\tilde{}}$. Taking $\dot{\tilde{\rho_{22}}} = 0$, $\dot{\tilde{\rho_{12}}} = 0$ in Eq. (2.11) and (2.12) we find

$$I \propto \rho_{22,ss}^{\tilde{}} = \frac{1}{2} \frac{\Omega^2}{\Delta^2 \frac{T_2}{T_1} + \frac{1}{T_1 T_2} + \Omega^2}. \tag{2.19}$$

The scattered intensity is actually composed of two parts[1]: $I = I_{\mathrm{coh}} + I_{\mathrm{inc}}$. The coherent term maps out the magnitude of off-diagonal density matrix elements as

$$I_{\mathrm{coh}} \propto \left|\rho_{12,ss}^{\tilde{}}\right|^2 = \frac{1}{4} \frac{\Omega^2 \left(\Delta^2 + T_2^{-2}\right)}{\left(\Delta^2 + \frac{1}{T_2^2} + \frac{T_1}{T_2}\Omega^2\right)^2} . \tag{2.20}$$

Figure 2.2 (left-hand side) provides a visualisation of the scattering intensity according to (2.19) for $T_2 = 2T_1$ as a function of detuning (in units of $1/\left(2\pi T_1\right)$) and square of the Rabi frequency Ω which scales as the power of the exciting field. The power scale is in units of the saturation power $\Omega_{\mathrm{sat}}^2 = 1/\left(2T_1^2\right)$. We see a saturation of the scattering intensity towards a steady-state population of $1/2$, and at the same time a broadening of the scattering response (power broadening)

[1] This can be seen in the quantum mechanical Langevin-Bloch equations which include a noise term. The noise term separates the spontaneous, incoherent emission originating from the influence of vacuum fluctuation on the QD dipole motion [69] from the coherent response of the dipole to the radiation field.

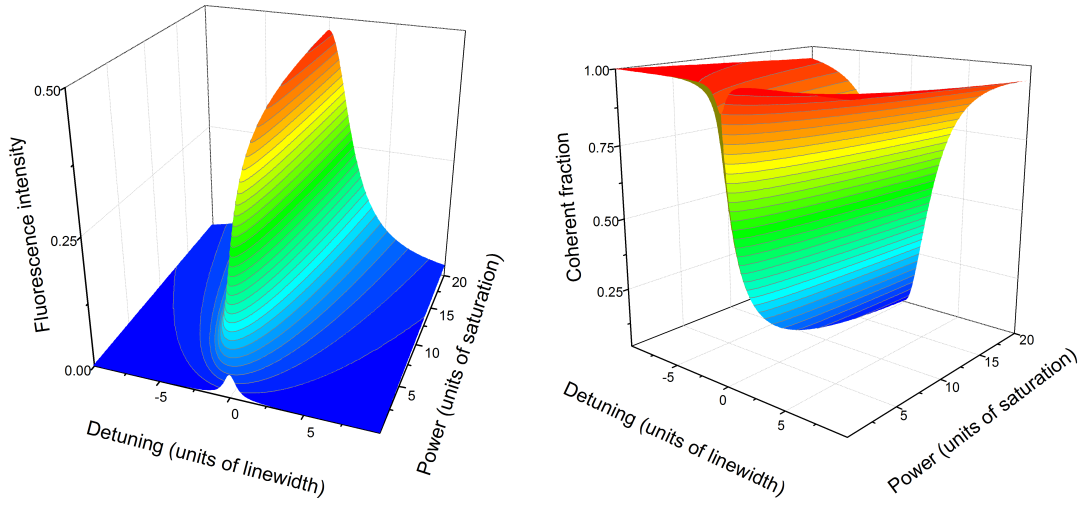

Figure 2.2: Plots of the total scattering intensity (left) and coherent fraction of the radiation (right). The linewidth is given by $1/(2\pi T_1)$ and the saturation power is proportional to $\Omega_{\text{sat}}^2 = 1/(2T_1^2)$.

as a function of excitation power. The plot on the right side shows the coherent fraction $F_{\text{coh}} = I_{\text{coh}}/I$ with the same parameters. Towards zero power, or strong detuning, the coherent part dominates the scattering. We assumed $T_2 = 2T_1$ for the two plots, which corresponds to an absence of pure dephasing. We illustrate the effect of pure dephasing on the coherent and incoherence intensity parts in Fig. 2.3 for the resonance condition ($\Delta = 0$). Panel a shows the power dependence of the coherent fraction for $T_2 = 2T_1$ (no pure dephasing) as blue curve, the green curve is for $T_2 = T_1$, while $T_2 = 0.5T_1$ for the red curve. In the right panel we show the total scattering intensity (black) together with the incoherent (blue) and the coherent (green) parts for a dephasing time $T_2 = T_1$. The coherent part reaches a maximum at the saturation point, where $F_{\text{coh}} = T_2/4T_1$. It approaches zero as the power is increased. The sensitivity of the coherent fraction to the pure dephasing rate makes it a good benchmark for measurements of T_2. We experimentally study the saturation behaviour for a single QD in Chapter 4.

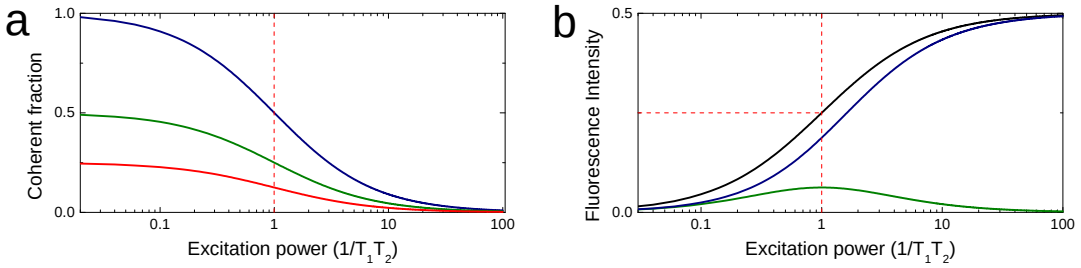

Figure 2.3: Influence of dephasing time on coherent and incoherent contributions to the fluorescence. a, coherent fraction for $T_2 = 2T_1$ (blue curve), $T_2 = T_1$ (green) and $T_2 = 0.5T_1$ (red).b, total scattering intensity (black), incoherent contribution (blue) and coherent contribution (green) for $T_2 = T_1$. The laser detuning is kept to zero detuning in both panels.

2.2 First-order coherence of resonance fluorescence

The first-order coherence of resonance fluorescence is evaluated through the correlation function

$$g^{(1)}(\tau) = \frac{\left\langle E^{-}\left(\hat{t}\right) E^{+}\left(\hat{t}+\tau\right)\right\rangle}{\left\langle E^{-}\left(\hat{t}\right) E^{+}\left(\hat{t}\right)\right\rangle} = \frac{\left\langle \sigma_{+}(t)\,\sigma_{-}(t+\tau)\right\rangle}{\left\langle \sigma_{+}(t)\,\sigma_{-}(t)\right\rangle}\,. \tag{2.21}$$

The challenge of evaluating $g^{(1)}(\tau)$ lies in calculating a two-time expectation value. The trivial case of $\tau = 0$ gives us

$$g^{(1)}(0) = 1\,. \tag{2.22}$$

Calculating Eq. (2.22) is made possible with the quantum regression theorem. It states that if the density matrices of a system (the two-level atom/QD) coupled to a reservoir (the radiation field modes) are uncorrelated at time $t = 0$, that is $\rho_{\text{system}-\text{reservoir}}(0) = \rho_{\text{system}}(0)\,\rho_{\text{reservoir}}(0)$, then the equation of motion for the two-time operator expectation values obeys that for the single-time operator expectation values. In other words, knowing the complete time dependence of the transition operators $\langle\sigma_{+}(t)\rangle$ and $\langle\sigma_{-}(t)\rangle$ is sufficient to calculate the first-order

coherence.

In particular, the equations of motion for the single- and two-time transition operator expectation values have the general solution [72]

$$\begin{aligned}\langle\sigma_-(t+\tau)\rangle e^{i\omega_L t+\tau} &= \alpha_1(\tau) + \alpha_2(\tau)\langle\sigma_-(t)\rangle e^{i\omega_L t} \\ &+ \alpha_3(\tau)\langle\sigma_+(t)\rangle e^{-i\omega_L t} \\ &+ \alpha_4(\tau)\langle\sigma_+(t)\sigma_-(t)\rangle \qquad (2.23)\end{aligned}$$

$$\langle\sigma_+(t)\sigma_-(t+\tau)\rangle e^{i\omega_L t} = \alpha_1(\tau)\langle\sigma_+(t)\rangle + \alpha_2(\tau)\langle\sigma_+(t)\sigma_-(t)\rangle e^{i\omega_L t} \qquad (2.24)$$

$$\begin{aligned}&+ \alpha_3(\tau)\langle\sigma_+(t)\sigma_+(t)\rangle e^{-i\omega_L t} \\ &+ \alpha_4(\tau)\langle\sigma_+(t)\sigma_+(t)\sigma_-(t)\rangle \qquad (2.25)\end{aligned}$$

Similar expressions hold for $\langle\sigma_+(t+\tau)\sigma_-(t+\tau)\rangle$ and $\langle\sigma_+(t)\sigma_+(t+\tau)\sigma_-(t+\tau)\sigma_-(t)\rangle$. In the two-time correlation function above the expectation values of the α_3 and α_4 vanish. Noting the relation between transition operator expectation values and the density matrix elements from (2.18) and that

$$\langle\sigma_-(t)\rangle = \tilde{\rho_{21}} e^{-i\omega_L t}\,, \qquad (2.26)$$

we conclude that a knowledge of the time evolution of the density matrix elements $\tilde{\rho_{12}}(t)$, $\tilde{\rho_{22}}(t)$ allows us to evaluate $g^{(1)}(\tau)$. Both derivation and the final solution for $\tilde{\rho_{12}}(t)$, $\tilde{\rho_{22}}(t)$, including finite detuning Δ and pure dephasing γ_p, are lengthy. For reference, a solution using Laplace transform was published by Torrey[1] [76] and we will not recreate it here. If we are interested in the stationary limit, that is, the steady-state first-order correlation function, we can take $t \to \infty$ and use the steady-state solutions to the optical Bloch equations in Eq. (2.25). From the first-order coherence $g^{(1)}(\tau)$ the emission spectrum follows directly as

$$S(\Delta\nu) \propto \int_0^\infty \mathrm{d}\tau \left\langle E^-(\tau) E^+(0)\right\rangle e^{-i\Delta\nu\tau} + \text{c.c} \qquad (2.27)$$

Explicit expressions for $g^{(1)}(\tau)$ and $S(\Delta\nu)$ are given in the Chapter 4 (Eq. (4.4) and (4.5)) and compared to the experimental measurements of QD resonance

[1] The original manuscript contains a number of typographic errors, for a corrected version see, for instance, Ref. [74], which contains only one mistake [75].

fluorescence.

2.3 Second-order coherence of resonance fluorescence

The second-order coherence of resonance fluorescence is defined by the second-order correlation function

$$g^{(2)}(\tau) = \frac{\langle E^-(t)\, E^-(t+\tau)\, E^+(t+\tau)\, E^+(t)\rangle}{\langle E^-(t)\, E^+(t)\rangle^2} = \frac{\langle \sigma_+(t)\, \sigma_+(t+\tau)\, \sigma_-(t+\tau)\, \sigma_+(t)\rangle}{\langle \sigma_+(t)\, \sigma_-(t)\rangle^2} . \tag{2.28}$$

Without the quantum regression theorem we can again only find the $\tau = 0$ value:

$$g^{(2)}(0) = 0 , \tag{2.29}$$

since $\sigma_+(t)\,\sigma_+(t) = |2\rangle\langle 1|\,|2\rangle\langle 1| = 0$ (and similarly for $\sigma_-(t)\,\sigma_-(t)$).
The formal derivation of the intensity correlation function follows the one outlined above for the field correlation function. However, we can arrive at the same result with a bit of physical insight. The experimental configuration relating to the intensity correlation function we are usually interested in consists of the time-resolved detection of a second photon conditioned on the detection of a first photon. A sketch of the experimental arrangement is provided in Fig. 2.4. The detection of the first photon projects the QD two-level system into the ground state. Measuring the averaged probability of photon detection at a subsequent time just maps out the excited state population

$$g^{(2)}(\tau) \propto \langle \sigma_+(\tau)\, \sigma_-(\tau)\rangle = \tilde{\rho_{22}}(\tau) \tag{2.30}$$

for the condition that $\tilde{\rho_{22}}(\tau = 0) = \tilde{\rho_{12}}(\tau = 0) = 0$. The normalisation is given by the steady state value of the excited state population. Using Torrey's solution

to obtain the time evolution of $\tilde{\rho_{22}}$ we find

$$g^{(2)}(\tau) = 1 - e^{-\eta|\tau|} \times \left(\cos(\mu|\tau|) + \frac{\eta}{\mu} \times \sin(\mu|\tau|) \right) , \tag{2.31}$$

where

$$\eta = \frac{1}{2} \times \left(\frac{1}{T_1} + \frac{1}{T_2} \right) ,$$
$$\mu = \sqrt{\Omega - \frac{1}{4} \times \left(\frac{1}{T_1} - \frac{1}{T_2} \right)^2} .$$

Figure 2.4 illustrates the three common interferometer types (used also in this thesis) to measure first- and second-order coherence, together with examplary curves for a strongly resonantly ($\Delta = 0$) driven two-level system. Panel a shows a cavity with a tunable mirror: a Fabry-Perot interferometer to record spectra. Panel b displays a Michelson interferometer for first-order coherence measurements, whereas panel c shows a Hanbury-Brown and Twiss interferometer for intensity correlation measurements. The setups will be discussed in more detail in section 3.4. The oscillations in the $g^{(1)}$ and $g^{(2)}$ curves in panels b and c are due to Rabi oscillations of the two-level system. The modulation of the fluorescence intensity due to the coherent oscillations gives rise to a three-peaked spectrum, the Mollow triplet - see panel a, where the sidebands are separated from the central peak by the Rabi frequency. Note that in the spectrum we have omitted the elastic contribution for simplicity.

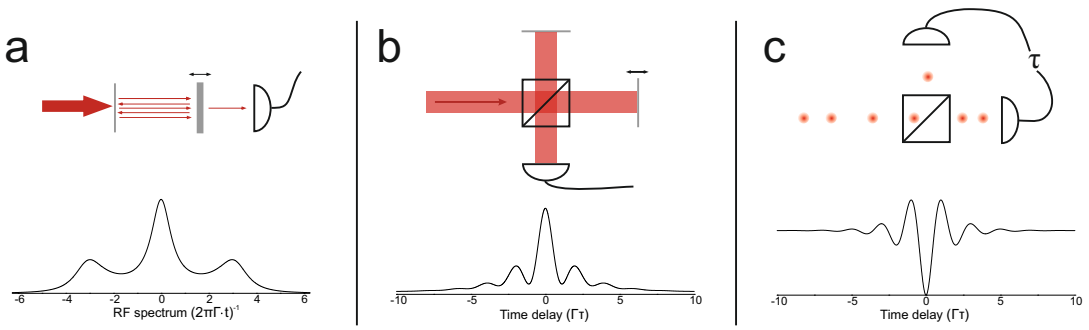

Figure 2.4: Schematics of optical interferometers to measure first- and second-order coherence (top) with examples of corresponding spectra/coherences (bottom). The bottom curves are simulations for a coherent two-level system and the abscissa is made dimensionless by normalising to $\Gamma = 1/T_1$. a, Fabry-Perot interferometer. b, Michelson interferometer. c, Hanbury-Brown and Twiss interferometer.

Chapter 3

Experimental setup and techniques

In this chapter we introduce the experimental setup and experimental techniques used in the following chapters. In the flow-chart 3.1 we attempt to give an overview and a quick summary. The diagram represents the techniques (and equipment) available in the lab. The confocal microscope with the QD sample forms the central part of the setup and will be described first. We briefly discuss the basics of confocal microscopy and microscope design and then follow the development from QD wafer to a Schottky diode device where the QD charge can be controlled using external electric field. Optical characterisation using above bandgap optical excitation as well as resonant spectroscopy are introduced in this context and we discuss the use of numerical aperture enhancing solid immersion lenses (SILs) to improve photon extraction. The properties and working principles of the optical interferometry techniques employed in the detection of QD fluorescence are covered at the end of the chapter.

3.1 Confocal microscopy

The central piece of the experimental apparatus consists of a confocal microscope that allows optical addressing and collecting the fluorescence from single QDs, which are held at, or close to, the liquid helium temperature of 4.2 K. Two

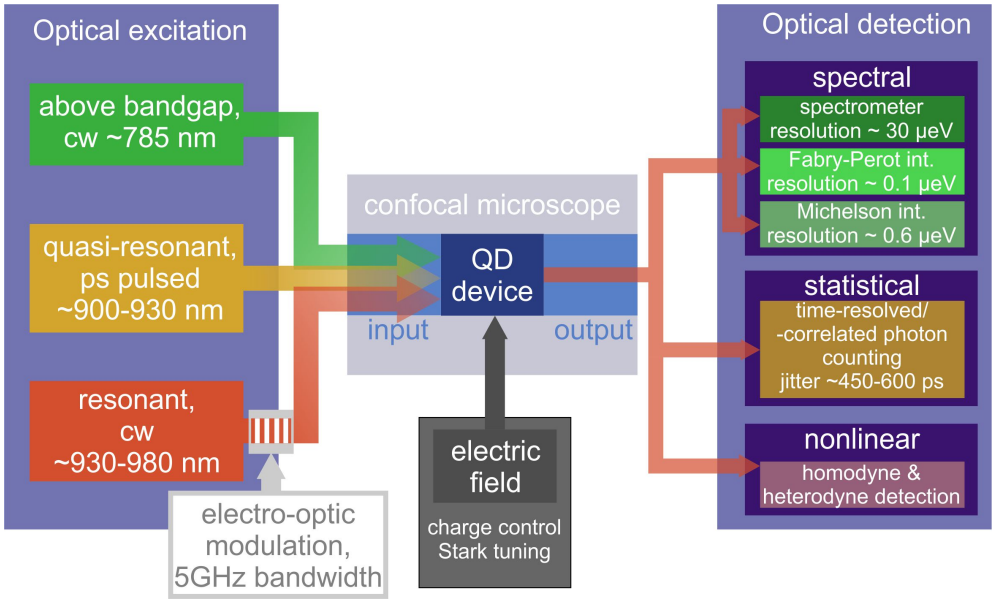

Figure 3.1: Summary of experimental setup and techniques. The optical excitation column on the left displays which laser wavelengths are available and what they are used for. The detection column summarises detection instruments and techniques, grouped according to the nature of the detection. cw: continuous wave.

confocal microscope setups were used in this thesis, one in conjunction with a liquid helium flow cryostat (Oxford Instruments MicrostatHires) and the other one attached to a liquid helium bath cryostat (similar to the attocube attoliquid system). The flow cryostat was used for QD wafer and sample characterisation, while long-term experiments were all performed with the bath cryostat system. However, the working principle is identical in both cases, so we will start with the general features.

Figure 3.2 provides a sketch of a confocal microscope setup. First, the microscope head and the sample need independent motional degrees of freedom. In the case of the flow cryostat setup, the sample is kept stationary, while the microscope sits on three stacked linear direct drive stages (PI 405.DG for lateral displacement, PI 451 for lifting). For the bath cryostat, the microscope is attached to the cryostat and the sample is positioned on piezoelectric slip-stick xyz-positioners (attocube ANPxyz101). The microscope provides four degrees of freedom in each arm to allow for accurate alignment of the excitation beam and efficient fibre coupling in the collection arm. As the microscopes are used for resonant spectroscopy, we

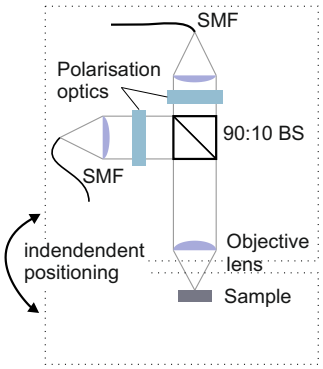

Figure 3.2: Confocal microscope with sample. Sample and microscope head can be moved independently from each other so that different positions on the sample surface are in focus. The confocal points in excitation (horizontal) and collection (vertical) arm are given by single-mode optical fibres (SMF). A beamsplitter (BS) with a high transmission to reflection ratio combines and separates the paths

cannot use dichroic mirrors to combine/separate excitation and collection paths. In order to minimise photon loss in the collection path (vertical arm in Fig. 3.2) the beamsplitter is strongly unbalanced, typically with a transmission to reflection ratio of ∼10:1. Single-mode fibres (SMF) are used for input and output to provide single mode beams and rejection of background light. Polarisers and waveplates can be inserted into each arm. In the case of the flow cryostat setup, the objective lens (Mitutoyo 50x M Plan APO NIR) is kept at room temperature outside the cryostat housing and at liquid helium temperatures inside the bath cryostat (Thorlabs C110TME-B or C240TME-B). The bath cryostat system is illustrated in greater detail in Fig. 3.3. In panel a we identify the confocal microscope elements discussed before (see sketch in Fig. 3.2) and highlight a few additional features. Panel b shows the part of the microscope that is kept at cryogenic temperatures during experiments, namely objective lens, sample, and positioners. To avoid mechanical failure of the objective lens during cooldown and at cold, we use single-piece aspheric lenses. The numerical aperture (NA) of 0.4 and 0.5 is chosen to match the light extraction with a zirconia super-hemispherical solid immersion lens (discussed later this chapter). Progressive close-ups of the sample in panels c and d show both sets of gates and a zirconia solid immersion lens glued to the sample surface.

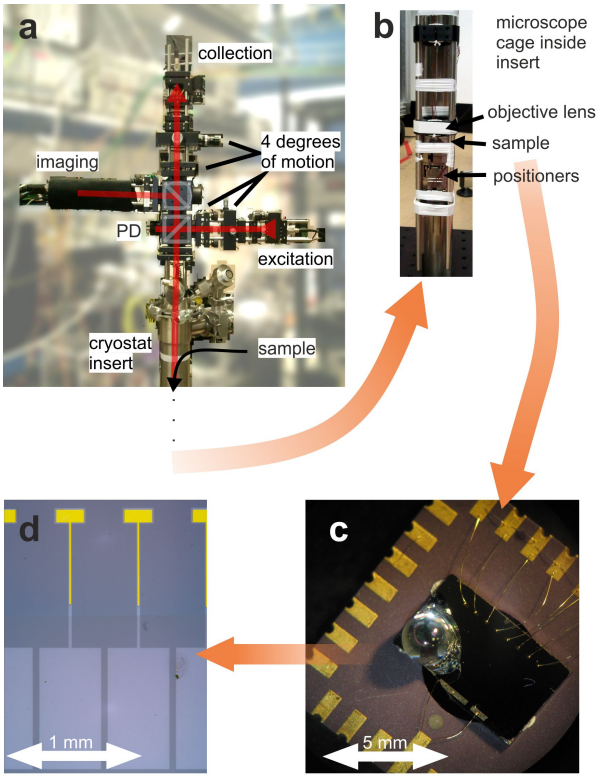

Figure 3.3: **a**, Photograph of helium bath cryostat insert and microscope when pulled out of cryostat. In comparison to the sketch in Fig. 3.2 an imaging camera (Watech 120N+) is included here. Rotational and translational elements are highlighted in both microscope arms. A photodiode (Thorlabs SM1PD1A) measures transmitted power of the excitation laser, enabling power calibration and stabilisation. The cryostat insert contains the objective lens, sample and sample positioners, held together in a 30mm cage system (see **b**). It is sealed off from the outside and provides optical access through a BK-7 glass window at the top. **b**, Photograph of bottom end of the microscope cage system when pulled out of the insert. The location of objective lens, sample and positioners are indicated by the arrows. Teflon strips (white) keep electric connections in place, out of the way of the optical beam and the outside edges of the cage. In order to cool down the insert (with sample etc.) is first vacuum pumped to $\sim 10^{-5}$ mbar and then filled with 20-25 mbar of helium gas. This helium gas provides heat exchange with the outside and cools sample and positioners to liquid helium temperatures when the insert is half-way immersed in helium in the bath cryostat. **c**, Close-up of a contacted QD sample with zirconia SIL. Gold wirebonds connect to the Schottky contacts on the top-right side. On the bottom-left, the bigger Ohmic contact are visible. **d**, Close-up of the Schottky contacts and bondpads. The light blue structure stems from the semi-transparent titanium gate that forms the Schottky contact. At the top, an additional layer of titanium and gold provides pads for wirebonding.

3.2 QD Sample

3.2.1 General considerations for sample design

The QD electronic level structure offers transitions to excited states that can be optically addressed and scatter single photons in response. It is via these single photons that information is obtained, e.g. about the spin state, and acting as flying quantum bits, entanglement can be generated or transferred to equivalent systems. As such the QD sample design is driven by efforts to maximise photon extraction. This is particularly crucial as the QDs are buried in a high refractive index semiconductor (GaAs, n$\sim$3.5) and total internal reflection at the semiconductor-air interface limits outcoupling of photons optics to $\sim$ 2%. Approaches to ameliorate this problem are nicely illustrated in Ref. [77]. One approach is to manipulate the local density of optical states, such that light is preferentially emitted into spatial modes that allow for good collection. This can be achieved by embedding the quantum dots into microcavities during semiconductor growth and post-processing. An alternative approach uses geometric optics, mainly relying on solid immersion lenses (SILs). Here the emitter properties are not modified; the strategy is to minimise total internal reflection by employing spherical interfaces. Cavity solutions can be processing-intensive, while the second approach is very simple and offers broadband improvements at the same time. The SIL approach is used throughout this thesis and will be explored in more detail in section 3.2.4 of this chapter.

To go from a QD sample to a useful QD device we have to add an element of control. Attempting to control individual spin qubits requires the ability to control the charge state of individual QDs first, making this a very desirable feature. We also note that using QDs as single-photon sources under resonant excitation may not be straightforward with samples without charge-control [78]. Charge-state control can be partly achieved by appropriate doping [52], i.e. by incorporating additional charges closeby and hoping these will be trapped in QDs. This is a probabilistic process, which does not guarantee QD charging stability. A more flexible solution was pioneered by Warburton *et al.* [11]. Here, the QD is placed between two electronic gates, one of which acts as electron reservoir and the po-

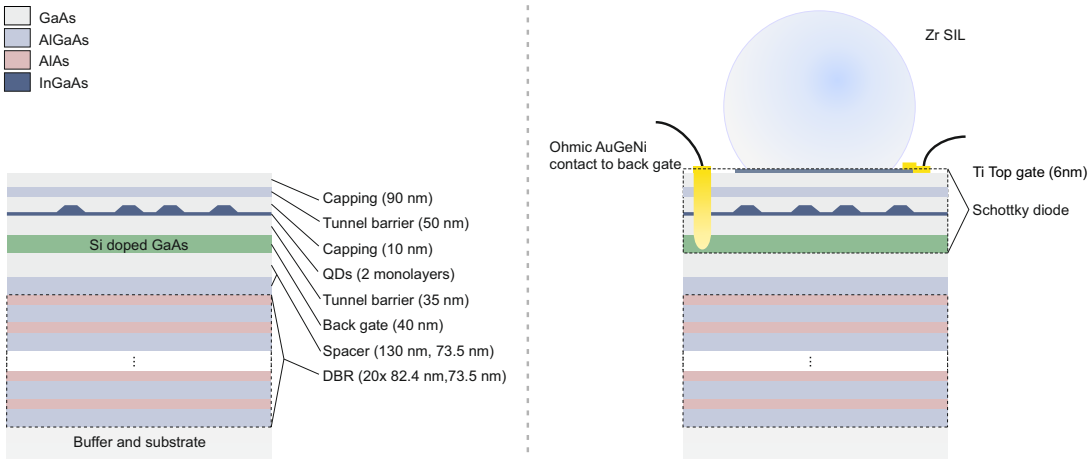

Figure 3.4: QD sample structure. Left: Colour-coded structure of the QD wafer 'Chef 2'. Layer thicknesses are indicated to the right of the sketch (not to scale). The Si doping concentration in the back gate is nominally $4 \cdot 10^{-18}$ cm^{-3}. DBR: distributed bragg reflector. Right: Schottky diode structure with zirconia solid-immersion lens (Zr SIL). An ohmic contact is formed with the back gate through GaAs etching and evaporating and annealing gold-germanium-nickel (AuGeNi) on the sample. The top gate is a Schottky contact made of a thin titanium film.

tential difference between them determines the potential of QD electronic levels with the respect to the Fermi level.

3.2.2 The 'Chef 2' sample

We will illustrate the concepts introduced above on the example of the sample used throughout most of this thesis. The wafer was grown by Maxime Hugues at the National Centre for III-IV Technologies in Sheffield and dubbed 'Chef 2'. A schematic of sample structure including layer thicknesses is shown on the left-hand side of Fig. 3.4. The right-hand side displays a sketch of the device after processing, highlighting the Schottky diode section. A zirconia solid immersion lens glued on to the sample surface enhances focussing and photon collection. Controlling the potential difference between top and bottom gate allows us to control the charge state of the QDs inbetween. Figure 3.5 illustrates the principle of this charge tuning (for electrons) by looking at the electronic band structure of the Schottky diode under different bias voltages. z denotes the growth direc-

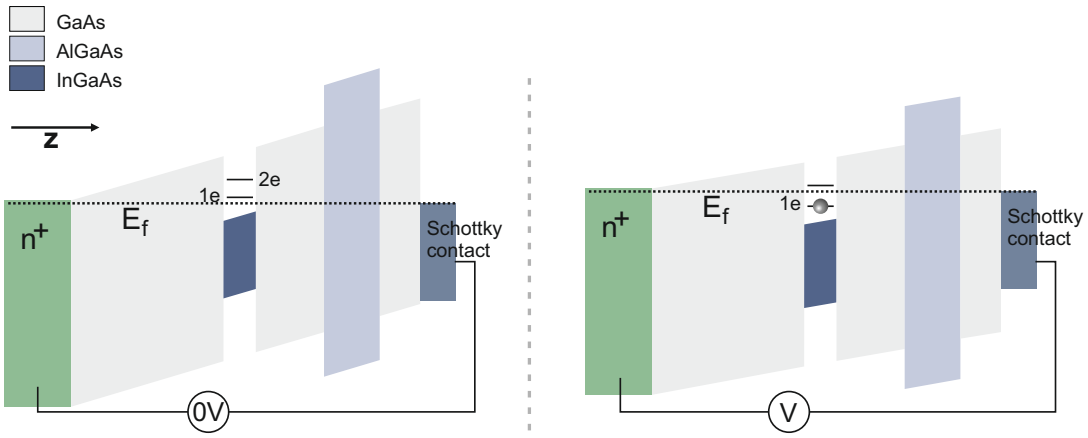

Figure 3.5: QD Charge control in Schottky diodes. Left: Electronic band structure of the QD diode heterostructure under zero applied bias. The Fermi level (E_f) is below the first QD electronic state, so the QD is uncharged. Right: Under forward bias the first QD level shifts below the Fermi energy and an electron tunnels in from the back contact.

tion. The layer materials are indicated in the same colour code as before. The back contact is GaAs heavily n-type doped with electron-donating silicon atoms replacing gallium in GaAs. The Fermi level E_f is then pinned to just below the GaAs conduction band edge in the n-doped layer and, at zero applied bias, halfway in between the conduction and valence band at the Schottky contact. The electronic levels for having the QD occupied with 1 or 2 electrons are indicated. Applying a gate voltage effectively shifts the QD energy levels with respect to the Fermi energy. Conduction band electrons from the Fermi sea in the back contact can only tunnel into the quantum dot if unoccupied states are below or within kT of the Fermi energy E_f. Due to its small size, and consequently a small capacitance, and its discrete energy levels a charging energy $\Delta E_{charging}$ is needed to place another electron into the QD [79]. For liquid helium temperatures ($\sim$ 4 K) $\Delta E_{charging} \gg kT$, such that the number of electrons in the dot is well defined as long as the Fermi energy is not aligned with the QD level (within kT of the energy level). This effect is known as *quantum Coulomb blockade*. Applying a forward bias, electrons are added one by one. These effects can be clearly seen in photoluminescence studies, where the energy of emitted photons changes abruptly as the number of resident electrons is changed [11; 80]. The electric field

across the diode also shifts the QD exciton energy levels via the DC Stark effect, which was introduced earlier (section 1.3.3). A bias-dependent map of the QD photoluminescence from a 'Chef 2' device is discussed later in this chapter.
From the band structure diagrams in Fig. 3.5 we can also understand the function of the other layers in the diode. Going up in z-direction from the back contact, the following GaAs layer provides the tunnel barrier between the Fermi sea in the back contact and the QD layer (cf. labels in Fig. 3.4). The barrier thickness determines the tunneling time for an electron in and out of the QD. Given the exponential tunneling time dependence on thickness this can stretch from sub-nanosecond to second timescales. For a different sample with a nominally identical barrier thickness of 35 nm a tunnelling time ≤ 0.1 s was deduced from spin relaxation measurements [26]. For the 'Chef 2' sample, a similar measurement suggests microsecond tunneling times. This difference may be due to the dopant diffusion in the back contact which varies with concentration. Next, the InAs QD layer is covered with 10 nm of GaAs [1]. Following the GaAs cap, 50 nm of AlGaAs form a barrier (due to the larger bandgap) for carriers that could tunnel from the Schottky contact into the QD layer. Finally, the top GaAs layer provides a cap that prevents the AlGaAs from oxidising.
The distributed Bragg reflector (DBR, see Fig. 3.4) consists of 20 layers of GaAs/AlGaAs with thicknesses such that reflection in the spectral region around 970-980 nm is enhanced. The relative position of the QD layer with respect to the DBR places the QDs in an antinode of the reflected field.

3.2.3 QD device processing

Once a sample structure is designed, growth is carried out externally. For the duration of this PhD work samples were purchased from the EPSRC National Centre for III-V Technologies in Sheffield. We are grateful to Maxime Hugues and Edmund Clarke who performed the growth there.

[1] The influence of this capping layer thickness has been subject of a recent study by Houel *et al.* [81]. The authors observe strong (several linewidths) fluctuations of the QD resonance frequency for 30 nm capping thickness, while this feature is strongly reduced for a capping thickness of 150 nm. The spectral jumps are attributed to charges trapped at the interface of capping layer and the following AlGaAs barrier. The capping layer thickness of 10 nm in our devices is chosen to avoid bound states at the QD energy levels at the GaAs/AlGaAs interface.

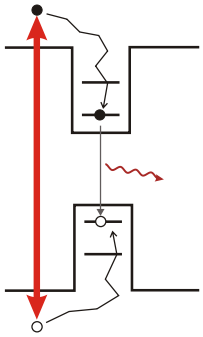

Figure 3.6: Schematic of QD photoluminescence through above bandgap excitation. When the energy of the exciting laser is greater than the GaAs bandgap, electrons are promoted from the valence to conductance band, leaving behind holes. These electron-hole pairs quickly diffuse into the lowest available energy configuration, e.g. the s-shell of a quantum dot, and recombine radiatively.

The QD density required for different applications (e.g. QD lasers vs. single QD spectroscopy) varies widely, and achieving a specific uniform density in growth requires careful calibration. For the low density samples we need for our research the rotation stop method is employed to provide some flexibility on the QD density. With this method the standard rotation of the wafer during growth is interrupted at the start of the InAs deposition, such that the InAs density and consequently the QD nucleation density varies across the two-inch wafer. Typically it varies from zero QDs in several mm^2 at one edge to many tens per μm^2 or higher at the opposite end. In between there is a strip where the density is appropriate for single QD research. Hence the first step in producing a good QD device is to identify the region of appropriate density.

3.2.3.1 QD photoluminescence

Characterisation of new wafers and sample processing relies on the ability to generate and detect QD fluorescence in a straightforward manner. Fortunately there is a very convenient method: photoluminescence. Excitons can be generated in abundance in the direct bandgap material GaAs by excitation at above bandgap energies. The electron-hole pairs relax quickly into the lowest available energy configuration and recombine radiatively. If quantum dots happen to be in the spatial vicinty, excitons can fall into these potential traps, giving rise to QD

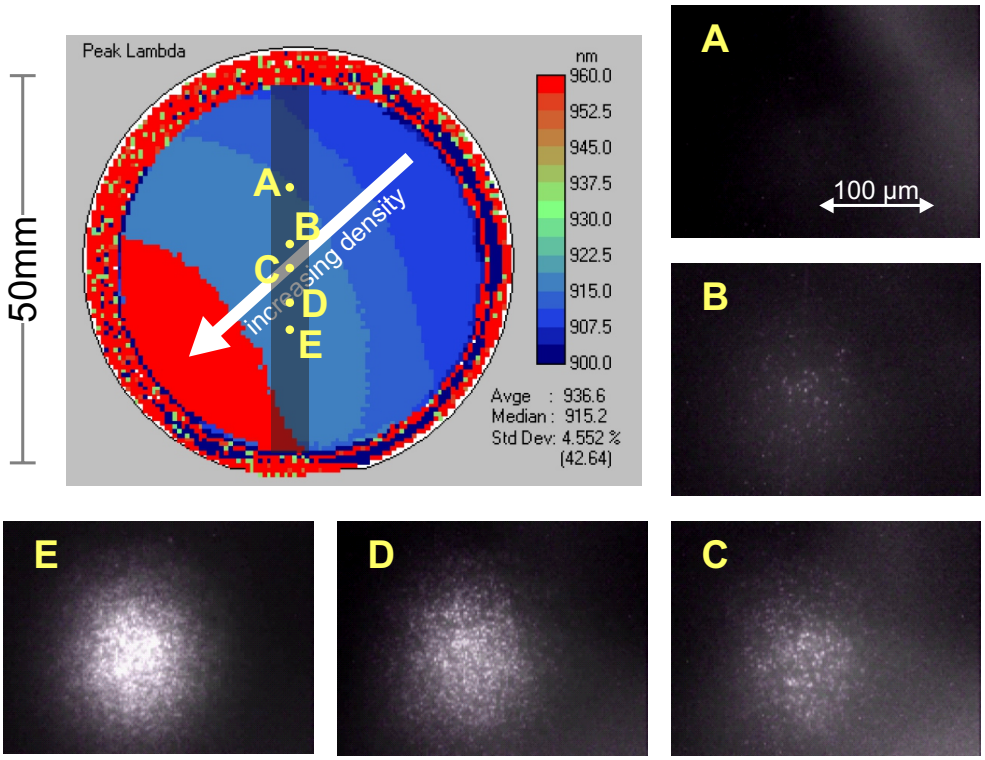

Figure 3.7: Investigation of QD density for a wafer grown with the rotation stop method. The top left image is taken from the wafer delivery note from the EPSRC National Centre for III-V Technologies in Sheffield. It is annotated to link the spatially resolved photoluminescence maps shown to the right and below to locations on the wafer.

photoluminescence on recombination (see Fig. 3.6). In our case, we employ a diode laser at 785 nm. Laser scattering and luminescence from the GaAs and the wetting layer quantum well is filtered out with a longpass filter (e.g. Thorlabs FEL0900)[1].

3.2.3.2 Sample density check

Investigating the QD density starts by cleaving a $\sim$ 6 mm wide strip off the wafer, either along the major or the minor wafer axis, roughly following the expected density gradient. After cooling down the strip in the flow cryostat

[1] Alternatively, exciting the InAs wetting layer provides an efficient venue for QD photoluminescence generation.

we employ above bandgap excitation and deliberately decollimate the 785 nm laser before the microscope objective, such that a large sample area (>100 x 100 μm^2) is illuminated. Imaging the sample surface through a 900 nm longpass filter reveals spatially localised fluorescence from individual QDs. Figure 3.7 displays on the top left a room temperature photoluminescence map supplied by EPSRC National Centre for III-V Technologies. The wavelength of the maximum intensity peak of the photoluminescence spectrum is colour-coded as function of position on the wafer. The map is annotated to illustrate the QD density measurements performed in our lab: The direction of the QD density gradient is indicated by the white arrow, the darker area shows the sample strip that was cleaved for analysis and the lettered dots show the approximate position of selected spatial luminescence maps. Points A and E are approximately 20 mm apart. For location E the QD density is in the region of 10 QDs/μm^2. At this density, individual QDs can still be easily addressed individually using resonant excitation, as they emit at different wavelengths. However, experiments showed that the QD optical properties suffered. Spectral jumps and strong spectral diffusion (evident in broad absorption lineshapes) were typically observed for the QDs investigated ($\sim$ a dozen). For densities of one to a few QDs per μm^2 (comparable to location **D** in Fig. 3.7) these problems are less severe, here about half of the QDs exhibit jumps and diffusion. QD samples with densities below 1/μm^2 are typically clean, with absorption linewidths close to the radiative limit at low excitation power and hence preferred for measurements going beyond above bandgap photoluminescence.

3.2.3.3 Cleanroom processing

Once the location of suitable QD density on the wafer is established, pieces of approximately 6 x 5 mm^2 size are cleaved and prepared for processing in the cleanroom of the Semiconductor Physics group at the Cavendish Laboratory. The sample size is determined by the size of mask features. A margin of about 1 mm is necessary to avoid problems with photoresist edge beads. The processing steps mostly follow standard procedures for high electron mobility Hall-bars. We give a brief outline of the procedure here.

1. **Ohmic contacts.** The Ohmic contacts require annealing, so they have to be done before other metal gates. After cleaning, the positive photoresist Shipley 1813 is deposited on the sample. Spinning the sample (5500 RPM for 30 seconds) distributes the photoresist evenly across the sample (save the edge beads), with a thickness of ~ 1.3 μm. After baking for 60 seconds at 115° C to harden the resist, the sample is exposed under the appropriate mask section (the one containing the ohmic contact shape). Developing uses MF-319 for about 2.5 minutes. To get a contact to the buried n-doped layer, we etch the sample (i.e. the now developed area) roughly 3/4 the distance to the n-doped layer using GaAs etch. The sample is cleaned in a 10 % HCl solution before thermal evaporation of about 200 nm of gold-germanium-nickel (AuGeNi). Following the lift-off, annealing is achieved in a rapid thermal annealer at a temperature of 370 °C.

2. **Schottky gates.** Preparations for the photolithography are similar to before, but the photoresist is baked at 90° C. After exposure, the sample is soaked in chlorobenzene for 2 minutes; this produces sharper edges in the development.
   Photon collection happens through the Schottky gate, so this needs to be as thin as possible. The evaporation of nominally 5 nm [1] titanium is performed by cleanroom staff (thanks are due to Graham Winiecki and Melanie Tribble of the Semiconductor Physics group) using electron beam physical vapour deposition. Due to the smaller feature size the lift-off process usually requires sonicating the sample very briefly (and carefully). The shape of the Schottky pads can be seen in Fig. 3.3 d.

3. **Schottky contacts.** Wirebonding to a 5 nm thin layer of titanium is more than challenging. To enable gold ball wirebonding, another deposition of titanium and gold is needed at the location of the bondpad. This area is shaded golden in the photograph in Fig. 3.3 d. The photolithography steps are identical to the ones for the Schottky gates. The evaporation is done in a thermal evaporator, typically 20 nm of titanium are deposited first, followed by 40 nm of gold. The additional titanium improves the adhesion

[1] Usually ends up being ~ 6 nm thick, occasionally also 30 nm ...

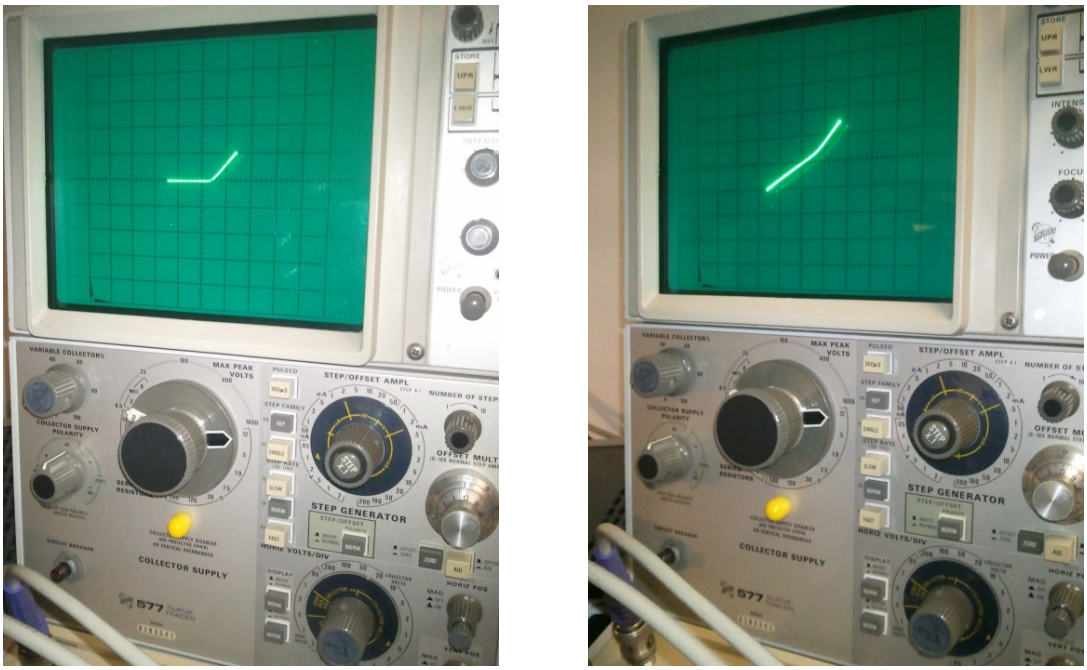

Figure 3.8: I-V characteristics of two QD diodes at room temperature. The left photograph represents a 'good' gate, the one on the right is a 'bad' gate.

of the gold layer.

4. **Diode behaviour check.** Before proceeding to the final steps of mounting the sample on the chip carrier and wirebonding, the I-V characteristics of each gate are checked at room temperature with a curve tracer. Figure 3.8 shows two photographs of the curve-tracer in the cleanroom. The horizontal scale is set to 0.5 V per division, the vertical scale is 50 μA per division. The photograph on the left displays a 'good' I-V curve. In forward bias, current starts passing at around 0.3 V. The photograph on the right (example of a bad gate) shows some Ohmic character, indicating leakage current between the gates.

5. **Packaging.** Sample processing is completed by mounting the sample on a leadless ceramic chip carrier (using silver paste as glue) and wirebonding the working gates to the metalised castellations on the chip carrier using

a goldball bonder[1]. The wirebonds for Schottky and Ohmic contacts are visible in Fig. 3.3.

3.2.3.4 Gate check at 4K

It is advisable to check the QD response to biasing the gates in the flow cryostat before placing it (semi-permanently) in the bath cryostat. This should show that devices with 'good' I-V curves (see Fig. 3.8 left) influence radiative recombination rates in accordance with the band diagram in Fig. 3.5. Figure 3.9 displays six spatial photoluminescence maps under increasing bias. Starting in reverse bias, we can make out two clearly separated areas on the sample surface (red lines show borders as guide to the eye). In reverse bias excitons ionise (electrons tunneling into the back gate) faster than radiative recombination in QDs can take place, so we do not expect luminescence. The dark area in the map for -150 mV bias is covered by the titanium gate, whereas QD emission is visible from regions not covered by the gate. Under increasing forward bias, QD emission is visible in the gated area indicating that radiative recombination occurs faster than tunneling timescales, whereas the ungated area looks unchanged. For this sample, emission is most intense around 450 mV bias; here most QDs are occupied by one or two electrons. At high forward bias, current starts passing between the n-doped layer and the Schottky gate and emission quenches.

3.2.4 Solid immersion lenses

The problem of efficient light extraction from QDs was already mentioned at the start of this section, together with the approach employed: solid immersion lenses. The solid immersion microscope was introduced by Mansfield and Kino in 1990 [82]. In analogy to liquid immersion, e.g. in oil, the idea is to fill the objective space with a material of high refractive index n_{SIL}, and thus increase the numerical aperture of the microscope to $NA = n_{\mathrm{SIL}} sin(\theta)$, where θ is the angular semi-aperture in the objective space. For optical studies of QDs there

[1]The gold wire can easily rip off the bondpad (and part of the sample surface) instead of sticking to it, rendering a week or two (and a precious piece of sample) useless. Patience and careful calibration of the bonder parameters are recommended.

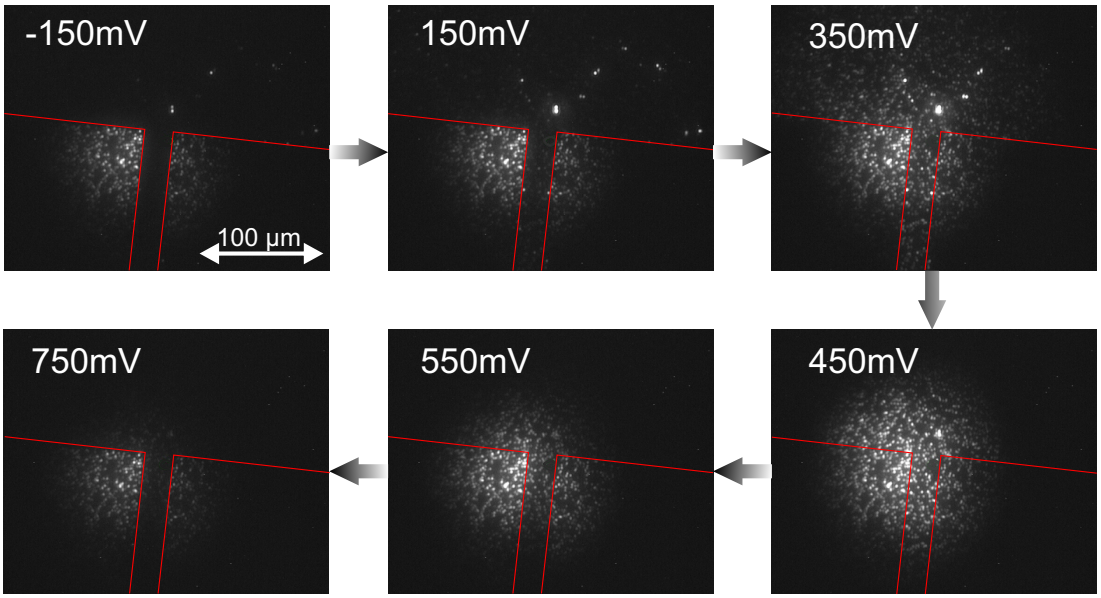

Figure 3.9: Influence of bias across the QD diode on the photoluminescence intensity under above bandgap excitation. The applied bias is displayed in the top left corner of each image, with positive voltages corresponding to forward bias. The edges of a Schottky gate are indicated by red lines. Only areas under the Schottky gate react to the bias.

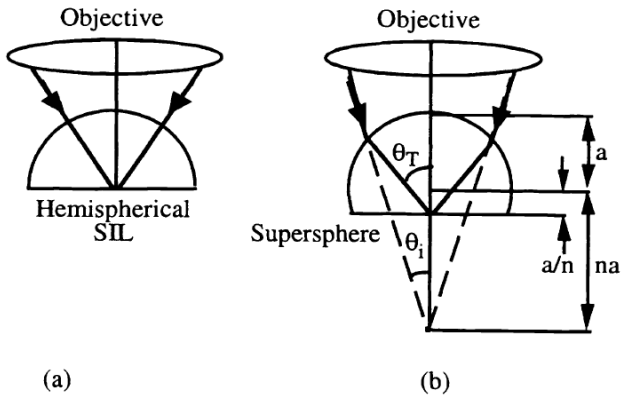

Figure 3.10: Illustration of solid immersion lens geometries, reproduced from *The solid immersion lens* by Kino [83]. The supersphere geometry is also known as *Weierstrass geometry*.

are two beneficial effect: improved focusing and light extraction.

In order to fill the objective space fully, spherical surfaces separating the immersion material from objective lens are desirable. Focal points form at two locations in spheres of high refractive index, so SILs come in two standard geometries which are illustrated in Fig. 3.10. For features directly underneath the planar surface of a hemispherical SIL the lateral magnification increases by n_{SIL} due to the wavelength being $\lambda_{\mathrm{SIL}} = \lambda_0/n_{\mathrm{SIL}}$, as does the NA, while the size of the focal spot is reduced by a factor $1/n_{\mathrm{SIL}}$ compared to the vacuum case. Super-hemispherical SILs (SSILs) ideally increase the magnification and the NA by n_{SIL}^2 (with n_{SIL} being the upper limit of the NA) while the spot size should decrease by $1/n_{\mathrm{SIL}}^2$. Beating the (vacuum) diffraction limit is possible with SILs and this has been demonstrated in a number of works [84], see Ref. [85] for a review.

The important advantage of using SILs for QDs is a reduction in total internal reflection, where an order of magnitude increase in photon extraction is predicted [77; 86], e.g. going from 1-2 percent without SIL to 30 percent with a GaAs SSIL. Successful implementations of SILs for QD spectroscopy and other nanophotonic applications have been reported in a number of works [87; 88; 89]. Using a high-index glass SIL and a GaA SSIL, respectively, a resolution of 350 nm (for λ=950 nm light) [90] and an increase in transmission contrast by a factor of seven [91]

were reported.

In practice, the achievable reduction in focal size and the NA enhancement depend on the optical quality of the SIL and the contact to the object. Simulations suggest that the size of any air gap between the SIL and the target material strongly influences focusing abilities [83; 88], as the evanescent part of the focused spot does not contribute to the intensity at the object location anymore. For less than 10 % deviation from the ideal case, the air gap should be on the order of $\lambda/5$. For some materials it has been possible to integrate the SIL directly into the device (most notably for diamond colour centres, see Refs. [92; 93] for example), thus eliminating the challenge of creating good optical contact, but this has not been achieved yet for GaAs.

However, even for imperfect contact with the sample SILs, and SSILs in particular, funnel QD emission that made it out of the semiconductor and reduce the NA necessary to collect it. It should also be pointed out that SSILs are highly achromatic [94] while SILs do not suffer from this.

In this thesis we employ 2 mm diameter SSILs made from cubic Zirconia. The refractive index of $n \sim 2.17$ is higher than that of most common 'optics' materials. In terms of refractive index, GaAs SSILs would be preferable, but these are not readily available. The Zirconia SSILs are glued on the sample surface using a transparent mounting compound [1]. The contact to the sample surface is checked by focusing a laser through the SIL and observing the reflection from the focal spot at the sample/SIL interface. Two distinct reflections are visible for air gaps on the order of 1 μm and bigger. Airgaps of a few hundred nm and smaller cannot be measured easily. Typically we see an enhancement in collection efficiency by a factor 5-10 in the flow cryostat system with an objective NA of 0.42.

Figure 3.11 illustrates the concepts of increased magnification and imaging with SILs with experimental (and hence flawed) data. A Zirconia SSIL and a GaAs SSIL are mounted on the same test sample and we image QD fluorescence in the flow cryostat setup with a 0.42 NA objective lens (Mitutoyo M Plan Apo NIR). The QDs can be approximated as point-sources, so imaging them is equivalent to measuring the point-spread-function (PSF) of the microscope. Fig. 3.11a dis-

[1] Obtained from the glass workshop in the Cavendish Laboratory. The exact product is not known, but it is similar (or identical) to the 'KLEER-MOUNT' acrylic resin from MetPrep.

plays this effective PSF for a QD not covered by either SIL. The linecuts through the image reveal a full-width-at-half-maximum (FWHM) of 8 pixels, which corresponds to a physical width of $\sim$ 1.4 μm. For a diffraction limited microscope and a point-source emitting at 950nm we would expect a PSF of $\sim$ 1.15 μm. The discrepancy is probably due to the fact that the microscope objective is not corrected for focussing through the glass cover of the flow cryostat (0.5 mm thickness). Figs. 3.11b and 3.11c show images for QDs under a Zirconia and a GaAs SSIL, respectively. Using SSILs the image should be magnified by n_{SIL}^2, so we divide the measured FWHM in pixels by n_{SIL}^2 to extract the PSF. The results are summarised in Fig. 3.11d and compared to the ideal case. We are quite a bit off the ideal case (about a factor of three). Reasons for this are likely to be the optical contact at the SIL/sample interface where an air gap of a few μm was measured, and chromatic dispersion[1]. However, in both cases we still reach a PSF equivalent to that of an ideal system (without SIL, but) with an NA of 1. We note that not reaching the diffraction limit also implies that the microscope alignment is less sensitive to movement of the sample with respect to the microscope - an advantage in liquid helium cryostats which need refilling or continous flow.

The addition of a SSIL with good optical contact to the gated sample concludes the device processing and preparation part. Finished samples can then be cooled down in the bath cryostat for resonant studies on single QDs. The relevant techniques are described in the following section.

3.3 Single QD spectroscopy

Three optical techniques are used for spectroscopy and time-resolved measurements: photoluminescence (PL), differential transmission/reflection (DT/DR) and resonance fluorescence. Characterisation of the optical transitions of individual QDs and QDMs employs all three techniques, where each plays a different role. The main results of this thesis rely on photon coherence properties and high measurement bandwidth and are obtained with resonance fluorescence.

[1]Sampling over a large number of QDs would give a more representative picture, as we would sample over a range of emission wavelengths at the same time.

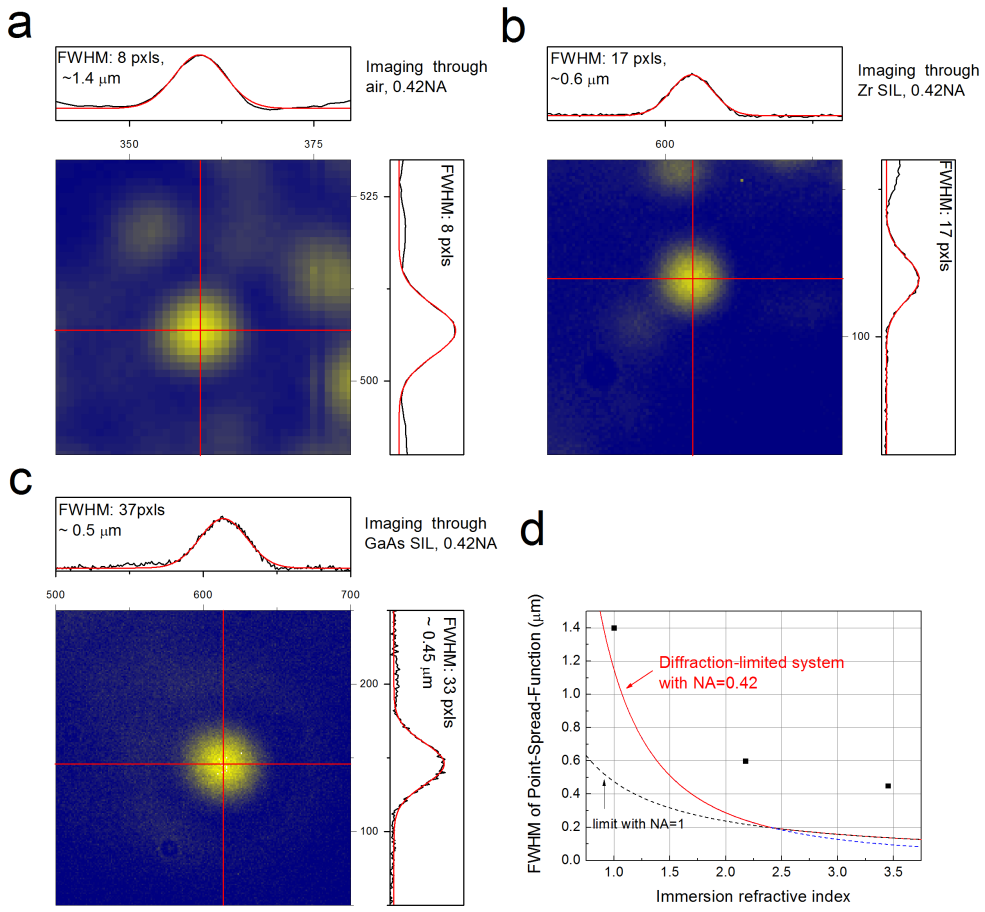

Figure 3.11: Point-spread function (PSF) of confocal microscope with and without SIL. The PSF is obtained by imaging the fluorescence from a single QD onto a camera and fitting a Gaussian to the intensity profile in two orthogonal directions. **a**, PSF for imaging through air with a 0.42 NA objective. **b**, PSF for imaging through a zirconia SIL in Weierstrass geometry (SSIL) with a 0.42 NA objective. **a**, PSF for imaging through a GaAs SIL in Weierstrass geometry with a 0.42 NA objective. **d**, Plot of the PSF versus the refractive index of the immersing medium. The black points show the data from a-c, the solid red line displays the theoretical PSF for a diffraction-limited setup (0.42 NA). The black dashed line shows the theoretical curve for a NA=1. We assume an emission wavelength of 950 nm here.

3.3.1 Gated photoluminescence

The process of photogeneration by above bandgap excitation was covered in 3.2.3.1. With the sample processed into a Schottky diode optical transitions of different charge states can be identified. This is illustrated in Fig. 3.12 where we present the photoluminescence/gate voltage map of a single QD. The photoluminescence is spectrally dispersed in a 0.75 m monochromator (Princeton Instruments SP2750) using a 1200 groves/mm grating and detected with a liquid nitrogen-cooled charge coupled detector. The electric field across the QD corresponding to the applied bias is given by the top abscissa. Operating far below saturation three distinct transitions are identified: the neutral exciton transition X^0 and the positively and negatively charged trion transitions X^{1+} and X^{1-}. The charges involved in the recombination are indicated next to the data. This map can be likened to an optical fingerprint of a QD as charging points, emission energies and splittings between transitions vary for each QD. However, some features are consistent for all QDs in our samples. Most prominently, the X^{1-} transition is redshifted typically by 4-4.5nm ($\sim$ 1.3 THz or 5.5 meV) with respect to the X^0 transition. The change of emission wavelength as function of the gate voltage is due to the DC Stark shift. It is worth noting that here we do not see a clear transition in gate voltage between different charge ground states, and the optical transitions overlap considerably in applied bias. The reason for this overlap is the slow tunneling time for charges in the QD: this may take place on a many μs timescale, much slower than radiative recombination. Hence the QD can be optically charged, and we see e.g. X^{1-} emission at a bias where the QD is empty in its ground state. PL spectroscopy is great in its simplicity, but has several drawbacks: The resolution is limited to the spectrometer resolution ($\sim$ 30 μeV for a 1800 groves/mm grating) while the transition linewidth of QD transitions is typically a few 100 MHz ($\sim 1\mu$eV).

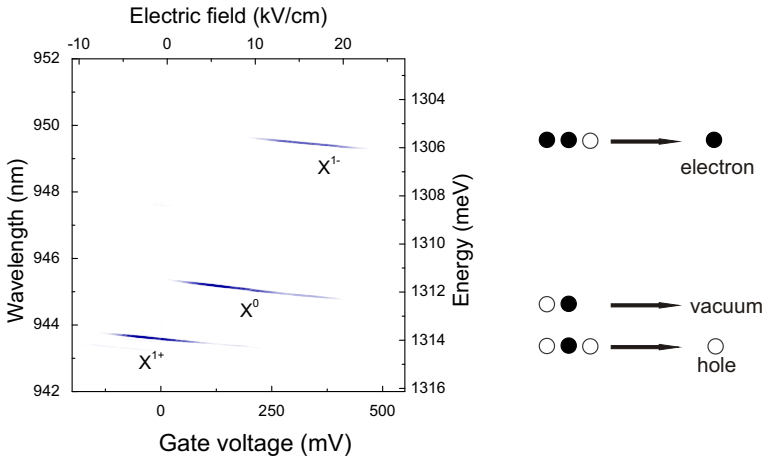

Figure 3.12: Photoluminescence map of a single QD. Sequential charging of the QD with gate voltage is visible. The linear shift of the emission energy with gate voltage is due to the Stark effect.

3.3.2 Differential transmission and reflection

Differential transmission and reflection (DT/DR) in the context of QD spectroscopy refers to a homodyne detection technique of resonant QD scattering which offers very high spectral resolution while being experimentally robust at the same time. Here we will only outline the method and its range of application; for a comprehensive description see Ref. [95]. The simplifying assumptions made there do apply in our case. DT and DR use interference of the laser radiation with the resonantly scattered field from the QD (homodyning) to pick up the weak QD scattering. If we consider a laser interacting resonantly with a single dipole transition, such as the X^0 transition in the QD, we have the electric field of the laser E_{L}, the coherent (Rayleigh) scattering from the dipole E_{coh} and the incoherent scattering E_{inc}. Putting the fields on a photodetector in transmission geometry we measure the intensity of the fields

$$\begin{aligned} I_{detected} =& \left|E_{\mathrm{L}} + E_{\mathrm{coh}} + E_{\mathrm{inc}}\right|^2 \\ =& I_{\mathrm{L}} + I_{\mathrm{coh}} + I_{\mathrm{inc}} + 2\Re\left(E_{\mathrm{L}} \cdot E_{\mathrm{coh}}\right) \\ &+ 2\Re\left(E_{\mathrm{L}} \cdot E_{\mathrm{inc}}\right) + 2\Re\left(E_{\mathrm{coh}} \cdot E_{\mathrm{inc}}\right). \end{aligned} \tag{3.1}$$

In a typical QD experimental system (in the absence of cavities) coupling the laser field to the QD transition is inefficient, i.e. $E_{\mathrm{L}} \gg E_{\mathrm{coh,inc}}$. In this case the second-order terms I_{coh} and I_{inc} are smaller than fluctuations in the laser intensity and can be neglected. For the cross-terms (the interference terms) we have to take phase relations and the detector bandwidth into account. Fields with random phase fluctuations faster than the detector bandwidth will average to zero and the interference terms will not contribute to measured intensity. This applies to the cross-term ($E_{\mathrm{L}} \cdot E_{\mathrm{inc}}$). However, the interference of laser and coherent scattering should be stable due to the fixed phase between them. Still this term is quite small compared to the laser intensity. To obtain a clean signal we modulate the cross-term by fast modulation of the gate voltage (few KHz) such that the QD transition is modulated in and out of resonance using the Stark shift. The laser intensity term is not affected. Phase-sensitive detection of the photodetector signal removes the laser intensity term and allows us to measure the absorption profile of the transition by scanning the laser frequency (or gate voltage) across the QD resonance.

Experimentally, the photodetector for DT (Thorlabs FDS-1010) is placed directly underneath the QD sample in the cryostat. For DR we use a fibre-coupled photodetector at room temperature (Femto photoreceiver EO-200). In both cases the photocurrent is converted to voltage and amplified by typically 10^8V/A before demodulation in the Lock-In amplifier (Stanford Research 830 DSP). The spectral resolution is only limited by the spectral stability of the resonant laser (<2 MHz in our case) which is much smaller than the QD linewidth. DT and DR are homodyne *spectral* measurements. The measurement bandwidth is determined by the gate modulation speed which sets a lower bound to the integration time constant of the Lock-In amplifier and the signal-to-noise given amplifier and lock-in amplifier specifications. In our setup the modulation frequency is typically $\sim$ 2 KHz with integration times of 10-100 ms.

First QD spectroscopy measurements using this technique were reported in Refs. [96; 97]. Since then it has become a well-used and important technique in the quantum dot community, enabling progress in the coherent control of single and coupled QDs [42] and metrology [24] by providing a resonant (and hence high resolution) observation tool. Given all the advantages it remains a purely spec-

troscopic technique. QIP applications require access to resonantly generated photons, i.e. collection of the QD resonance fluorescence only, where the excitation laser is suppressed.

3.3.3 Resonance fluorescence

Applications in quantum communication and computation rely on high coherence indistinguishable photons [98], and the ability to create entanglement between spin qubits and photonic qubits [2]. This can only be achieved with resonant excitation and collection of the resonance fluorescence.

Following the first calculations of the resonance fluorescence spectrum by Mollow [70] in 1969 this direct photon generation method was quickly demonstrated in atomic beams [99; 100; 101]. Resonance fluorescence is now routinely employed in optical investigations of atomic gases, single trapped ions and atoms [102]. In these systems an orthogonal geometry for excitation and collection of the fluorescence can be employed, such that the excitation laser does not make it to the detector. This is crucial as the fluorescence signal is orders of magnitude weaker than the laser and both are essentially at the same frequency.

For quantum dots the first attempts replicated the orthogonality of excitation and detection in a semiconductor environment using waveguide structures to confine the excitation light to one plane [103; 104] or a one-dimensional waveguide [105]. In our experimental setup we excite and collect both QD fluorescence and laser scattering along the same path (see Fig. 3.3). The QD transition dipole has a preferential in-plane orientation, independent of excitation orientation and polarisation, therefore we excite in a linear polarisation at $\sim$ 45 degrees to the transition polarisation and collect in the orthogonal polarisation. This cross-polarisation ideally removes all laser at the cost of filtering half of the scattered QD photons. Since the first demonstration of QD resonance fluorescence with this method [106] the laser suppression has been improved and is on par with trapped atom systems [107]. The experimental performance of our setup will be discussed at the beginning of the following Chapter.

The realisation of techniques to access the resonance fluorescence from quantum dots has enabled advances in the quantum dot field: the strictly resonant excita-

tion was shown to reduce photonic decoherence when compared to nonresonant excitation [108]. Further, taking advantage of the spin-selective QD transitions, required for spin-based QIP applications, QD resonance fluorescence allowed detailed studies of spin dynamics [26; 109], excitation-induced sideband broadening [110] and the realization of single-shot spin readout [111], subject of Chapter 7. The recent demonstration of QD spin-photon entanglement [53; 65] is a further key achievement, enabled by the ability to access QD resonance fluorescence.

3.4 Quantum optics in the lab: interferometric measurement techniques

This section explains the basics and the setups used for interferometric measurements. In analogy to the theoretical chapter we take a look at first-order coherence (time-resolved and spectrally) and second-order coherence. In Fig. 3.1 we already indicated the experimental capabilities and Fig. 2.4 of Chapter 2 illustrated the three common interferometer types used in this thesis. Below we discuss our particular setups in more detail.

3.4.1 Spectral measurements

Figure 3.13 shows the setup of the Fabry-Perot interferometer (FPI) on the left side. The interferometer (Exfo TL Laser Spectrum Analyzer) has a free spectral range of 30 GHz and can be aligned to a finesse of better than 1000 with a transmission of $\sim 25\%$. Two single mode optical paths are aligned trough the cavity, one with maximum finesse for the QD fluorescence and one with moderate finesse (~ 150) for a reference laser. The job of the reference laser is to stabilise and scan the cavity across the QD fluorescence spectrum. To this end the reference laser is frequency-stabilised before entering the interferometer (linewidth < 2 MHz) and the transmission through the FPI is detected on a photodiode. The measured transmission feeds back to control the distance between the cavity mirrors, hence fixing the cavity resonance relative to the reference laser frequency. By scanning the reference laser frequency we scan the cavity resonance at the same time. For improved stability during scans the reference laser is further power stabilised in

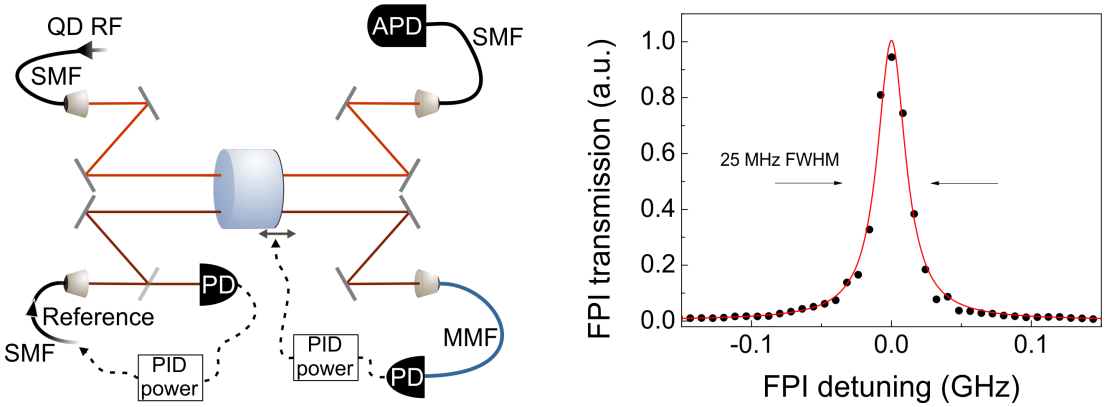

Figure 3.13: Setup of Fabry-Perot interferometer (left) and measurement of its resolution (right). RF: resonance fluorescence, APD: avalanche photodiode, PD: photodiode, PID: Proportional-Integral-Differential gain controller, SMF: single-mode fibre, MMF: multi-mode fibre.

the FPI setup. Both stabilisation procedures indicated in Fig. 3.13 employ commercial PID controllers (Standford Research Systems SIM960). The right side of Fig. 3.13 shows a measurement of the FPI linewidth. Here the signal (QD RF in the setup) is given by a single mode laser at fixed frequency (linewidth of a few MHz) and the reference laser scans the cavity resonance across the signal frequency in steps of 8 MHz. The signal is recorded by a single photon counting avalanche photodiode (APD). The Lorentzian fit to the data, displayed as red curve, yields a full width at half maximum or equivalently, a spectral resolution, of 25 MHz. The alignment of the cavity is controlled by three independent piezoelectric transducers attached to one cavity mirror and as such suffers from piezo creep. In our setup a finesse greater than 1000 can be sustained for $\sim$ 1 hour (sometimes considerably shorter), then realignment of the piezoelectric transducers is necessary.

3.4.2 First-order coherence

The first-order coherence of light is related to its spectrum by a Fourier transform, so the information obtained in either measurement should be equivalent. However, experimentally there are advantages and disadvantages associated with the specific setups used and both measurement techniques can complement each

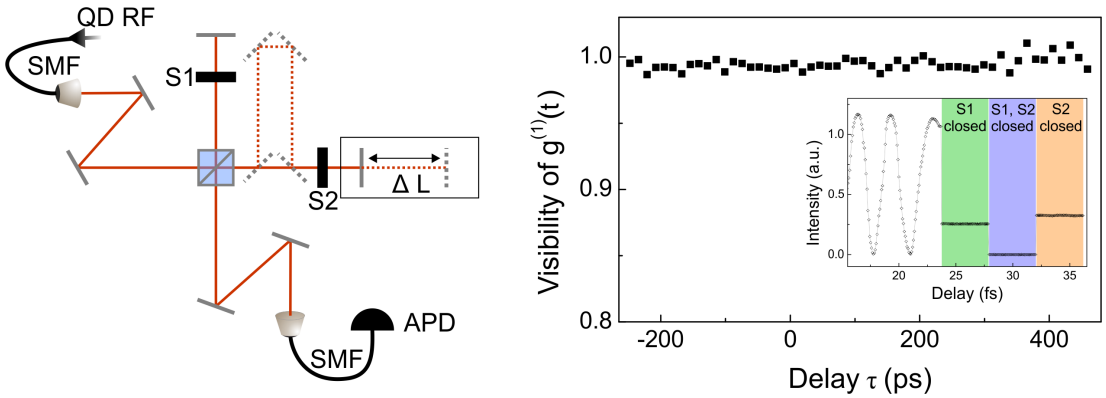

Figure 3.14: Setup and calibration of the Michelson interferometer. Left: The input signal (QD resonance fluorescence here) is sent through a single-mode fibre (SMF), split into stationary and moving paths, recombined on the same beamsplitter and coupled into a SMF connected to an avalanche photodiode (APD). Two shutters (S1, S2) allow measurements of the intensity in each path. An additional delay is indicated by dashed lines. Right: Measurement of the visibility of the first-order coherence for a single-mode laser. The inset displays part of a fringe measurement and the calibration procedure used to obtain the data points in the main figure.

other.

The setup for the Michelson interferometer is shown on the left in Fig. 3.14. The signal (QD RF) is divided into two arms by a beamsplitter (nominally 50:50). One arm is stationary: the signal is reflected back onto itself and coupled into a single-mode fibre connected to an APD. The mirror on the other arm sits on a linear stage (Physik Instrumente DG505.6DG) with 17 nm design resolution and 150 mm travel such that a delay of up to 1 ns can be reached relative to the stationary arm. An additional delay can be incorporated, indicated by the dashed path and mirrors, which covers delay times around 2.5-3 ns.

Measuring the first-order coherence of the signal field requires careful alignment: the reflected/transmitted paths from stationary and moving arm need to be collinear and spatially overlapping. Non-collinearity results in a phase variation across the beam (averaging out interference when integrating over the beam area), while imperfect beam overlap reduces the amplitude of the interference. A good method of aligning is to use a high coherence laser as signal and project the recombined beam onto a surface a long way away and observe the fringe pattern that arises through the spatially varying phase difference. Minimising the

number of interference fringes while keeping the beam overlap one should arrive at the point where the beam can be completely extinguished by slowly scanning the moving arm. Coupling the beam into the single mode fibre and recording the APD signal as the moving arm is scanned then shows the expected sinusoidal intensity dependence. Assuming an (infinitely) coherent input field the visibility of the interference signal, defined as

$$V = \frac{I_{\max} - I_{\min}}{I_{\max} + I_{\min}}, \tag{3.2}$$

where $I_{\max}(I_{\min})$ corresponds to the maximum (minimum) of the intensity, quantifies the instrument response function. A visibility of 1 characterises the ideal situation.

In our case the linear stage is not completely flat such that scanning the moving arm across the full range shows a nonlinear variation in beam overlap. The first-order coherence of the input field is obtained from measuring the fringe visibility for a number of set delays between the arms. To calibrate the interference signal at each delay, two mechanical shutters (S1 and S2 in Fig. 3.14) are employed. First we slowly move the stage and measure the fringe visibility for a number of periods (5-10), then close shutter S1 and record the intensity in the moving arm, close shutter S2 to record any background signal (APD dark counts mostly) and open S1 to record the intensity in the stationary arm. Exemplary data for this procedure is displayed in the inset on the right of Fig. 3.14

When measuring the first-order coherence of QD resonance fluorescence a sequence is added in the calibration where the QD transition is shifted off resonance via gate control and laser leakage is recorded. Given different intensities I_1, I_2 in each arm, the expected visibility for a monochromatic source is

$$V = \frac{I_{\max} - I_{\min}}{I_{\max} + I_{\min}} = \frac{2\sqrt{I_1 I_2}}{I_1 + I_2} \tag{3.3}$$

and the measured visibility is compared to this ideal case. After the calibration measurement, the stage moves to the next set delay (e.g. a distance of 1 mm) and the procedure repeats.

The plot on the right in Fig. 3.14 displays the results for a laser (several MHz

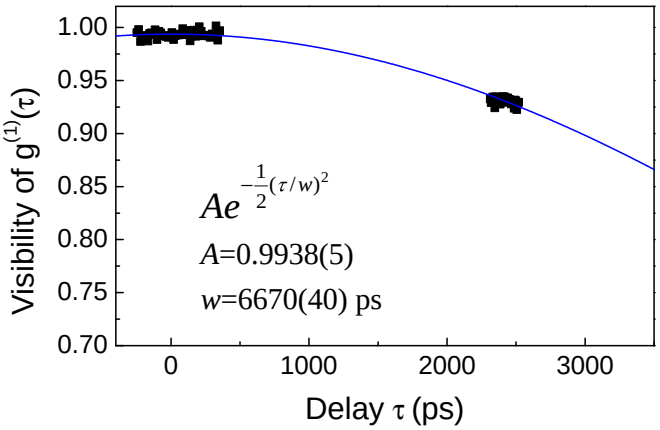

Figure 3.15: Coherence meaurement for a free-running external cavity laser (Toptica DL pro 940). The data at short delays is the same as in Fig. 3.14, the long delay data is obtained using the additional delay line.

linewidth) as input field. The visibility across the travel range is consistently around 99% (average 99.3%, standard deviation <0.5%), very close to the ideal case[1]. At longer delays, for example when the additional delay stage is incorporated, the finite laser coherence becomes apparent. Figure 3.15 displays the $g^{(1)}(\tau)$ measurement for a free-running external cavity diode laser. It is reasonable to expect a Gaussian decay of laser coherence in this kind of measurement: The laser linewidth is narrow at short timescales ($<$ 100 KHz for $\sim \mu s$ acquisition), however mechanical instabilities broaden the linewidth on slower timescales. Roughly speaking, the laser central frequency may wander monotonously in one direction on sub-second timescales, and randomly when measured longer. The parameter for a Gaussian fit (blue curve) are shown in the lower left of the figure.

3.4.3 Second-order coherence

The second-order coherence or intensity-correlation function $g^{(2)}(\tau)$ describes the light's intensity statistics in time. This is equivalent to the arrival time statistics of photons at a detector. Hence with a perfect detector we only have to record a sufficiently long timetrace of detector clicks and then evaluate the correlation

[1]For positive delays $>$ 300 ps the noise is higher, due to decreasing beam overlap at the end of the travel range of the stage.

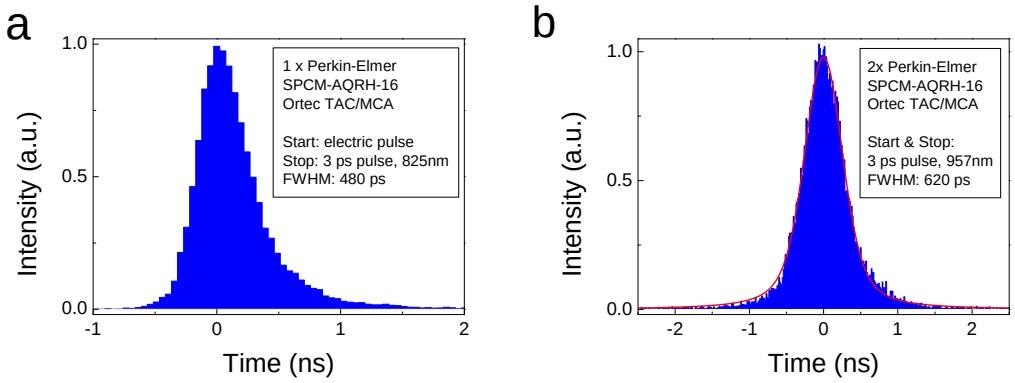

Figure 3.16: Timing resolution of APD single photon counters. a, Response of single APD to a pulses of a few ps width at 825 nm recorded in a START-STOP configuration with the Ortec TCA/MCA. A modelocked Ti:Sa laser provides optical pulses at $\sim$ 80 MHz repetition rate. The start trigger is obtained by sending a fraction of the pulsed laser light to a photodiode with 1.4 GHz bandwidth and amplifying the output. After heavy attenuation the laser pulsetrain is coupled into the APD whose electrical output gives the stop signal. The jitter of the electric start pulse is negligible compared to the APD jitter. b, Response function of two APDs in a Hanbury-Brown and Twiss configuration. The red line is least-squares fit to the data using a Voigt function. The Lorentzian contribution to the linewidth is about 1/3.

function, i.e. the detection time differences for all pairs of clicks. For real detectors we run into problems when the features of interest, typically the intensity correlation function at small delays, occur on timescales smaller than the detector deadtime. The way around this is to measure $g^{(2)}(\tau)$ in a Hanbury-Brown and Twiss setup [112], a sketch of which was shown in Fig. 2.4. The signal is split into two parts of (ideally) equal intensity and sent to two detectors. Each detector may have a large deadtime, but the time difference between two closely spaced photons can still be resolved if they leave different output ports of the beamsplitter.

The experimental (optics) setup for $g^{(2)}(\tau)$ measurements is less involved than that for $g^{(1)}(\tau)$ or the spectrum $S(\nu)$ as no moving parts are involved. The signal from a single-mode fibre is sent to a free-space beamsplitter and the two output ports are coupled into single photon detectors via coupling into single-mode fibres. Alternatively, the signal is coupled directly into a fibre-based beamsplitter (FONT Canada) with the two output fibres plugged into the detector fibre ports.

Two systems are available in the lab that convert the detector coincidences into correlation data. The first one is the time-to-amplitude converter from Ortec (ORTEC Model 567). It converts pulse detection time differences between the two input ports (start and stop are fixed) into the amplitude of an ouput pulse. The pulse height is digitised and stored with a multi-channel analyser (MCA 926M) before being sent to a computer. The timing resolution of the instrument amounts to $\sim$ 20 ps for coincidence time delays of 100-200 ns. The second system is the 8-channel time-to-digital converter 'quTau' from quTools. In addition to recording time-differences between any two of the input channels it also allows time-tagging events from all channels in the same run (no loss of information). The timing resolution is specified as 81 ps.
In almost all measurements presented in this thesis we use fibre-coupled Perkin-Elmer single photon counting modules (SPCM-AQRH16). At 950 nm wavelength they feature a detection efficiency about 20-25 % and dark count rates $\sim$ 20 Hz. The timing jitter of individual modules varies between 450-500 ps, depending on module, detection wavelength and detection rate [113]. In the Hanbury-Brown and Twiss configuration this corresponds to a measurement uncertainty of 600-700 ps. These numbers are important as they, together with the timing resolution of the correlation electronics, represent the system response function and any measured signal is a convolution of the actual signal with the response function of the instrument. Two measurements for the system response function are presented in Fig. 3.16, for single photon detection on the left and two-photon detection on the right.

Chapter 4

A two-level system in a solid-state environment: resonant QD spectroscopy

Having covered some theoretical background on the near-resonant light-matter interaction of two-level systems in Chapter 2, and described our experimental capabilities in Chapter 3, we now turn to the experimental study of a real system. Subject of study are the resonantly driven neutral exciton (X^0) and the negatively charged trion (X^{1-}) QD transitions at zero external magnetic field. With a fine-structure splitting of several GHz for our samples both X^0 transitions individually should behave like a good two-level system. As for the X^{1-} transitions at zero external magnetic field, we would naïvely expect the two sets of transitions to be degenerate and hence also follow the predictions for a two-level system.
In this chapter we explore the properties of QD resonance fluorescence. We look at the standard features expected for two-level systems: saturation behaviour, power broadening and the first- and second-order correlation functions. In the low and moderate excitation power regime (around saturation and below) we find that the X^0 transition approximates an ideal two-level system well. In the Heitler regime we directly observe highly coherent scattering from a single QD; a first for solid-state single photon emitters. A closer look at the spectral and statistical properties of the fluorescence reveals deviations from the ideal two-level

behaviour. We identify and quantify influences on the QD emission properties: Spectral diffusion modifies scattering rates, exciton-phonon coupling provides a dephasing mechanism and finally, the nuclear Overhauser field invalidates the two-level approximation for the X^{1-} transition.
Some of the material in section 4.1 was published in [114]. Measurements of the acoustic phonon sidebands (Fig. 4.11) were taken and analysed together with Claire Le Gall.

4.1 Subnatural linewidth single photons

4.1.1 Performance of the measurement system

The technical challenge to observe the QD resonance fluorescence is to suppress sufficiently the laser background at the same frequency. Quantifying the performance of our experimental system in terms of the laser background suppression versus the collection and detection efficiency of QD photons has to be the first step in our investigation.
Our experimental arrangement, discussed in detail in the previous chapter, relies on a confocal microscope where we use the combination of cross-polarisation and confocal rejection of the collection fiber to suppress laser reflections in the detection path. The two polarisers are aligned to the dark-field configuration by sending a strong laser at the QD resonance frequency through the confocal microscope and minimising the transmission. Starting from the dark-field configuration and rotating the collection polariser to maximise transmission we measure a factor of 10^7-10^8 difference in power at the collection fibre end. Conversely, comparing the photoluminescence intensity from a saturated X^{1-} transition in the dark-field configuration to the intensity measured when the collection polariser is absent, we find about a factor two difference. Translating this suppression of laser reflection into a QD signal-to-laser background ratio depends on the excitation Rabi frequency Ω_R, on how efficiently we excite the transition and how well we collect the QD fluorescence.
Figure 4.1 a-d presents the excitation power dependence of the resonance fluorescence from QD 'Claude' in order to quantify both the collection efficiency of our

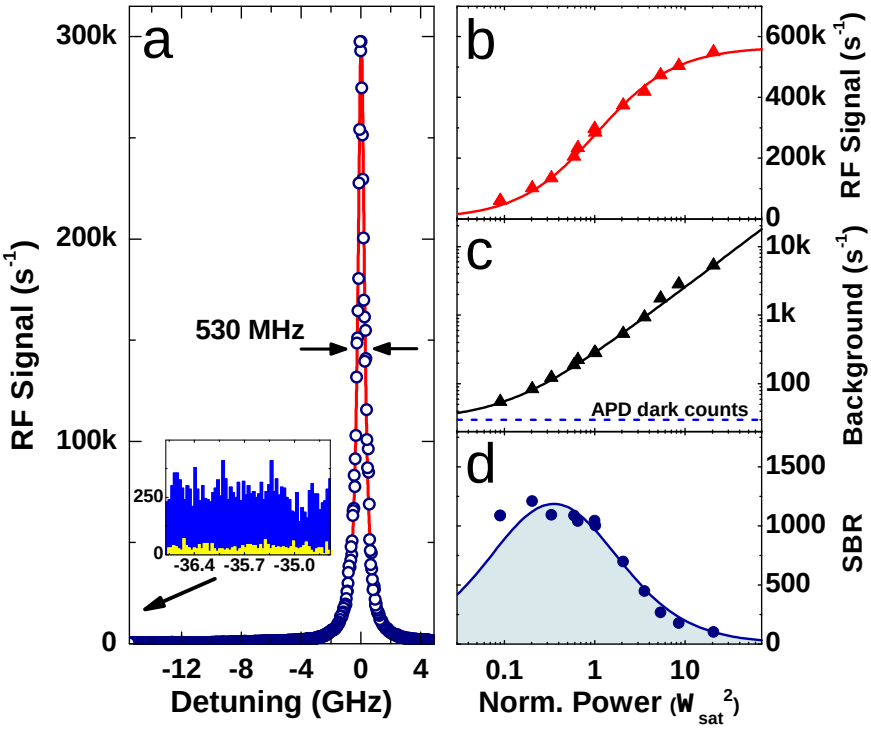

Figure 4.1: Analysis of collection efficiency and background contribution of resonance fluorescence on the example of QD 'Claude'. a, Integrated photon counts for resonance fluorescence at the saturation point as a function of laser detuning. The red curve is a Lorentzian fit to the data (open circles). Inset: Total off-resonance background counts (blue bars) compared to the APD dark counts alone (yellow bars). b, Integrated photon detection events when the laser is on resonance with the QD transition (red triangles) and c, off resonance (black triangles). d, resonance fluorescence signal-to-background ratio (SBR). At saturation ($\Omega_{sat}^2 = 1/(T_1 T_2)$) a value of 1050 is achieved. The excitation power for b-d is scaled in units of the saturation power.

system and the fraction of residual laser background in the detected photons. In panel a the laser frequency is fixed and photodetection events from a single-photon counting avalanche photodiode (APD) are recorded (open blue circles) as a function of gate bias. The bias Stark-shifts the QD transition and is expressed as frequency detuning here. The full-width at half-maximum of the Lorentzian fit (red curve) to the data is 530 MHz in linear frequency. Here, the excitation power corresponds to the saturation point. The inset displays the residual background for large detunings (blue bars) which includes the contribution of APD dark counts, measured separately and shown in yellow. In panels b and c the red and the black triangles display the total photodetection events per second on- and off-resonance, respectively, as a function of excitation power normalized to the saturation power. The solid curves represent the theoretically expected behaviour for the data in each panel and the dashed blue line indicates the mean dark count level.

For an excitation power at the saturation point ($\Omega_{sat}^2 = 1/(T_1 T_2)$, where Ω denotes the Rabi frequency and T_1, T_2 lifetime and pure dephasing time) we collect photons at a rate of 1.2-1.5 MHz into our single-mode optical fiber, while the laser and detector background contribute <0.01% of the total signal. With a detector quantum efficiency in the range of 20-25% we register $3 \cdot 10^5$ detector clicks per second. The blue circles in panel d show the obtained ratio of the resonance fluorescence signal to total background (SBR) for each laser power along with the expected power dependence (blue curve). At a tenth of saturation, the residual laser contribution to the background falls below the dark count level (30 Hz) limiting the SBR.

Turning to the combined photon collection and detection efficiency, we can estimate this number from the saturation curve and the QD excited state lifetime. For a lifetime of 600-700 ps, which is typical for our sample we estimate a modest 0.1% total collection and detection efficiency for QD Claude. Starting from the detector and working towards the QD sample we estimate the losses in the collection path as follows: detector efficency ~ 0.2, coupling into the collection fibre ~ 0.5, polarisation suppression ~ 0.5, polariser transmittance ~ 0.85, beamsplitter transmittance $\sim 0.9^2$, transmittance through glass plate/objective lens/SSIL ~ 0.8. Altogether this give $0.0275 \approx 1/35$. The remaining factor then sets the

outcoupling efficiency to 3.5 %[1].

4.1.2 Saturation and power broadening

4.1.2.1 Saturation of a two-level system

The data in Fig. 4.1 b follows the saturation behaviour we expect for the two-level system and was already discussed in the theoretical background. As a reminder, the emission rate Γ_{RF} is given by the excited state population and its lifetime:

$$\Gamma_{RF} = \rho_{22} \times \frac{1}{T_1} = \frac{1}{T_1} \times \frac{1}{2} \frac{\Omega^2}{(T_1 T_2)^{-1} + \Omega^2}, \tag{4.1}$$

where we assume resonant excitation at zero detuning. The square of the Rabi frequency (Ω^2) is proportional to laser power, which is the experimentally measurable quantity. The link between excitation power and Rabi frequency is made through the saturation point; where the emission rate is half of its maximum. This point can be determined very reproducibly and from Eq. (4.1) we can see that the saturation power corresponds to $\Omega_{sat}^2 = 1/(T_1 T_2)$. Using this to rearrange we have

$$\Gamma_{RF} = \frac{1}{2T_1} \times \frac{s \times (T_1 T_2)^{-1}}{(T_1 T_2)^{-1} + s \times (T_1 T_2)^{-1}} = \frac{1}{2T_1} \times \frac{s}{1+s}, \tag{4.2}$$

where s is the saturation parameter[2].

4.1.2.2 Power broadening

Power broadening of a two-level system is expected to follow

$$\Gamma_{\mathrm{FWHM}} = \frac{2\hbar}{T_2} \times \sqrt{1 + \Omega^2 T_1 T_2} = \Gamma_{\mathrm{FWHM}}(0) \times \sqrt{1+s}, \tag{4.3}$$

[1] We note that the DBR stopband for this sample is centred around 980 nm (designed to be 960 nm) and reflectivity measurements show a intensity difference of factor 2-3 between the centre of the stopband and the wavelength of QDs we usually work with (950-960 nm). Count rates above 1 MHz have been measured at longer wavelengths

[2] One of the assumptions of the two-level model is that lifetime and dephasing time do not change with excitation power. The former is a solid assumption while the latter is not necessarily true [110; 115; 116]. However, this effect becomes only apparent for s $\gg$1.

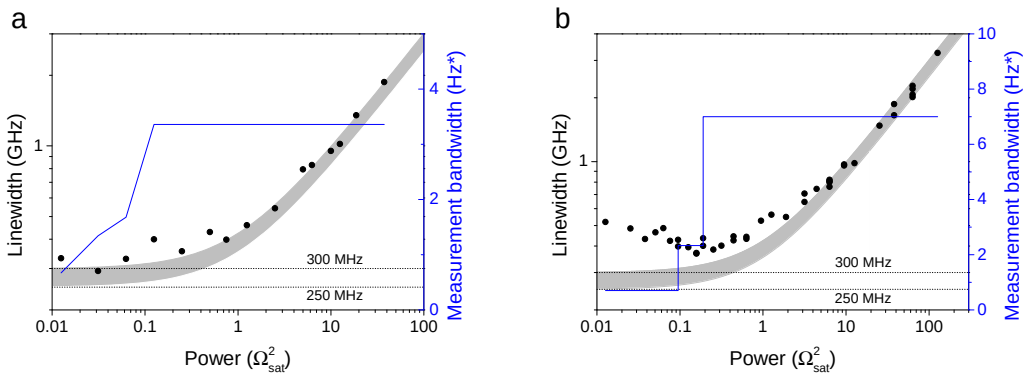

Figure 4.2: Power broadening of the X^0 (a) and X^{1-} (b) transitions of QD 'Claude'. Experimental data is shown as black dots. The grey shaded area displays the theoretical behaviour for zero-power linewidths of 250 MHz (lower boundary) and 300 MHz (upper boundary). An effective measurement bandwidth is indicated by the blue curve.

where the saturation parameter is used again to simplify the expression. Ideally, the linewidth in the limit of small Rabi frequencies reflects the dephasing time T_2 and with the knowledge of the lifetime T_1 we can extract a pure dephasing time. In the absence of pure dephasing ($T_2 = 2T_1$), the radiative linewidth is recovered. It is important to note that the linewidth here is the absorption linewidth, obtained, for example, by scanning a narrow-band laser across the transition and recording the total emission intensity. This should be distinguished from the emission linewidth, which can be considerably different and is treated in the next section. Figure 4.2 a and b display the linewidth of the X^0 and X^{1-} transitions of QD 'Claude', respectively. The data, shown as black dots, are extracted by fitting Lorentzians to absorption linescans such as the one in Fig. 4.1 a. The linewidth uncertainty for each fit is about the size of the dots in the figure. The grey band indicates the line broadening expected from 4.3 for radiative linewidths between 250 and 300 MHz and no pure dephasing. 250 MHz radiative linewidth is expected from lifetime measurements for this sample. Above the saturation point the experimental data are mostly within this band, while the mismatch with theory is clear below saturation, in particular for the X^{1-} data set. Also shown is the effective measurement bandwidth (blue line): It is the inverse of the time it takes to scan across a 250 MHz window (one radiative linewidth). This is in the range of 1-10 Hz, i.e. measuring the FWHM of the transition takes

about 1 s for the measurements presented. The deviations from the ideal case are attributed to spectral diffusion, rather than fast dephasing and will be explored in the second half of this chapter (see section 4.2.1). Further, the difference between the X^0 and X^{1-} is due to the nuclear Overhauser field (see section 4.2.3).

4.1.3 Spectral and statistical properties at low powers

The spectrum of resonance fluorescence. Resonant excitation of a two-level system drives the coherences and population in the Bloch sphere according to the optical Bloch equations presented in the theoretical background. The emitted photons directly reflect the dynamics of the system, both of the population (in the emission rate) and the coherences (in the spectrum). In order to capture the full picture through measurements we need to look at the spectral and statistical properties of the photons using the correlation functions introduced theoretically and experimentally earlier.

The spectrum of resonance fluorescence for a laser exactly on resonance is given by[1] the sum of incoherent and coherent components:

$$\begin{aligned}
S(\Delta\nu) &= I_{inc}\,\tilde{S}_{inc}(\Delta\nu) + I_{coh}\,\tilde{S}_{coh}(\Delta\nu) \\
&= \rho_{22}\left(1-\frac{1}{2}\frac{\tilde{T}_2}{\tilde{T}_1+\Omega^2\tilde{T}_1^2\tilde{T}_2}\right)\tilde{S}_{inc}(\Delta\nu) + \rho_{22}\left(\frac{1}{2}\frac{\tilde{T}_2}{\tilde{T}_1+\Omega^2\tilde{T}_1^2\tilde{T}_2}\right)\tilde{S}_{coh}(\Delta\nu) \\
&= \rho_{22}\Bigg\{\left(1-\frac{1}{2}\frac{\tilde{T}_2}{\tilde{T}_1+\Omega^2\tilde{T}_1^2\tilde{T}_2}\right)\frac{1}{2\pi\rho_{22}\left(\left(\Omega^2\tilde{T}_1^2\right)^{-1}+2\right)}\times\Bigg[\frac{1/\tilde{T}_2}{\Delta\nu^2+1/\tilde{T}_2{}^2} \\
&\quad + \frac{2\rho_{22}}{\Omega^2}\times\left(\frac{A\eta/2-B(\Delta\nu-\mu)/(8\mu)}{(\Delta\nu-\mu)^2+\eta^2}+\frac{A\eta/2+B(\Delta\nu+\mu)/(8\mu)}{(\Delta\nu+\mu)^2+\eta^2}\right)\Bigg] \\
&\quad + \left(\frac{1}{2}\frac{\tilde{T}_2}{\tilde{T}_1+\Omega^2\tilde{T}_1^2\tilde{T}_2}\right)\delta(\Delta\nu)\Bigg\}
\end{aligned} \tag{4.4}$$

[1] It is surprisingly difficult to write down this equation without typographic mistakes and wrong signs - a good proportion of QD resonance fluorescence papers suffer from this issue.

where $\Delta\nu$ is the emission detuning in linear frequency, $\tilde{T}_{1,2} = 2\pi T_{1,2}$, $\tilde{S}$ refers to the normalised (area of unity) spectrum and we use shorthands

$$
\begin{aligned}
A =& \Omega^2 + \frac{1}{\tilde{T}_1\left(1/\tilde{T}_1 - 1/\tilde{T}_2\right)},\\
B =& 2\Omega^2 + \left(\frac{3}{\tilde{T}_1} - \frac{1}{\tilde{T}_2}\right) - \frac{2}{\tilde{T}_1}\left(\frac{1}{\tilde{T}_1} - \frac{1}{\tilde{T}_2}\right),\\
\mu =& \sqrt{\Omega^2 - \frac{1}{4}\left(\frac{1}{\tilde{T}_1} - \frac{1}{\tilde{T}_2}\right)},\\
\eta =& \frac{1}{2}\left(\frac{1}{\tilde{T}_1} + \frac{1}{\tilde{T}_2}\right).
\end{aligned}
$$

The normalisation of Eq. 4.4 is then such that the integrated intensity corresponds to the excited state population ρ_{22}, linking it to the saturation curve we are familiar with.

At high excitation power the incoherent component reveals the Mollow triplet, while at low excitation power the spectrum is single-peaked. The emergence of sidebands in the spectrum of resonance fluorescence at Rabi frequencies $\Omega \gg \Omega_{sat}$ arises as a consequence of Rabi oscillations between ground and excited states and is considered the hallmark of resonance fluorescence. It was among the first features sought and observed experimentally, first for atoms [99], but also for QDs [103; 104; 105; 106]. In this limit of Rabi frequency, the emission is spontaneous and incoherent with respect to the excitation laser. Remarkably, resonance fluorescence is expected to show a crossover from incoherent to coherent photon scattering, accompanied by a drastic change in the emission spectrum as a function of Rabi frequency. Perhaps surprisingly, the limit of vanishing Rabi frequency in the resonant interaction has remained relatively unexplored for atoms, ions and any single solid-state emitter [117]. Here, we will investigate this limit for QD resonance fluorescence and report on the first direct observation of highly coherent light scattering from a solid-state emitter. We employ a shorthand, the 'Heitler regime', to denote the situation where the Rabi frequency is much smaller than the spontaneous emission rate and pure dephasing is negligible, after W. Heitler who described the response of a two-level system to monochromatic

excitation in the early days of quantum optics.

Figure 4.3 displays a series of resonance fluorescence spectra for QD 'Claude'. For each row of the figure the excitation laser power is fixed and its frequency is set on resonance with the QD transition. The resonance fluorescence spectrum is recorded with the scanning Fabry-Perot cavity (see section 3.4.1 for instrument details and response function). In the left panels we plot the experimental data (as filled red circles) and a calculated spectrum based on Eq. (4.4) and the Fabry-Perot response function (green continuous line) in linear scale. The middle panels show the data and the convolved theoretical spectrum (green dashed line) in a semi-logarithmic scale, together with the coherent (blue continuous line) and incoherent (red continuous line) components. Both components of the spectrum are convolved with the FP response function and offset for clarity. The panels on the right give the theoretical spectra without convolution. These spectra integrate to give the value of ρ_{22}. To the right of the plot we note the experimental saturation parameter s and the parameters for the theoretical spectra.

The excitation laser bandwidth is very narrow on small timescales ($<$ 100 KHz for $\sim \mu s$ acquisition), however slow spectral wandering broadens the linewidth on the timescale of the data acquisition ($\sim$ seconds) to a few MHz. In the simulation we take a top-hat function of 3 MHz width to account for this laser linewidth. This is the narrow peak on top of the incoherent component in the right panels. This spectrum in the right panels is convolved with a Lorentzian of 25-35 MHz width and scaled to the data to arrive at the spectra (green lines) in the left and middle panel.

Starting from the top, at a laser power corresponding to $s = 2.35$ both components are clearly visible in a linear scale (left panel). The incoherent part dominates the deconvolved spectrum (right panel); here the coherent fraction is 0.3. As we decrease the laser power, going down the panels, the incoherent component is increasingly masked by the coherent part. Above saturation, some structure is visible on a semi-logarithmic scale in wings of the incoherent part, whereas for $s \leq 1$ the incoherent spectral component is reduced to a single peak. At $s = 0.1$ where theory predicts a coherent fraction of 0.9 the entire measured spectrum collapses to a Fabry-Perot cavity resolution-limited Lorentzian. Any residual incoherent component of resonance fluorescence in this regime is less

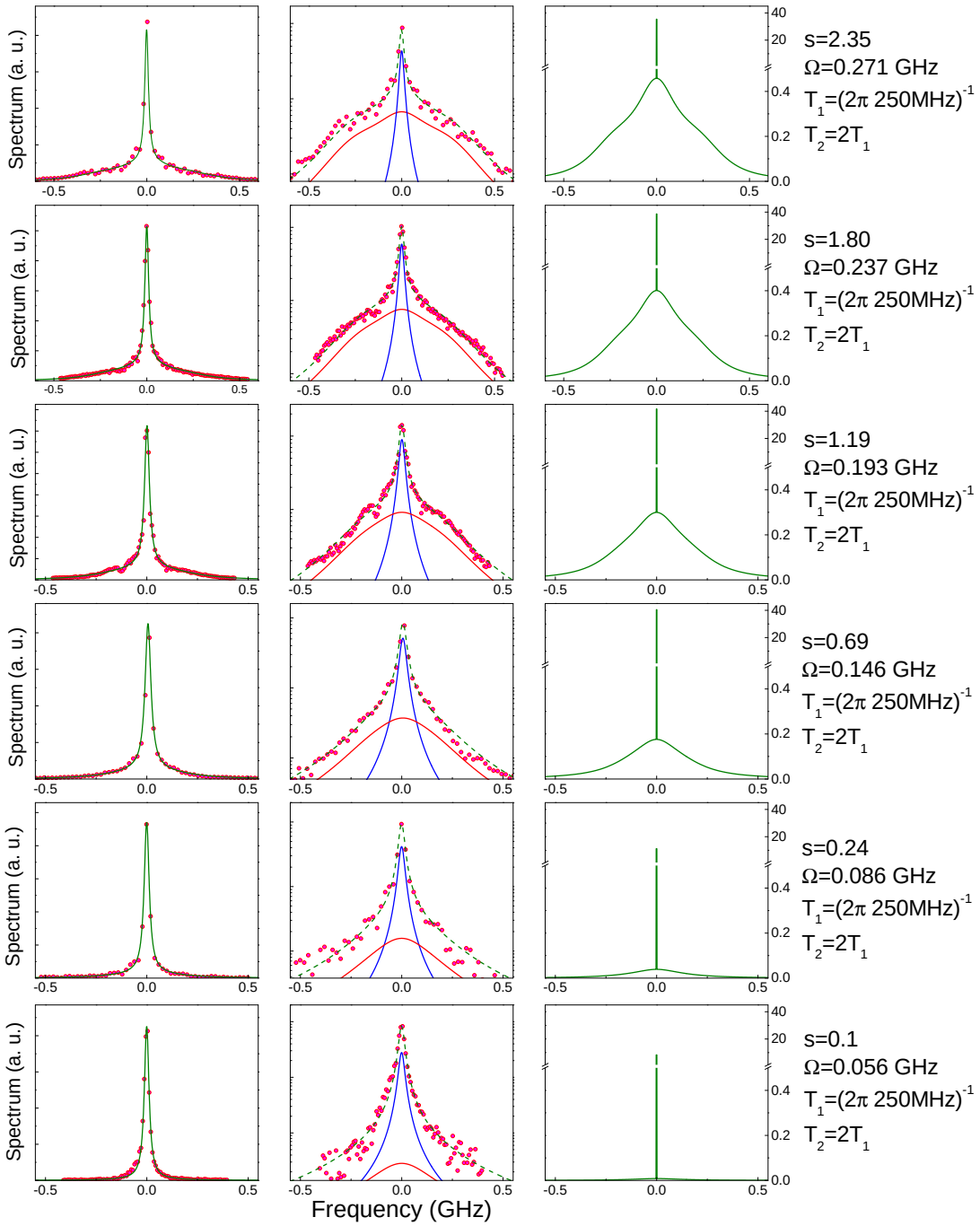

Figure 4.3: Resonance fluorescence spectra of QD 'Claude' as function of exitation power. The data (red circles) are recorded with a scanning Fabry-Perot cavity of 30 MHz resolution. Continuous and dashed lines show calculated spectra for the respective experimental parameters. With the exception of the right panels, the calculated spectra are further convolved with the Fabry-Perot response function and scaled to the data. Left panels: data and convolved calculated spectrum. Middle panel: as before, but in a semi-logarithmic scale. Coherent (blue) and incoherent (red) components are shown individually for clarity. Right panels: Calculated spectra without convolution.

than the detectable level within the spectral resolution and the signal-to-noise ratio of our measurements. We clearly observe subnatural linewidth fluorescence here, consistent with predictions for a simple two-level system in the absence of any pure dephasing. In fact, the theory curves for a purely radiatively broadened system, i.e. $T_2 = 2T_1$, fit the measured spectra for all power levels presented in Fig. 4.3. This is strong evidence that QDs provide clean atomic-like optical transitions with little to no dephasing at timescales comparable to their lifetime. The spectral resolution of the Fabry-Perot cavity of ~ 30 MHz limits us at this point to perform more quantitative analysis of the QD resonance fluorescence spectrum. We switch to Fourier transform spectroscopy and measure the first-order correlation function in a Michelson interferometer (see section 3.4.2 for details on the setup).

The first-order correlation of resonance fluorescence. The derivation of the first-order correlation for a resonantly driven two-level system was sketched out in the theoretical background. Separating the spectrum into incoherent and coherent components and neglecting the oscillations at the optical wavelength we have:

$$\begin{aligned} g^{(1)}(\tau) &= I_{inc}\, g^{(1)}_{inc}(\tau) + I_{coh}\, g^{(1)}_{coh}(\tau) \\ &= \rho_{22}\left(\frac{1}{2}\exp^{-|\tau|/T_2} + \exp^{-|\tau|/2\left(\frac{1}{T_1}+\frac{1}{T_2}\right)}\left(N\cos(\mu|\tau|) + M\sin(\mu|\tau|)\right)\right) \\ &\quad + \rho_{22}\,\frac{1}{1+\Omega^2 T_1 T_2}\,\frac{T_2}{2T_1}, \end{aligned} \tag{4.5}$$

where τ is the time delay between the fields interfered in the interferometer and we have taken the detuning to be zero. The coherent part of eq. (4.5) has to be modified to account for the finite laser coherence and laser spectral wandering encountered in experiments. From the instrument calibration (cf. Fig. 3.15) a Gaussian decay is reasonable, such that

$$I_{coh}\, g^{(1)}_{coh}(\tau) = \left(\rho_{22}\,\frac{1}{1+\Omega^2 T_1 T_2}\,\frac{T_2}{2T_1}\right)\exp^{-\frac{1}{2}\left(\frac{|\tau|}{\tau_L}\right)^2}, \tag{4.6}$$

where τ_L is around 5-7 ns. The amplitude of the $g^{(1)}(\tau)$ expression given above scales as the excited state population ρ_{22}. In order to compare it to measured interference visibilities we divide by ρ_{22} and obtained an expression with unity amplitude for all Rabi frequencies.

Experimental results on first-order coherence measurements for the X^0 transition of QD 'Claude' are presented in Fig. 4.4. Here we drive the QD on resonance with a free-running external cavity diode laser; the measurement protocol is detailed in section 3.4.2. Figure 4.4 a shows experimental data as open symbols and fits according to Eqs. (4.5), (4.6) as solid lines for four excitation powers, indicated on the right-hand side in terms of the saturation parameter s.

We make two immediate observations. First, in agreement with the subnatural linewidth emission spectra from Fig. 4.3, the coherence of the QD resonance fluorescence is sustained on timescales considerably longer than the spontaneous lifetime of ~ 640 ps (250 MHz radiative linewidth). Second, we would expect the visibility measured around zero time delay to be equal to that of the laser (~ 0.99, see Fig. 3.14 for reference). For QD resonance fluorescence the maximum amplitude is ~ 0.88. This discrepancy suggests the presence of a very fast coherence decay channel for part of the fluorescence. For a stepsize of about 10 ps in Fig. 4.4 a, the spectral width of the fast decay channel is expected to be in the THz frequency range, which is consistent with phonon-assisted transitions as we will see later in this chapter.

Panel b presents a power series of interference visibilities obtained at long delays (filled symbols), together with the measurement for the excitation laser (open squares). The laser coherence was measured at intensities and scanning speeds similar to the resonance fluorescence data and allows us to account for the finite laser coherence. In panel c, we plot the coherent fraction as extracted from the fits in panel a (blue circles) and the power series in b (black squares) as a function of excitation power. To compare to the predictions for a simple two-level system we consider only the zero-phonon line (ZPL) here[1] and correct for the

[1] that is, we correct for the finite visibility at zero time delay

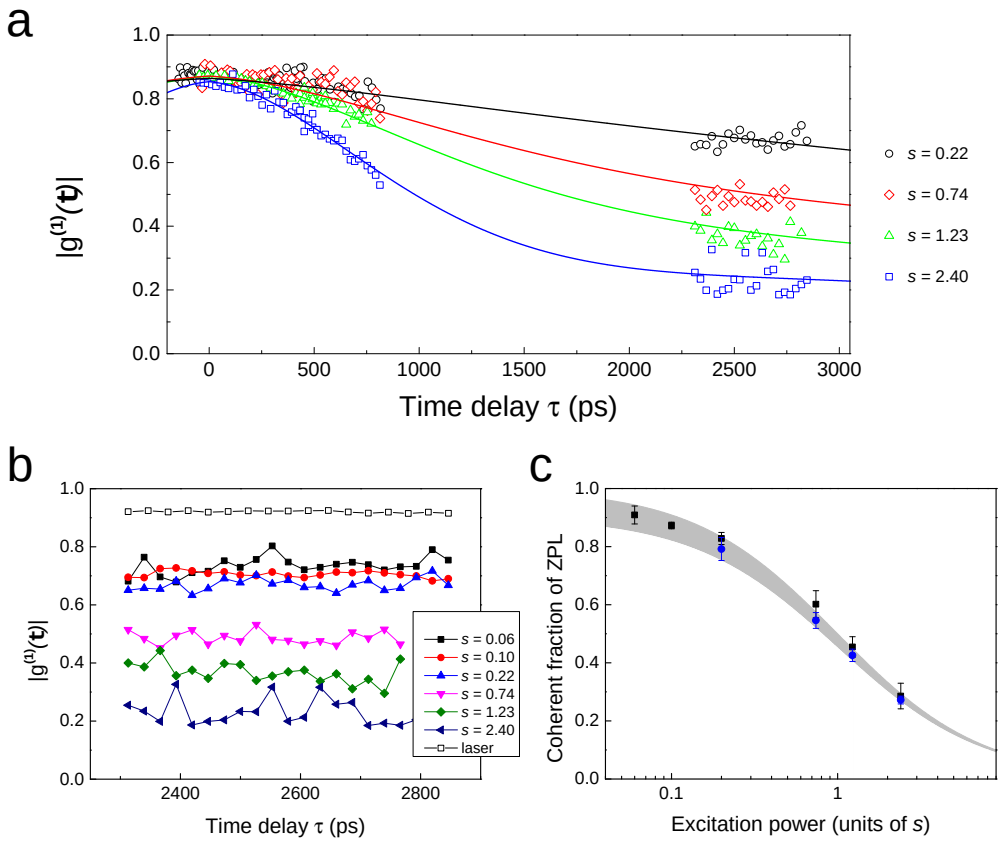

Figure 4.4: First-order coherence measurements of QD resonance fluorescence and evaluation of the coherent fraction. a, $g^{(1)}$ measurements at short and long delays (data as open symbols) with fits according to Eqs. (4.5) and (4.6). b, Long delay measurements for a series of excitation powers compared to the laser coherence. c, Coherent fraction of QD resonance fluorescence as extracted from panels a and b. The grey band gives the theoretical prediction for $1.8T_1 < T_2 < 2T_1$.

laser coherence. The grey band displays the coherent fraction according to

$$F_{coh} = \frac{1}{1+\Omega^2 T_1 T_2}\,\frac{T_2}{2T_1} = \frac{1}{1+s}\,\frac{T_2}{2T_1}, \tag{4.7}$$

where the upper limit is set by $T_2 = 2T_1$ and the lower limit by $T_2 = 1.8T_1$.

4.1.4 Wave-particle duality in the Heitler regime

The concept that two-level systems emit photons one at a time is well-known in quantum optics. First proposed theoretically by Kimble and Mandel [118] in 1976, the first measurement of photon antibunching in the intensity correlation $g^{(2)}(\tau)$ was shown by Kimble, Mandel and Dagenais a year later [101; 119]. Since the potential of single photon sources in quantum communication [98] and computation [120] was estabilised, research into this field has exploded. First antibunching measurements using above bandgap excitation on quantum dots stem from 2000 [121; 122], and great experimental efforts have led to efficient optically pumped QD single photon sources [123], and also electrically controlled QD single photon diodes in laboratories [19]. Under resonant excitation the photon statistics, captured through the second-order correlation function $g^{(2)}(\tau)$, reflect the dynamics of the driven system, and allowed the observation of QD exciton Rabi oscillations [104].

Where $g^{(1)}(\tau)$, or equivalently the emission spectrum, measures the wave properties of the photons, the intensity autocorrelation $g^{(2)}(\tau)$ represents the photon's particle nature. These are, of course, complementary features. For incoherent pumping, i.e. above band excitation the intensity autocorrelation $g^{(2)}(\tau)$ is linked to the excited state lifetime T_1, whereas the field correlation function $g^{(1)}(\tau)$ links to its coherence time T_2. In other words, the coherence $\tau_{c,\mathrm{photon}}$ of the single photons is constraint to the emitter lifetime: $\tau_{c,\mathrm{photon}} = T_2 \leq 2T_1$.

Under resonant excitation in the Heitler regime, however, photons scatter elastically: When the Rabi frequency is much smaller than the spontaneous emission rate and pure dephasing is negligible, QD emission is predominantly coherent. Then the coherence properties of resonance fluorescence photons (and thus their

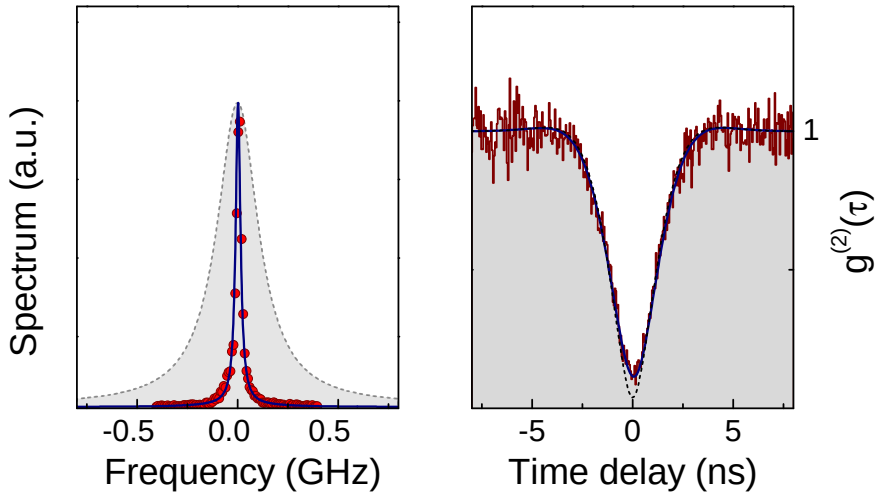

Figure 4.5: Wave-particle duality in the Heitler regime. Left: The emission spectrum is Fabry-Perot resolution limited, and much narrower than the radiative linewidth (indicated by the shaded area). The subnatural linewidth indicates a coherence $T_2 \gg 2T_1$. Right: The intensity autocorrelation at the same measurement setting demonstrates antibunching on the timescale of the excited state lifetime.

spectrum) are liberated from the QD transition lifetime. Instead, the coherence is derived from the excitation laser properties. The subnatural linewidth emission spectrum from the previous section is displayed on the left-hand side in Fig. 4.5 together with the radiative linewidth as grey shaded area. On the right-hand side we display the $g^{(2)}(\tau)$ intensity autocorrelation measurement under identical excitation conditions. The data (dark red curve) demonstrates clear antibunching on the timescale of the excited state lifetime. Here, the recorded curve is limited by the detector response, such that the dip close to the zero time delay cannot be fully resolved. The dotted black line shows a deconvolved fit to the data, based on equation (2.31)[1].

These results reveal the counter-intuitive nature of resonance fluorescence in the Heitler regime: The QD operates as a quantum converter of a weak coherent state into a coherent single photon stream. The photons arrive one at a time to our detection system, but are phase-correlated with each other and with the laser

[1]Spectral diffusion of the QD transition during the long $g^{(2)}(\tau)$ measurement needs to be taken into account to produce the blue fit curve. This will be discussed in more detail in section 4.2.1.

field from which they originated.
At this point we can draw some intermediate conclusions from the combination of spectral, $g^{(1)}(\tau)$ and $g^{(2)}(\tau)$ measurements:

- Fits to spectra and $g^{(1)}(\tau)$, in particular the evaluation of the coherent fraction in Fig. 4.4, allow us to put a number on the QD transition coherence time of $T_2 = (0.95 \pm 0.05) \cdot 2T_1$. The results show that QD transitions are intrinsically mostly free of pure dephasing, contrarily to earlier reports [104].

- In the limit of weak excitation and negligible pure dephasing (the Heitler regime), photons are predominantly coherently scattered. Their coherence is no longer bound by the transition lifetime; it can be significantly longer. Our measurements point to a time-averaged linewidth of several MHz. At the same time, antibunching persists on the timescale of the transition lifetime.

- Within the measurement uncertainty the coherently scattered photons follow the coherence of the laser which is limited by spectral wandering to several MHz. In other words, a quantum dot generates single photons with laser-like coherence free from any dephasing processes affecting the QD light emission.

The observation of highly coherent scattering is relevant and exciting for a number of applications in quantum information processing with QDs. First, issues thought to be inherent in solid-state systems, such as spectral diffusion, modify the probability to scatter a photon, but do not change its spectral properties. This, in combination with the fact that the absolute photon frequency is pinned to the laser frequency can be of crucial advantage in quantum interference applications, where indistinguishable photons are needed at different times or from separate sources. Second, not only the frequency, but also the photon phase is expected to be determined by the excitation laser, which should allow us to shape phase and spectrum of single photons deterministically. Some of these ideas will be explored experimentally in chapter 6.
We note that Nguyen *et al.* report similar measurements, see Ref. [124].

4.2 Effects of the solid-state environment

The first part of this chapter explored experimental evidence of the near-ideal behaviour of QD emission under low power resonant excitation. However, even in these basic quantum optical measurements, deviations from the theoretical predictions were present: Absorption linewidths were broader than expected, particularly for the X^{1-} transition (cf. Fig. 4.2), the contrast of the first-order coherence was limited (cf. Fig. 4.4) and the antibunching dip in the second-order coherence was narrower than predicted (Fig. 4.5).
To explain these effects we have to consider the solid-state environment of the QD. Here we focus on three effects in particular: spectral diffusion, exciton-phonon coupling and the nuclear Overhauser field.

4.2.1 Spectral diffusion

Spectral diffusion describes the effect of transition resonance shifts over time. It is usually attributed to the uncontrolled electric fields arising from the dynamics of defects (metastable trapped charges) or other QDs nearby. The time-dependent electric fields shift the QD resonance via the Stark effect (see intro section). Particular sample circumstances and models of defect dynamics have been subject of a number of studies recently [78; 81; 125; 126]. Timescales and magnitudes vary greatly between different structures and samples in these reports. Here we want to quantify the severity of spectral diffusion in our gated sample (Chef 2 sample), and we employ resonance fluorescence to obtain precise information on bandwidth and amplitude of spectral diffusion[1]. Information is extracted from time-resolved resonance fluorescence detection: We record a series of 10-s long resonance fluorescence detection time traces with a resolution of 10 μs and treat the data using statistics on photon arrival probabilities and time and compare the result to a simple model.

[1]Note added: High quality measurements, also using QD resonance fluorescence and yielding similar results, were obtained in the group of R. Warburton very recently [127].

4.2.1.1 Spectral diffusion amplitudes

First we take the 10-s long timetraces and compile histograms of the probability to detect a set number of counts per detection bin. Given the overall small collection and detection efficiency ($< 0.2\%$) of the setup we expect the detections to obey Poissonian statistics. Then, for a mean number of m photons per bin, the probability distribution of k_{bin} counts per bin is

$$P\left(k_{\text{bin}}\right) = \frac{m^{k_{\text{bin}}} \exp^{-m}}{k!}. \tag{4.8}$$

The mean m is linked to the QD fluorescence through the collection and detection efficiency $\eta_{\text{detection}}$ and the excited state population (see Eq. (4.2)):

$$m\left(s, \Delta\right) = \eta_{\text{detection}} \times t_{\text{bin}} \times \frac{1}{2T_1} \frac{s}{1 + s + 2\left(2\pi\Delta\right)^2 T_1 T_2}, \tag{4.9}$$

where t_{bin} is the duration of a detection bin and Δ is the detuning of the laser from resonance. For numerical data treatment it is convenient to work with

$$m\left(s, \Delta\right) = a \times \frac{s + 1}{1 + s + 2\left(2\pi\Delta\right)^2 T_1 T_2}, \tag{4.10}$$

where the fraction is normalised to unity for zero detuning ($\Delta = 0$) and the prefactor a can be conveniently linked to the experimental mean for a given bin size.

The effect of spectral diffusion is to make the laser detuning into a time-varying quantity $\Delta\left(t\right)$. When measuring for sufficiently long we expect to cover the full extent of the spectral diffusion, such that $\Delta\left(t\right)$ can be described by a probability distribution. In terms of the probability distribution of k_{bin} counts per bin, the Poisson distribution (4.8) is modified to

$$P\left(k_{\text{bin}}\right) = \sum_{\Delta} \mathrm{W}\left(\Delta\right) \times \frac{m\left(s, \Delta\right)^{k_{\text{bin}}} \exp^{-m(s,\Delta)}}{k!}. \tag{4.11}$$

The weighting function $\mathrm{W}\left(\Delta\right)$ effectively describes how much time is spent at each detuning, and we can reasonably assume that it follows a Gaussian distribution

for long measurement times:

$$\mathrm{W}(\Delta) = e^{-\frac{1}{2}\left(\frac{\Delta-\delta}{\Delta_{\mathrm{FWHM}}}\sqrt{8\ln 2}\right)^2}. \tag{4.12}$$

To allows us to describe the effect of spectral diffusion when setting (or attempting to set) the laser at a finite detuning δ from the QD resonance the Gaussian is centred on δ. The amplitude of the spectral diffusion is given by the width of the Gaussian (Δ_{FWHM}) and the running variable is Δ.

Predictions from the model (Eqs. (4.11), (4.12)) are compared to the experimental data in Fig. 4.6. Here the laser is set on resonance with the X^{1-} transition of QD 'Isidor II' and resonance fluorescence counts are recorded continuously for 10 s with 10 μs resolution. The measurement is repeated a number of times and for different excitation powers. The data are rebinned to move the mean counts per bin to around 30 or greater to allow accurate fitting. The resulting histograms are normalised to unity and displayed as circles in Fig. 4.6 a-f. The blue curve is a fit of the model to the data; the main parameters are displayed in the top right corner of each plot. The red curve shows the histogram expected for a transition without spectral diffusion. In panels a,c and e the data are well fitted[1] assuming the laser (or equivalently the weighting function $\mathrm{W}(\Delta)$) is set on resonance, and the diffusion coefficient Δ_{FWHM} is in the range of 100-150 MHz. This is consistent with most of the 10-s long pieces of data of which we only display a few here. In some cases however, histograms such as in panels b, d and f are obtained. The data agree very well with the model assuming that the QD resonance is centred on a fixed detuning from the laser for the duration of the measurement. At the same time, the diffusion coefficients for these data is similar to the zero detuning cases.

We note that the histogram shape (and amplitude) is a sensitive function of both the diffusion width and the detuning, and a particular shape is uniquely described by both parameters.

In panel g, we summarise the diffusion coefficients for a few data sets (including data with non-zero detuning). For this particular QD, the diffusion coefficients

[1] An additional peak is visible in the histogram data, mainly for higher excitation power. This is attributed to a distinct spectral jump of the QD resonance, a feature commonly observed in high-density samples.

range between 100-200 MHz on a timescale of 10 s, with the data in panels b, d, f implying that an average of the full extent of spectral diffusion is not reached in 10 s. Panel h displays the effect spectral diffusion is expected to have on (slow) absorption linewidth measurements: We take the measured diffusion amplitudes Δ_{FWHM} from panel g and calculate the resulting absorption lineshape. Roughly speaking, the spectral diffusion broadens the absorption lineshapes by 50 MHz compared to the transform limit (250 MHz radiative linewidth) which is given by the lower limit of the grey band. This compares reasonably well with the experimental data presented earlier (cf. Fig. 4.2).

4.2.1.2 Spectral diffusion timescales

To access information on the diffusion timescale we could divide the 10-s long data into smaller chunks and repeat the histogram treatment, but the analysis is fairly cumbersome and becomes less accurate as the amount of data is reduced. At the same time, the assumption of a Gaussian detuning distribution is a priori not valid anymore. Two more suitable methods for analysing the spectral diffusion dynamics are decomposition into Fourier components (via Fast Fourier Transforms) in the frequency domain and calculating the intensity autocorrelation in the time domain. Both of them are very powerful tools for this purpose. Here, we concentrate on the autocorrelation[1]. The intensity autocorrelation function $g^{(2)}(\tau)$ was introduced earlier as a way to quantify the photon statistics at timescales comparable to transition lifetimes. As a reminder, the intensity autocorrelation is given by

$$g^{(2)}(\tau) = \frac{\langle I(t)\, I(t+\tau)\rangle}{I_{\mathrm{av}}^2}. \tag{4.13}$$

Calculating the correlations between events separated in time is a means to pick up on dynamics in the data. For a source with entirely Poissonian character, such as an ideal laser, the intensity output is entirely uncorrelated for any τ, such that the autocorrelation is alway unity. Fluctuations manifest themselves as bunching (i.e. $g^{(2)}(\tau) > 1$) in the correlation function, with their characteristic

[1]Note: A detailed analysis of noise in resonance fluorescence using FFTs was recently put on the arXiv by the group of R. Warburton [127].

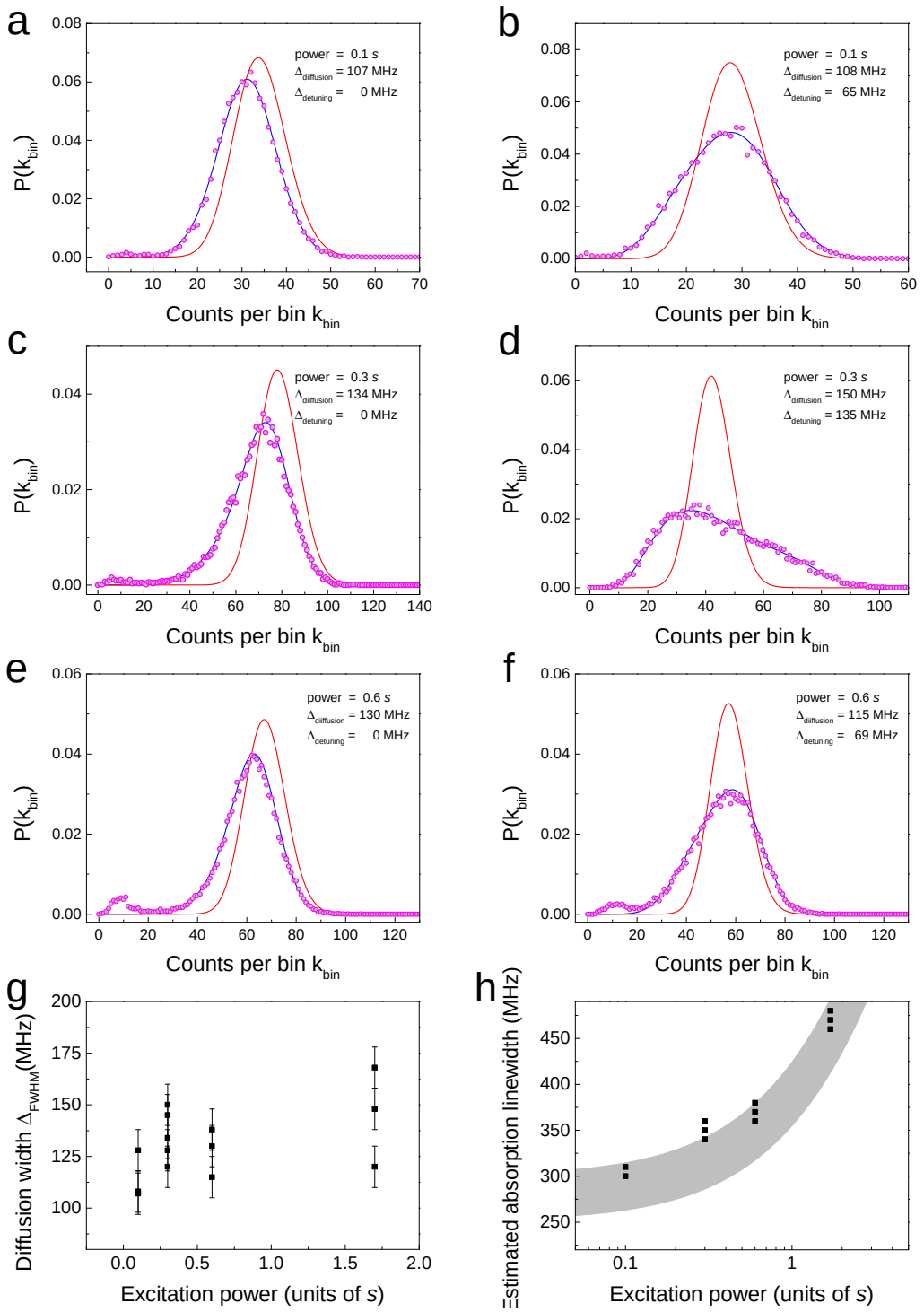

Figure 4.6: Histogram analysis of spectral diffusion effects. a-f, The QD X_{1-} transition is driven on resonance (nominally) and detection events are recorded for 10 s each time. Intensity statistics for rebinned data are shown as circles. Fits using the spectral diffusion model are shown as blue curves and the histograms expected in the absence of spectral diffusion are shown as red curves.g, Summary of diffusion amplitudes. h, Extrapolated effects on the absorption linewidth.

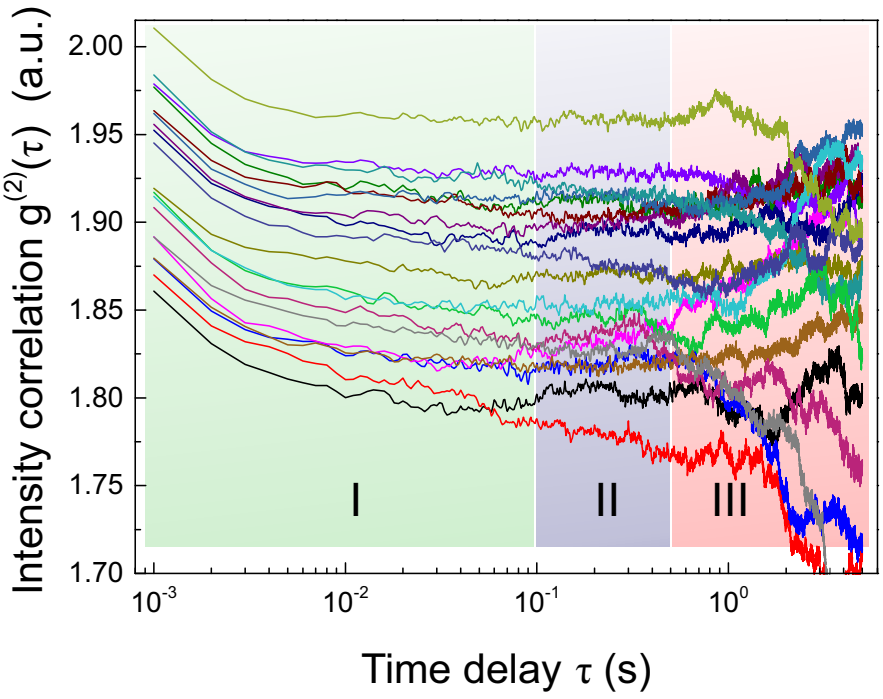

Figure 4.7: Intensity autocorrelation functions for 19 resonance fluorescence time traces. The data are binned to 1 ms resolution. Three regions of different behaviour are identified and colour-coded.

timescales and their amplitudes directly mapped to the amplitude and decay time (the correlation time) of the bunching. We apply this method to QD resonance fluorescence.

To get a first impression of the situation we have a look at a set of measurements, binned to a low resolution. Figure 4.7 presents a semi-logarithmic plot of the unnormalised[1] second-order correlation functions for 19 resonance fluorescence time traces, each of 10-s length and binned to 1 ms resolution. The antibunching effect at delays τ comparable to the emitter lifetime does not play a role here as the time resolution $t_{\mathrm{bin}} \gg T_1$.

We identify three regions of different behaviour: All correlations show clear bunching and a strong similarity with each other for time delays up to $\sim$ 100 ms (lightly shaded region marked 'I'). For the intermediate time delays indicated by region 'II' in the plot ($\sim$ 100 ms to $\sim$ 500 ms) the correlation functions for

[1] to keep the curves separated

individual time traces follow a mostly monotone trend, but differ from each other. Region 'III', with delays greater than 0.5 s looks messy. There are no obvious trends, the $g^{(2)}(\tau)$ amplitude varies widely (wildly), and each individual time trace shows unique behaviour.

Let us start with the analysis of the behaviour in region 'III'. We first note that the curves are inherently more noisy here as τ approaches the total recording time of 10 s. On top if that, if spectral diffusion-induced fluctuations in the resonance fluorescence persisted only on timescales shorter than the measurement time, we would expect to reach a steady-state in the correlation function. There would be no correlation between detection events separated by large delays τ: $g^{(2)}(\infty) \longrightarrow 1$ (for a normalised distribution). No such steady-state is reached in our data which covers correlation delays up to 5 s. We conclude that the correlation time for slow fluctuation is $\gg 5$ s and these fluctuations contribute the largest amplitude to the total noise.

Region 'II' in Fig. 4.7 shows the transition from the fast to the slow fluctuation regime and does not yield much additional insight, so we move to the fast dynamics in region 'I'. To maximise the resolution, the data is kept in the original bin size of 10 μs here. Figure 4.8 displays four exemplary autocorrelations (a-d) as green continuous curves in a semi-logarithmic scale, two on resonance (a, c) and two for a moderate detuning (b, d). The bunching signature already observed in Fig. 4.7 is resolved in good detail. It is dominated by a decay on a ~ 1 ms timescale. A weaker decay feature can be made out at fast timescales (~ 20 μs), in particular for the resonant cases. A third decay is present around 10 ms time delay; this one is more obvious for detuned excitation. Using a sum of three exponential decays we can generate good fits to the data, which are shown as dashed red lines.

Revealingly, there is additional structure in the detuned $g^{(2)}(\tau)$: a series of alternating peaks and troughs at delays times which are multiples of 10 ms. This is the manifestation of 50 Hz noise and points to electric field noise picked up via the sample gates. Panels e-h summarise the decay times and amplitudes found through fitting. The three correlation times (shape- and colour-coded) are consistently in the same range for different data sets and powers. The picture is similar for detuned excitation (panel f), but it is not always possible to identify the fast

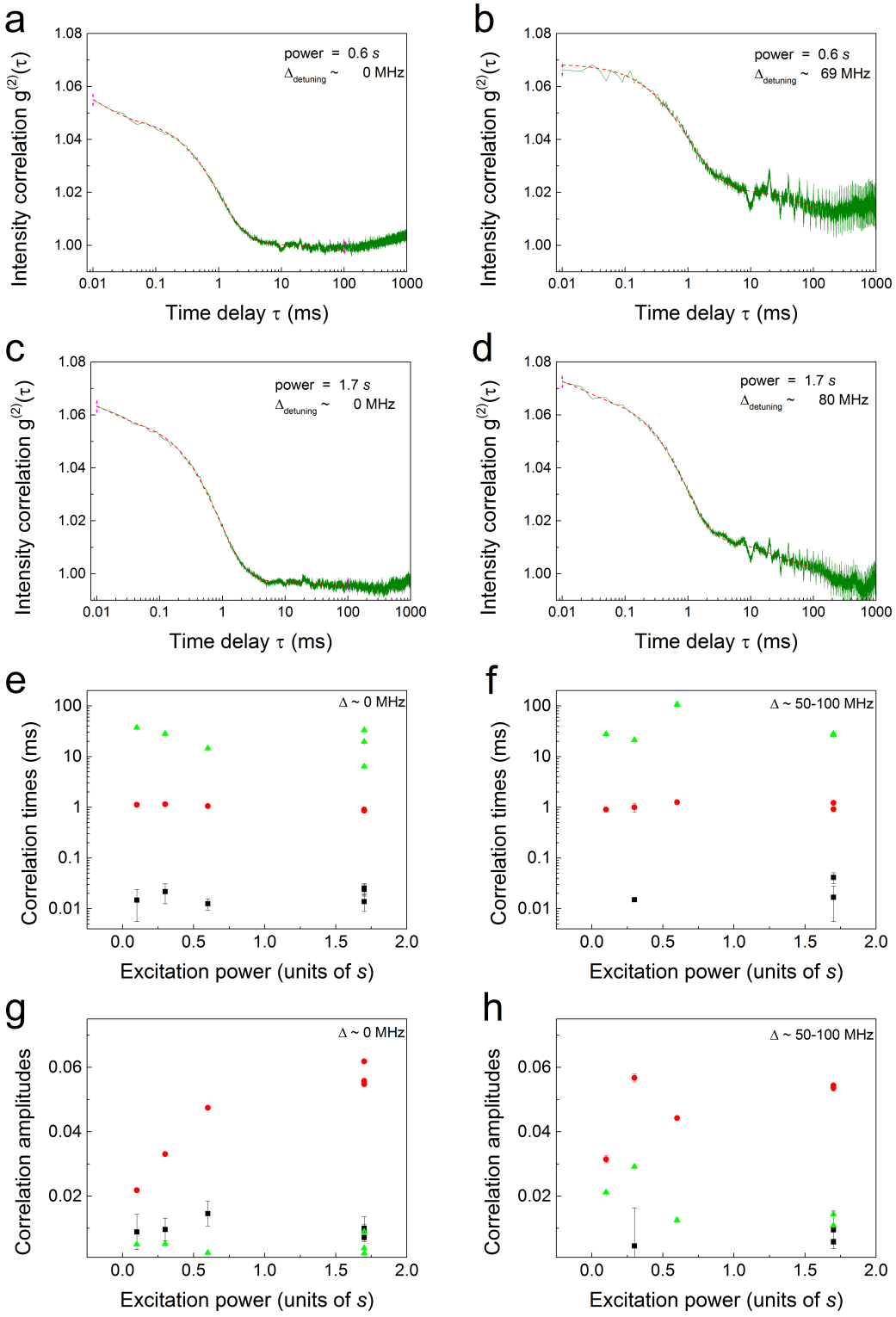

Figure 4.8: Spectral diffusion timescales and amplitudes. a-d, Intensity correlations for QD resonance fluorescence with a timing resolution of 10 μs. Three decay timescales are identified and summarised in panels e-h.

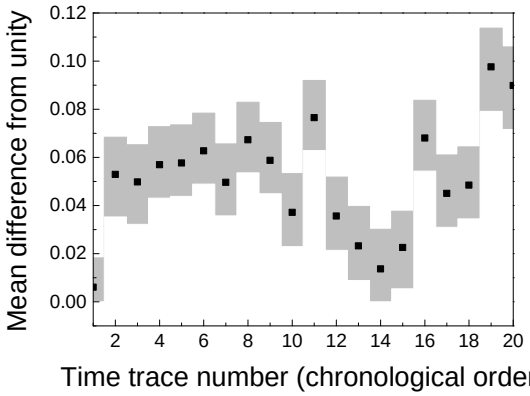

Figure 4.9: Analysis of slow diffusion amplitudes. Using data from region 'III' in Fig. 4.7 absolute deviations from the steady-state ($g^2(\infty) = 1$) are evaluated. The black squares show the mean of the deviations for each time trace, the grey rectangles display the range of the deviations.

decay timescale and reasonable fits can be generated with two exponential decays only. The plots of the correlation amplitudes (panels g and h) use the same shape and colour code as before and confirm the 1 ms correlation to be the dominant feature.

Having identified the noise amplitudes and timescales in region 'I', can we complete the picture and also quantify the amplitude of the very slow fluctuations? Going back to Fig. 4.7 we calculate the absolute deviation from the ideal steady-state value for $g^{(2)}$ ($\tau > 1$ s). The mean (black squares) and the extent of the deviations (grey shaded rectangles) for 20 consecutive resonance fluorescence time traces are presented in Fig. 4.9. The amplitude ($\sim$ maximum of the grey area) of the deviation is greater or comparable to the 1 ms noise contribution for most of the individual 10-s long time traces. Over the course of the measurement for the 20 traces, the total deviations exceed the magnitude of the fast contributions (cf. Fig. 4.8 g, h) significantly.

The origin of spectral diffusion. The intensity autocorrelation is a powerful tool to obtain quantitative information about spectral diffusion timescales and amplitudes. Can we link the results to their origin, i.e. identify which diffusion timescale stems from which physical mechanism? The two diffusion mechanisms we have to consider are electric and magnetic field noise. Electric fields shift the

QD transition resonance via the Stark effect and give rise to an effective detuning of the excitation laser from resonance. Part of the electric field noise is of external origin, such as the 50 Hz noise we have seen earlier. Some will be due to the dynamics of charges close to the QD. The magnetic field noise comes from the randomly varying cumulative Overhauser field from the nuclear spin environment of the QD. The data shown in this section are from the negatively charged trion transition X^{1-}, so any magnetic field splits the ground and excited state with the respective splitting determined by the direction and magnitude of the field. Then we go from a simple two-level system to four levels that, again depending on the orientation of the B-field, support two or four optical transitions (and mixtures of these). In any case, however, there is a splitting between the optical transitions. The effects on absorption lineshapes are sketched out in Fig. 4.10, in a for electric fields, and b for magnetic fields. The top panels of a and b show two lineshapes each which represent the absorption profile at two different times. In the sketch for electric field fluctuations (panel a) the two Lorentzians are shifted by 100 MHz, in b we change the splitting between a sum of two Lorentzians from 100 to 200 MHz. The bottom panels display the absolute difference between two lineshapes. The amplitude of the absolute difference tells us how sensitive the fluorescence intensity is to E- and B-field fluctuations as a function of laser detuning from the unperturbed QD transition resonance. The sensitivity to electric field noise is greatest at the slope of the absorption lineshape. In contrast, the sensitivity to magnetic fields is greatest on resonance.

Relating this information to the correlation times and amplitudes in Fig. 4.8, we tentatively assign the 10 μs noise to the nuclear Overhauser field dynamics. It is stronger on resonance, and the timescale is about the same order of magnitude as expected for the nuclear correlation time [33]. The 10 ms noise is quite clearly due to electric field fluctuations: its amplitude is dramatically enhanced at finite detuning. With regards to the 1 ms dynamics, the situation is less clear. The correlation amplitudes on- and off-resonance do not differ much. At the same time, the amplitude shows a dependence on the excitation laser power and possibly a saturation behaviour. With the currently presented data we cannot clearly link it to laser-induced fluctuations of the environment and this will be further investigated. As for the very slow noise, this can be compensated by manually

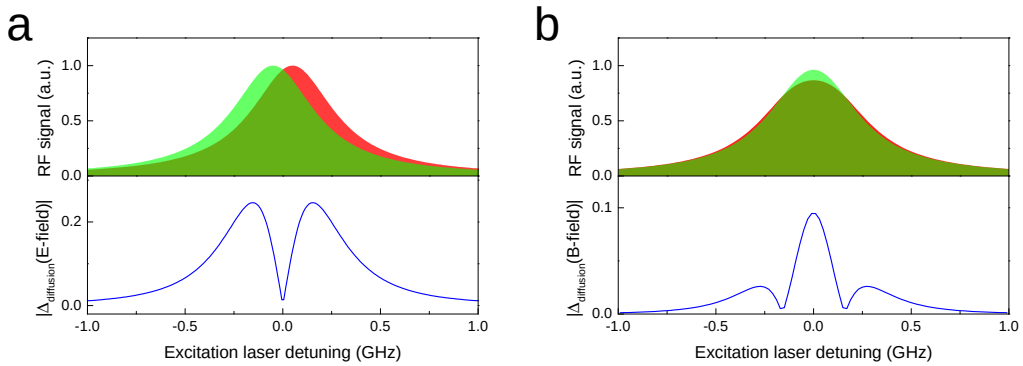

Figure 4.10: Effects of electric (a) and magnetic (b) field changes on the QD trion transition. a, A change in the electric field at the QD Stark shifts the transition frequency. The magnitude of the change is greatest at the slope of the resonance. b, A change in the magnetic field changes the splitting between the optical transitions and it most strongly felt on resonance.

changing the applied gate voltage and hence is due to changes of electric-field.

Consequences for long measurements: high-resolution intensity correlations. Experiments based on two-photon detection with sub-nanosecond timing resolution, such as measuring antibunching in a Hanbury-Brown and Twiss setup, or cross-correlations in a Hong-Ou-Mandel interferometer may require acquisition times of many hours, depending on the excitation power and detuning. As such, these measurements can suffer significantly from spectral diffusion. Care must be taken in the data treatment then to include the diffusion effects. We give an appropriate expression for the intensity autocorrelation $g^{(2)}(\tau)$:

$$g^{(2)}(\tau, \Delta, \Delta_{\mathrm{FWHM}}, \delta) = \frac{\sum_{\Delta} g^{(2)}(\tau, \Delta) \times \mathrm{W}(\Delta_{\mathrm{FWHM}}, \Delta, \delta) \times \mathfrak{L}^2(\Delta)}{\sum_{\Delta}(\ldots, \tau \to \infty)}. \tag{4.14}$$

Here, we calculate the sum of $g^{(2)}$ curves for a range of excitation detunings Δ, weighted by a product with the Gaussian diffusion function $\mathrm{W}(\Delta_{\mathrm{FWHM}}, \Delta, \delta)$ (centred on δ with a FWHM of Δ_{FWHM}) and the square of the power broadened Lorentzian linewidth $\mathfrak{L} = \frac{s+1}{1+s+2(2\pi\Delta)^2 T_1 T_2}$ (decribing the amplitude of the two-photon signal). The expression is normalised by division with its long-time limit.

We will use this formalism in section 4.3 of this chapter for $g^{(2)}$ measurements at finite detuning.

4.2.2 Phonon coupling

The electron and hole wavefunctions of excitons in QDs are given by an envelope function depending on QD shape and composition and the fundamental Bloch functions of the solid-state lattice potential. As such the excitons couple to the lattice vibrations of the embedding matrix and this coupling provides a dissipation mechanism. While the confinement in quantum dots gives rise to discrete energy levels and inhibits phonon-driven population relaxation (the 'phonon bottleneck' [128; 129]), dephasing of the optical transition can still be phonon assisted.

4.2.2.1 Acoustic phonon sideband

Experimentally, phonon coupling in QDs was first observed in the photoluminescence spectra of II-IV QDs [130]. At cryogenic temperatures the spectrum was composed of a narrow peak sitting on top of a broad asymmetric background. The narrow peak is known as the zero-phonon line, as the emission energy is determined by the optical transition only, while the broadband is due to acoustic phonon-assisted fluorescence and referred to as the phonon sideband. Similar results were obtained for InAs/GaAs QDs using four-wave mixing [131], and later also in photoluminescence [132; 133].

To investigate the effects of exciton-phonon coupling in our samples, we have to record the resonance fluorescence emission spectrum over a much wider frequency range than covered earlier in the scanning Fabry-Perot experiments. Measurements of the QD resonance fluorescence spectrally dispersed in the spectrometer on a 1200 grooves/mm grating are presented in Fig. 4.11 using a logarithmic intensity scale. The broad phonon sideband is very clearly visible. Before going into details of the data we will briefly review the theoretical background.

A comprehensive treatment of linear exciton-phonon coupling based on the independent boson model was published by Krummheuer *et. al* in 2002 [134] and accounts for the phonon sidebands. Dephasing of the zero-phonon line can be included with quadratic coupling to acoustic phonons [135; 136] but will be ne-

glected here. Following Ref. [134], the exciton-phonon coupling Hamiltonian is given by

$$H_{\text{exc-phon}} = \hbar \sum_{\mathbf{q}} \left(g^e_{\mathbf{q}} b_{\mathbf{q}} c^\dagger c - g^h_{\mathbf{q}} b_{\mathbf{q}} d^\dagger d + \text{H.c.} \right), \tag{4.15}$$

where the sum is over the phonon wavevectors $\mathbf{q}$ and there is a summation for each phonon branch (e.g. the longitudinal acoustic, longitudinal optical and transverse acoustic phonons). The phonon coupling matrix elements $g^{e/h}_{\mathbf{q}}$ quantify the coupling for the specific branch, phonon wavevector and the charge carrier (electron e or hole h) involved. c and $c^\dagger$ (d and $d^\dagger$) are the annihilation and creation operators for electrons (holes) and vice versa for the phonons ($b_{\mathbf{q}}$, $b^\dagger_{\mathbf{q}}$). The coupling matrix elements are specified by a form factor, given by the wavefunction, and a factor linked to the specific coupling mechanism. The coupling mechanisms are known from bulk electron-phonon interaction as the deformation potential (for acoustic phonons), the piezoelectric electron-acoustic phonon coupling and the electron-optical phonon Fröhlich interaction [137].

For excitons in QDs the deformation potential is the dominant coupling mechanism by a wide margin [134; 138]. A simple physical picture of the exciton-phonon interaction and how it leads to phonon sidebands is obtained when we consider the exciton creation and annihilation. The exciton is localised in the small volume of the QD and its presence affects the lattice equilibrium position. Upon photon absorption the lattice deforms (polaron formation) to reach the new equilibrium position, and the process repeats when the exciton recombines. The deformation process is fast (high bandwidth), meaning that the interaction with phonons is strong on this first very short timescale and weak thereafter.

The phonon dispersion of longitudinal acoustic phonons is linear for small wavevectors and the density of states is proportional to the square of the phonon energy. The form factor determines which wavevectors are coupled via the deformation potential. The range of phonon energies involved is given by the spatial extent of the electron and hole wavefunctions and thus linked to the shape of the QD: smaller QDs probe a wider range of frequencies than larger QDs and should therefore couple more strongly to acoustic phonons. Intuitively we can understand this as an averaging of the carrier-phonon interaction over the size of the QD: when

the phonon wavelength is considerably shorter than the smallest extent of the QD, its effect will not be felt. In the emission spectra of Fig. 4.11 the size of phonon sideband directly reflects the range of acoustic phonon frequencies that contribute to the interaction. Further, the sideband is very strongly asymmetric with almost its entire weight on the lower energy side of the zero-phonon line.
This can be linked to the phonon occupation probability which is governed by the Bose-Einstein distribution:

$$n\left(q\right) = \frac{1}{e^{\hbar\omega(q)/k_bT} - 1}. \tag{4.16}$$

At 4.2 K k_bT (k_b being the Boltzmann constant) corresponds to 0.36 meV. The probability of absorption of a phonon with energy $\hbar\omega_q$ is proportional to the occupation number $n\left(q\right)$, while the emission of a phonon goes as $n\left(q\right)+1$. At low energies the emission process is overwhelmingly more likely than absorption. Hence the QD fluorescence is shifted to the red as some energy is taken away by phonon emission.
Figure 4.11 a and c show the emission spectra (normalised to the peak intensity) for the neutral exciton transition X^0 (a) and for the charged exciton transition X^{1-} (c) driven at about twice their saturation powers. The similarities of their spectra is confirmed in Fig. 4.11 b, where both spectra are displayed on the same scale by subtracting the energy of the zero-phonon line peak. The similarity extends over the entire spectrum, even the small hump at 1 meV is consistent for both transitions. We can conclude that the interaction with acoustic phonons takes place exclusively in the excited state, and the presence of an additional charge carrier does not affect the interaction.
The weight of the phonon sideband relative to the total emission intensity is consistently around 12% for different QDs. The existence of a strong phonon sideband provides an explanation for the limited constrast in first-order coherence measurements of the QD resonance fluorescence (cf. Fig. 4.4): The coherence time of the sideband photons is inversely proportional to the sideband width and can only be detected in a range of a few ps around zero time delay.
Figure 4.11 d shows a close-up of the X^0 phonon sideband in linear scale for an excitation power significantly above saturation. An additional weak peak is

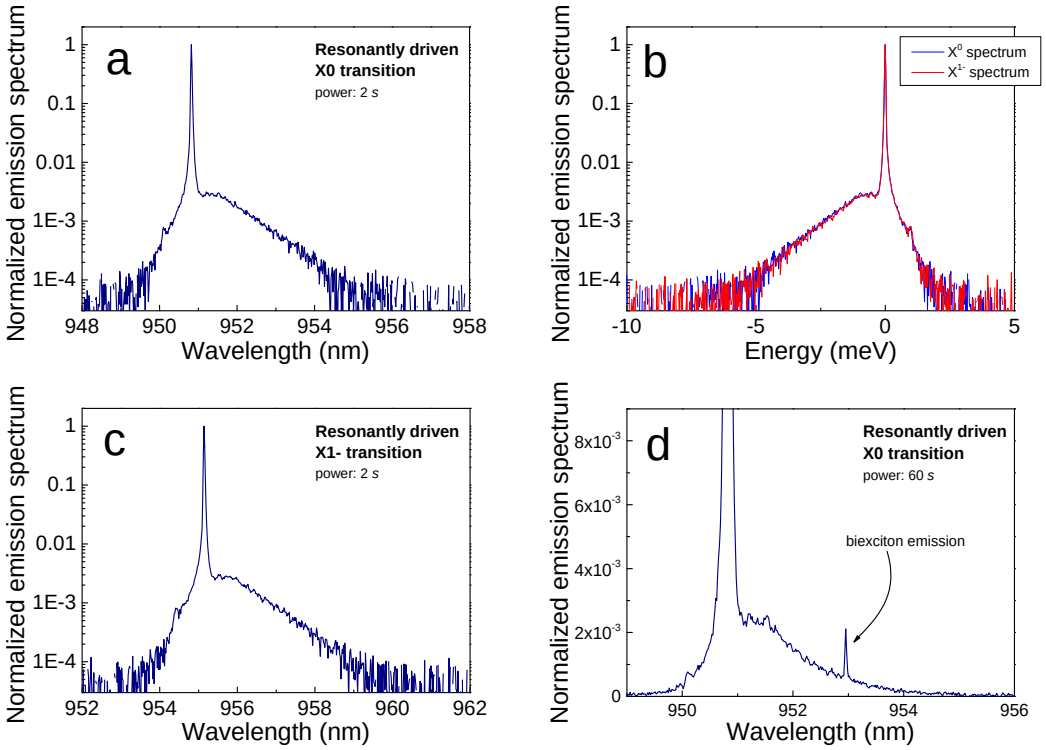

Figure 4.11: Acoustic phonon sidebands in QD resonance fluorescence. a, spectrum for X^0 transition. c, spectrum for the X^{1-} transition. b, Comparison of the two. d, Phonon-assisted two-photon processes appear for strong excitation powers.

present in this spectrum and its energy corresponds to the biexciton line of the QD. It is only detected for high excitation powers ($> 10 \times s$) and the intensity grows as the square of the excitation power. This points to a two-photon absorption process, where the emission of an acoustic phonon bridges the energy gap between the exciton and the biexciton state.
The details of the phonon sidebands will not be discussed further here. Considering the implications for QIP with QD resonance fluorescence we have to consider that sideband photons have very short decoherence times ($\sim$ ps) and are not suitable for interference applications (such as distant entanglement through interference). In these cases the QD fluorescence has to be filtered to exclude the phonon sideband. Where only the fluorescence intensity matters, as it is the case for state readout there are no negative effects.
We also note that the contribution of the phonon sideband to the fluorescence can vary considerably between different samples. For instance Konthasinghe *et al.* report a sideband contribution of 5% [125]. Finally, given the very good signal-to-noise ratio with which we resolve the sideband, resonance fluorscence is a suitable technique to study exciton-phonon effects in QDs.

4.2.2.2 Phonon-broadening of the zero-phonon line

In the previous discussion of phonon coupling we focussed on the acoustic sidebands. These are satisfactorily explained considering a Hamiltonian linear in the phonon displacement [134], and good quantitative agreement to experimental data can be found for realistic (i.e. non-Gaussian) wavefunctions [139]. The model does not predict a broadening of the zero-phonon line itself, however, while this was observed in the first experiments already [130; 131]. The broadening as a function of lattice temperature can be recovered in a theoretical treatment that accounts for a quadratic coupling to acoustic phonons [136].
Recently, an additional excitation power-dependent dephasing has been found in several experiments under resonant excitation [110; 115; 116]. The importance of this excitation-induced dephasing is significant: ultrafast optical control of spin qubits relies on the optically excited state to achieve fast spin rotations via virtual transitions [22; 42]. For excitonic qubits (see Ref. [140] for example) it is the

coherence between ground and excited state that has to be addressed optically and it is therefore strongly sensitive to such a mechanism.
Excitation-induced dephasing has been treated theoretically [115; 116; 141; 142] and explains published experimental data well. The additional dephasing is a consequence of Rabi oscillations under high power resonant excitation excitation. Rabi oscillations dress the two-level system such that three optical transitions are created. The size of the splitting of ground and excited state is given by the Rabi frequency Ω and achievable Rabi frequencies are in the energy range where acoustic phonons couple to the QD exciton. The presence of the additional levels enhances phonon transitions at the Rabi frequency. For a range of Rabi frequencies $\sim$ few GHz $< \Omega < \omega_c$, where ω_c is the cutoff frequency for QD exciton-phonon coupling, the dephasing is predicted to behave as the square of the Rabi frequency.
Measuring the excitonic coherence (through the spectrum or the first-order correlation function) for Rabi frequencies in this regime is experimentally challenging as the signal, given by the QD fluorescence, is limited to its saturation value, while the laser background increases (without bound) as the square root of the Rabi frequency. To extract information about dephasing times with less strict conditions on signal-to-background ratios one can chose to measure part of the spectrum only, e.g. the Mollow triplet sidebands [110]. These are spectrally removed from the excitation laser background and their width is related to the dephasing time.
Here we present measurements of the full first-order correlation signal from a single QD driven in continuous-wave mode. Rabi oscillations can be recorded in a time-resolved fashion via the first-order correlation and the decay of the oscillations is directly linked to the dephasing time T_2. Performing these measurements is possible in our case due to the good suppression of laser background (cf. Fig. 4.1). Additionally, at laser powers where $s \geq 200$ we modulate the QD resonance between on- and off-resonance with respect to the excitation laser using the DC Stark effect. Phase-sensitive detection is then employed to pick up the QD resonance fluorescence contribution. The modulation speed is on the order of 1 KHz and serves to eliminate fluctuations in the laser background during the course of an interference fringe measurement (see section 3.4.2 for the measurement pro-

tocol). Using this technique we recover the original resonance fluorescence signal provided there is no interference between laser leakage and the QD signal, i.e. the coherent fraction $F_{\mathrm{coh}} \ll 1$. This condition is well satisfied for excitation at zero detuning and $s > 100$.

Figure 4.12 a-j presents a series of first-order correlation measurements on the X^{1-} transition of QD 'Claude'. Blue squares represent experimental data and the red line is a fit according to Eq. (4.5). The values for the main fit parameters, the Rabi frequency Ω and the dephasing time T_2, are indicated in each panel. To relate the Rabi frequency to the saturation parameter used in previous sections, Fig. 4.12 a is for an excitation power of $s \sim 10$, and Fig. 4.12 j for $s \sim 4000$.

The oscillations in the visibility of $g^{(1)}$ are the signature of Rabi oscillations: Starting with the maximum visibility at zero time delay[1] a π rotation of the two-level system is obtained when the visibility reaches the first minimum. A revival of visibility follows until we reach a time delay corresponding to a 2π rotation, where the fringe amplitude is maximum again.

The agreement between data and theory is remarkable for intermediate Rabi frequencies ($\Omega \leq 4$GHz) and a trend of decreasing T_2 times with increasing power is clear. At higher Rabi frequencies differences to the fit function appear, most visible at longer delays and highest powers. Figure 4.12 i contains data for longer delays and is a particularly clear example: Here the amplitude of the coherent oscillations goes through a minimum, while maintaining an intermediate level of coherence. At longer delays the oscillations pick up again, but the phase is flipped by π. The presence of this additional beat note in the data points to more frequency components in the spectrum than accounted for in the fit function, which is for an ideal two-level system. Since the data is based on the fluorescence from a singly charged QD (the X^{1-} transition), a likely reason for the beating is a nuclear Overhauser-split ground state. We will confirm this suspicion in the next section and ignore it for now. To be able to extract meaningful numbers for the T_2 time the fits to the data are made to fit the amplitude of the Rabi oscillations after the beating. Still, this is a caveat for the data interpretation. A proper treatment would account for the effect of the nuclear field, but this is beyond the

[1] The amplitude of the first-order correlation around zero time delay is limited by the phonon sideband contribution, as discussed earlier.

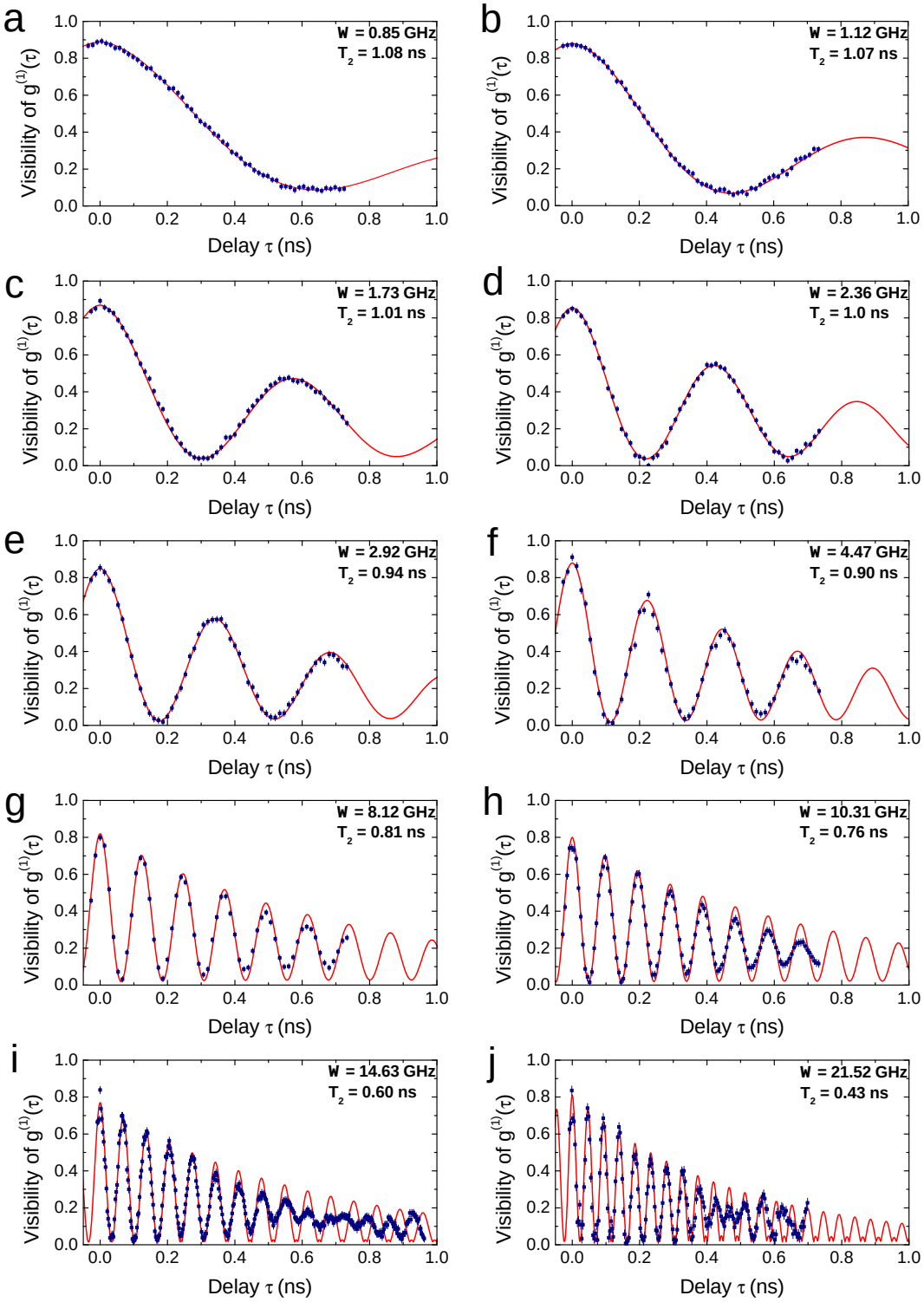

Figure 4.12: First-order coherence measurements for the X^{1-} transition of QD Claude under strong resonant excitation. Data is shown as blue squared, error bars are indicated by vertical lines. Fits according to Eq. (4.5) are shown as continuous red lines.

scope of this section (and this thesis[1]).
In Fig. 4.13 we summarise the findings from the first-order correlation measurements. Panel a shows the power dependence of the pure dephasing rate

$$\gamma_{\mathrm{p}} = \frac{1}{T_2} - \frac{1}{2T_1}. \tag{4.17}$$

Data are shown as open triangles. The upwards pointing red triangles were obtained from $g^{(1)}$ measurements taken in the space of a few days (in between two helium refills of the cryostat) such that the optical alignment was very similar. The downwards pointing blue triangles originate from different data sets. First, before going into details on the exact dephasing behaviour, we note there is a marked dependence of the dephasing rate on the Rabi frequency: In the range studied here, the dephasing rate increases (within the scatter of independent measurements) monotonously with Rabi frequency over one order of magnitude, from $\gamma\,(\Omega \approx 1\ \mathrm{GHz}) \sim 25$ MHz to $\gamma\,(\Omega \approx 20\ \mathrm{GHz}) \sim 260$ MHz.
Two black lines, one dashed and one dotted show fits to the data: The dashed line assumes a parabolic dependence on the Rabi frequency with a constant offset (no linear term), while the dotted line is based on a linear dependence with a constant offset. For Rabi frequencies below 10 GHz the linear function matches the data well, but strongly deviates at higher frequencies. In contrast, the quadratic function (dashed) yields good agreement only at higher Rabi frequencies ($\Omega >$ few GHz). The constant term in the fit overestimates the dephasing significantly as we go towards small Rabi frequencies. In the inset the same data is shown, but with the abscissa scaled as the square of the Rabi frequency. Here we can see, perhaps more clearly, that the dephasing rate is approximately linear in Ω^2 at higher powers and deviates from this behaviour at lower powers. This deviation is at odds with the expected Ω^2-dependence predicted by acoustic phonon-coupling and currently there is no intuitive explanation. We note that the effect of the Overhauser field at different excitation powers is not clear: The beating is obvious at high Rabi frequencies, but the beat note shifts to lower frequencies at lower powers. Further, the regime where the dephasing rate fits a linear Ω dependence is not covered in the published experimental investigations [110; 115; 116].

[1] at this point

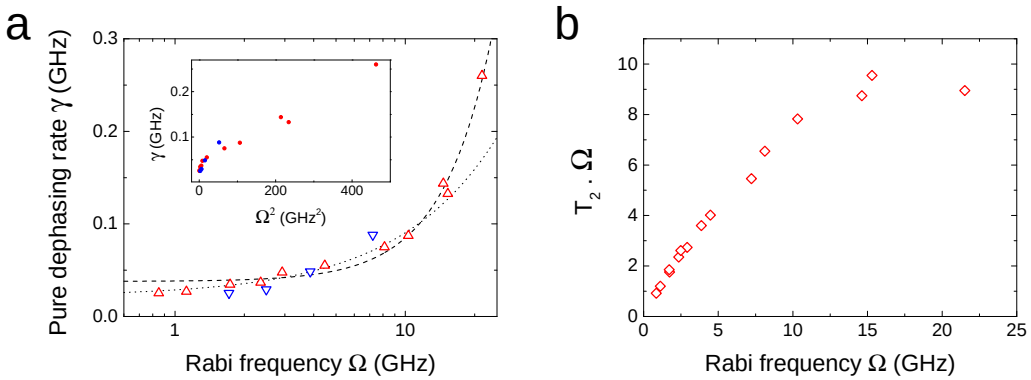

Figure 4.13: Power-dependence of pure dephasing rates from the data in Fig. 4.12. a, Pure dephasing rate as a function of Rabi frequency (inset: as function of squared Rabi frequency). Dashed line: fit according to $a + b\Omega^2$. Dotted line: fit according to $e + d\Omega$. b, Number of 2π oscillations within the dephasing time as a function of Rabi frequency.

Finally, panel b of Fig. 4.13 illustrates the consequences of excitation-induced dephasing for coherent control schemes that involve QD excitonic states. Here we show the product of the dephasing time T_2 and the Rabi frequency Ω. This quantifies the number of full (2π) Rabi oscillations performed within the dephasing time. In the absence of excitation-induced dephasing the data should follow a straight line. In contrast, the product saturates within the accessible range of Rabi frequencies, reaching a maximum rotation of $9 \times (2\pi)$. Extrapolating this trend to even larger Ω, the product should decrease until the Rabi frequency exceeds the cut-off frequency of the exciton-phonon coupling. The cut-off can be estimated from the peak of the phonon sideband in Fig. 4.11 as $\omega_c \sim 1$ meV $\approx$ 250 GHz. For QIP applications it is of course desirable to operate at $\Omega \gg \omega_c$, however reaching these powers is not feasible in cw with current sample structures. Excitation with ps pulses may allow us to reach this goal in the foreseeable future.

Overcoming the issue of dephasing due to phonon coupling with very strong excitation is one option. Another interesting approach would be to engineer the density of phonons states, for instance through microfabrication [143].

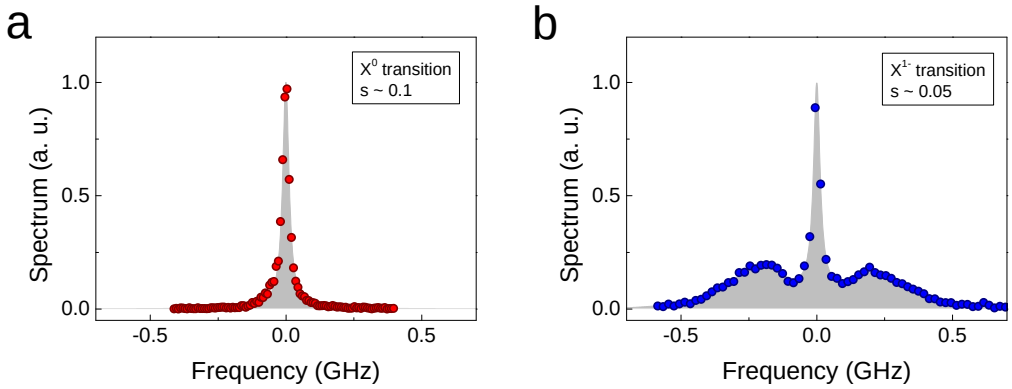

Figure 4.14: Emission spectra of resonantly driven X^0 (a) and X^{1-} (b) transitions. The excitation power is such that ≥ 90 % of the scattering should be coherent.

4.2.3 Nuclear Overhauser field

The effects of the nuclear spin bath on properties of a single resident electron spin in a self-assembled QD were discussed briefly in the introductory chapter. Here we present the experimentally observable signatures of the nuclear Overhauser field in the resonance fluorescence emission spectra of a single QD. The effect is most accessible when we excite weakly, far below the saturation power, but present at any excitation power. We start the discussion by comparing the emission spectra in Fig. 4.14 of the X^0 and X^{1-} transitions from the same QD ('Claude') at similar excitation conditions. The X^0 spectrum shows the familiar resolution-limited coherent Rayleigh peak. The X^{1-} spectrum sports two sidebands in addition, spaced roughly symmetric about the Rayleigh peak and centred at $\pm$ 200 MHz. To understand the origin of the sidebands we have to consider the optical level structure of the trion transitions in the presence of the Overhauser field.

For any orientation the Overhauser field may be decomposed into two components, see the left-hand side of Fig. 4.15: a Faraday-like field parallel to the optical axis (out-of-plane), and a Voigt-like field which is orthogonal to the optical axis and can point in any in-plane direction. We note that the comparison to Faraday and Voigt configurations is not entirely accurate. The ground states split in the same way, but the analogy is not valid for the excited state, where any splitting is due to the heavy-hole response to the field. Given the vanishing Fermi contact hyperfine interaction for hole spins the excited state splitting

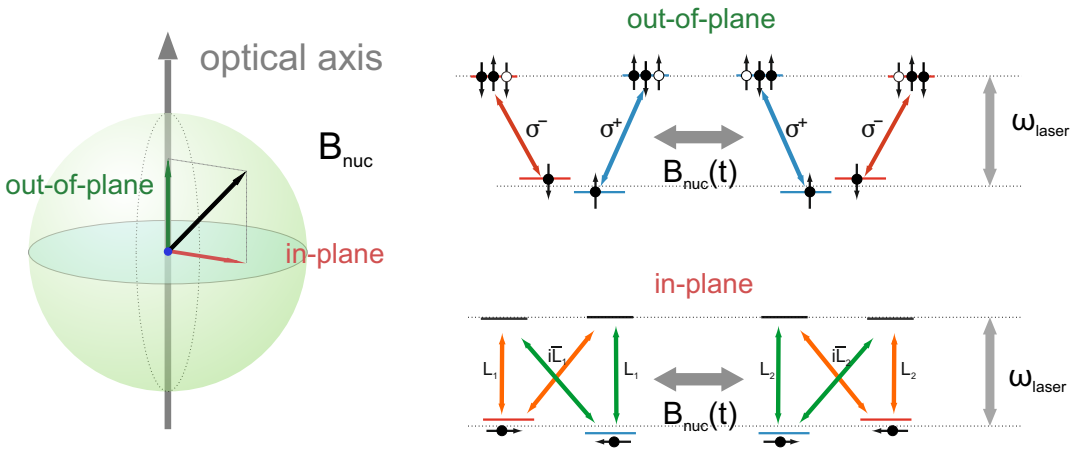

Figure 4.15: Influence of the Overhauser field on the transition selection rules. The out-of-plane component gives rise to Faraday-configuration selection rules, while the in-plane components give rise to Voigt configuration selection rules. For a Faraday field we expect a single emission frequency in the Heitler regime, while three emission frequencies are available in Voigt configuration.

is negligible. For convenience we continue the analogy with Voigt and Faraday components, however. The Faraday component splits the X^{1-} into two circularly polarised transitions with little cross-talk (branching ratio $\sim$ 200:1). Changes in the Faraday component of the Overhauser field change the splitting between the two transitions. For instance, if the Faraday field were to switch direction, the transition energies would switch (see sketch on the top right-hand-side of Fig. 4.15). The exciting laser is linearly polarised and its energy corresponds to the mean of the two transitions, i.e. the transition energy in the absence of the Overhauser field. Considering the weak excitation limit where coherent scattering dominates we expect to scatter Rayleigh photons from either of the two transitions with equal weight. Raman scattering is not allowed by the selection rules and only occurs rarely. Hence the spectrum should be similar to the X^0 spectrum: we expect a single peak at the laser frequency.

The electron g-factor is isotropic so a Voigt field splits the spin ground state as before (cf. sketch at the bottom right-hand side of Fig. 4.15). For holes in our sample the valence band mixing is small [26; 28] and hence the in-plane g-factor is small. At the same time the hyperfine interaction with the nuclei is weak as the hole orbitals have p-symmetry. With the resulting negligible excited state

splitting the level structure can be approximated by a Λ-system: both ground states couple equally to the excited state. The transition energies vary with the magnitude of the Voigt Overhauser field and the in-plane direction determines the linear selection rules with respect to the laser polarisation: the two transitions are orthogonally polarised (indicated by L and $\bar{\text{L}}$ in the sketch) for any in-plane direction, but the exact polarisation state varies with the azimuthal angle. For weak excitation both transitions still scatter Rayleigh photons, but at the same time coherent Raman scattering into either ground state is allowed, such that three optical frequencies exist. While the energy of the Rayleigh scattering is fixed by the laser, the Raman photon energy is determined by the ground state splitting. For a given Voigt field we expect Raman photons blue and red detuned from the Rayleigh peak by half the ground state splitting. A Voigt field with a fixed magnitude then gives rise to three narrow (subnatural linewidth) peaks. As the Voigt Overhauser field evolves it changes the ground state splitting and the energy difference between Raman and Rayleigh scattering follows. The resulting spectrum should feature two symmetric and extended Raman sidebands[1].

The X^{1-} spectrum from Fig. 4.14 b can be qualitatively explained when both out-of-plane and in-plane nuclear Overhauser fields are considered. To verify this picture and gain quantitative insight on the nuclear field amplitude Jack Hansom and Claire Le Gall have developed a numerical model to calculate the emission spectra of the four-level trion system in the presence of a Gaussian nuclear field. The model shall not be explained here in detail as it is not my work (see Ref. [144]). Here it is used to compare simulation results to a few experimental spectra. Figure 4.16 shows X^{1-} spectra obtained for QD 'Claude' at different excitation powers (experimental data as green squares). Emission spectra are calculated for a range of Overhauser field variances. In the calculation the field variance is varied in steps of 10 MHz (corresponding to $\sim$ 2.5 mT magnetic field) up to 200 MHz ($\sim$ 50 mT) while experimental parameters (e.g. excitation parameter s and lifetime T_1) are fixed. We display three theoretical curves for each experimental spectrum: a best-fit is shown as continuous red curve, a dashed curve for a variance about 100 MHz and a dotted curve for a variance of 200 MHz.

The main features of the measured spectra are well reproduced for a nuclear field

[1] this holds for detuned excitation we well

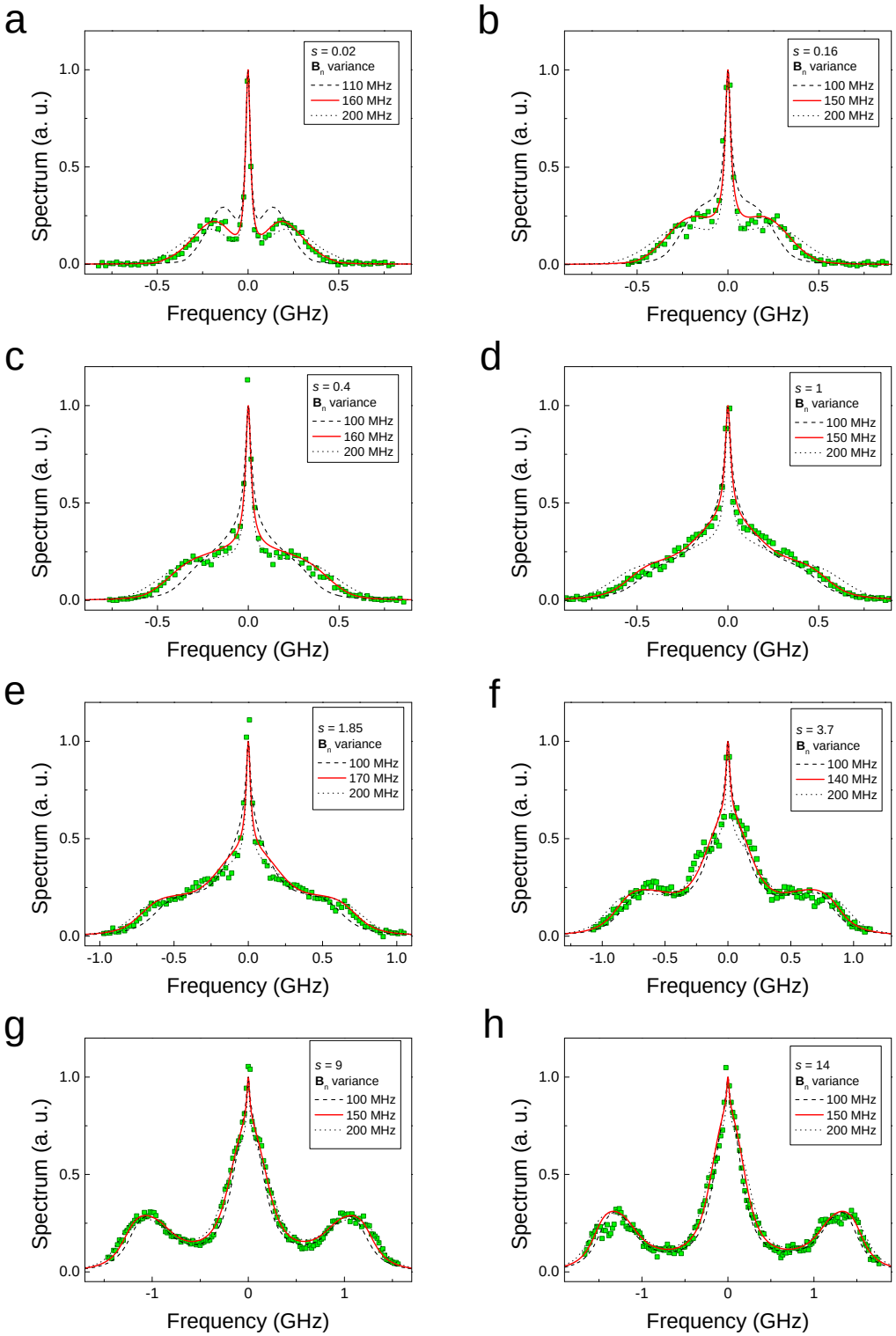

Figure 4.16: Emission spectra for resonantly excited X^{1-} transition at zero external magnetic field. Data (green squares) are measured with a scanning Fabry-Pero cavity of $\sim$ 30 MHz resolution. The continuous curves (red, black dashed, black dotted) are results from simulations for a four-level system and Gaussian nuclear field variance.

variance of $\sim$ 140-160 MHz corresponding to $\sim$ 25 mT. The emission spectra are most sensitive to the Overhauser field for weak excitation and the pronounced sidebands allow accurate determination of the variance. At higher excitation powers the effect of the nuclear field on the emission spectra is visually less striking than in the low power limit. Here, the central peak of the Mollow triplet is broadened and the sidebands assume an asymmetric shape in addition to being broadened. We note that in panels g and h, the sidebands appear to split into two peaks, while the simulated spectra are always single-peaked and smooth. This points to a non-Gaussian field distribution, possibly due to a laser-driven dynamic spin polarisation [35]. An actual splitting of the sidebands would be consistent with the beating observed in the first-order coherence measurements at very high excitation powers (cf. Fig. 4.12).

In conclusion, the emission spectra of the negatively charged trion transition can be well explained by taking a fluctuating nuclear Overhauser field into account. Conversely, the resonance fluorescence spectra serve as a direct and sensitive probe for interactions with the nuclear spin bath. Along these lines it may be interesting to measure the positively charged trion transition to investigate hole-nuclear spin dynamics [109; 145]. Finally, we note that the Overhauser field could be used as a resource for coherent control of spins in the absence of an external field [144].

4.3 Detuned excitation: quantum to classical Rayleigh scattering

The correspondence principle states that in some limit, usually for large particle number or high temperature quantum effects are masked and classical physics can describe a system adequately. When considering resonant light scattering, the limit of strong excitation gives rise to Rabi oscillations and the Mollow triplet, manifestations of quantum coherence between the optically coupled levels. At low driving powers however, the coherent part of resonance fluorescence dominates (resonant Rayleigh scattering) and the spectrum corresponds to that of a classi-

cal driven harmonic oscillator. The statistical properties of the fluorescence still remain profoundly quantum mechanical though: antibunching is observed at all excitation powers. This interesting property was discussed earlier. Rayleigh scattering is usually thought of as a classical effect and antibunching is not expected. A trivial reason not to observe antibunching is that Rayleigh scattering is rarely measured on the single-particle level, but as we shall see there is more subtle physics going on.

Where antibunching signifies the quantum-ness of single two-level systems, a second-order correlation of unity is reserved for coherent fields, i.e. lasers. Classical fields are thermal and this is characterised by a bunching behaviour in the second-order correlation: $g^{(2)}_{\text{thermal}}(\tau \to 0) > 1$. Rayleigh scattering is usually associated with a strong detuning (many linewidths) of the polarising field from the atomic resonance. Large excitation detunings provide an alternative way (to low power resonant excitation) to generate elastic scattering. More precisely, for detunings $2\pi\delta > \frac{1}{T_2}\sqrt{1+s}$, i.e. detunings greater than the half-width at half maximum of the absorption linewidth, elastic scattering becomes dominant, even at high driving powers. We will use a QD to investigate off-resonant elastic scattering in the single-emitter limit.

Here we use the QD X^0 transition (of QD 'Isidor II') and set the excitation power to the saturation value (s=1) to have a a decent signal strength while avoiding to dress the two-level system. Figure 4.17 a shows the QD fluorescence spectrum in a semi-logarithmic scale for a set of detuning values between $\sim \pm 1$ GHz. Two of the experimental spectra are highlighted to illustrate the effect of detuning. Close to resonance (dark blue shaded spectrum, $\delta \sim 50$ MHz) coherent and incoherent parts exist with roughly equal strength. As detuning is increased the broad incoherent component dies away, and at $\delta \sim 750$ MHz the coherent peak alone remains visible. Figure 4.17 b displays the theoretical prediction for the dependence of the coherent fraction on detuning (for s=1, $T_2 = 1.9T_1$) in the absence (red dashed line) and in the presence of spectral diffusion (blue line).

The coherent fraction of the total fluorescence F_c behaves as

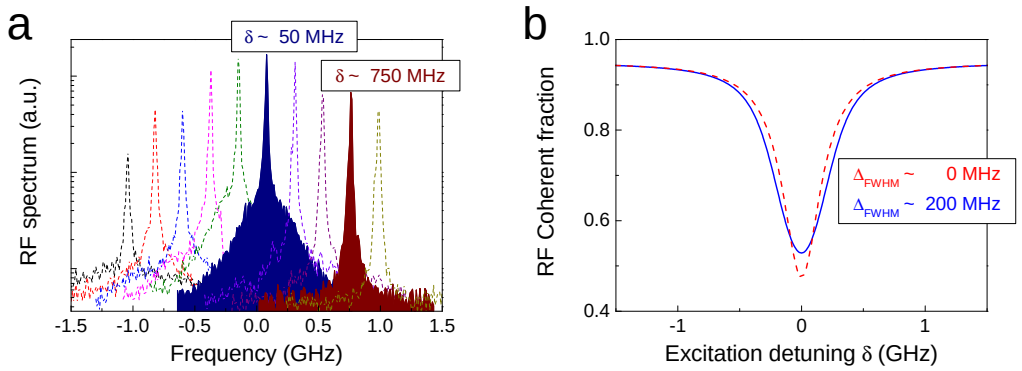

Figure 4.17: Dependence of emission spectra and coherent fraction on detuning of the excitation laser. a, Emission spectra for X^0 transition for $s = 1$ on a logarithmic intensity scale. The coherent fraction increases strongly with laser detuning. b, Theoretically expected detuning dependence of coherent fraction in the presence (dashed red) and absence (blue) of spectral diffusion for $s = 1$ and $T_2 = 1.9T_1$.

$$F_\mathrm{c} = \frac{(2\pi\delta)^2 T_2 (2T_1)^{-1} + (2T_1T_2)^{-1}}{(2\pi\delta)^2 + (1+s) T_2^{-2}} \tag{4.18}$$

as a function of detuning. In analogy to the spectral diffusion model used before, the expression is modified to

$$F_{\mathrm{c,diffusion}}(\delta) = \frac{\sum_\Delta F_\mathrm{c}(\Delta) \times \mathfrak{L}(\Delta) \times \mathrm{W}(\Delta_\mathrm{FWHM}, \Delta, \delta)}{\sum_\Delta \mathfrak{L}(\Delta) \times \mathrm{W}(\Delta_\mathrm{FWHM}, \Delta, \delta)}. \tag{4.19}$$

In general, the coherent fraction is enhanced at small detuning $\delta \sim 0$, and decreased at larger detuning.

The intensity autocorrelation $g^{(2)}$ is recorded for each detuning $|\delta|$ in Fig. 4.17 a. Figure 4.18 displays four representative measurements with detailed fit functions. The top panels contain the data as dark red curve with grey shading. The blue continuous curve is a convolution of the theoretical expression based on Eq. (2.31) and including spectral diffusion (see Eq. 4.14) and the system response function (cf. Fig. 3.16). The deconvolved fit is plotted as dashed black curve. For clarity the convolved (middle panels) and deconvolved (bottom panel) curves are displayed again without the data in the lower panels. Here, the blue curves are based on the fits to the data, while the red curves neglect spectral diffusion,

but use the same parameters otherwise.
The detuning modifies the effective Rabi frequency according to $\widetilde{\Omega} = \sqrt{\Omega^2 + (2\pi\delta)^2}$, where $\Omega = s/(T_1 T_2)$ is the bare Rabi frequency. In the limit of large detuning, i.e. large effective Rabi frequency, the amplitude of the coherent oscillations in the intensity autocorrelation is not centered around unity, unlike in the case for large Rabi frequencies at zero detuning. In the latter case the oscillations go from zero at $\tau = 0$ to two after a π rotation and decay symmetrically around unity within the coherence time T_2. With a large excitation detuning the intensity autocorrelation can exceed the value of 2, which is the $\tau = 0$ limit for chaotic light. The deconvolved fit to the data in Fig. 4.18 crosses this limit. As the detector resolution is finite, the contrast of the oscillations washes out and we average between peaks and troughs. For the largest detuning presented here, $\delta \sim$ 810 MHz, the antibunching signature has almost completely vanished and the autocorrelation is dominated by the first peaks on either side. The data might be described more accurately as *bunching*, instead of *antibunching*!
This discussion may seem a bit artificial here; of course the fluorescence is still antibunched - as it always is for a single two-level system. It is the timing resolution that prevents us from measuring this part. Extending the scheme from Fig. 4.18 further in experiments is challenging, since the signal is strongly reduced for large detuning and the data acquisition becomes unreasonably long. To complete the picture we keep the theoretical prediction only and set the detuning to twenty times the natural linewidth. The result is presented in Fig. 4.19. The amplitude of the oscillation approaches four around $\tau = 0$. Averaging over an oscillation period gives a simple curve

$$g^{(2)}(\tau)_{\text{averaged}} = 1 + \exp^{-|\tau|/T_2} \tag{4.20}$$

which is consistent with the behaviour of a classical light source.
The apparent bunching in the fluorescence can be explained intuitively[1] with higher-order corrections to Rayleigh scattering [69]. We note that off-resonant QD excitation and sideband correlations were explored in the strong excitation regime by Ulhaq *et al.* [146].

[1] i.e. no quantitative analysis will be given

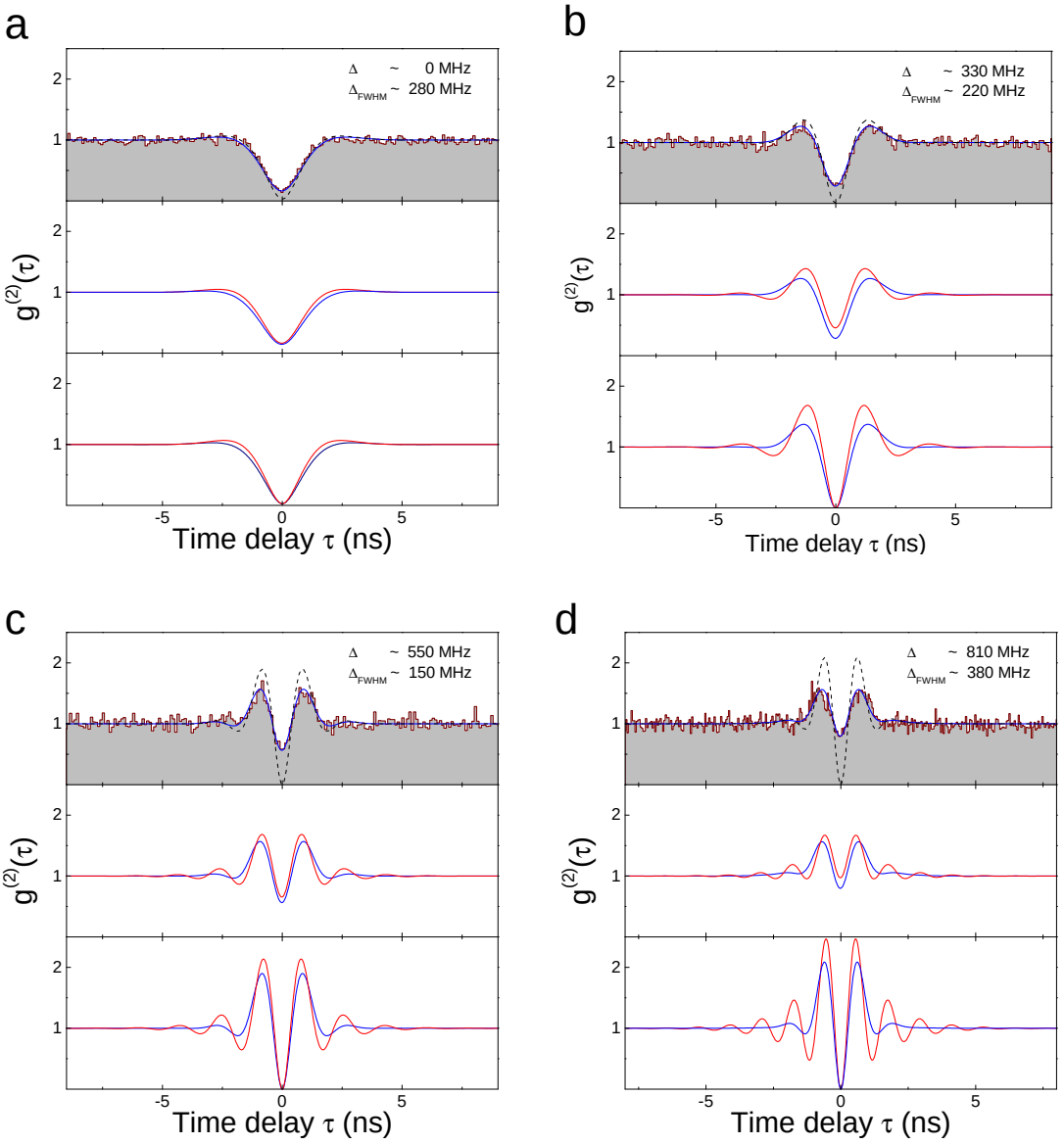

Figure 4.18: Second-order correlation functions for finite detunings. Top panels: data (noisy red, grey shading) with a fit (blue curve) taking into account spectral diffusion and the system resolution and the deconcolved fit (dashed black). Middle panels: Convolved fit with (blue) and without (red) spectral diffusion. Bottom panels: deconvolved fit with (blue) and without (red) spectral diffusion.

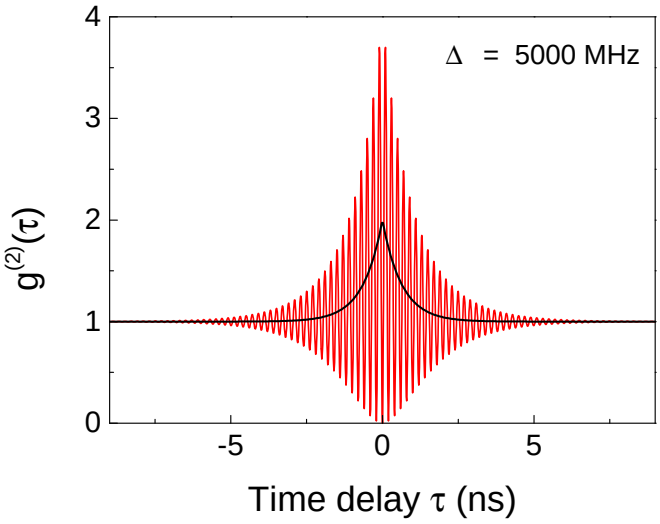

Figure 4.19: Calculated intensity correlation function for $s = 1$, Δ =5000 MHz (red curve). The blue curve shows the effect of finite timing resolution for this calculation.

Chapter 5

Optical manipulation of electric fields and quantum dot electrometry

It has been observed by a number of groups working on resonant QD spectroscopy [58; 81] that the QD transition shifts as a function of the resonant excitation power. This effect has not been explored in detail, to my knowledge, but is important in the context of coherent optical spin manipulation [22], as resonance shifts in the optical transitions lead to phase shifts in the spin evolution. If not properly accounted for, this is a source of dephasing.

Here, we study the power dependence of resonance shifts in the steady-state, i.e. under continuous-wave illumination, and time-resolved shifts under pulsed excitation. Ruling out laser-induced heating we identify charging of the heterostructure via optical absorption in the QD gates as the cause. The effect may be exploited for fast spectroscopy, or optical switches.

Data acquisition and analysis for this chapter has benefited from collaboration and discussion with the members of the QD team. In particular, I am grateful to Martin Geller for fruitful discussions on thermometry and how to measure of the Fermi-Dirac distributions. Rob Stockill contributed to the thermometry and electometry measurements. I am grateful for the patience of other QD team members while these measurements were taken.

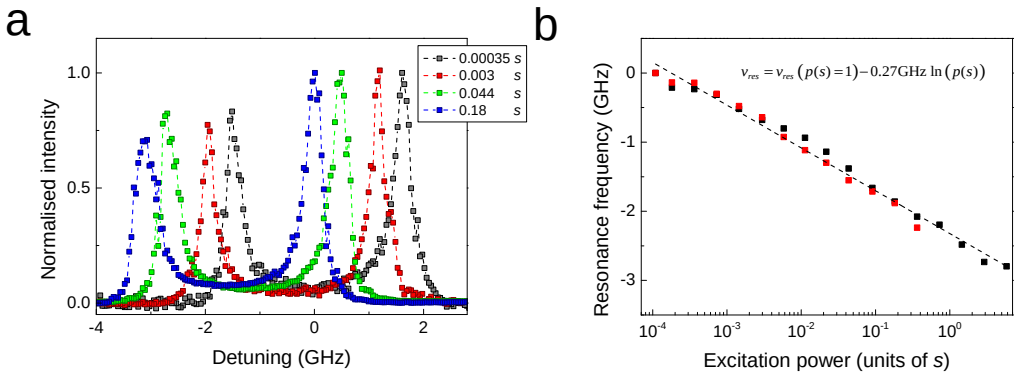

Figure 5.1: Shifts of QD resonance as a function of resonant excitation power. a, Series of absorption lineshapes obtained by scanning the gate voltage across the X^0 transitions for different laser powers.b, Summary of resonance shifts as function of power. For the red data points the power is decreased in subsequent measurements, while it is increased for black data points. The dashed line is a fit according to Eq. (5.1).

5.1 The observation

5.1.1 One-colour steady-state measurements

In this section we describe the observation of laser-induced resonance shifts and quantify the magnitude of the shifts. Figure 5.1 a shows a series of absorption lineshapes of the neutral exciton transitions (QD 'Isidor II') for different excitation powers. We keep the excitation laser frequency fixed for all powers and scan the gate voltage across the two resonances. Knowing the Stark shift ($\sim$ 410 MHz/mV) the gate voltage is translated into frequency again. For the range of powers displayed the QD resonance shifts by almost 2 GHz, which exceeds the transition linewidth by far. Panel b shows the frequency shifts over five orders of magnitude in excitation power on a semi-logarithmic scale. For reference, the saturation point (s=1) corresponds to about 10 nW power incident on the QD sample. Data from two sets of measurements are presented. For the red data points the excitation power of successive line scans was approximately halved (i.e. starting at higher powers), while we doubled the power with each scan for the black data points. If the shift were to originate from a QD-intrinsic property we would expect to see a saturation behaviour as the QD is strongly driven. This

is clearly not the case. On a semi-logarithmic scale, the resonance shifts follow a straight line. A fit to the data using the empirical model

$$\nu_{\mathrm{res}} = \nu_{\mathrm{p}=s} + a \times \ln\left(p\left(s\right)\right) \tag{5.1}$$

is shown as dashed black line. The constant in Eq. 5.1 gives a reference frequency and the constant of proportionality is $a \approx -270$ MHz. This corresponds to a redshift of the QD transition of approximately one radiative linewidth every time the power is increased by a factor 2.5. Over the range of powers studied there is no significant deviation from the logarithmic dependence.

5.1.2 Modulated shifts: Two-colour steady-state

We can repeat the measurement, but this time keeping the resonant laser power fixed while adding a second laser. This second laser, denoted pump laser, is strongly red-detuned from the QD excitonic resonance (by about 15 nm). Its energy is then also far below the bandgap of GaAs and the wetting layer. We use a grating to remove the pump laser from the detection path. Figure 5.2 a shows a two-dimensional plot of the X^0 lineshapes as function of the pump laser power. The first data column in the plot shows the case where only the resonant laser, now called probe laser, is incident on the sample. Then the pump laser is added and its power is doubled with each column. The QD transition frequency shifts in a similar fashion to the single colour experiments of Fig. 5.1. We conclude that the resonance shift depends on total (below bandgap) laser power incident on the sample, regardless of the detuning to the QD transition: it is not a resonance phenomenon.

Next, we investigate the bandwidth of the resonance shifts. To this end, the probe laser is kept operating in continuous-wave mode while the pump laser amplitude is modulated (modulated depth of 1) by a square wave of variable frequency. The corresponding data is shown in 5.2 b. Here, the peak power of the pump laser is 12 times higher than the probe laser power. At low modulation frequencies four transitions are distinctly visible: the fine-structure split X^0 transitions jump between their steady-state resonances at the two power levels. Going to faster modulations first broadens the individual transitions and then smears out the

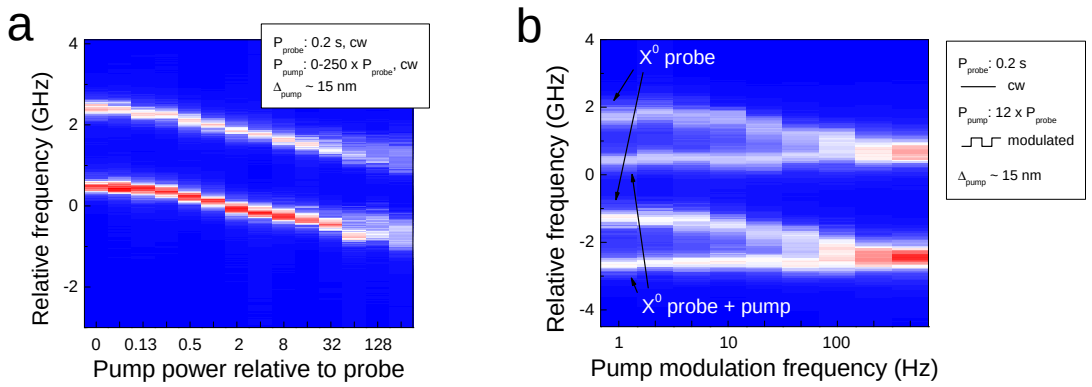

Figure 5.2: Two-colour shifts of QD resonance. a, the resonant laser (probe laser) is kept at constant power and the X^0 lineshapes are measured as a function of the strongly detuned pump laser power. b, The probe power is constant and the pump laser amplitude is modulated on and off for a range of modulation frequencies.

transition between the steady states. At a modulation frequency of about 1 KHz only two transition frequencies remain and a new steady-state is reached: The modulation exceeds the bandwidth of the laser-induced shifts, and the response corresponds to that for a time-averaged incident power.

5.2 The origin

We consider two mechanisms that could lead to resonance shifts as a function of incident power: build-up of an electric field and local heating of the sample due to residual absorption. First we discuss sample heating and QD thermometry.

5.2.1 Temperature

It is well known that increasing the temperature of a semiconductor leads to shrinkage of the band gap, due to thermal expansion of the lattice and increased electron-phonon scattering. This is observed as a red-shift in the optical emission from semiconductors, both for bulk and confined states. For a wide temperature range the famous empirical Varshni model [147] describes the band gap-temperature relation well. Early measurements on QD ensembles seemed to confirm the validity of the model [148]. At very low temperatures deviations from

the Varshni model are apparent, however, and photoluminescent spectroscopy of single QDs enabled accurate measurements here [149]. Recently, the temperature dependence of the resonance frequency of single QDs has been measured in resonant transmission experiments by Kroner *et al.* [150] with very high resolution ($\sim \mu$eV). They found a saturation of the resonance frequency for temperatures $<$ 10 K. QD resonance fluorescence measurements as a function of temperature on a different sample agree qualitatively while still resolving resonance shifts below 10 K temperature [151]. Close to the liquid helium temperature resonance shifts remain small, however, in this case too. Based on these reference we can estimate the change of temperature corresponding to our measured resonance shifts to be on the order of several K ($\sim$ 5 K). To confirm or refute local heating as source of the resonance shifts we should attempt to measure the local temperature independently.

QD Thermometry A possible indicator of the QD temperature was introduced in the previous chapter: phonon sidebands in the resonance fluorescence. The strength, and more sensitively, the shape of the sideband depends on temperature as the thermal occupation of phonon modes changes [130; 131]. Power-dependent sideband measurements do not show such a change in our measurements however, despite the good quality of the data (cf. Fig. 4.11).
There is an alternative way to measuring temperature in our gated devices. The back contact is made conductive by Si-doping and the chemical potential μ_F is pinned at the dopant energy level. The broadening of the chemical potential is given by the Fermi-Dirac distribution

$$n_\mathrm{FD} = \frac{1}{e^{(E-\mu_\mathrm{F})/(k_\mathrm{B}T)}+1}. \tag{5.2}$$

If this broadening can be measured we have access to a primary thermometer. We wish to probe the broadening with the QD ground state. The idea relies on carrier thermalisation between the back contact and the QD ground state and is sketched in Fig. 5.3: The occupation of the QD electronic ground state is linked to the occupation in the back contact at the same energy. For instance, when the energy of the QD one-electron state is more than $k_\mathrm{B}T$ below the chemical potential the

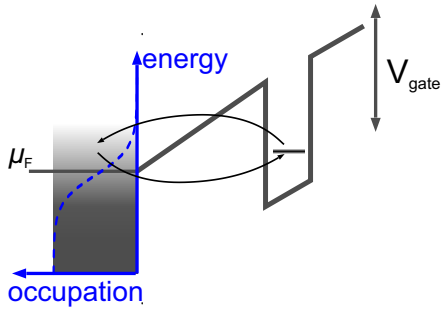

Figure 5.3: Sketch of the conduction band for part of the QD device. On the left is the Si-doped back contact. The chemical potential μ_F is determined by the dopant concentration. The occupation of electronic states in the back contact obeys the Fermi-Dirac distribution which is shown as blue curve (occupation vs. energy) and additionally indicated by the shading. The QD ground state (e.g. the single electron ground state) is tunnel-coupled to the reservoir such that the occupation is in equilibrium with the occupation in the back contact. Probing the QD ground state occupation as a function of the gate voltage provides a way to map out the Fermi-Dirac distribution.

single electron is stable in the QD. Tunneling to and from the back contact does not occur because no free states are available at this energy in the back contact. When the QD one-electron energy level is raised to the chemical potential plenty of free states are available in the back contact and the QD occupation of 0.5 reflects the occupation of the back contact. Increasing the reverse bias further empties the QD as states of the same energy are not occupied in the back contact.

Continuing to use the example of the single electron ground state the occupation of the ground state can be measured through optical absorption at the trion transition energy. Sweeping the QD one-electron ground state energy through the chemical potential via the applied bias and measuring the trion absorption probability should then map out the Fermi-Dirac distribution.
Figure 5.4 a shows an exemplary two-dimensional voltage-frequency map of the X^{1-} resonance fluorescence intensity. The gate voltage range is chosen such that the QD moves from the zero to the one-electron ground state. In Fig. 5.4 b we plot the peak intensity for each data row from panel by fitting Lorentzians to the gate voltage sweeps at fixed frequency. The abscissa scale is obtained by translating the gate voltage into energy relative to the chemical potential using

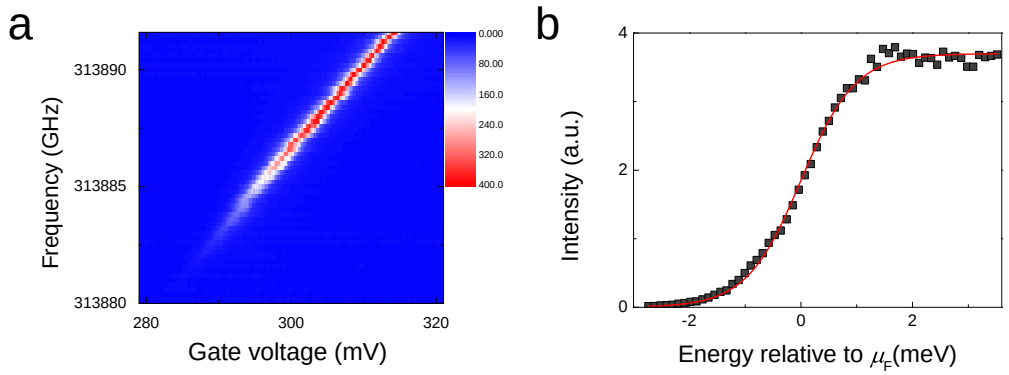

Figure 5.4: QD thermometry with resonance fluorescence. a, Gate voltage-frequency map of the X^{1-} transition. For low gate voltages the QD is empty and there is no signal. As the forward bias is increased the QD ground state occupation moves smoothly from 0 to 1 electron and the resonance fluorescence signal is recovered - proportional to the single electron ground state occupation. b, Plot of the resonance fluorescence intensity as function of energy detuning between QD ground state and chemical potential. The red line is a fit to the Fermi-Dirac distribution.

the lever arm method:

$$\Delta E_{\mathrm{1e,\,gs}} = e\frac{d_{\mathrm{barrier}}}{d_{\mathrm{diode}}} \times \Delta V_{\mathrm{gate}}, \tag{5.3}$$

where the change in energy of the one-electron ground state $E_{\mathrm{1e,\,gs}}$ depends on the change in applied bias ΔV_{gate} and the ratio of distance between the back gate and the QD layer (d_{barrier}) to the total length of the Schottky diode (d_{diode}). A fit to the Fermi-Dirac distribution (Eq. (5.2)) is shown as red curve and gives the temperature as 5.6 ± 0.2 K. It should be pointed out here that the lever arm method is a first-order approximation and prone to systematic errors. In particular, the distance d_{barrier} varies from the value specified for the growth as charges from the doped back contact spill into the tunnel barrier and shorten the distance. This leads to an overestimate of the temperature. Further, the laser power should be kept constant throughout the measurement, also while scanning the frequency. Stabilisation on the optical table is possible to considerably better than 1 %, but the microscope beamsplitter transmission/reflection shows a frequency dependence, which, depending on the particular frequencies, can give rise to a 10 % change in power at the QD over ∼ 10 GHz. These systematic errors

should not keep us from testing the laser-induced heating hypothesis though, as long as conditions can be kept comparable in subsequent measurements.
In Fig. 5.5 we present an analysis of QD resonance maps with a resonant probe and an off-resonant pump laser. The raw data is shown in panels a, b and c. Here, the resonant laser is fixed at 0.05 of the saturation power and the pump is, in order of the panels, absent, ten times the power of the probe and 100 times the probe power (panels a-c respectively). The analysis follows the procedure outlined above, and panel d displays the peak fluorescence intensity as function of QD ground state detuning from the chemical potential. Data for the three measurements and fits according to Eq. (5.2) are colour-coded: red corresponds to the data in panel a, green to panel b and black to panel c. The similarity between the data sets is striking and the temperatures given by the fits agree with each other within their errors[1].
To summarise: so far, we have not seen any evidence for laser-induced heating. We would expect a temperature change of several K, but this is ruled out by measurements of the Fermi distribution. However, the QD resonance maps of Fig. 5.5 do provide us with evidence of laser-induced electric-fields that shift the QD transition and this is subject of the next section.

As an aside, we note that Fermi distribution measurements with optically active QDs may be used in thermometry applications. Here we obtain a precision close to 100 mK. The accuracy is limited by systematic errors in the lever arm calculation to about 2-3 K. A big improvement here could be a more accurate determination of the effective tunnel barrier thickness d_{barrier} (see Eq. (5.3)), for instance through cross-sectional scanning tunneling microscopy of the QD heterodiode structure. For practical purposes, integrating a Schottky diode for thermometry may not be convenient in some applications, and the required electric field can additionally affect the semiconductor environment. By nature the QD thermometer is local, so to achieve a spatial temperature map we need to measure a set of QDs at reasonably well-resolved positions. The spatial temper-

[1]We note the temperatures are different from what was obtained for the exemplary data in Fig. 5.4. The current data set was recorded at a different time (time difference of some weeks) and as such the alignment of the microscope was different, mainly in the excitation polarisation. Consequently the frequency dependence of microscope beamsplitter reflectance and transmittance differs for both measurements.

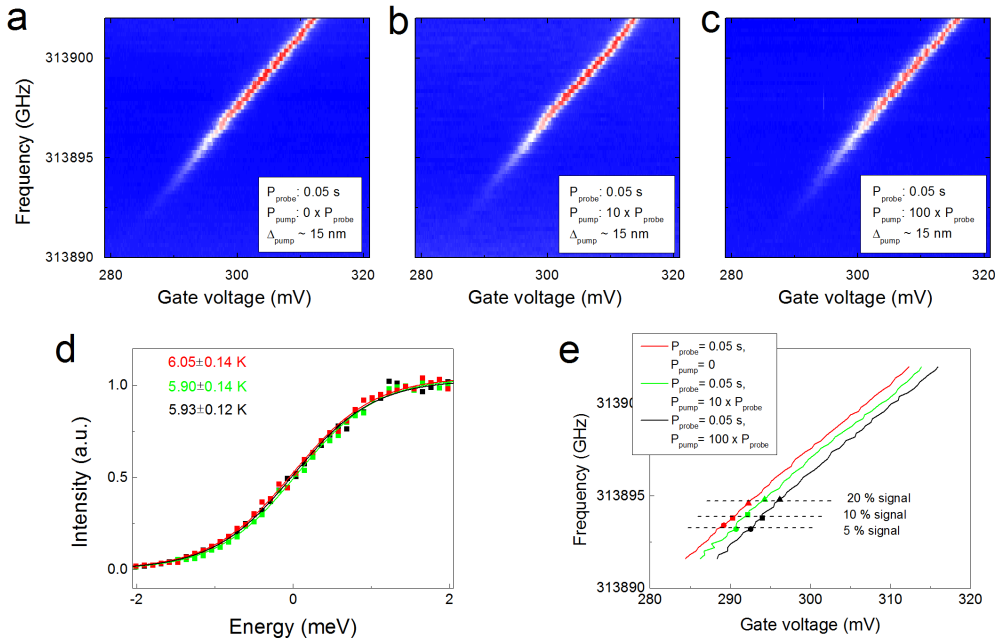

Figure 5.5: QD thermometry in the presence of a pump laser. a-c, QD resonance fluorescence maps in gate voltage-frequency space for pump powers of zero (a), ten times the probe power (b), and 100 times the probe power (c). d, Peak intensities versus detuning from the chemical potential, fitted with the Fermi-Dirac distribution. Red data points and fit correspond to panel a data, green to panel b and black to panel c. e, Position of QD resonance in gate voltage-frequency space for panels a-c. Positions where the intensity exceeds 5, 10 and 20 % of the full intensity are highlighted.

ature resolution is then given by the ability to map the QD locations. As for the accessible temperature range, QDs are efficient emitters up to $\sim$ 50 K and this limits the use to cryogenic temperatures. The main attraction of this method is that we have a primary thermometer, that is, the thermometer does not require calibration. We note that other methods, for example temperature-dependent emission energy can be exploited for thermometry purposes (see Ref. [152] for a review) and this principle has been successfully applied for colloidal II-VI QDs [25].

5.2.2 Electric field

QD resonance shifts through temperature and electric-field changes can be told apart by their dependence on the bias applied to the Schottky diode. If we consider the 2D QD resonance maps in gate voltage and transition frequency space (see Fig. 5.5 a-c) a temperature increase will push the entire transition to smaller frequencies. The gate voltage range should remain unchanged, as it is determined by the QD charging properties, which are tied to the applied bias. In contrast, electric field changes (independent from the applied bias) should not alter the transition frequencies, but shift it along the gate voltage axis. Going back to the analysis in Fig. 5.5, we move to panel e. Here, we plot the QD resonance positions from the 2D maps as lines. The colour code is indicated in the legend and was already used in panel d. The resonance position is obtained through Lorentzian fits to each data row of panels a-c. For ease of comparison, three data points are highlighted for each measurement. These mark the positions (in gate voltage/frequency) where the QD transition reaches $\geq$ 5, 10 and 20 % of the full signal strength. Within the noise these positions occur at constant frequency, but shifted gate voltage. Hence the observed resonance shifts can be firmly attributed to a laser-induced change in the electric field felt by the QD.
When the pump laser shifts the QD resonance, the gate voltage needs to be increased to recover the QD resonance. In our case the laser-induced electric field counteracts the applied field, it acts to reduce it. Further, the reversibility and 'smoothness'[1] of the shifts suggests that it is not due to dynamics of local defects,

[1] and the reproducibility on different QDs

but rather due to free carrier absorption in the gates of the heterostructure.
In the following section we will investigate details of the electric-field shift from an electrometry point-of-view, with particular regard to the dynamics of the electric field.

5.3 Time-resolved electric field dynamics and QD electrometry

Here we turn to time-resolved measurements to obtain more information on the bandwidth of the resonance shifts, and at the same time investigate the performance of resonance fluorescence-based electrometry.

5.3.1 Considerations for QD electrometry

First, we discuss our results in the context of QD electrometry. Using the QD resonance shifts as means to infer details about the QD environment was already used in the investigation of spectral diffusion in section 4.2.1. To recap: changes in the electric field around the QD act on the permanent dipole of the electron-hole pair[1] of excited QD states and as such translate to change in the QD transition frequency. This Stark shift is linear in the range of electric field changes studied here. The electric field sensitivity then depends on the change in optical signal versus the noise in the detection.
The ability to probe electric fields using the optical response from QDs under resonant excitation was explored in Ref. [24]. There, the use of homodyne detection in differential transmission and reflection schemes was advocated to pick up on both DC and AC fields with a Lockin-Amplifier. Houel *et al.* used differential transmission to locate the position of defects in the tunnel barrier close to a QD [81]. The recent work by Kuhlmann *et al.* exploits resonance fluorescence to measure electric (and nuclear) field noise timescales [127].
One strategy for using QD resonance fluorescence for electrometry is to set the probe laser frequency at a detuning where the response to electric-field changes

[1] in particular in the growth direction

is greatest. This detuning is given by the maximum of the first derivative of the lorentzian QD absorption lineshape and corresponds to

$$\delta_{max} = \frac{1}{2\pi}\sqrt{\frac{1+s}{6T_1T_2}}. \tag{5.4}$$

Electric fields can be sensed if the signal change due to the QD resonance shift exceeds the shot noise of the signal at the set detuning. If the QD photon detection rate as a function of detuning Δ and detection/collection efficiency η is given by $I(\Delta) = \eta \times \frac{\rho_{22}}{T_1}$ and the Stark shift coefficient by α, then electric field changes δE for which

$$\delta E \geq \frac{\sqrt{I\left(\delta_{max}\right)}}{\frac{\partial}{\partial\Delta}I\left(\delta_{max}\right) \times \alpha} \tag{5.5}$$

can be measured. To give an example using parameters from our system and sample, for a typical QD with a natural linewidth of 250 MHz, a Stark shift coefficient of 80 KHz $(\mathrm{V/m})^{-1}$ and a combined collection/detection efficiency giving 500 kcounts/s on resonance at saturation we obtain a theoretical electric field sensitivity of

$$\delta E \gtrsim 50\frac{\mathrm{V}}{\mathrm{m}}\sqrt{\mathrm{Hz}}^{-1} \tag{5.6}$$

In practice, some of this sensitivity is taken away by constant 'sensing' of spectral diffusion. While this is in principle already electric field sensing, it reduces our ability to detect electric field changes on top of this background.
A different strategy to electric field sensing is to scan across the QD resonance while detecting photons and fit the absorption lineshape to obtain the exact QD resonance. This approach, employed in the next sections yields experimental sensitivities around 50 $(\mathrm{V/m})/\sqrt{\mathrm{Hz}}$ or better, on top of the uncontrolled spectral diffusion and without operating under optimum conditions.
For the remainder of this chapter we will shift the focus back to investigating the dynamics of the laser-induced electric field. For simplicity we will continue working in units of gate voltages, but we keep in mind that the following results are a practical application of electrometry: to convert the changes in gate voltage

into electric field changes we just have to divide by the length of the QD diode (185 nm).

5.3.2 Dynamics of laser-induced electric field

Measurement technique Measurements with a modulated pump laser were introduced in Fig. 5.2. Now, the duty cycle of the modulated pump laser is reduced ($\ll 1$) to allow the transition to relax back into its steady-state after the pump pulse. We use an electro-optic modulator with high bandwidth (5 GHz) modulated by a digital delay/pulse generator (SRS DG645) with a transition time < 2 ns to create fast laser pulses and record time-resolved fluorescence detection events with a time-to-amplitude converter (quTools quTAU). Figure 5.6 shows a time-resolved map of the QD fluorescence for a pump pulse of 20 μs duration and a repetition rate of 50 Hz. The probe laser frequency is fixed and time-resolved data is recorded for 60 seconds at each gate voltage. Data acquisition is triggered by the same pulse generator that drives the EOM and lasts in this case for 20 ms with a resolution of 200 ns. The top left panel shows the first 100 μs of the raw data, where the pump pulse is incident after about 20 μs, while the top right panel shows the remainder of the data, here binned to 2 μs resolution. In the bottom panels we trace the QD resonance position, obtained through Lorentzian fits for each time delay (200 ns resolution in both bottom panels).
The QD response to the pump pulse is characterised by a fast and monotonous resonance shift during the pulse. Two timescales are present in this response risetime; this will be discussed for higher timing resolution data presented later on. Following the pump pulse, the transition drops rapidly to slightly lower gate voltages and then slowly relaxes to its equilibrium position. The rapid drop is instantaneous within the resolution of this data, while the slow relaxation happens on the order of milliseconds. Comparing these timescales to the bandwidth measurement with a square-wave modulated pump in Fig. 5.2 we identify the slow millisecond relaxation time as the dominant part: When the repetition rate exceeds roughly 1 KHz, the transition does not relax back to its 'unperturbed' resonance and a new steady-state exists.

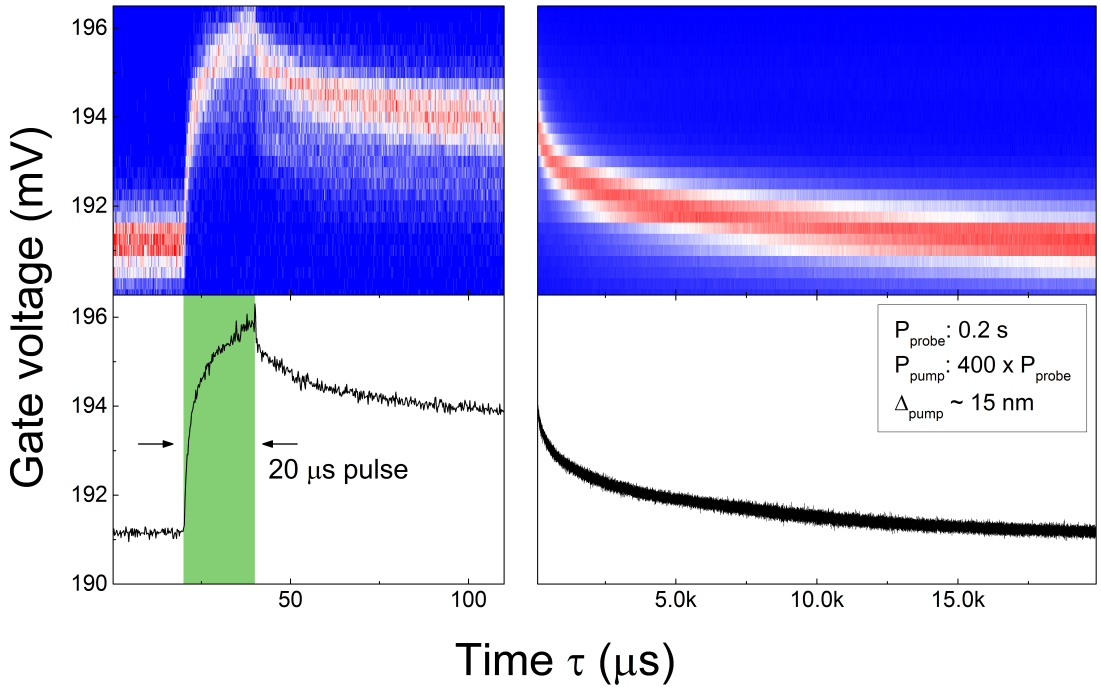

Figure 5.6: Time-resolved response of QD transition to a pump pulse of 20 μs duration. Top panels show the raw data, bottom panels the QD resonance (in gate voltage) which is obtained by fitting Lorentzians to constant-time cuts in the top panels. Top left: pixel timing resolution of 200 ns, 0.6 ms integration per pixel. Top right: pixel timing resolution of 2 μs, 6 ms integration. Bottom: Timing resolution of 200 ns in both panels. The pump pulse peak power 400 times the probe power.

Detailed dynamics Having introduced the experimental technique to measure the laser-induced electric field changes we take a closer look at the dynamics now. The timing resolution in Fig. 5.6 was too low to resolve the the response to the onset of the pump pulse, so here we use faster pump pulses and higher timing resolution. In Fig. 5.7 we present data for pulses of nominally 2 and 10 ns duration. The plots on the left (a and c) show the system response functions for the two pulses. These are measured by sending the pump laser only to the QD and detecting part of its reflection into the collection fibre, using the same equipment as for the time-resolved pump-probe experiments. For a rectangular pulse of nominally 2 ns duration we obtain am approximately Gaussian shaped pulse with a FWHM of 1.4 ns. The shape is determined almost entirely by the bandwidth of the pulse generator. Panel b shows the dynamics of the QD resonance in a pump-probe measurement using the pump pulse from panel a. The data is derived from a time-detuning map as before in Fig. 5.6. The response of the QD resonance suggests that the pump-induced electric field follows the pulse intensity closely, but the width of the feature ($\sim$ 3 ns) is broader than the pump pulse width. The fall time of the response seems to be slightly slower than the rise time. Taking into account the original width of the pump pulse, the response of the electric field felt by the QD is about 2.5 ns, corresponding to a bandwidth of 400 MHz. Panels c and d of Fig. 5.7 display the pulse shape and the QD resonance response for a pump pulse of nominally 10 ns duration.

Interestingly, the QD resonance displays an 'overshoot' behaviour: once the pump pulse has passed, the QD resonance shifts slightly past its original resonance into the opposite direction, before relaxing back to the original resonance setting within 10-100 ns. This phenomenon may be related to a backaction of the charge distribution in the QD gates after the quick build-up and discharge of the pump-induced field, but this is not resolved at the moment.

To complete the picture we employ QD electrometry to look at laser-induced fields for pump pulses with durations ranging from 100 ns to 200 μs in Fig. 5.8. In each panel we show the dynamics of the QD resonance over the full time range of the measurement in the main plot. The immediate response to the pump pulse is shown in more detail in the insets of each panel. Here we highlight the timing of the pulse and its duration by shading the respective area in the inset in green.

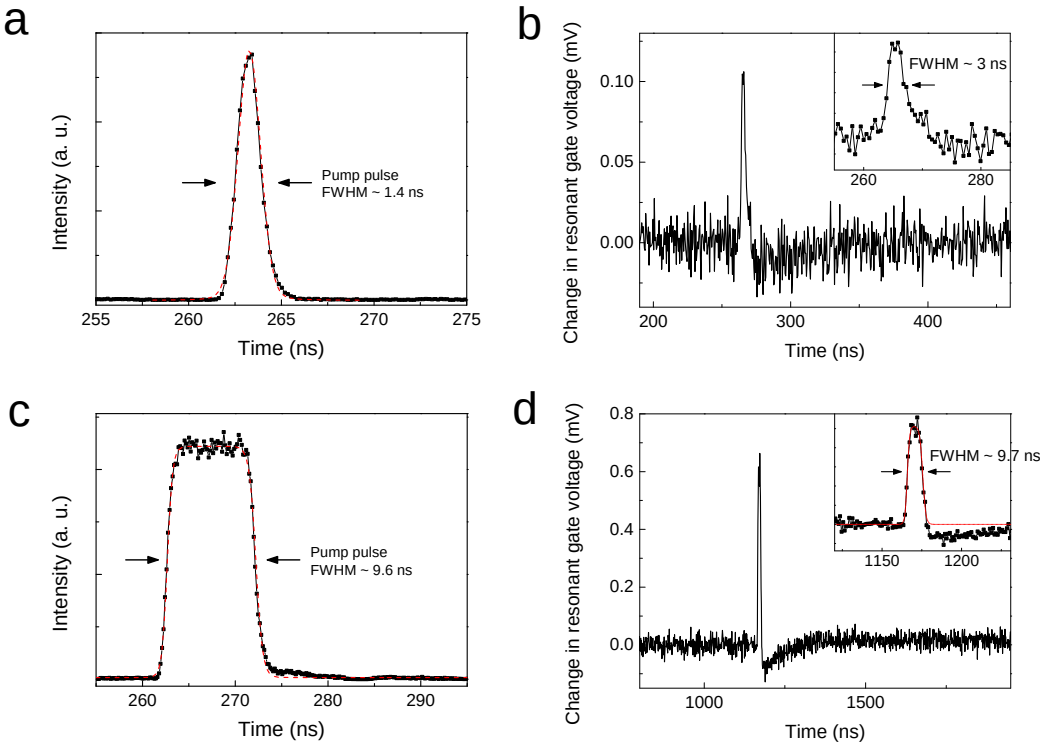

Figure 5.7: Time-resolved QD electrometry for pump pulses of 1.4 ns (a, b) and 10 ns (c, d) duration. a, c, Measurements of the pump pulse intensity profile. b, d, Response of the QD resonance. The timing resolution in panels a-c is about 0.5 ns, limited by the APD jitter. The timing resolution of panel d data is 1 ns. The integration time per pixel for the original data for b is 25 ms and 5 ms for d.

For a pump pulse of 100 ns (see Fig. 5.8 a) the response follows the rectangular shape of the pump initially. Similarly to the data for shorter pulses presented in Fig. 5.7 there is an overshoot immediately following the pump pulse. However, the response curve crosses the steady-state (0 mV on the ordinate axis) a second time, reaches a maximum and only then decays monotonically back to the equilibrium gate voltage. Increasing the pump pulse duration to 500 ns in panel b we find clear differences between the intensity profile of the pump pulse and the electric field response felt by the QD: After the initial fast rise of the response curve (which follows the rise time of the optical pulse closely) the QD resonance continues to shift in the same direction while the pump laser power is constant, but at a much slower rate. In panel b this shift is approximately linear in time. The sharp drop of the response curve follows the fall time of the optical pulse again, but no overshoot is visible this time. Further increasing the pump pulse duration to 2 and 200 μs in panels c and d, respectively, it becomes obvious that the QD resonance approaches a new steady-state position during the constant intensity part of the pump pulse. Here the behaviour is approximated by a $(1 - \exp(-t/\tau_c))$ dependence. The characteristic time scale τ_c is some tens of microseconds (cf. panel d).
The slow final decay back to the unperturbed resonance shows a non-trivial dependence on pump pulse power and duration. It varies from few tens of microseconds to milliseconds for the data presented here. The decay is further influenced by the finite repetition rate of the measurement scheme. For a detailed study of the relaxation rate the repetition rate should be significantly reduced.

In conclusion, we have presented a detailed study of laser-induced QD resonance shifts, quantifying both amplitudes and the timescales. Performing QD thermometry and electrometry we have identified the origin of the resonance shifts as laser absorption in the QD sample gates leading to the build-up of an electric field. While this conclusion is perhaps less exciting it allows us to disentangle this unwanted effect from other experimental data. Further, the investigation confirms the potential of optical electrometry, where resonance fluorescence enables high sensitivity and high bandwidth operation. Finally, having identified the sample gates as problematic, we can look into sample structures which avoid the issue.

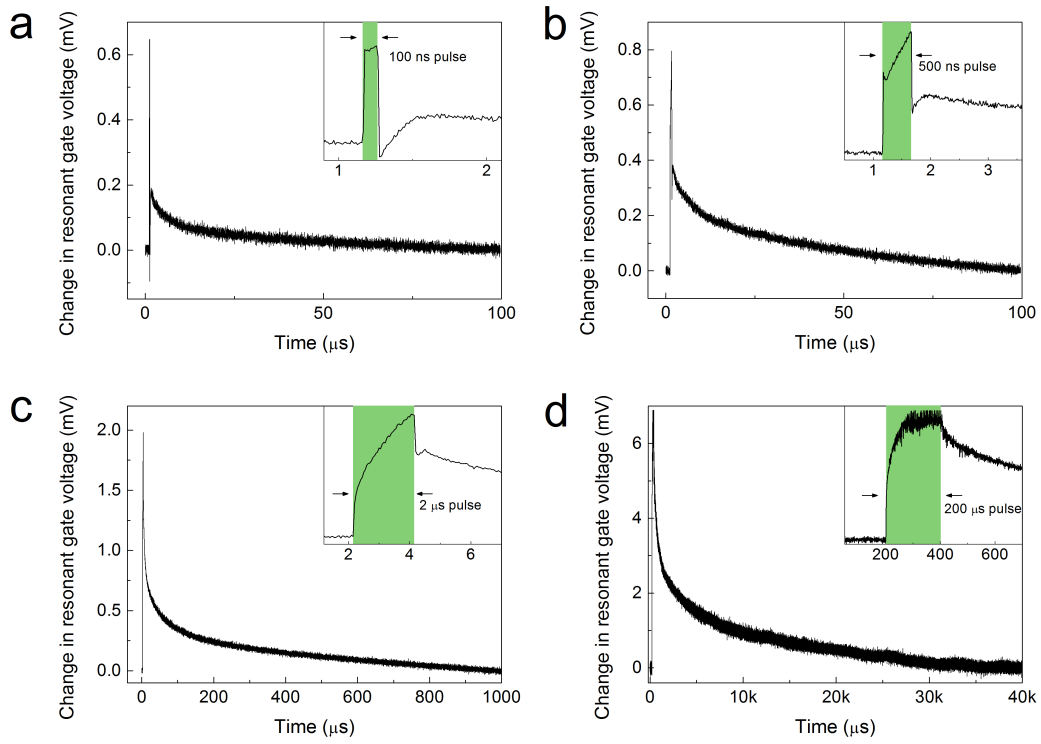

Figure 5.8: Tracing the QD resonance for pump pulses from 100 ns to 200 μs duration. The inset displays the dynamics around the pump pulse in greater detail. a, 30 ms integration time per time bin of 10 ns. b, as a. c, 15 ms integration time per time bin of 50 ns. d, 60 μs integration time per 400 ns time bin.

Chapter 6

Coherent single QD photons for quantum optical networks

The 'Quantum Internet' envisions remote stationary qubits connected via flying qubits, where local operations and entanglement between the distant qubits enables quantum computation. Quantum dots offer a natural solution where a trapped spin encodes the stationary qubits, while resonantly scattered photons can carry the spin information over macroscopic distances. The latter was recently exploited to demonstrate spin-photon entanglement for QDs [53; 65; 66]. The missing link so far is an experimental demonstration of distant QD spin entanglement. Distant entanglement has been successfully demonstrated for other physical systems, most notably for trapped atoms [153; 154] and recently also for the nitrogen-vacancy defect centre in diamond [155]. Entanglement is created by interference and detection of two photons - each entangled with the host qubit they originate from. This non-local entanglement based on photon quantum interference has been identified as a promising and robust approach [156; 157]. The robustness stems from the probabilistic nature of entanglement creation, placing fewer constraints on detection efficiencies, but relies crucially and fundamentally on indistinguishable photons from separate qubits: In the presence of pure dephasing or spectral diffusion photons become distinguishable and do not interfere. Photon detection then erroneously heralds qubit entanglement. Coherent scattering from a QD provides an attractive way of generating dephasing-free photons,

protected to some degree from spectral diffusion, and we investigate their potential for quantum interference here.

This chapter builds on the observation of subnatural linewidth QD photons detailed in Chapter 5. Ref. [158] contains the publication of material from this chapter. We first demonstrate that the coherently generated single photons from a single self-assembled InAs quantum dot display mutual coherence with the excitation laser on a timescale exceeding three seconds. Exploiting this degree of mutual coherence we tailor the coherent photon waveforms by shaping the excitation laser field. In contrast to post-emission filtering, this technique avoids both photon loss and degradation of the single photon nature. By engineering pulsed waveforms of single photons, we then demonstrate that separate photons generated coherently by the same laser field are fundamentally indistinguishable, lending themselves to creation of distant entanglement through quantum interference.

Results presented in this chapter stem from a collaborative effort of the QD team. In particular, Carsten H. H. Schulte built the heterodyning setup and performed and analysed the measurement on QD fluorescence - laser mutual coherence (see Fig. 6.1). Martin Geller and Claire Le Gall contributed greatly to the long and tiring process of getting to the stage of collecting good two-photon interference data[1].

6.1 Considerations for two-photon interference

QD photon coherence is affected by the generation process. Above bandgap excitation, while technically easy to implement, relies on the incoherent relaxation of excitons in the QD ground state and emitted photons suffer from pure dephasing. This was confirmed by interference of two photons emitted by the same QD at different times. Keeping this time separation to a few nanoseconds avoids spectral diffusion affecting interference of the photon pair and interference contrasts of $\sim$ 70% were reported [159; 160]. However, two separate QDs experience independent environmental dynamics: the environmental noise is uncorrelated. In this

[1] This includes two-photon interference measurements with two independent quantum dots during the autumn and winter of 2011-2012 which did not make it into this thesis.

case two-photon interference from separate QDs using above bandgap excitation showed only a modest contrast of 18 % [161].
Resonance fluorescence avoids optically exciting the host material and therefore suppresses these dynamics. However, the ambient charge fluctuations, for example, can still broaden a transition via spectral wandering as we discussed in section 4.2.1. While not causing significant pure dephasing, the 'wobble' of the QD resonance renders the use of QDs in a quantum optical network problematic. Understanding the origin of these dynamics and eliminating them is a key challenge. Alternatively, approaches to suppress their effects should be pursued.

6.2 Mutual coherence: Phase-locking of QD fluorescence to laser

Elastic scattering from an optical transition represents an alternative approach to high quality photon generation, which avoids significant population in dephasing-prone excited states. Unlike the spontaneously emitted photons, the elastically scattered photons in the Heitler regime are expected to be phase-locked to the excitation laser. This phase-locking translates to an ideally infinite mutual coherence and accentuates their potential for quantum interference applications [162]. In well-isolated experimental systems, such as trapped atoms and ions, this mutual coherence was observed via an optical heterodyning technique [163], which allowed studying the broadening of elastic scattering due to motional and vibrational dynamics [164; 165], when the species are driven by a single frequency laser. The effect of environment dynamics, apparent through spectral wandering for instance, can still limit the mutual coherence between the excitation laser and the photons generated in the Heitler regime: QD resonance shifts translate to phase shifts between the elastically scattered single photons and the excitation laser. Therefore, phase-sensitive heterodyning measurements to determine the extent to which phase-locking to the excitation laser occurs are necessary in order to determine the suitability of these photons as flying qubits.
Figure 6.1 a shows the experimental arrangement used to perform optical heterodyning measurements. QD resonance fluorescence at frequency ν superimposed

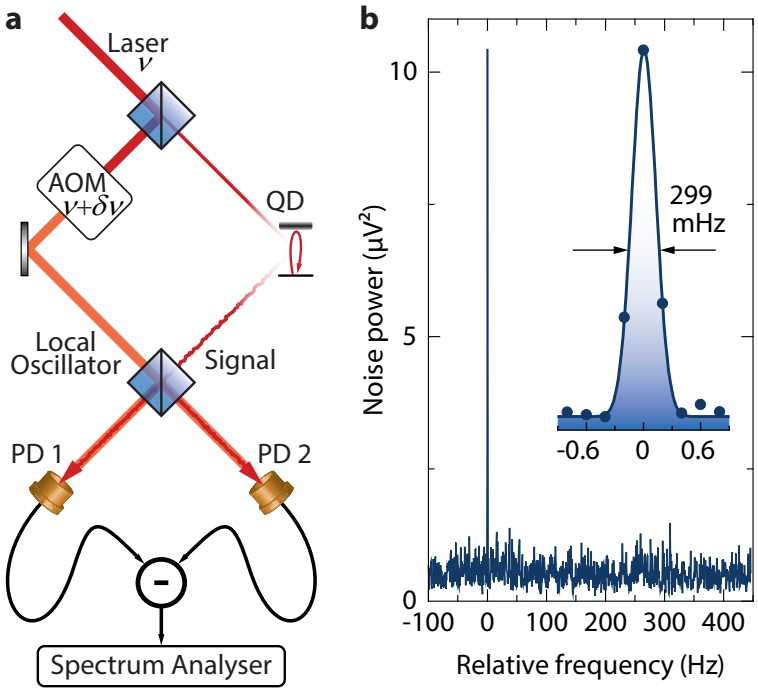

Figure 6.1: Mutual coherence between QD resonance fluoresence and the excitation laser. a, Illustration of the experimental arrangement used for optical heterodyning of QD resonance fluorescence. Acousto-optical modulation (AOM) provides the shift of the local oscillator frequency by $\delta\nu$ 210 kHz. The outputs of the two photodiodes (PD1,2) are subtracted electrically and sent to a spectrum analyser. b, Typical power spectrum of the beating signal as a function of frequency relative to $\delta\nu$. Inset: high-resolution spectrum for 5 s of continuous data acquisition. Spectra with sub-hertz resolution reveal phase coherence between QD photons and excitation laser on a timescale of seconds.

with a strong local oscillator originating from the excitation laser but shifted in frequency by $\delta\nu \sim 210$ kHz. This frequency difference results in a beat note in the difference signal of two balanced photodiodes (PD1,2). A spectrum analyser calculates the power spectrum via a fast Fourier transform (FFT) algorithm. The linewidth and the lineshape of the power spectrum reflect directly the phase stability, i.e. the mutual coherence, between the two fields during the course of the measurement. In particular, periodic dynamics of the relative phase appear as sidebands and aperiodic fluctuations appear as broadening of the spectrum. Figure 6.1 b displays a representative raw spectrum with a strong peak at the beating frequency. The inset shows that a Gaussian lineshape with a FWHM of 299 mHz fits the data of 5-second continuous acquisition. We note here that the spectral bandwidth is partly due to the the system response resolution of 200 mHz for the measurement settings and any external noise sources in the setup. Longer acquisition time yields higher spectral resolution, hence narrower linewidths (e.g. 172 mHz for 10-second acquisition time), but phase fluctuations induced by the mechanical instability of the setup (and any spectral diffusion) reduce the signal quality and limit the obtainable linewidth.
Nevertheless, even these raw linewidths indicate that every photon is phase-locked to the excitation laser with mutual-coherence time exceeding 3 seconds, which corresponds to a mutual-coherence length of one million kilometres. These results confirm the prediction for an ideal two-level system that each photon inherits fully the coherence properties of the excitation laser in this alternative photon generation process. The absence of significant linewidth broadening in this measurement confirms that the main contribution to spectral diffusion for our sample (and this QD) occurs on timescales of seconds or slower.

6.3 Photon shaping

Methods currently available to control single photon wavepackets include direct spectral filtering of the photons [166] and phase [167] or amplitude [168; 169] manipulation via photon transmission through electro-optic elements. Wavepacket control during the photon generation process has only been achieved for trapped atoms inside optical cavities using multi-pulse sequences [170; 171].

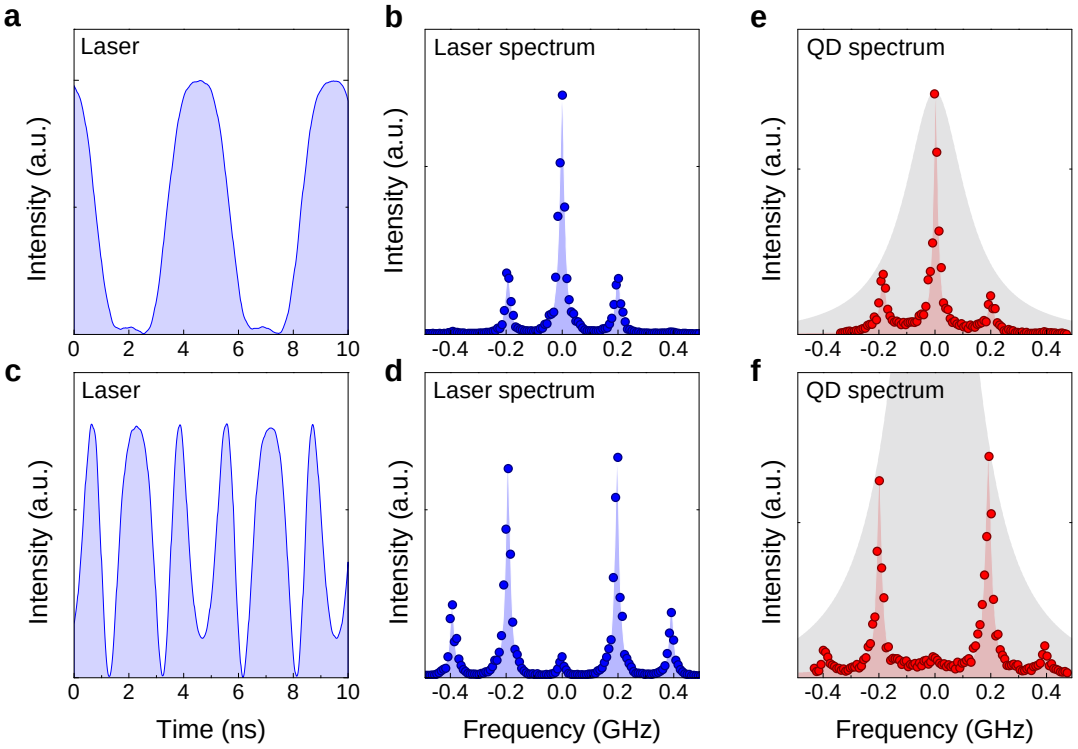

Figure 6.2: Tailoring waveforms of single photons. a, The intensity of the excitation laser is modulated in time using an electro-optic modulator driven with a 200-MHz sine wave. b, The spectrum of the modulated laser, measured through a FabryPerot cavity (resolution $\sim$ 20 MHz), shows sidebands at the modulation frequency. c, d, A different waveform modulation with the corresponding spectrum for the laser. This waveform is designed to suppress the spectral component at the original carrier frequency. e, f, Measured spectra of the QD photons generated from the two synthesized laser waveforms given in a, c, respectively. The elastically scattered photons replicate the laser spectrum within the linewidth of the transition, which is indicated by the shaded grey area.

The coherent nature of elastic scattering provides a means for coherent synthesis of single photon waveforms directly in the photon generation process without the need for spectral filtering or optical cavities. In order to demonstrate this ability, we use an electro-optic modulator (Jenoptik AM980) driven by a sine wave signal generator (Rohde & Schwarz SMF100A) to encode the excitation laser field. The throughput I of the EOM as a function of applied bias V_{bias} follows

$$I\left(V_{\text{bias}}\right) \propto \frac{1}{2}\cos\left(kV_{\text{bias}} + \phi_{\text{offset}}\right) + \frac{1}{2}, \tag{6.1}$$

where constant k relates the bias voltage to a phase shift of the cosine function and ϕ_{offset} determines the working point of the EOM. Consider driving the EOM with a sine wave of frequency ν_{mod} and amplitude A. The intensity modulation of the laser is then given by

$$I\left(t\right) \propto \frac{1}{2}\cos\left(kA\sin\left(\nu_{\text{mod}}t\right) + \phi_{\text{offset}}\right) + \frac{1}{2} \tag{6.2}$$

Complex intensity patterns can be generated with when the amplitude of the modulation exceeds the π-Voltage of the modulator: $kA > \pi$. The resulting spectrum is given by the Fourier transform of the first-order correlation function of the output field of the EOM.

Figure 6.2 presents two examples of coherent control of single photon waveforms by this technique. The first example of a synthesized laser waveform and the corresponding spectrum are displayed in panels a and b, respectively. The temporal measurement in panel a is performed using a photodiode with 8-GHz bandwidth, while the spectrum in panel b is measured using the scanning Fabry-Perot interferometer. The amplitude modulation of the laser in time gives rise to sidebands in the spectrum at the modulation frequency of 200 MHz. Panels c and d display another example for encoding the laser field with a more complicated pattern. The amplitude of the applied modulation is greater than the π-Voltage and in the resulting spectrum the component at the carrier frequency (zero detuning) is strongly suppressed.

The single photon QD emission spectra for the two examples are presented in panels e and f. The 200-MHz spectral spacing and the relative strength of the

frequency components are dictated by the laser spectrum for each example, in addition to being weighted by the QD transition linewidth. The radiative linewidth (250 MHz) is indicated as gray shaded areas in panels e and f for comparison[1]. In both cases (Fig. 6.2 e,f), antibunching in the intensity-correlation measurements is fully sustained. We note that while these examples are based on amplitude modulation of the laser field, encoding phase to each spectral component is possible in this scheme.

These measurements demonstrate that, as a consequence of their mutual coherence with the laser field, the single photon waveforms can be synthesized deterministically without post-generation filtering which can lead to photon loss and degradation of the single photon quality. The accessible bandwidth for waveform synthesis is restricted only by the mutual coherence for low frequencies, and the QD transition linewidth for high frequencies.

6.4 Photon indistinguishability

A key requirement of a photonic link in a quantum network is the ability to create time-synchronised indistinguishable single photons from separate sources. However, the uncorrelated environment fluctuations experienced by separate QDs under nonresonant excitation lead to variations in temporal and spectral overlap of photon wavepackets [161; 172; 173]. Imparting mutual coherence on independent photons via a common excitation laser can therefore be a crucial advantage in achieving indistinguishable wavepackets. Therefore, we perform Hong-Ou-Mandel style two-photon interference [174] experiments of two QD photons scattered from the same QD at different times to quantify the indistinguishability of synthesised photon waveforms with complex spectra. We note that in all interference measurements that follow, the QD fluorescence is spectrally filtered via a 1600 grooves per millimeter grating to remove the phonon sideband.

A schematic of the experimental setup is shown in Fig. 6.3 a. Figure 6.3 b displays the laser pulse train (top panel) used to generate coherent QD photons in the Heitler regime (bottom). The laser pulses are derived from a continuous

[1]We note that the measured QD spectrum is broadened by spectral diffusion beyond the radiative limit.

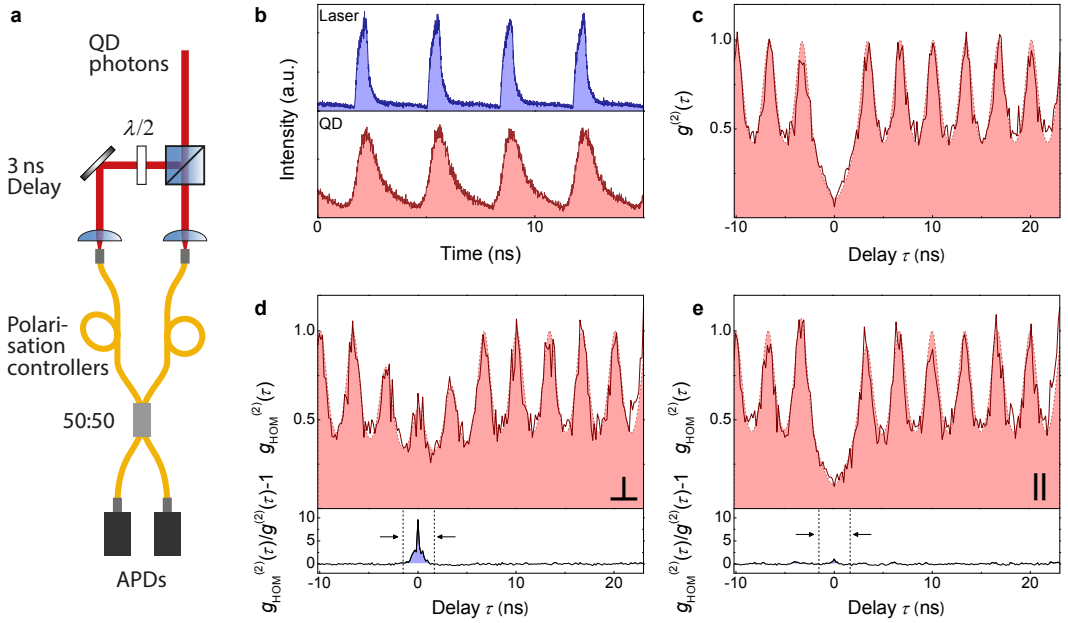

Figure 6.3: Indistinguishability of waveform-synthesised photons. a, Illustration of the experimental setup for two-photon interference from a single QD. b, Time-synchronised single QD photons (bottom panel) are generated by exciting the QD transition with laser pulses of 500-ps width and 300-MHz repetition rate (top panel). c, The intensity autocorrelation function for QD photons is recorded in a Hanbury-Brown and Twiss setup. A two-photon probability per pulse below 5% demonstrates the quantum nature of the emitter. d,e Two-photon interference measurements for QD photons of orthogonal (d) and parallel (e) polarisation. The bottom panels display the normalised differences to the intensity autocorrelation in c, respectively. The lack of two-photon interference for orthogonally polarized photons in d gives rise to coincidences at zero time delay, yielding a peak in the bottom panel. For photons of parallel polarisation, the absence of coincidences around zero time delay reflects successful two-photon interference in e. The ratio of the areas in the bottom panels yields a raw visibility of 0.926. Experimental data in ce are shown as continuous dark red curves, while a simulation for each case based on system parameters is shaded in light red. The data are recorded in 162-ps time bins with 600-ps timing resolution.

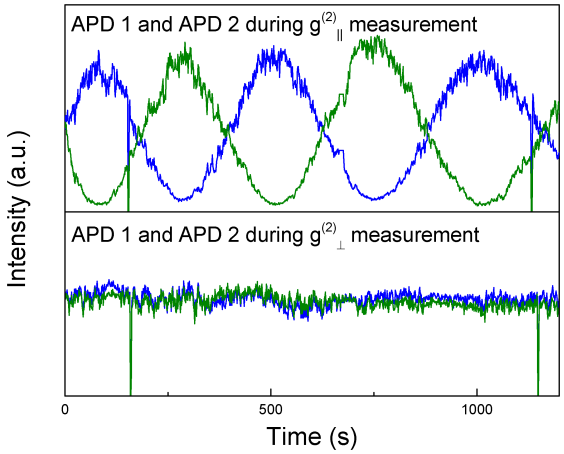

Figure 6.4: First-order interference in the Hong-Ou-Mandel interferometer. We monitor single photon detection events during the Hong-Ou-Mandel experiment. Top panel: First-order interference occurs for coherent QD photons as a consequence of varying phase difference between both interferometer arms. The contrast of first-order interference quantifies the fraction of coherently scattered QD emission. Bottom panel: The time traces of detection events for photons of orthogonal polarisation stay nearly constant, as photons are distinguishable in their polarisation. The QD transition is shifted out of resonance periodically via DC Stark effect to monitor the background counts. This is visible as abrupt drops in intensity.

wave laser by modulating the EOM transmission with independent control on the duration and the repetition rate. Here, the laser pulses are 500-ps long with a repetition rate of 300 MHz. For these settings the temporal response of the QD transition is visible as an exponential tail in the coherent conversion of laser pulses into single photons[1]. Before we describe the two-photon interference measurements in detail we want to confirm that the the pulsed single photon stream predominantly consists of coherent scattering.

First-order interference in the Hong-Ou-Mandel interferometer. In addition to the coincidence events that manifest the two-photon interference we also record the individual detection events on both avalanche photodiodes (APDs) (see Fig. 6.3 a). Figure 6.4 presents two 1200-s long measurement of the single-photon detections of pulsed QD fluorescence on the two APDs. The top panel

[1] As an aside, it may be interesting to create photons with the Gaussian or double-exponential waveforms, which can improve the excitation probability [175].

corresponds to the case where the photons in both interferometer arms have the same polarisation, while the bottom panel shows a detection time trace for photons of orthogonal polarisation. In the former case, the single-photon count rate shows signatures of first-order interference. This is due to the phase fluctuations between both interferometer arms as the path lengths vary slowly over time due to mechanical wandering and slight changes in ambient temperature[1]. This first-order interference is strongly suppressed, as it should be, for photons of nominally orthogonal polarisation in the bottom panel. The contrast of first-order interference quantifies the fraction of coherently scattered QD emission F_{coh} which is $F_{\mathrm{coh}} \approx 0.92$ for the data in Fig. 6.4.

Two-photon interference Figure 6.3 c shows the measured intensity-correlation function $g^{(2)}(\tau)$ for these photons. The missing peak at zero time delay in coincidence detection evidences strong antibunching. For pure photonic states, a Hong-Ou-Mandel-style two-photon interference measurement in the vicinity of zero time delay is expected to follow

$$g^{(2)}_{\mathrm{HOM}}(\tau) = \left(t_1^2 + r_1^2\right) g^{(2)}(\tau) + 2 r_1 t_1 \left(1 - \eta + \eta g^{(2)}(\tau)\right) , \tag{6.3}$$

where t_1 and r_1 are the transmission and reflection coefficients of the first beamsplitter used to form the two input arms of the second beam splitter (cf. Fig. 6.3 a). The variable η quantifies the photon indistinguishability including any imperfections of the measurement apparatus. For fully indistinguishable ($\eta = 1$) photons $g^{(2)}_{\mathrm{HOM}}(\tau)$ reduces to $g^{(2)}(\tau)$, while for fully distinguishable ($\eta = 1$) photons Eq. (6.3) takes the form $g^{(2)}_{\mathrm{HOM}}(\tau) = (t_1^2 + r_1^2)\, g^{(2)}(\tau) + 2 r_1 t_1$. We use the polarisation of the input photons as means to vary η , such that parallel (orthogonal) polarisation leads to a maximum (minimum) value for η. These measurements, performed in conditions identical to those of Fig. 6.3 c , are shown in panels 6.3 d and 6.3 e for orthogonal and parallel input polarisation states, respectively.
In order to quantify the two-photon interference fidelity we compare the data

[1]Further, for the purpose of data calibration the QD transition was periodically shifted out of resonance with respect to the exciting laser, so that the background counts due to detector dark counts and laser leakage were recorded. This is visible as sharp drops in intensity in the data

directly with the ideal case of $g^{(2)}_{\mathrm{HOM}}(\tau) = g^{(2)}(\tau)$: the bottom panels of Fig. 6.3 d and e show

$$\frac{g^{(2)}_{\mathrm{HOM}}(\tau) - g^{(2)}(\tau)}{g^{(2)}(\tau)}$$

for their respective interference measurement. Integrating the normalised difference curves for both polarisation cases over one repetition period (~ 3.3 ns) centred around zero time delay, we can extract a raw contrast of the two-photon interference of $C_{\mathrm{HOM}} = 1 - \left(A_{\parallel}/A_{\perp}\right) = 0.926 \pm 0.016$.

The raw contrast of the two-photon interference constitutes a lower bound to photon wavepacket indistinguishability, as the measurement is affected by imperfections of the setup. In our case these include polarisation degradation in the single mode fibre beamsplitter and an imbalance of beamsplitter coefficients. The conventional treatment of these imperfections [159; 176] assumes that the photon coherence time τ_c is much shorter than the time delay in the interferometer, $\tau_c \ll \Delta t_{\mathrm{delay}}$. The expected interference contrast is then

$$C_{\mathrm{HOM}} = 1 - \frac{A_{\parallel}}{A_{\perp}} = 1 - \frac{2r_2 t_2 p_{\parallel}(D-1) + r_2^2 + t_2^2}{2r_2 t_2 p_{\perp}(D-1) + r_2^2 + t_2^2} \tag{6.4}$$

where D is the distinguishability of photon pairs. Experimentally we measure the fraction $A_{\parallel}/A_{\perp}$ then determine $1-D$, knowing the values and error estimates for all parameters involved in Eq. (6.4). For the data in Fig. 6.3 we obtain a corrected contrast of unity within the experimental uncertainty ($C_{\mathrm{cor}} = 1.03 \pm 0.05$). For coherently scattered photons the correction for the interferometer imperfections is not straightforward as their coherence time exceeds the interferometer time delay, therefore we choose to correct only for the polarisation mismatch which affects coherent and incoherent photons in the same way. The expected interference contrast then yields

$$C_{\mathrm{HOM}} = 1 - \frac{A_{\parallel}}{A_{\perp}} = 1 - \frac{1 - p_{\parallel} + Dp_{\parallel}}{1 - p_{\perp} + Dp_{\perp}}. \tag{6.5}$$

This lower bound on photon wavepacket indistinguishability evaluates to 0.96 ± 0.04 and is still higher than all indistinguishabilities reported for non-resonantly generated QD photons. He *et al.* obtained similar interference visibilities for

resonantly generated incoherent photons recently [177]. We stress that the lack of correlation between the environment dynamics of multiple QDs will inevitably lead to the degradation of photon indistinguishability for the incoherently generated photons, while the coherent generation process reported here offers some protection from such effects.

6.5 Chapter discussion and outlook

We have demonstrated the generation of fundamentally indistinguishable, coherent single photons from a solid-state quantum emitter with a high degree of control and flexibility in waveform synthesis. These phase-locked photons are ideally suited for quantum interference applications, which form the basis of quantum communication [162], linear optics quantum computation [98; 120], and distant entanglement schemes [156; 157]. The price to pay for this unprecedented photon quality is excitation efficiency. To obtain a coherent fraction of about 0.9 in pulsed excitation, photons are probabilistically generated with 5-10% efficiency (1.5-3 $\cdot 10^7$ Hz for the two-photon interference measurements presented here).
While generation rates are lower than those achievable in deterministic excitation schemes, the trade-off between photon rates and photon quality is well justified for two main reasons: first, quantum interference applications can work well with probabilistic gates [157; 178], while the low photon quality reported so far [161; 173] rules out the use of QD photons in quantum information applications. Further, non-unity photon collection and detector efficiencies evidently render any measurement-based schemes probabilistic. Second, an entanglement rate scaling with the two-photon detection efficiency [157] is replaced advantageously by one-photon detection [156; 162] utilising the first-order coherence of the coherently scattered photons.
The technique presented in the work is not limited to QDs and can be extended to other quantum systems in the optical domain as well as to superconducting circuits in the microwave domain.

One next immediate step in the direction of a quantum network is to extend the two-photon interference to two independent quantum dots. We have attempted

this measurements, in fact before measuring the two-photon interference presented in this chapter. Raw visibilities in the pulsed experiment around 40% were obtained, however, without filtering the phonon sideband and limited polarisation control. The main reason the experiment was not pursued further was that the second QD sample showed strong spectral diffusion and blinking (due to the high QD density). Correcting for the experimental imperfections gave a lower bound on photon indistinguishability of $> 70\%$, but was not reported due to the experimental imperfections. We note that Konthasinghe *et al.* have reported on continuous-wave two-photon interference from two independent QDs under resonant excitation recently [179]. In the presence of strong spectral diffusion they obtain a two-photon visibility around 40%.

Chapter 7

Single-shot readout of the electron spin

In this chapter we discuss the dynamics of few spins confined to a pair of vertically stacked QDs. The electronic levels of the two QDs can be tuned into resonance so that tunnel coupling leads to the development of molecular states. We demonstrate how transitions into these molecular states can be used to monitor the spin projection of a single electron confined to one of the QDs. This chapter is based on [111].

In the first part of this chapter we explain how spectroscopy of QD molecules (QDMs) can be linked to electron tunnel coupling in various spin and charge configurations. In this context the detailed energy level structure for the case of a single electron confined to one QD and a neutral exciton transition in the other QD is derived and compared to measurements. The concept of spin readout by recycling a molecular transition is picked up: We investigate if there are any obvious shortcomings to using the transition to the molecular $T_{+1/2}$ state as readout channel. In the second part time-averaged and time-resolved measurements demonstrate the conditionality of the molecular transitions on the single electron spin state and we show that spin dynamics can be monitored in real-time. The fidelity of the spin readout is discussed.

Despite being the last experimental chapter of this thesis, the work was actually done first (2009-2010). As such, both the photon collection efficiency and the

suppression of laser background for resonance fluorescence for the measurements presented here are somewhat worse than the performance described in earlier chapters. In the final part of this chapter we extrapolate from the measured spin readout fidelities to fidelities potentially afforded by the improved collection efficiency and background suppression. I also note that measurements were devised, performed and analysed in a strong collaboration with Chao-Yang Lu and Dr Nick Vamivakas who share equal credit for the results. I also acknowledge the contribution of Yong Zhao whose calculations on QDM energy level served as a model for those I present in this chapter. Antonio Badolato and Stefan Fält grew the sample.

7.1 Why quantum dot molecules?

We may remember from the QD level structure discussion and the summary on coherent QD spin control schemes in Chapter 1 that spin state readout is a bottleneck for single spin qubits in optically active QDs: Fast optical initialisation and manipulation on the one hand and reliable readout on the other hand cannot be realised at the same time in this system. Our approach is to decouple the two parts using a tunnel-coupled quantum dot molecule. With a single electron resident in one QD of the pair while the other QD is empty we expect optical transitions into four different molecular states (see Fig. 7.1) when an exciton is added in the empty QD. The nomenclature for ground and excited states is explained in the figure caption. Transitions of the single electron charged QD, denoted 'host' QD, can be used for state initialisation via optical pumping as discussed before, whereas the transitions to molecular states via the second QD, denoted 'readout' QD, are reserved for readout. Under magnetic field the four molecular transitions are separated in energy, and backaction effects on the host electron spin should be strongly reduced compared to the single QD case. Previous research by Kim *et al.* [180] has shown in time-averaged measurements that the transition to the $T_{+1/2}$ state is robust against spin pumping and conditional on the host spin state.

Our aim is to perform real-time spin readout by observing intermittent resonance fluorescence from the $1 \rightarrow T_{+1/2}$ transition. For ions, intermittent resonance fluo-

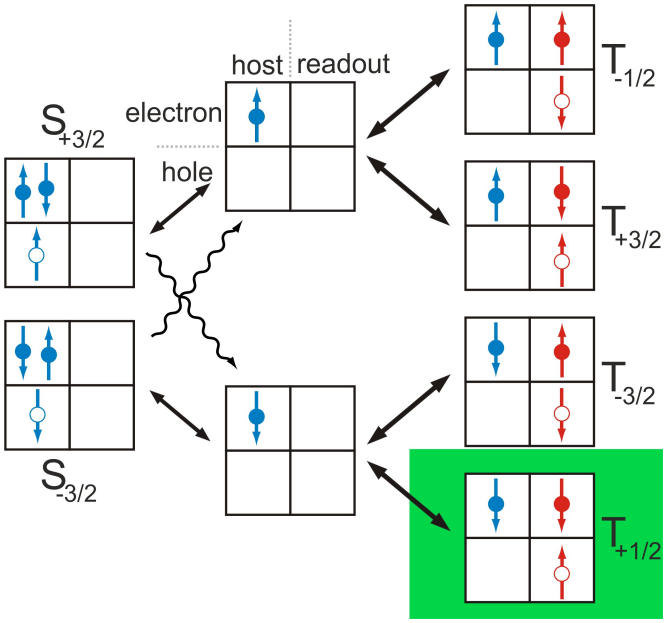

Figure 7.1: Cartoon of the ground and excited states of the QDM. The left (right) half of each square shows charges in the host (readout) QD where top (bottom) squares contain electrons (holes). Double-ended arrows denote optical transitions, single-ended arrows show weak decay channels. The single electron ground states are labeled 0 and 1, the 'atomic' trion states in the host QD are $S_{+3/2}$, $S_{-3/2}$ (electrons in singlet state) and the molecular states are denoted T_x. Subscripts give the total angular momentum in each case.

rescence has revealed quantum jumps back in 1986 already [181; 182; 183] and it was later observed for other systems [184]. The $1 \rightarrow T_{+1/2}$ transition is expected to be a robust recycling transition and the suitability of this transition as readout channel for the host electron spin will be investigated.

7.2 Quantum dot molecule sample

The sample is a Schottky diode heterostructure (see Fig. 7.2) with two InAs QD layers separated by 13 nm (separation of bottom of the first wetting layer to bottom of the second wetting layer). The distance to the ohmic contact is 30 nm, and the length between the ohmic and Schottky gate is 200 nm. Growth conditions are such that the energy levels in the readout QD (marked red in the sketch) are redshifted in comparison to levels in the host QD (blue). Electron

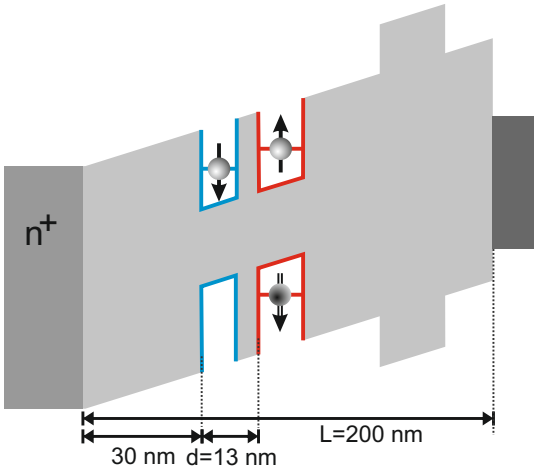

Figure 7.2: Dimensions of the sample.

tunneling in the configuration of a single electron in the host QD and an exciton in the readout QD is possible by tuning the gate voltage. Hole energy levels in the two QDs are far detuned so that hole tunneling does not occur.

7.3 Quantum dot molecules

Tunnel-coupling between QDs shows characteristic signatures in photoluminescence spectra, most prominently avoided crossings, or anticrossings [185]. These avoided crossings are a result of hybridisation of the two energy levels that are brought into resonance. Detailed (magneto-)photoluminescence studies have been published, identifying which charge and pin configurations in the QDM are involved in tunneling at each of the observed anticrossings [27; 185; 186; 187].

Fig. 7.3 shows a PL-gate voltage map of the host (a) and the readout QD (b). The magnitude of the anticrossings give information about the strength of the tunnel coupling for the charge states involved. While we extract values for exchange splittings and tunnel coupling from these PL maps we rely on the resonant high-resolution differential transmission (DT) to identify optical transitions and their respective ground states unambiguously.

Before moving on to the DT measurements and theoretical modelling we briefly discuss the simplest case that can give rise to an anticrossing, a single electron

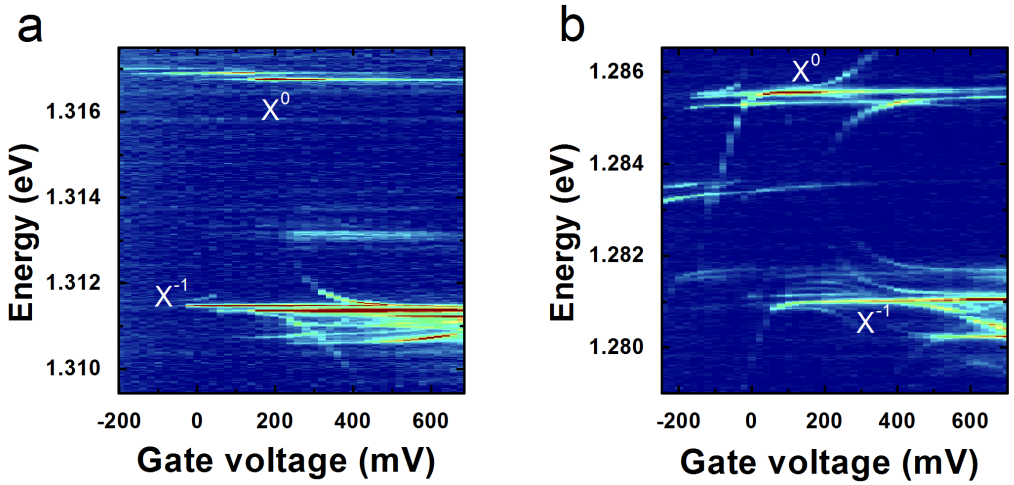

Figure 7.3: PL map of the the host QD (a) and readout QD (b). Neutral exciton and trion emission lines have been indicated.

in the QDM, to obtain some intuition for the more complex cases. We define the basis states of the system as the electron being in the host QD ($|1\rangle$) and the electron being in the readout QD ($|2\rangle$):

$$|1\rangle = e^{\dagger}_{\text{host}} |0\rangle$$
$$|2\rangle = e^{\dagger}_{\text{readout}} |0\rangle ,$$

where $e^{\dagger}_{\text{QD}}$ is the fermionic creation operator for an electron in the QD defined in the subscript and $|0\rangle$ denotes the vacuum state. The energy levels for the two states can be tuned into resonance by changing the gate voltage. We relate the energy difference δE between the two levels to the gate voltage and sample dimensions:

$$\delta E = \frac{e\,(V_0 - V_g)}{L} d + \delta E_0, \tag{7.1}$$

where V_0 is the offset of the conduction band edge and the Schottky contact at zero bias, L is the distance between the gates, d is the distance of charges in the host QD to charges in the readout QD (cf. Fig. 7.2). δE_0 provides a constant offset. We designate state $|1\rangle$ to be the energy reference: as we are only interested in the relative energies we subtract the single particle energy and only state $|2\rangle$ depends linearly on the applied gate voltage. The matrix tunneling element

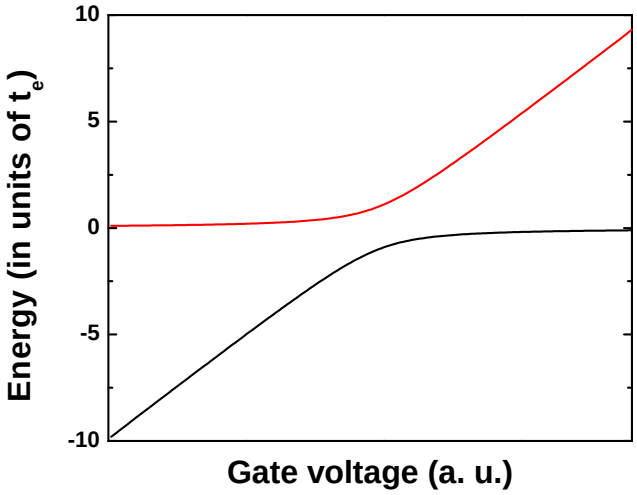

Figure 7.4: Energy levels for a single electron in a tunnel-coupled QDM.

is given by $t_e = \langle \phi_{\text{host}} | \mathbf{h} | \phi_{\text{readout}} \rangle$, where ϕ_{host} and ϕ_{readout} are the orthonormal wavefunctions of the electron in state $|1\rangle$ and $|2\rangle$, respectively, and $\mathbf{h}$ is the single-particle Hamiltonian. The Hamiltonian for the coupled system is then

$$H_{1\text{e}} = \begin{pmatrix} 0 & t_e \\ t_e & \delta E \end{pmatrix}. \tag{7.2}$$

Solving for the eigenvalues we obtain energies $E_{1,2}$

$$E_{1,2} = \frac{\delta E}{2} \pm \frac{1}{2}\sqrt{\delta E^2 + 4t_e^2} \tag{7.3}$$

The energies (7.3) are plotted in Fig.7.4 The anticrossing is $2t_e$ in magnitude.

7.4 Quantum dot molecule spectroscopy

We are interested in the gate voltage regime where the QDM ground state is given by a single electron in the host QD, and the QDM excited state has an exciton added in the readout QD.

Here, we present a calculation of the QDM's electronic states and optical tran-

sition energies relevant for our readout scheme. We compute the dependence of the energies on gate voltage and external magnetic field and compare the simulation to our measured DT maps. In the model we choose basis states that are eigenstates in the limit of weak electron-hole exchange and no tunnel coupling between the host and readout QD. As we will see later this choice of basis comes rather close to the actual set of eigenstates under high magnetic fields. The numerical model allows us to make a statement about the 'purity' of the readout state $T_{+1/2}$, and hence possible errors in the readout scheme. The effects of state mixing, e.g. due to heavy-light hole mixing, can be discussed in this context as well.

The QDM ground state consists of a single electron in the host QD whereas the excited states consist of two electrons and one hole within the two QDs. In the excited state the two electrons occupy the lowest orbital levels and can both reside in the same QD or one electron can be in each dot. For our model (and sample) the heavy hole is localized in the readout QD. From the DT spectroscopy (see Fig. 7.5) it is obvious that tunnel coupling takes place in the excited states, so we consider the following 12 excited states of two electrons and one hole:

$$
\begin{aligned}
|1\rangle &= e^\dagger_{\mathrm{host}\uparrow} e^\dagger_{\mathrm{host}\downarrow} h^\dagger_{\mathrm{readout}\Uparrow} |0\rangle & \qquad |7\rangle &= e^\dagger_{\mathrm{host}\uparrow} e^\dagger_{\mathrm{host}\downarrow} h^\dagger_{\mathrm{readout}\Downarrow} |0\rangle \\
|2\rangle &= e^\dagger_{\mathrm{readout}\uparrow} e^\dagger_{\mathrm{readout}\downarrow} h^\dagger_{\mathrm{readout}\Uparrow} |0\rangle & |8\rangle &= e^\dagger_{\mathrm{readout}\uparrow} e^\dagger_{\mathrm{readout}\downarrow} h^\dagger_{\mathrm{readout}\Downarrow} |0\rangle \\
|3\rangle &= e^\dagger_{\mathrm{host}\uparrow} e^\dagger_{\mathrm{readout}\downarrow} h^\dagger_{\mathrm{readout}\Uparrow} |0\rangle & |9\rangle &= e^\dagger_{\mathrm{host}\uparrow} e^\dagger_{\mathrm{readout}\downarrow} h^\dagger_{\mathrm{readout}\Downarrow} |0\rangle \\
|4\rangle &= e^\dagger_{\mathrm{host}\downarrow} e^\dagger_{\mathrm{readout}\uparrow} h^\dagger_{\mathrm{readout}\Uparrow} |0\rangle & |10\rangle &= e^\dagger_{\mathrm{host}\downarrow} e^\dagger_{\mathrm{readout}\uparrow} h^\dagger_{\mathrm{readout}\Downarrow} |0\rangle \\
|5\rangle &= e^\dagger_{\mathrm{host}\uparrow} e^\dagger_{\mathrm{readout}\uparrow} h^\dagger_{\mathrm{readout}\Downarrow} |0\rangle & |11\rangle &= e^\dagger_{\mathrm{host}\uparrow} e^\dagger_{\mathrm{readout}\uparrow} h^\dagger_{\mathrm{readout}\Uparrow} |0\rangle \\
|6\rangle &= e^\dagger_{\mathrm{host}\downarrow} e^\dagger_{\mathrm{readout}\downarrow} h^\dagger_{\mathrm{readout}\Downarrow} |0\rangle & |12\rangle &= e^\dagger_{\mathrm{host}\downarrow} e^\dagger_{\mathrm{readout}\downarrow} h^\dagger_{\mathrm{readout}\Uparrow} |0\rangle
\end{aligned}
$$

Here $(e,h)^\dagger_{\mathrm{dot},\sigma_z}$ is the fermionic creation operator for an electron (e) or a hole (h) in host or readout dot, with spin projection σ_z. States $|1\rangle$, $|2\rangle$, $|7\rangle$, $|8\rangle$ are the only configurations with two electrons in the same dot. The electrons are in a spin-singlet state in these cases; triplet states are far removed in energy and do not take part in any interactions. The states $|4\rangle$, $|6\rangle$, $|9\rangle$, $|11\rangle$ are 'dark', whereas the states $|3\rangle$, $|5\rangle$, $|10\rangle$, $|12\rangle$ are 'bright'.
The Hamiltonian we consider is:

$$H = H_{\text{particle}} + H_{\text{Coulomb}} + H_{\text{exchange}} + H_{\text{tunnel}} \tag{7.4}$$

For the purpose of a numerical solution we note

1. H_{particle} is the sum of single particle energies. The absolute energies of two electrons and one hole in the potential of the quantum dot molecule in different spin configurations are very similar, so we choose the configuration with all charges in the readout dot (states $|2\rangle$ and $|8\rangle$) as reference energy and calculate energies relative to the reference. This reference is set in the absence of Coulomb and exchange interactions and does not change with applied gate voltage.

2. The Coulomb terms for two particles a and b are defined as before (Eq. (1.1)). We reduce the Coulomb interactions to four terms. The subscripts denote which charges are considered and if the interaction is direct (both particles in the same dot) or indirect (in separate dots). Values can be estimated from photoluminescence (PL) maps and found in the literature [185; 187; 188; 189]:

$$\begin{aligned} V_{ee,\text{direct}} &\approx 20\text{meV} \\ V_{ee,\text{indirect}} &\approx 10\text{meV} \\ V_{eh,\text{direct}} &\approx -24\text{meV} \\ V_{eh,\text{indirect}} &\approx -10\text{meV} \end{aligned}$$

3. Exchange interaction is defined in Eq. (1.3). Two of the three terms for electron-hole exchange can be deduced from spectroscopic data. The isotropic exchange splitting between dark and bright excitons can be extracted from the PL map in Fig. 7.3 to be $\delta_0 \approx 220\ \mu$eV. The anisotropic exchange δ_1 can be measured from the DT spectrum in Fig. 7.5a when the host QD is charged with two electrons and hence in a spin singlet configu-

ration. Then the host QD spins do not take part in exchange interactions and we measure $\delta_1 \approx 17.6$ μeV. The dark exciton splitting δ_2 is not visible in photoluminescence measurements, but expected to be of the same order as δ_1. The interdot electron-electron exchange J_{ee} is very small, from [185] we estimate it to be ~ 1 μeV. It couples states $|3\rangle$ to $|4\rangle$ and $|9\rangle$ to $|10\rangle$.

4. Tunnel coupling takes place between states $|1\rangle$, $|2\rangle$ and $|3\rangle$, $|4\rangle$ and between $|7\rangle$, $|8\rangle$ and $|9\rangle$, $|10\rangle$. The magnitude can be extracted from the PL maps and is $t_e \approx 330$ μeV for this QDM.

   Lastly, changing the gate voltage shifts the detuning δE between electron energy levels in the host dot and readout dot, enabling electron tunneling. Expressing the Hamiltonian of Eq. (7.4) in the basis $|1\rangle$-$|12\rangle$ block diagonalizes the Hamiltonian into 2 blocks. One block couples states $|1\rangle$-$|6\rangle$ and the other couples states $|7\rangle$-$|12\rangle$ [1]. Eq. (7.5) is the Hamiltonian matrix for states $|1\rangle$-$|6\rangle$ (the block for states $|7\rangle$-$|12\rangle$ is essentially the same).

$$H_{|1\rangle-|6\rangle} = \begin{pmatrix} -2\delta E + V_1 & 0 & t_e & -t_e & 0 & 0 \\ 0 & V_2 & t_e & -t_e & 0 & 0 \\ t_e & t_e & -\delta E + V_3 + \delta_0 & J_{ee} & \delta_1 & 0 \\ -t_e & -t_e & J_{ee} & -\delta E + V_4 - \delta_0 & 0 & \delta_2 \\ 0 & 0 & \delta_1 & 0 & -\delta E + V_5 + \delta_0 & 0 \\ 0 & 0 & 0 & \delta_2 & 0 & -\delta E + V_6 - \delta_0 \end{pmatrix} \tag{7.5}$$

Due to space constraints placeholders were used instead of the full Coulomb

[1] D. Kim et al. [180] observe another anticrossing in the excited state level structure where coupling between states $|5\rangle$ and $|9\rangle$ occurs. We see the same effect in other dot pairs, but for this particular one it happens at magnetic fields outside the range of data presented. A phenomenological term (2 μeV) has been included in the final Hamiltonian.

matrix elements:

$$
\begin{aligned}
V_1 &= 2V_{eh,\text{indirect}} + V_{ee,\text{direct}} \\
V_2 &= 1V_{ee,\text{direct}} + 2V_{eh,\text{direct}} \\
V_3 &= V_{eh,\text{direct}} + V_{eh,\text{indirect}} + V_{ee,\text{indirect}} \\
V_4 &= V_{eh,\text{indirect}} + V_{eh,\text{direct}} + V_{ee,\text{indirect}} \\
V_5 &= V_{eh,\text{direct}} + V_{eh,\text{indirect}} + V_{ee,\text{indirect}} \\
V_6 &= V_{eh,\text{direct}} + V_{eh,\text{indirect}} + V_{ee,\text{indirect}}
\end{aligned}
$$

Diagonalising the Hamiltonian we determine both the eigenenergies and eigenstates as a function of gate voltage and magnetic field which we then compare with the measured data.

Fig. 7.5 presents differential transmission (DT) spectra of the host and readout QD optical transitions as a function of gate voltage at zero external magnetic field. The top panel displays the trion transition of the host QD where the labels 0e/1e/2e denote the ground state charge configurations and the vertical dashed lines indicate the 1-electron ground state range. The bottom panel gives the transition map for the readout QD in the same gate voltage range. Throughout the relevant gate voltage range the readout QD remains uncharged. The voltage dependence of the splitting between the two optical transitions indicates tunnel coupling between host and readout QD. Signs of the avoided crossing are only visible in the readout QD spectrum, so the tunnel coupling takes place between the exciton electron and the host dot electron, as assumed in the calculation. In Fig. 7.5 b we present the calculated level structure by diagonalising Eq. (7.5) near the anticrossing. The linear Stark shift common to all lines in the measured spectrum has been neglected in the simulation. The five lines show the evolution of the doubly degenerate eigenenergies with applied gate voltage (the two eigenenergies not shown in Fig. 7.5 b are higher in energy and take no part in the interactions in this gate voltage range). We can relate the transitions observed experimentally (Fig. 7.5 a) to the green and blue lines in the simulation. We

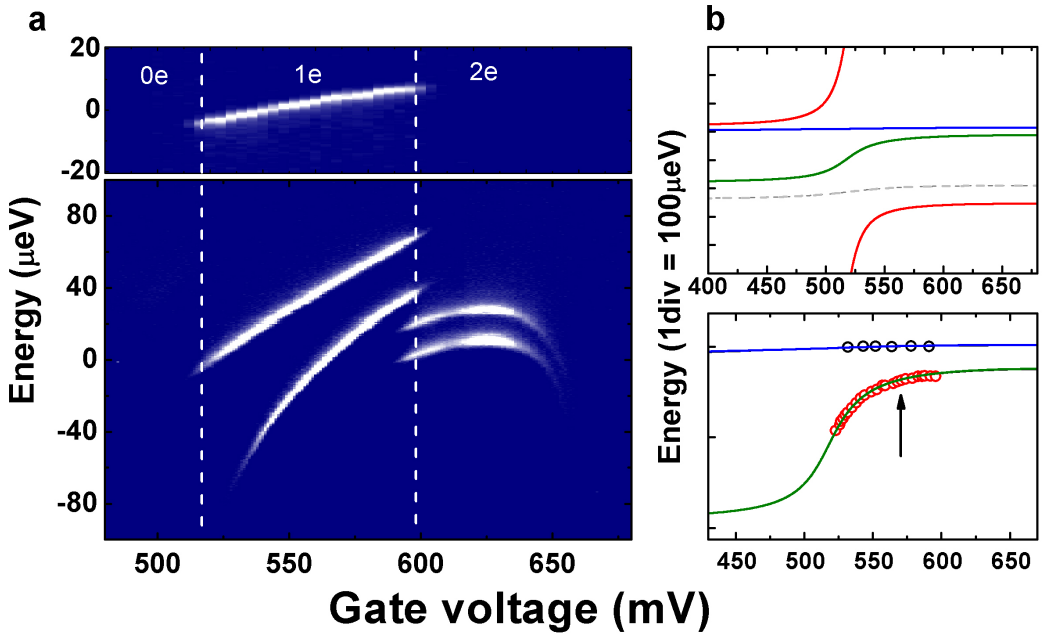

Figure 7.5: Transmission spectroscopy on the quantum dot molecule and calculated level structure. a, Transmission spectra for the QDM at zero magnetic field. The laser frequency is scanned for fixed gate voltages. The top panel shows the transmission spectrum for the host QD trion transition. The 0e/1e/2e labels denote the ground state charge configuration of the host. The bottom panel shows the transmission spectrum of the readout QD transitions. In the gate voltage range bounded by the vertical white lines the readout QD ground state is uncharged. **b, top panel** Calculated level structure for the QDM at zero magnetic field around the avoided crossing. The red lines correspond to the singlet-like spin configuration and anticross. The blue doublet passes through the avoided crossing unaffected and can be associated with the bright basis states with parallel electron spins ($T_{\pm}$-like), while the dashed grey line originates from the parallel electron spin dark states. The green line goes from dark to bright as it wiggles through the avoided crossing. It consists of basis states with antiparallel electron spins and has T_0-character. **b, bottom panel** Comparison of data from **a** to the simulation. The arrow indicates the gate voltage region where time-resolved measurements are performed later.

subtract the Stark shift from the data and compare simulation and experiment directly (Fig. 7.5 c). None of the other transitions show up in the spectrum as they are far detuned (red lines) and/or optically dark (grey lines).

A closer look at the evolution of the eigenvector reveals how we can understand the effect of tunnel coupling between two electrons in the presence of a hole. Going back to Fig. 7.5 b, the red line is the only one to show an anticrossing, which would be expected from a singlet state for a 2-electron system. The eigenvector at the lower gate voltage end is composed mostly of basis states $|3\rangle$ and $|10\rangle$, which are antiparallel spin combinations of one electron in each dot with opposite hole spins. Moving closer to the anticrossing the basis states with both electrons in the host dot ($|1\rangle$ and $|7\rangle$) are gaining importance. At the anticrossing the states $|1\rangle$,$|7\rangle$ and $|3\rangle$,$|10\rangle$ are roughly of equal strength and weakly admixed with the dark states $|4\rangle$ and $|9\rangle$. At even higher gate voltages (cut off in the figure) basis states $|1\rangle$ and $|7\rangle$ dominate. The lower red line shows reverse character. We associate this behaviour with a molecular singlet state modified by electron-hole exchange. Next, the blue line shows almost no dependence on gate voltage as it moves through the anticrossing, characteristic of a molecular triplet state. Its eigenvector is a combination of initially all bright basis states ($|3\rangle$,$|5\rangle$,$|10\rangle$,$|12\rangle$). $|5\rangle$ and $|12\rangle$ contribute the most, and around the anticrossing the eigenvector is almost entirely made up of the parallel electron spin combinations $|5\rangle$ and $|12\rangle$. The green line starts off as an admixture of all dark basis states ($|4\rangle$,$|6\rangle$,$|9\rangle$,$|11\rangle$). As it wiggles through the anticrossing region its composition changes to include the bright antiparallel spin basis states ($|3\rangle$,$|10\rangle$) at the expense of the dark parallel spin ones ($|6\rangle$,$|11\rangle$). On the higher gate voltage side of the avoided crossing the bright states $|3\rangle$,$|10\rangle$ dominate, reminiscent of a T_0 triplet in the 2-electron case. The lower grey dashed lines are very similar in nature to the green line at low gate voltages: they are combinations of all dark states. For gate voltages above the avoided crossing only the contributions from the dark parallel spin states ($|6\rangle$,$|11\rangle$) remain. In the comparison to the two-electron case the green and grey lines represent $T_\pm$ states and do not take part in the tunnel coupling.
We move on to discuss the magnetic field dependence in Faraday geometry of the bright QDM transitions relevant for the readout scheme (green and blue line

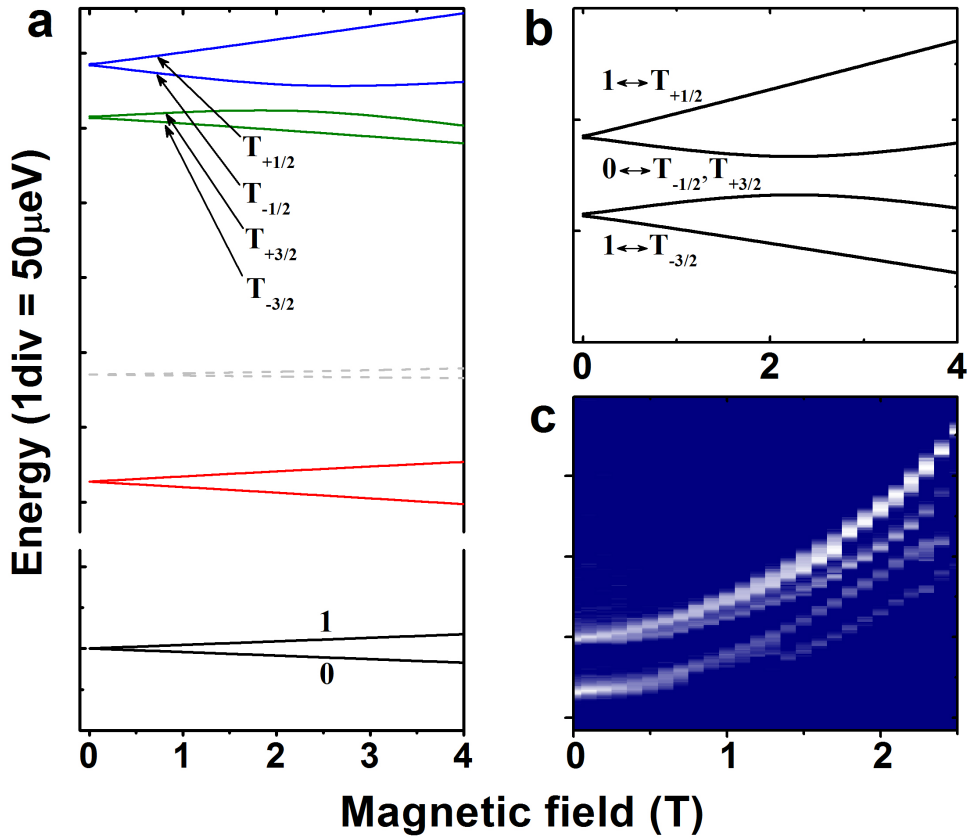

Figure 7.6: Energy levels and QDM optical transitions as a function of magnetic field. a, Evolution of eigenenergies with magnetic field at the gate voltage marked by the arrow in Fig. 7.5 c. The degeneracy of different angular momentum states is lifted for all lines. From top to bottom we have the bright molecular triplet-like states, the dark (optically forbidden) triplets and the molecular singlet-like ones. The black pair at the bottom shows the splitting of the single electron ground state. **b,** The transition energies are obtained by subtracting the respective ground state energies from each excited state. **c,** DT spectra for the readout QD transitions as a function of magnetic field in the Faraday configuration. The first avoided crossing between $T_{+3/2}$ and $T_{-1/2}$ states occurs at 2 T as indicated by the red rectangle. At larger magnetic fields the two highest frequency transitions are $T_{+3/2}$ and $T_{+1/2}$, respectively.

in Fig. 7.6b and 7.6c). Figure 7.6 presents simulation (Fig. 7.6a and 7.6b) and experiment (7.6c) for DT spectra as a function of magnetic field. In the simulation we only consider Zeeman shifts, neglecting the diamagnetic shift which is also present in the data and common to all transitions. Figure 7.6a shows the QDM eigenenergy evolution as a function of magnetic field. Electron and hole g-factors are found from the data in Fig. 7.6c. The top 4 lines correspond to the 4 bright triplet-like eigenstates and at the bottom of the figure the single electron ground states are shown in black. For convenience we label these four eigenstates according to the basis state that contributes most in each case. This is the notation used when we introduced the readout scheme in section 7.1. At low magnetic fields going from higher to lower energies we have the $T_{+1/2}$ state (corresponding basis state $|12\rangle$ in Eq. (7.4)), the $T_{-1/2}$ state (basis state $|5\rangle$) and then the $T_{+3/2}$ (basis state $|3\rangle$) and $T_{-3/2}$ states (basis state $|10\rangle$). Around 2 T magnetic field the $T_{+3/2}$ state and the $T_{-1/2}$ state anticross so that the $T_{+3/2}$ state is second highest in energy for higher magnetic fields. Fig. 7.6b displays the transition energies expected from the energy level scheme in Fig. 7.6a using these labels. The experimental raw data is given in Fig. 7.6c.

In order for our readout to work efficiently we need the $T_{+1/2}$ readout state to have as little admixture of basis states other than $|12\rangle$ as possible. We use the numerical model to evaluate the composition of the $T_{+1/2}$ state in terms of the basis states at 2.3 T, the magnetic field value which is later used for readout. The four biggest contributions to the eigenvector are:

$$T_{+1/2}\,(B = 2.3T) = \sqrt{0.9813}\,|12\rangle + \sqrt{0.0181}\,|10\rangle + \sqrt{3.3 \cdot 10^{-4}}\,|9\rangle + \sqrt{4 \cdot 10^{-5}}\,|5\rangle\,.$$

All remaining contributions are $\leq \sqrt{10^{-5}}$. The admixture of $|10\rangle$ means that the polarisation of emitted photons is slightly elliptical, but it does not introduce errors in the readout, as the host spin state is 1. Reduced readout fidelities are caused by admixtures of the basis states with host spin 0: $|9\rangle$ and $|5\rangle$. Considering that radiative recombination of $|9\rangle$ is dipole-forbidden the admixture of $|5\rangle$ is expected to be the dominant contribution to readout error. In this case, measurement of a photon from the $T_{+1/2}$ excitation has a fidelity error of $< 10^{-4}$. This is expected to be much smaller than other experimental errors. As such we

consider the $T_{+1/2}$ state to be satisfactorily 'pure' for the purpose of spin readout.

Having discussed the purity of the readout state, we briefly turn to the other transitions. Due to the anticrossing at 2 T the intermediate transitions are roughly equal superpositions of basis states $|3\rangle$ and $|5\rangle$ at 2.3 T. A second anticrossing is expected at higher fields between the two lower energy levels (pair of green lines in Fig. 7.6 a) [180]. This anticrossing mixes basis states of different host spin orientations. The optical transition to the $T_{+1/2}$ state remains the only transition that does not hybridise with the other transitions.
The analysis confirms that the $1 \rightarrow T_{+1/2}$ transition is suitable as a recycling transition to deduce the host QD spin state.

7.5 Steady-state spin dynamics

In order to show that there is a direct link between the transitions to specific molecular states and the host spin orientation we perform time-averaged two-colour resonance fluorescence measurements. The host spin is deterministically set to either 0 or 1 by continuous optical pumping [48] and we monitor resonance fluorescence counts while driving the $1 \rightarrow T_{+1/2}$ transition. Unless specified otherwise, all following experiments are performed at 2.3 T and the laser is linearly polarised. A 1 nm bandwidth filter is used to reduce laser leakage from the pumping laser.

In the left panel of Fig. 7.7a the pumping laser is scanned across the $0 \rightarrow S_{+3/2}$ transition (detuning δ_{pump}) while the readout laser is fixed and detuned from the $1 \rightarrow T_{+1/2}$ transition by $\delta_{readout}$ (see sketch at the bottom of Fig. 7.7 for the transitions involved). For finite pump detuning δ_{pump}, i.e. inefficient pumping into the 1 state, we observe a constant resonance fluorescence signal when the readout laser is resonant with the $1 \rightarrow T_{+1/2}$ transition. In the double resonance case spin pumping into state 1 is efficient and the resonance fluorescence signal from the readout transition is enhanced. In the right panel of Fig. 7.7a the pumping laser initialises state 0 continuously when its detuning δ_p from the $1 \rightarrow S_{-3/2}$ transition is small. Here the resonance fluorescence signal is suppressed in the double resonance case.

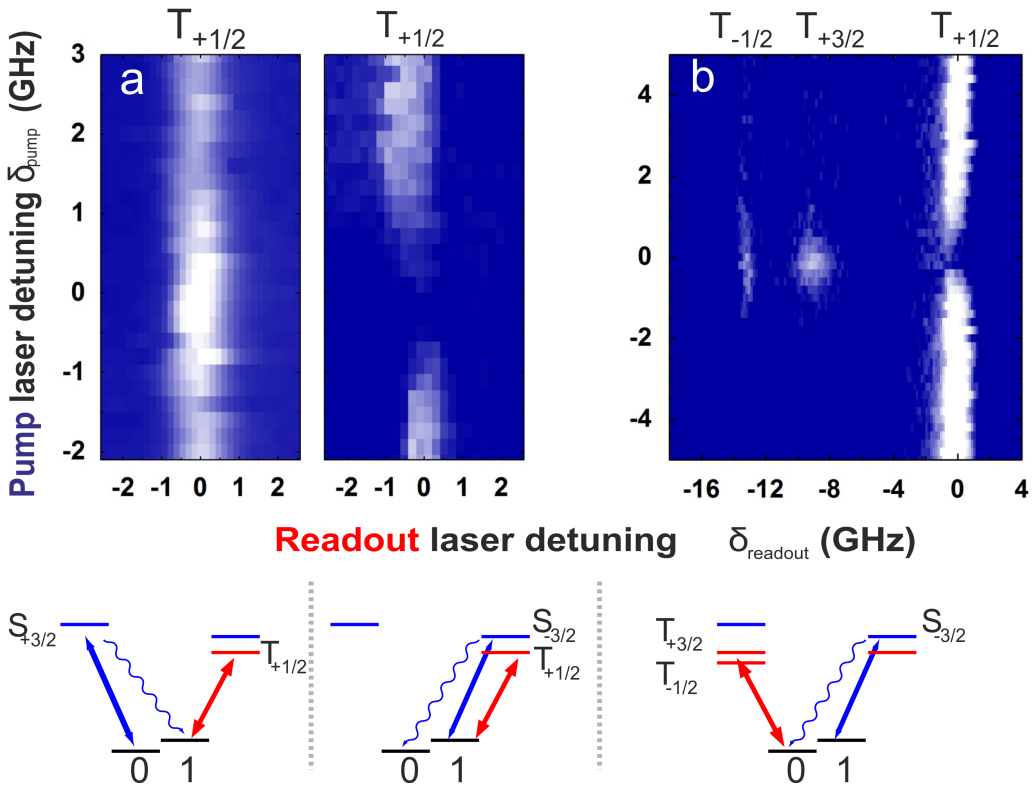

Figure 7.7: Steady-state spin dynamics monitored via molecular transitions. Sketches at the bottom of the figure indicate which transitions are being driven. The red (blue) arrow denoted the readout (pump) laser.

A third test of the conditionality of the molecular transitions on the host spin state is shown in Fig. 7.7b. The pumping laser is set to initialise the host spin in state 0. The right part of Fig. 7.7 b is identical in conditions to the right panel of a, but as the readout laser is red detuned further, it hits resonance with the molecular transitions $0 \rightarrow T_{+3/2}$ first and then $0 \rightarrow T_{-1/2}$. These transitions light up as the host spin is pumped into the 0 state, consistent with the reduction of signal in the $1 \rightarrow T_{+1/2}$ channel.
Another interesting feature is observed in Fig. 7.7 b: when the pumping laser is off-resonant, i.e. not preparing the host spin state, no resonance fluorescence signal is visible from the $0 \rightarrow T_{+3/2}, T_{-1/2}$ transitions, while the $1 \rightarrow T_{+1/2}$ is continuously very bright. This points to a spin pumping process where the host spin state is flipped by driving the molecular $0 \rightarrow T_{+3/2}, T_{-1/2}$ transitions.

7.6 Time-resolved spin dynamics

Having confirmed the purity of the $T_{+1/2}$ readout state in simulations and verifying that

1. resonance fluorescence from the readout transition shows conditionality on the host spin state and

2. it does not exhibit optical spin pumping unlike the two spectrally closest transitions,

we move on to real-time resonance fluorescence monitoring from the readout transition. Host spin dynamics are expected to be reflected in intermittent resonance fluorescence.

Fig. 7.8a shows a 300-ms long time trace of the resonance fluorescence (2 ms time bins) when the readout laser is driving the $1 \rightarrow T_{+1/2}$ transition below saturation. Clear jumps in the fluorescence between two levels are observed. We denote the bright fluorescence level as 'on' and the dark levels as 'off'. The histogram for the frequency of fluorescence counts per time bin for 1200 seconds of data is displayed in Fig. 7.8b. It shows two modes which we associate with 'on' and 'off'. In 7.8c the frequency histogram for 'off' durations, i.e. the duration

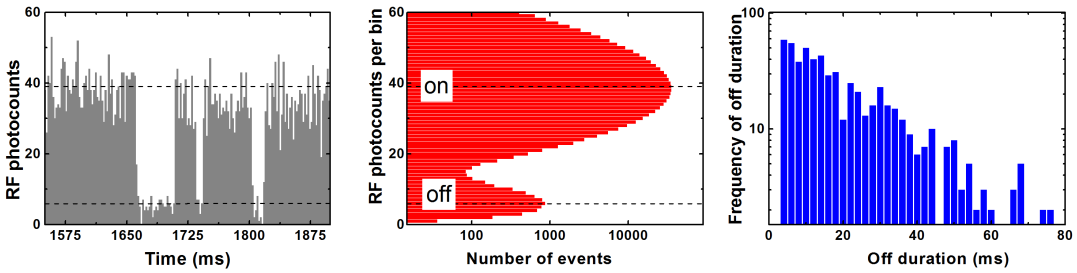

Figure 7.8: Time-resolved resonance fluorescence from the readout transition. **a** 300 ms of intermittent resonance fluorescence. **b,** Histogram of photocounts. The distribution is considerably broader than would be expected from **a**, this is due to spectral diffusion during the 1200 seconds of recording data. **c,** Statistics 'on' the off durations reveal single exponential decay.

of a dark period, is plotted. It follows a single exponential decay with a decay constant T_{off}=14.9 ms.

Next, we monitor resonance fluorescence while pumping the host spin into state 1 or 0, in analogy to the time-averaged measurements. Fig. 7.9a shows counts in 250 μs time bins, where for negative times the readout laser only is active. The time trace exhibits switching between on and off levels as before. At positive times a pumping laser resonant with the $1 \rightarrow S_{-3/2}$ transition forces the host spin into state 0 and the readout fluorescence is quenched. In the top right panel of Fig. 7.9b we show a histogram of fluorescence counts when only the readout laser is driving the $1 \rightarrow T_{+1/2}$ transition on resonance (time bin of 4 ms). The left panel shows a zoom-in of the lower tail of the histogram, which is due to 'off' periods in the fluorescence stream. The same arrangement of plots is used in the bottom panel of b where a weak pumping laser drives the $0 \rightarrow S_{+3/2}$ transition. Counts in the lower histogram tail are reduced by a factor of 3.

These time-resolved measurements demonstrate the same conditionality of fluorescence on the host electron spin as the time-averaged measurements: Dark periods in the photonstream can be associated with spin state 0 and bright periods with spin state 1.

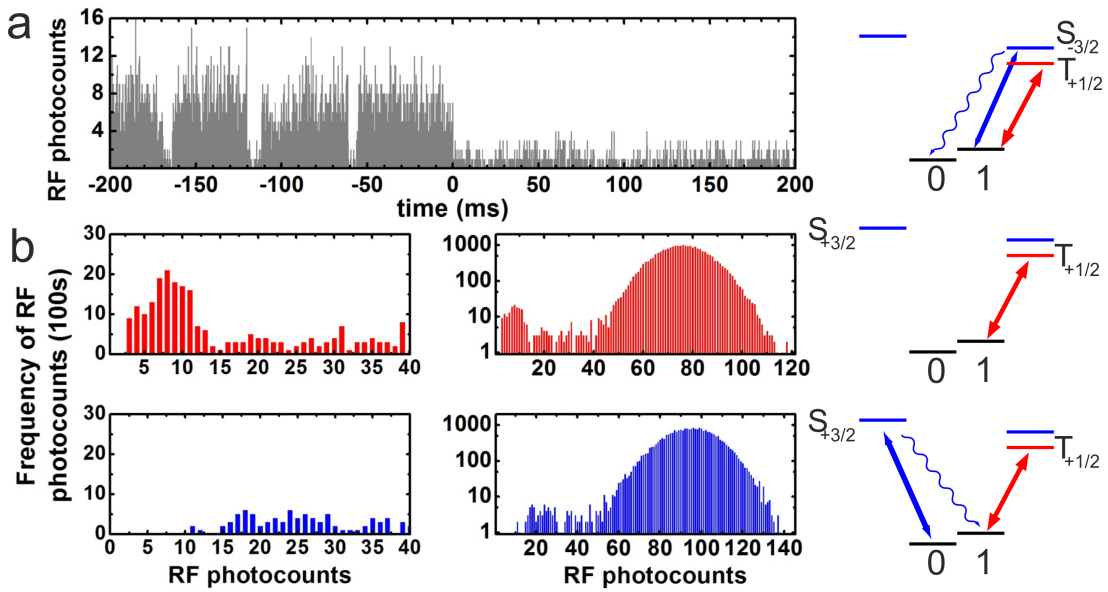

Figure 7.9: Time-resolved resonance fluorescence from two-colour experiments. a, Quenching of fluoresence when the pumping laser initialises the spin state to 0 at positive times. **b,** Comparison of count histograms when only the readout laser is active (top panels) to simultaneously pumping into spin state 1. The left panels show the lower tails of the full histograms in more detail.

7.6.1 State mixing and spin pumping in quantum dot molecules

Before quantifying the fidelity of the readout technique we need to discuss a puzzling feature of the resonance fluorescence counts histograms: In Fig. 7.8b, and even more obviously in Fig. 7.9 b the modes corresponding to 'on' and 'off' are highly imbalanced. For thermal equilibrium we expect the population of the Zeeman sublevels to obey Boltzmann statistics. In our case this corresponds very closely to a balanced distribution, so that the histogram areas for 'on' and 'off' should be equal. We associate the imbalance of populations with the optical pumping observed in Fig. 7.7 b when the host spin state is 0. We expect that measurement-induced spin flips originate from these transition being driven nonresonantly when the $1 \rightarrow \mathrm{T}_{+1/2}$ transition is probed on resonance by the readout laser. In order to quantify the optical spin pumping we use a previously reported protocol [26] to measure the spin pumping rate directly for the transition spectrally closest to the readout transition. Fig. 7.10 a explains the protocol in a sketch. Panel b exhibits the timescale for optical pumping as a function of spectral detuning. The shortest resonance fluorescence decay constant is (0.324±0.020) μs obtained on resonance when the transition is driven strongly into saturation.

At the magnetic field used throughout these measurements (2.3 T) the main mechanism relaxing the optical selection rules for single QDs is the heavy-light hole mixing, and the induced spin-flip rate was shown to be independent of the external magnetic field (beyond 1T) [26]. For QDMs the hole-mixing induced spin-flip rate can be further enhanced by a lateral offset between the two QDs [187]. We define an admixed heavy-hole state $\widetilde{\Uparrow} = \Uparrow(+3/2) + \epsilon_+ \Uparrow(+1/2) + \epsilon_- \Uparrow(-1/2)$. Optical spin pumping can be mediated through the following mechanism then

$$\begin{pmatrix} \uparrow & 0 \\ 0 & 0 \end{pmatrix} \xrightarrow{\hbar\omega} \begin{pmatrix} \uparrow & \downarrow \\ 0 & \widetilde{\Uparrow} \end{pmatrix} \xrightarrow{t_e} \begin{pmatrix} \uparrow\downarrow & 0 \\ 0 & \widetilde{\Uparrow} \end{pmatrix} \xrightarrow{t_e} \begin{pmatrix} \downarrow & \uparrow \\ 0 & \widetilde{\Uparrow} \end{pmatrix} \xrightarrow{\hbar\omega} \begin{pmatrix} \downarrow & 0 \\ 0 & 0 \end{pmatrix},$$

where we have used the illustration of QDM states from Fig. 7.1 . We expect to observe efficient spin pumping from transitions that have contributions from

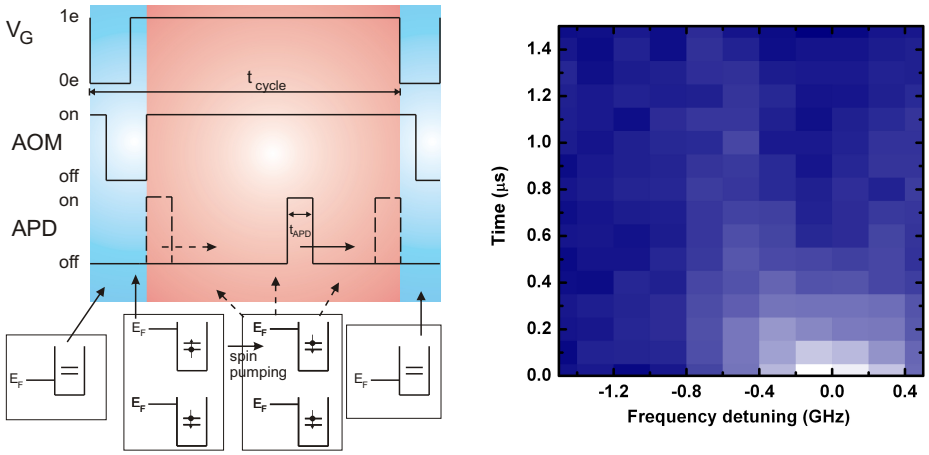

Figure 7.10: Measurement of optically induced spin-flip transition timescale from the $0 \rightarrow \mathrm{T}_{+3/2}$ transition. Left panel, Protocol for spin pumping measurements. The $0 \rightarrow \mathrm{T}_{+3/2}$ transition is driven when the AOM is on. The gate voltage is set to recycle the host QD electron at the beginning of each cycle. The APD 'on' window moves in consecutive cycles across the region shaded in red. The Zeeman sublevels of the host QD electron relative to the Fermi level and their occupation at several stages of the pulse sequence are indicated schematically below. For spin relaxation processes much slower then spin pumping times, $T_1 \gg T_{sp}$, and $t_{cycle} \geq T_{sp}$, an electron initially in the 1 state will stay in the 1 state until it is recycled. **Right panel,** laser detuning dependence of the time-resolved RF at 2.3 T magnetic field obtained for strong excitation laser power. The shortest exponential decay constant occurs on resonance (0.324 $\pm$ 0.020 μs) and is prolonged for finite detunings.

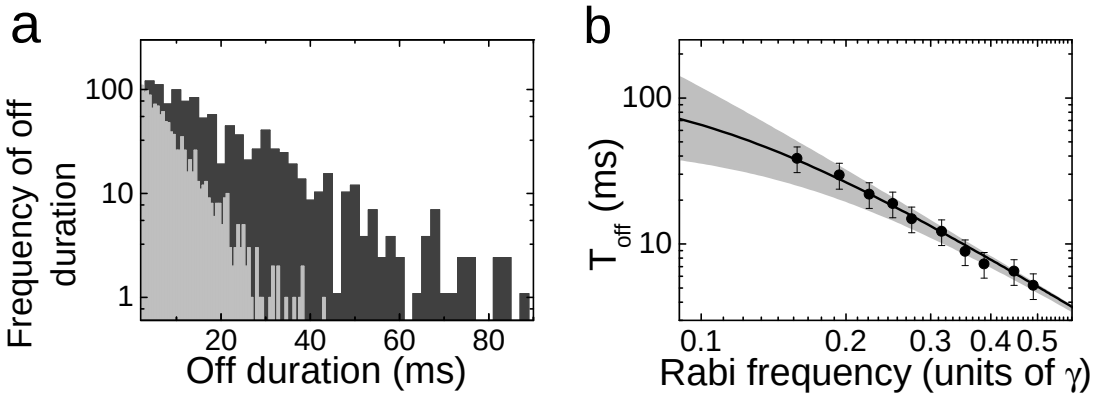

Figure 7.11: Statistics on off durations for different laser powers. **a,** Frequency of off duration for laser power $\Omega \sim 0.45T_1^{-1}$ ($s = 0.4$), light grey ($\Omega \sim 0.23T_1^{-1}(s = 0.1)$, dark grey) yields a decay constant T_{off} =6.5 ms (T_{off} =14.9 ms). **b,** T_{off} as a function of laser power.

the antiparallel electron spin basis states $|3\rangle$ and $|10\rangle$ (specifically the the $0 \rightarrow \mathrm{T}_{+3/2}$ and $1 \rightarrow \mathrm{T}_{-3/2}$ transitions). At 2.3 T both the $0 \rightarrow \mathrm{T}_{+3/2}$ and $0 \rightarrow \mathrm{T}_{-1/2}$ transitions are admixtures containing basis state $|3\rangle$, consistent with the observation of optical spin pumping.

From the optical pumping rate obtained on resonance we can estimate that the readout laser, detuned from the $0 \rightarrow \mathrm{T}_{+3/2}$ transition by $2\pi\times8$ GHz, causes spin flips in a few to tens of ms when the host electron is in state 0, depending on its driving power. In order to provide evidence for this off-resonant pumping we vary the readout laser power and compare the duration of dark periods. Fig. 7.11a shows two 'off' duration histograms for laser powers of $s = 0.4$(light grey) and $s = 0.1$ (dark grey), giving decay constants T_{off} of 6.5 ms and 14.9 ms, respectively. In Fig. 7.11b we plot the extracted T_{off} values for a range of laser powers. The expected dependence of T_{off} on laser and external parameters is

$$\frac{1}{\mathrm{T}_{\text{off}}} = \frac{1}{\mathrm{T}_{0\rightarrow1}} + \frac{\gamma_{sf}\Omega^2}{4\Delta^2 + T_1^{-2} + 2\Omega^2}, \tag{7.6}$$

where Ω, T_1, Δ, γ_{sf} and $\mathrm{T}_{0\rightarrow1}$ denote the Rabi frequency, excited state lifetime, spectral detuning between the readout laser and the $0 \rightarrow \mathrm{T}_{+3/2}$ transition, rate of optically induced spin flips from state 0 to 1 and the natural spin relaxation time from state 0 to 1. We set $\Delta = 2\pi\times8$ GHz, $1/T_1 = 2\pi\times250$ MHz and

$\gamma_{sf} = 2\pi \times 0.49$ MHz from our measurements. The solid black line is obtained for $T_{0\to1}$ =140 ms, while the lower and upper boundaries of the region shaded in grey are for $T_{0\to1}$ =50 ms and $T_{0\to1}$ =1 s, respectively.

7.7 Spin readout fidelity

The fact that we can observe abrupt jumps in the fluorescence level, corresponding to spin flips of the host electron, means that we can determine the spin state for each measurement time bin. We can think of a time trace of the readout transition fluorescence as a continuous stream of single-shot readout attempts.

In order to estimate the fidelity of our readout technique we analyse a set of continuous wave (cw) photodetection time traces, like the one shown in Fig. 7.8 a. We consider each time bin of the time trace to be a single-shot readout attempt. Every time bin below a set threshold is labeled as 'off', and we assign spin state 0 to the host QD electron, and vice versa for time bins above the threshold. The fidelity is evaluated as $1 - p_1 e_1 - p_0 e_0$, where p_1 and p_0 are the probabilities of finding the electron in state 1 or 0, and e_1 and e_0 are the errors in assigning state 1 and 0. A readout error is made when the fluoresence count of a time bin is above (below) the threshold, but the electron spin was actually in state 0 (1) at the start of the measurement.

We identify two sources of error when deciding if a particular time bin is 'on' or 'off'. The first one ($e_0^{\mathrm{n}}/e_1^{\mathrm{n}}$) is due to photon shot noise: as the photons obey Poisson statistics we observe a spread of photocounts per time bin. We can associate one distribution with each of the two host electron spin states. The distribution for state 0 is given by the shot noise of the laser leakage through the crossed polarisers, while the distribution for state 1 is given by both the laser leakage and the shot noise of photodetection from cycling the readout transition $1 \to T_{+1/2}$. Both distributions can be obtained individually from the time traces. The fraction of each distribution on the other (wrong) side of the threshold value constitutes the error $e_0^{\mathrm{n}}/e_1^{\mathrm{n}}$ in each case. There is one more step involved in obtaining the error value. When operating in cw mode, the spin flips due to off-resonant pumping of the $0 \to T_{+3/2}$ transition skew the histogram in favour of the 1 state. The imbalance of state 0 and 1 populations is a consequence of the

cw readout, so we rescale the distributions obtained for states 0 and 1 to equal areas, corresponding to the case of equal populations, i.e. no spin information prior to a single measurement attempt: $p_1 = p_0 = 0.5$. For the data in Fig. 7.8 the overlap is below 0.1%. The best threshold value is the one that minimises the overlap of the rescaled distributions in this case.
The second, more severe source of error ($e_0^{\mathrm{d}}/e_1^{\mathrm{d}}$) is spin flips during the course of a time bin/readout attempt. We note that a spin flip during the measurement does not necessarily lead to a readout error: spin flips that happen towards the end of a time bin do not affect the correct measurement outcome, since the photocounts remain on the correct side of the threshold. Spin flips early in the time bin, however, do result in erroneous assignment of the spin state. Where exactly we cross the line from correct to incorrect readout depends on where the threshold value between 'on' and 'off' is. For a threshold that is approximately centred between the 'on' and 'off' distributions we can say that only spin flips during the first half of the time bin lead to wrong readout. The spin flip time from 0 to 1 (T_{off}) has been measured for various laser powers and is presented in Fig. 7.11. For the data set of Fig. 7.8 this value is T_{off}=14.9 ms and the time bin is 2 ms. From this, the probability of a spin flip in the first half of the time bin, i.e. in 1 ms is $\approx 1/14.9 \approx 0.07$. For spin flips from 1 to 0 we assume a timescale of $\sim$ 100 ms which is a conservative estimate of the natural T_1-time from Fig. 7.11b. The chance of a spin flip in 1 ms is then $\approx 1/100 = 0.01$. Summing up the errors yields a fidelity of

$$1 - p_0 e_0 - p_1 e_1 = 1 - 0.5(0.07 + 0.01 + \mathcal{O}(10^{-3})) = 0.96.$$

The magnitude of the $e_0^{\mathrm{d}}/e_1^{\mathrm{d}}$ error is determined by the length of the time bin compared to the spin-flip timescale: longer time bins increase the signal-to-noise ratio as they separate the shot noise distributions for states 0 and 1 and hence reduce the $e_0^{\mathrm{n}}/e_1^{\mathrm{n}}$ error. At the same time longer time bins increase the chance that a spin flips during a readout attempt. We analyse the fidelity of the high laser power data set ($\Omega \sim 0.49\mathrm{T}_1^{-1}$ in Fig. 7.11b). The time bin for this measurement is 300 μs, while T_{off} has been determined as 5.2 ms, so that the e_0^{d} error is reduced ($\approx 0.15/5.2 \approx 0.03$). This is at the expense of the $e_0^{\mathrm{d}}/e_1^{\mathrm{d}}$ error, which is of similar

magnitude. We sum the errors and obtain

$$1 - p_0 e_0 - p_1 e_1 = 1 - 0.5(0.03 + 0.002 + 0.035 + 0.055) = 0.94$$

in this case. We conduct a systematic analysis of error dependencies on integration times and driving powers in the next section.

7.8 Improving readout fidelities

Compared to the QDM sample used for spin readout, the devices based on the 'Chef 2' wafer used in the earlier chapters represent an improvement of factor $\sim$ 4 in photon extraction and the background suppression is improved by a factor of $\sim$ 20. With these parameters we can project what readout fidelities are possible with a QD molecule sample with optimised structure and a DBR layer.
We quickly summarise the strategy for spin readout and an optimisation of the readout fidelity first: State-readout using resonance fluorescence is achieved by probing a spin-selective transition for a set duration and comparing the number of photodetection events to a suitably chosen threshold. Essentially, distinguishing two spin state translates to telling if a particular transition is active/on or off: If the number of photodetection events is above the threshold the transition is assumed to be on (and the spin state is deduced), if the number of detections is below the threshold the transition is off. An erroneous assignment of the spin state is made when the photodetection counts are above the threshold even though the transition is off and vice versa. The readout error is given by the weighted probabilities of these events; denoting the individual errors e_{on} and e_{off} we have a total error of $e = 1/2\,(e_{\mathrm{off}} + e_{\mathrm{on}})$ in the case of equal spin populations. In general, two sources contribute to readout error, both dependent on the duration of the readout attempt, the binsize. On the one hand, the photodetection obeys poissonian statistics and two distributions can be associated with the on and off cases. Any overlap of the two distribution gives rise to an error proportional to the overlap. Minimising this error, i.e. separating the distributions requires increasing the binsize. On the other hand, finite spin lifetimes mean that during some measurement attempts a spin flip occurs that can obscure the

readout. Spin flips contribute to the area between the on/off distributions.
Any measurement should be short compared to the spin lifetime and smaller binsizes decrease this type of error. Additionally, processes that shorten the natural spin lifetime such as optical pumping can limit the fidelity further. Once the statistics for spin dynamics and photon detection are known the threshold for readout is chosen such that the overall error is minimised.

We mimic spin readout by switching the X^{1-} transition of QD 'Claude' (single QD, Chef 2 sample, zero external magnetic field) on and off resonance with respect to the exciting laser and comparing photon statistics for the two cases. This gives us the first type of error discussed above. Figure 7.12 a displays the statistics for an excitation laser power at saturation. APD counts are recorded on and off resonance with 10 μs resolution for a cumulative duration of 2 seconds. The inset shows an exemplary timetrace where the trion transition is driven for 100 ms on resonance first and then 100 ms off resonance. The timetraces are rebinned to 30 μs resolution for the histogram. APD dark counts have been measured separately and are shown as well. The dashed curves are distributions expected from poissonian statistics. In Fig. 7.12 b we plot the overlap of on/off histograms vs. binsize for a range of powers from a tenth of saturation to close to 200 times saturation. For a given bin size, we see the overlap decrease first as the driving power and hence the QD emission rate is increased until it reaches a minimum and increases for higher powers as the background rises while QD emission saturates. Due to the finite sample size all on/off histograms separate completely for larger bin sizes. Kinks and non-monotonous decay with bin size are due to the discrete nature of photon counting.
Next, we include lifetime and spin pumping effects: From Eq. (7.6) and Fig. 7.11 we have a natural spin lifetime of $T_{0\to1} \sim 140$ ms. No spin pumping effects are observed for spin down (state 1), but spin up (state 0) is pumped into the down state when the readout laser is active. This is due to off-resonant (detuning $\Delta = 2\pi\times8$ GHz) driving of a transition that pumps the spin efficiently from up to down at a rate of $\gamma_{sf} = 2\pi\times0.49$ MHz when on resonance with the spin-pumping transition.
The results, see Fig. 7.13, are given for two excitation powers. Here, red corre-

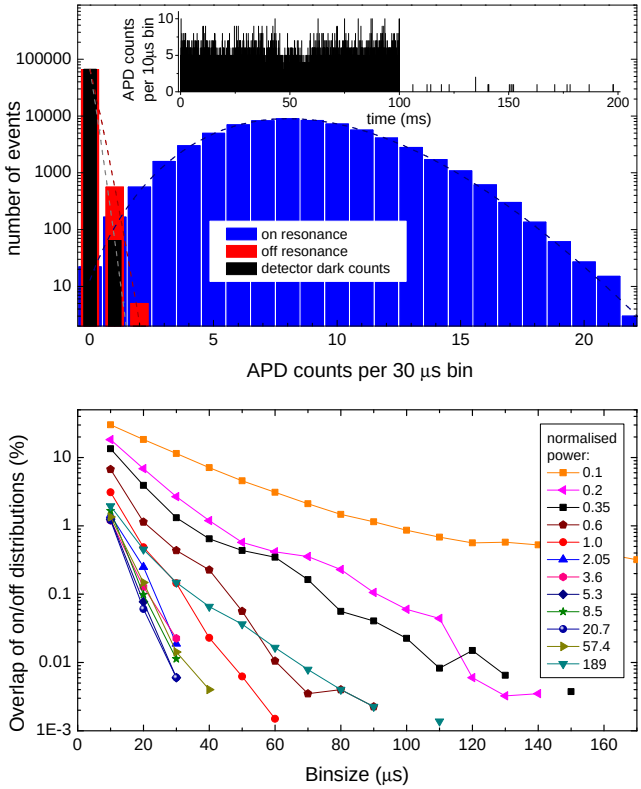

Figure 7.12: Signal-to-background and noise analysis of resonance fluorescence for spin readout. Photodetection events are recorded with 10 μs resolution when the QD transition is driven on and off resonance (see inset of a for exemplary time traces). a, Histogram of photocounts per time of 30 μs for resonant driving (blue), off-resonant driving (red) and no driving (black). b, Overlap of on-resonance and off-resonance photodetection histograms as function of detection binsize for a series of excitation powers.

sponds to the readout error at saturation whereas green is for a fifth of saturation power. We include the individual errors for spin up (up-pointing triangles) and spin down (down-pointing triangles) and the average (filled circles). Fidelities higher than 99 % can be reached within 20 μs at saturation and a peak fidelity of 99.59 % is achieved in 40 μs. Slightly higher fidelities are possible at smaller excitation powers, but come at a cost of significantly larger binsizes: we predict 99.73 % fidelity for a fifth of saturation and a binsize of 120 μs (see arrows in Fig. 7.13).

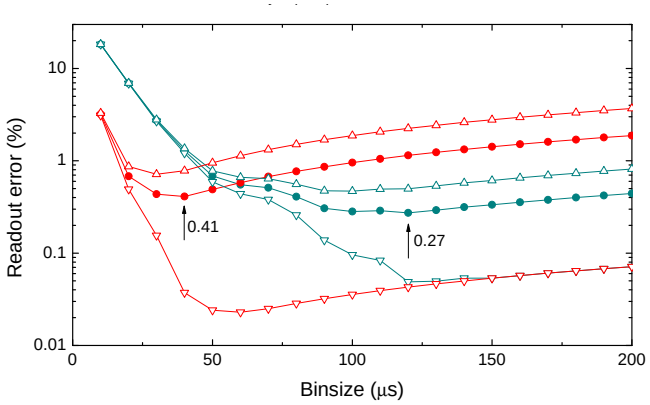

Figure 7.13: Estimated spin readout error for a QDM with improved photon collection efficiency (corresponding to the efficiency obtained with the Chef 2 sample). The QDM parameters, such as off-resonant spin pumping rate and spin lifetime, are from measurements on the actual QDM sample. Spin pumping, spin lifetime and the histogram overlap from Fig. 7.12 contribute to the calculation. Red data is for a readout power at saturation ($s = 1$), while the green data is for $s = 0.2$. Up-pointing triangles give the error for spin up readout, down-pointing triangles for spin down readout, and the solid circles represent the average error.

A promising approach to improve the readout fidelities further might be to optimise parameters limiting QDM readout. In our case this is spin pumping of the up spin on the order of ms. Increasing the parameter Δ in Eq. (7.6) by a factor two (which can be achieved by increasing the tunneling interaction slightly) would bring the maximum fidelity up to 99.9 %.

We note that all results here rely on a simple threshold method; more sophisticated methods, such as maximum likelihood have been shown to greatly improve readout fidelities [107]. Quantum error correction schemes typically assume readout errors on the order of 10^{-3}, which can be satisfied even with the threshold

methods.

7.9 Chapter outlook

In conclusion, we have observed spin-dependent quantum jumps in a QDM via resonance fluorescence. The spin state of a single electron confined to one QD of the vertically stacked QD pair is monitored by virtue of a molecular recycling transition that is conditional on the electron spin state. The use of a QDM eliminates the need to address the same transition for spin state manipulation and readout, overcoming a main limitation of single QD qubits. While QDM molecules have been investigated before, also with respect to spin readout, the combination of this physical system with the high bandwidth of resonance fluorescence has made single-shot readout possible. Our measurements with the QDM indicate single-shot fidelities of $\sim 95\%$ for measurement times of 250 μs, but with the improved collection efficiency and signal-to-background ratio we extrapolate a readout fidelity $> 99.5\%$ for a measurement time of 30 μs. Equally exciting, the prospect of using single-shot readout in a verification scheme for distant spin entanglement would decrease the measurement time by the inverse of the squared combined collection/detection efficiency when compared to the use of single QDs. For current collection efficiencies this time gain would be at least a factor of 1000.

Chapter 8

Conclusions and outlook: towards a small-scale quantum network

Eight chapters on - how does this thesis fit together as a whole and where do we go from here? In the introduction we outlined the vision of the quantum internet: A quantum optical network of individual quantum dots, or better quantum dot molecules, entangled through quantum interference of their single photons. The smallest possible network would be just two remote spin qubits which can be manipulated individually and entangled via two-photon interference.

Removing obstacles in the way of achieving this next step of a small-scale network has provided the motivation throughout the thesis. We were concerned with two issues mainly:

1. **Photon quality.** This was driven by the following question: Can we entangle two QDs - with high fidelity - using photon interference? Splitting this question into smaller parts we aimed to answer: How can we generate high coherence single photons from a QD? What are the limits on coherence? How do environmental dynamics affect the photon quality?

2. **Spin readout.** Single-shot readout was, out of the first five, the only missing DiVincenzo criterium for spins in QDs at the start of this thesis work. Can we overcome the limitation of laser backaction flipping the spin

before its state is determined? What are the readout fidelities and how can they be optimised?

The first point was investigated in Chapters 4,5 and 6 of this thesis. We set out to systematically study the first- and second-order coherence of QD resonance fluorescence in the previously unexplored regime of small Rabi frequencies, $\Omega \lesssim 1/T_1$. We could report the direct observation of highly coherent single photon emission - a somewhat novel feature in the solid-state community that dominates QD research, despite being a standard topic in quantum optics textbooks. The emission of subnatural linewidth single photons was detailed in the first part of Chapter 4 and is one of the main results of this thesis.
While this observation is a sign of negligible pure dephasing we still found marked deviations from the properties predicted for an isolated two-level system. These influences of the solid-state environment - spectral diffusion, exciton-phonon coupling and Overhauser field dynamics - were explored in the second half of Chapter 4. One other influence on the QD optical transition, this time not a 'natural' but laser-induced effect, was identified as an optically induced electric field in Chapter 5.
The sensitivity of the QD transition to these additional interactions spell out a serious challenge for the realisation of entanglement:

- Uncorrelated spectral diffusion for independent QDs reduces their spectral overlap and hence limits photon interference probabilities.
- Uncorrelated Overhauser fields dephase independent spin qubits within the inhomogeneous dephasing time of a few nanoseconds.

Characterising and quantifying the extent of these challenges is a first step. The next important step is to minimise or to avoid them.
Chapter 6 detailed one approach to the photon interference part: relying on coherent QD scattering locks the scattered photon's frequency to that of the exciting laser and avoids any pure dephasing. We used two-photon interference of single QD emission to confirm that photons created this way are fundamentally indistinguishable and envision that for entanglement purposes separate QDs are addressed by the same laser. Of course, there are downsides to this scheme, most

importantly the low excitation efficiency. A better solution would be to eradicate spectral diffusion in the first place... Future work will pursue the two approaches. A starting point for the reduction of spectral diffusion will be an active stabilisation of the QD transition.

Going to the second main issue of single-shot spin readout: For the simple optical level structure of a singly charged QD there are limited resources to satisfy all of the first five DiVincenzo criteria at once. In particular, spin initialisation and optical spin rotations rely on excited states coupled strongly to both qubits basis states. This translates to a balanced branching ratio of excited to ground state transitions. Spin readout on the other hand requires, in the face of non-unity probability of photon collection and detection, a recycling transition.
Since these opposing requirements cannot be satisfied for single QD we turned to quantum dot molecules in Chapter 7. There, the level structure is far more complex than the simple two-level system we considered all the way up to Chapter 8, but it allows for a spin-sensitive recycling transition.
The more complex level structures of QDMs gives rise to further options for coherent spin control and it is likely that QDMs will replace single QDs as the main workhorse for QIP applications. This is evidenced by the ongoing research which has enabled 2-qubits gates [42] and protected qubits states [44] already.

Distant spin entanglement remains the motivation for further work. This thesis provides solutions to some of the challenges we face along the road, but some remain to be solved.
We finish this chapter and the thesis by listing a few of the challenges which will be taken on next.

- *Improving the collection efficiency.* Total internal reflection at the semiconductor-air interface limits outcoupling of photons into the collection optics to 1-2%.We have employed solid immersion lenses to ameliorate this issue and increased outcoupling efficiency to 6-7%. However, theoretical considerations suggest that optimal index matching alone should allow an increase in extraction to 30% [77] and with improved sample design the extraction efficiency should approach 99% [190]. We will explore new sample designs

following these proposals.

This technical improvement is particularly crucial if we want to verify spin-spin entanglement. In the protocol of Duan *et al.* [153; 157] two-photon interference and detection projects the qubits into entanglement. Hence the probability of an entanglement event scales as the square of the collection/detection efficiency. Then the spin states need to be measured to verify the entanglement. Using a single QD as qubit host we only scatter 1-2 photons in the readout attempt so the readout success rate for both qubit scales as the square of the collection/detection efficiency again. Verified entanglement rates then go as the fourth power in total. With our current system this translates to roughly one event every ten minutes. If single-shot readout is available, however, the rate scales as the square only, which would be a significant improvement. Entanglement rates could be further increased using Cabrillo's entanglement protocol [156] for example, but technical requirements increase.

- *Spin coherence and the Overhauser field.* Long spin coherences have been reported for frequency-domain measurements in combination with optical feedback on the nuclear field [39]. The use of feedback with time-domain spin rotations is still outstanding though. Further, dynamical decoupling schemes, which have been applied very successfully for electrically defined QDs [55] and NV centres [191], are an outstanding challenge as well.

- *Efficient coherent scattering.* Coherent scattering rates are 10-20 times lower than for deterministic excitation schemes. It may be possible to combine deterministic photon generation with coherent scattering: A very short (picoseconds) optical pulse moves the population almost entirely into the excited state and then a long weak pulse creates the two-level system coherences necessary for coherent scattering. This should keep the generation process deterministic while still allowing coherent scattering to exist alongside spontaneous emission.

References

[1] Rolf Landauer. Information is physical. *Physics Today*, 44(5):23–29, 1991. 1

[2] H. J. Kimble. The quantum internet. *Nature*, 453(7198):1023–1030, 2008. 2, 5, 6, 52

[3] Daniel Loss and David P DiVincenzo. Quantum computation with quantum dots. *Physical Review A*, 57(1):120, 1998. 2

[4] David P DiVincenzo et al. The physical implementation of quantum computation. *arXiv preprint quant-ph/0002077*, 2000. 2, 4

[5] P.W. Shor. Polynomial-time algorithms for prime factorization and discrete logarithms on a quantum computer. *SIAM Review*, pages 303–332, 1999. 3

[6] Peter W. Shor. Scheme for reducing decoherence in quantum computer memory. *Physical Review A*, 52(4):R2493–R2496, Oct 1995. 4

[7] S. Braunstein and H.K. Lo. Experimental Proposals for Quantum Computation, volume 48, 2000. 5

[8] Jelena Stajic. The future of quantum information processing. *Science*, 339 (6124):1163–1163, 2013. 5

[9] LP Kouwenhoven, TH Oosterkamp, MW Danoesastro, M. Eto, DG Austing, T. Honda, and S. Tarucha. Excitation spectra of circular, few-electron quantum dots. *Science*, 278(5344):1788, 1997. 5

[10] S. Tarucha, D. G. Austing, T. Honda, R. J. van der Hage, and L. P. Kouwenhoven. Shell filling and spin effects in a few electron quantum dot. *Physical Review Letters*, 77(17):3613–3616, Oct 1996. 5

[11] Richard J Warburton, C Schäflein, Dirk Haft, F Bickel, Axel Lorke, Khaled Karrai, Jorge M Garcia, W Schoenfeld, and Pierre M Petroff. Optical emission from a charge-tunable quantum ring. *Nature*, 405(6789):926–929, 2000. 5, 34, 36

[12] Y. Arakawa and H. Sakaki. Multidimensional quantum well laser and temperature dependence of its threshold current. *Applied Physics Letters*, 40: 939, 1982. 6

[13] M.J. Kelly. *Low-dimensional semiconductors: materials, physics, technology, devices*. Oxford University Press, New York, 1995. 6

[14] R. Hanson, L. P. Kouwenhoven, J. R. Petta, S. Tarucha, and L. M. K. Vandersypen. Spins in few-electron quantum dots. *Rev. Mod. Phys.*, 79(4): 1217, 2007. 7

[15] E.L. Wolf. *Nanophysics and nanotechnology*. Wiley-VCH, Weinheim, 2004. 7

[16] A. Zrenner, L. V. Butov, M. Hagn, G. Abstreiter, G. Böhm, and G. Weimann. Quantum dots formed by interface fluctuations in alas/gaas coupled quantum well structures. *Physical Review Letters*, 72(21):3382–3385, May 1994. 7

[17] E. Bauer. Phänomenologische Theorie der Kristallabscheidung an Oberflächen. I. *Zeitschrift fur Kristallographie*, 110:372–394, January 1958. 7

[18] C Schneider, S Hofling, and A Forchel. Growth of iiiv semiconductor quantum dots. *Quantum Dots: Optics, Electron Transport and Future Applications*, page 1, 2012. 7

[19] Zhiliang Yuan, Beata E Kardynal, R Mark Stevenson, Andrew J Shields, Charlene J Lobo, Ken Cooper, Neil S Beattie, David A Ritchie, and Michael Pepper. Electrically driven single-photon source. *Science*, 295(5552):102–105, 2002. 8, 73

[20] Tobias Heindel, Christian A Kessler, Markus Rau, Christian Schneider, Martin Fürst, Fabian Hargart, Wolfgang-Michael Schulz, Marcus Eichfelder, Robert Roßbach, Sebastian Nauerth, et al. Quantum key distribution using quantum dot single-photon emitting diodes in the red and near infrared spectral range. *New Journal of Physics*, 14(8):083001, 2012. 8

[21] J. Berezovsky, MH Mikkelsen, NG Stoltz, LA Coldren, and DD Awschalom. Picosecond coherent optical manipulation of a single electron spin in a quantum dot. *Science*, 320(5874):349, 2008. 8

[22] David Press, Thaddeus D Ladd, Bingyang Zhang, and Yoshihisa Yamamoto. Complete quantum control of a single quantum dot spin using ultrafast optical pulses. *Nature*, 456(7219):218–221, 2008. 8, 15, 16, 91, 107

[23] JM Taylor, P Cappellaro, L Childress, L Jiang, D Budker, PR Hemmer, A Yacoby, R Walsworth, and MD Lukin. High-sensitivity diamond magnetometer with nanoscale resolution. *Nature Physics*, 4(10):810–816, 2008. 8

[24] AN Vamivakas, Y Zhao, S Fält, A Badolato, JM Taylor, and M Atatüre. Nanoscale optical electrometer. *Physical Review Letters*, 107(16):166802, 2011. 8, 51, 117

[25] Jui-Ming Yang, Haw Yang, and Liwei Lin. Quantum dot nano thermometers reveal heterogeneous local thermogenesis in living cells. *ACS nano*, 5(6): 5067–5071, 2011. 8, 116

[26] C.-Y. Lu, Y. Zhao, A. N. Vamivakas, C. Matthiesen, S. Fält, A. Badolato, and M. Atatüre. Direct measurement of spin dynamics in inas/gaas quantum dots using time-resolved resonance fluorescence. *Physical Review B*, 81(3):035332, Jan 2010. 9, 16, 37, 53, 98, 158

[27] M. F. Doty, J. I. Climente, A. Greilich, M. Yakes, A. S. Bracker, and D. Gammon. Hole-spin mixing in inas quantum dot molecules. *Physical Review B*, 81(3):035308, Jan 2010. 9, 142

[28] M. Bayer, G. Ortner, O. Stern, A. Kuther, A. A. Gorbunov, A. Forchel, P. Hawrylak, S. Fafard, K. Hinzer, T. L. Reinecke, S. N. Walck, J. P. Reithmaier, F. Klopf, and F. Schäfer. Fine structure of neutral and charged excitons in self-assembled in(ga)as/(al)gaas quantum dots. *Physical Review B*, 65(19):195315, May 2002. 9, 10, 98

[29] D. Gammon, E. S. Snow, B. V. Shanabrook, D. S. Katzer, and D. Park. Fine structure splitting in the optical spectra of single gaas quantum dots. *Physical Review Letters*, 76(16):3005–3008, Apr 1996. 9

[30] A. Abragam. *Principles of Nuclear Magnetism (International Series of Monographs on Physics)*. Oxford University Press, USA, reprint edition, October 1983. ISBN 019852014X. 10

[31] A Högele, M Kroner, C Latta, M Claassen, I Carusotto, C Bulutay, and A Imamoglu. Dynamic nuclear spin polarization in the resonant laser excitation of an ingaas quantum dot. *Physical Review Letters*, 108(19):197403, 2012. 10

[32] NA Sinitsyn, Yan Li, SA Crooker, Avadh Saxena, and DL Smith. Role of nuclear quadrupole coupling on decoherence and relaxation of central spins in quantum dots. *Physical Review Letters*, 109(16):166605, 2012. 10

[33] IA Merkulov, Al L Efros, and M Rosen. Electron spin relaxation by nuclei in semiconductor quantum dots. *Physical Review B*, 65(20):205309, 2002. 11, 14, 85

[34] Bernhard Urbaszek, Xavier Marie, Thierry Amand, Olivier Krebs, Paul Voisin, Patrick Maletinsky, Alexander Högele, and Atac Imamoglu. Nuclear spin physics in quantum dots: An optical investigation. *Reviews of Modern Physics*, 85(1):79, 2013. 11

[35] C. Latta, A. Hogele, Y. Zhao, A. N. Vamivakas, P. Maletinsky, M. Kroner, J. Dreiser, I. Carusotto, A. Badolato, D. Schuh, W. Wegscheider, M. Atature, and A. Imamoglu. Confluence of resonant laser excitation and bidirectional quantum-dot nuclear-spin polarization. *Nature Physics*, 5(10):758–763, August 2009. 11, 101

[36] I. T. Vink, K. C. Nowack, F. H. L. Koppens, J. Danon, Yu, and L. M. K. Vandersypen. Locking electron spins into magnetic resonance by electron-nuclear feedback. *Nature Physics*, 5:764–768, August 2009. 11

[37] D. J. Reilly, J. M. Taylor, J. R. Petta, C. M. Marcus, M. P. Hanson, and A. C. Gossard. Suppressing Spin Qubit Dephasing by Nuclear State Preparation. *Science*, 321(5890):817–821, 2008. 11, 14

[38] S. Foletti, H. Bluhm, D. Mahalu, V. Umansky, and A. Yacoby. Universal quantum control of two-electron spin quantum bits using dynamic nuclear polarization. *Nature Physics*, 5:903–908, December 2009. 11, 16

[39] Xiaodong Xu, Wang Yao, Bo Sun, Duncan G. Steel, Allan S. Bracker, Daniel Gammon, and L. J. Sham. Optically controlled locking of the nuclear field via coherent dark-state spectroscopy. *Nature*, 459(7250):1105–1109, June 2009. 11, 14, 171

[40] E. A. Chekhovich, M. N. Makhonin, K. V. Kavokin, A. B. Krysa, M. S. Skolnick, and A. I. Tartakovskii. Pumping of nuclear spins by optical excitation of spin-forbidden transitions in a quantum dot. *Physical Review Letters*, 104(6):066804, Feb 2010. 11

[41] Sandra Foletti, Hendrik Bluhm, Diana Mahalu, Vladimir Umansky, and Amir Yacoby. Universal quantum control of two-electron spin quantum bits using dynamic nuclear polarization. *Nature Physics*, 5(12):903–908, 2009. 11

[42] Danny Kim, Samuel G Carter, Alex Greilich, Allan S Bracker, and Daniel Gammon. Ultrafast optical control of entanglement between two quantum-dot spins. *Nature Physics*, 7(3):223–229, 2010. 11, 16, 51, 91, 170

[43] Alex Greilich, Samuel G Carter, Danny Kim, Allan S Bracker, and Daniel Gammon. Optical control of one and two hole spins in interacting quantum dots. *Nature Photonics*, 5(11):702–708, 2011. 11, 15, 16

[44] KM Weiss, JM Elzerman, YL Delley, J Miguel-Sanchez, and A Imamoğlu. Coherent two-electron spin qubits in an optically active pair of coupled ingaas quantum dots. *Physical Review Letters*, 109(10):107401, 2012. 11, 15, 170

[45] A Kuther, M Bayer, A Forchel, A Gorbunov, VB Timofeev, F Schäfer, and JP Reithmaier. Zeeman splitting of excitons and biexcitons in single in_ {0.60} ga_ {0.40} as/gaas self-assembled quantum dots. *Physical Review B*, 58(12):R7508–R7511, 1998. 12

[46] Richard J Warburton, C Schulhauser, Dirk Haft, C Schäflein, Khaled Karrai, Jorge M Garcia, W Schoenfeld, and Pierre M Petroff. Giant permanent dipole moments of excitons in semiconductor nanostructures. *Physical Review B*, 65(11):113303, 2002. 12, 13

[47] Anthony J Bennett, Raj B Patel, Joanna Skiba-Szymanska, Christine A Nicoll, Ian Farrer, David A Ritchie, and Andrew J Shields. Giant stark effect in the emission of single semiconductor quantum dots. *Applied Physics Letters*, 97(3):031104–031104, 2010. 13

[48] M. Atature, J. Dreiser, A. Badolato, A. Hogele, K. Karrai, and A. Imamoglu. Quantum-dot spin-state preparation with near-unity fidelity. *Science*, 312(5773):551–553, 2006. 14, 153

[49] Xiaodong Xu, Yanwen Wu, Bo Sun, Qiong Huang, Jun Cheng, D. G. Steel, A. S. Bracker, D. Gammon, C. Emary, and L. J. Sham. Fast spin state initialization in a singly charged inas-gaas quantum dot by optical cooling. *Physical Review Letters*, 99(9):097401, Aug 2007. 14

[50] B. D. Gerardot, D. Brunner, P. A. Dalgarno, P. Ohberg, S. Seidl, M. Kroner, K. Karrai, N. G. Stoltz, P. M. Petroff, and R. J. Warburton. Optical pumping of a single hole spin in a quantum dot. *Nature*, 451(7177):441–444, January 2008. 14

[51] J. R. Petta, A. C. Johnson, J. M. Taylor, E. A. Laird, A. Yacoby, M. D. Lukin, C. M. Marcus, M. P. Hanson, and A. C. Gossard. Coherent Manipulation of Coupled Electron Spins in Semiconductor Quantum Dots. *Science*, 309(5744):2180–2184, 2005. 14, 16

[52] David Press, Kristiaan De Greve, Peter L McMahon, Thaddeus D Ladd, Benedikt Friess, Christian Schneider, Martin Kamp, Sven Höfling, Alfred Forchel, and Yoshihisa Yamamoto. Ultrafast optical spin echo in a single quantum dot. *Nature Photonics*, 4(6):367–370, 2010. 14, 34

[53] WB Gao, Parisa Fallahi, Emre Togan, Javier Miguel-Sanchez, and Atac Imamoglu. Observation of entanglement between a quantum dot spin and a single photon. *Nature*, 491(7424):426–430, 2012. 14, 16, 17, 53, 125

[54] A. Greilich, D. R. Yakovlev, A. Shabaev, Al. L. Efros, I. A. Yugova, R. Oulton, V. Stavarache, D. Reuter, A. Wieck, and M. Bayer. Mode Locking of Electron Spin Coherences in Singly Charged Quantum Dots. *Science*, 313 (5785):341–345, 2006. 14

[55] Hendrik Bluhm, Sandra Foletti, Izhar Neder, Mark Rudner, Diana Mahalu, Vladimir Umansky, and Amir Yacoby. Dephasing time of gaas electron-spin qubits coupled to a nuclear bath exceeding 200 [thinsp][mu] s. *Nature Physics*, 7(2):109–113, 2010. 14, 171

[56] Kristiaan De Greve, Peter L McMahon, David Press, Thaddeus D Ladd, Dirk Bisping, Christian Schneider, Martin Kamp, Lukas Worschech, Sven Höfling, Alfred Forchel, et al. Ultrafast coherent control and suppressed nuclear feedback of a single quantum dot hole qubit. *Nature Physics*, 7(11): 872–878, 2011. 15

[57] TM Godden, JH Quilter, AJ Ramsay, Yanwen Wu, P Brereton, SJ Boyle, IJ Luxmoore, J Puebla-Nunez, AM Fox, and MS Skolnick. Coherent optical control of the spin of a single hole in an inas/gaas quantum dot. *Physical review letters*, 108(1):017402, 2012. 15

[58] Erik D. Kim, Katherine Truex, Xiaodong Xu, Bo Sun, D. G. Steel, A. S. Bracker, D. Gammon, and L. J. Sham. Fast spin rotations by optically

controlled geometric phases in a charge-tunable inas quantum dot. *Physical Review Letters*, 104(16):167401, Apr 2010. 15, 107

[59] A. Greilich, S. E. Economou, S. Spatzek, D. R. Yakovlev, D Reuter, Reinecke T. L Wieck, A. D., and M. Bayer. Ultrafast optical rotations of electron spins in quantum dots. *Nature Physics*, 5(3):262–266, 2009. 15

[60] F. H. L. Koppens, C. Buizert, K. J. Tielrooij, I. T. Vink, K. C. Nowack, T. Meunier, L. P. Kouwenhoven, and L. M. K. Vandersypen. Driven coherent oscillations of a single electron spin in a quantum dot. *Nature*, 442 (7104):766–771, August 2006. 16

[61] ST Yılmaz, P Fallahi, and A Imamoğlu. Quantum-dot-spin single-photon interface. *Physical Review Letters*, 105(3):033601, 2010. 16

[62] Julien Claudon, Joël Bleuse, Nitin Singh Malik, Maela Bazin, Périne Jaffrennou, Niels Gregersen, Christophe Sauvan, Philippe Lalanne, and Jean-Michel Gérard. A highly efficient single-photon source based on a quantum dot in a photonic nanowire. *Nature Photonics*, 4(3):174–177, 2010. 16

[63] Mete Atature, Jan Dreiser, Antonio Badolato, and Atac Imamoglu. Observation of faraday rotation from a single confined spin. *Nature Physics*, 3 (2):101–106, January 2007. 16

[64] J. Berezovsky, M. H. Mikkelsen, O. Gywat, N. G. Stoltz, L. A. Coldren, and D. D. Awschalom. Nondestructive optical measurements of a single electron spin in a quantum dot. *Science*, 314(5807):1916–1920, December 2006. 16

[65] Kristiaan De Greve, Leo Yu, Peter L McMahon, Jason S Pelc, Chandra M Natarajan, Na Young Kim, Eisuke Abe, Sebastian Maier, Christian Schneider, Martin Kamp, et al. Quantum-dot spin-photon entanglement via frequency downconversion to telecom wavelength. *Nature*, 491(7424):421–425, 2012. 17, 53, 125

[66] JR Schaibley, AP Burgers, GA McCracken, L-M Duan, PR Berman, DG Steel, AS Bracker, D Gammon, and LJ Sham. Demonstration of quan-

tum entanglement between a single electron spin confined to an inas quantum dot and a photon. *Physical Review Letters*, 110(16):167401, 2013. 17, 125

[67] Rodney Loudon. *The quantum theory of light*. Oxford University Press, Oxford, 2000. 18

[68] Marlan O Scully and M Suhail Zubairy. *Quantum Optics*. Cambridge University Press, Cambridge, 1997. 18

[69] Pierre Meystre and Murray Sargent. *Elements of quantum optics*. Springer Verlag, Berlin, 2007. 18, 23, 104

[70] BR Mollow. Power spectrum of light scattered by two-level systems. *Physical Review*, 188(5), 1969. 18, 52

[71] HJ Carmichael and DF Walls. A quantum-mechanical master equation treatment of the dynamical stark effect. *Journal of Physics B: Atomic and Molecular Physics*, 9(8):1199, 1976. 18

[72] BR Mollow. Resonant scattering of radiation from collision-damped two-level systems. *Physical Review A*, 2(1):76, 1970. 19, 26

[73] Felix Bloch, WW Hansen, and Martin Packard. Nuclear induction. *Physical Review*, 70(7-8):460–474, 1946. 22

[74] GA Morris and PB Chilvers. General analytical solutions of the bloch equations. *Journal of magnetic resonance. Series A*, 107(2):236–238, 1994. 26

[75] GA Morris and PB Chilvers. Erratum: Volume 107, number 2, series a (1994) in the note," general analytical solutions of the bloch equations," by gareth a. morris and paul b. chilvers, pages 236-238. *Journal of Magnetic Resonance, Series A*, 111(2):232, 1994. 26

[76] HC Torrey. Transient nutations in nuclear magnetic resonance. *Physical Review*, 76(8):1059, 1949. 26

[77] WL Barnes, Gunnar Björk, JM Gérard, P Jonsson, JAE Wasey, PT Worthing, and Valéry Zwiller. Solid-state single photon sources: light collection strategies. *The European Physical Journal D-Atomic, Molecular, Optical and Plasma Physics*, 18(2):197–210, 2002. 34, 45, 170

[78] Hai-Son Nguyen, Gregory Sallen, Christophe Voisin, Ph Roussignol, Carole Diederichs, and Guillaume Cassabois. Optically gated resonant emission of single quantum dots. *Physical Review Letters*, 108(5):057401, 2012. 34, 76

[79] L.P. Kouwenhoven, C.M. Marcus, P.L. McEuen, S. Tarucha, R.M. Westervelt, and N.S. Wingreen. Electron transport in quantum dots. *Mesoscopic Electron Transport*, 345:16–23, 1997. 36

[80] M. Ediger, G. Bester, A. Badolato, P. M. Petroff, K. Karrai, A. Zunger, and R. J. Warburton. Peculiar many-body effects revealed in the spectroscopy of highly charged quantum dots. *Nature Physics*, 3(11):774–779, November 2007. 36

[81] J Houel, AV Kuhlmann, L Greuter, F Xue, M Poggio, BD Gerardot, PA Dalgarno, A Badolato, PM Petroff, A Ludwig, et al. Probing single-charge fluctuations at a gaas/alas interface using laser spectroscopy on a nearby ingaas quantum dot. *Physical Review Letters*, 108(10):107401, 2012. 37, 76, 107, 117

[82] Scott Marshall Mansfield and GS Kino. Solid immersion microscope. *Applied Physics Letters*, 57:2615, 1990. 43

[83] G Kino. The solid immersion lens. In *Proc. SPIE*, volume 3740, pages 2–6, 1999. 45, 46

[84] Qian Wu, Luke P Ghislain, and VB Elings. Imaging with solid immersion lenses, spatial resolution, and applications. *Proceedings of the IEEE*, 88(9): 1491–1498, 2000. 45

[85] Keith A Serrels, Euan Ramsay, Paul A Dalgarno, Brian Gerardot, John O'Connor, Robert H Hadfield, Richard Warburton, and Derryck Reid. Solid

immersion lens applications for nanophotonic devices. *Journal of Nanophotonics*, 2(1):021854–021854, 2008. 45

[86] Valery Zwiller and Gunnar Bjork. Improved light extraction from emitters in high refractive index materials using solid immersion lenses. *Journal of Applied Physics*, 92(2):660–665, 2002. 45

[87] Bennett B Goldberg, SB Ippolito, Lukas Novotny, Zhiheng Liu, and MS Unlu. Immersion lens microscopy of photonic nanostructures and quantum dots. *Selected Topics in Quantum Electronics, IEEE Journal of*, 8(5): 1051–1059, 2002. 45

[88] S Moehl, Hui Zhao, B Dal Don, S Wachter, and H Kalt. Solid immersion lens-enhanced nano-photoluminescence: Principle and applications. *Journal of Applied Physics*, 93(10):6265–6272, 2003. 45, 46

[89] Zhiheng Liu, Bennett B Goldberg, Stephen B Ippolito, Anthony N Vamivakas, M Selim Unlu, and Richard Mirin. High resolution, high collection efficiency in numerical aperture increasing lens microscopy of individual quantum dots. *Applied Physics Letters*, 87(7):071905–071905, 2005. 45

[90] BD Gerardot, S Seidl, PA Dalgarno, RJ Warburton, M Kroner, K Karrai, A Badolato, and PM Petroff. Contrast in transmission spectroscopy of a single quantum dot. *Applied Physics Letters*, 90(22):221106–221106, 2007. 45

[91] AN Vamivakas, M Atatüre, J Dreiser, ST Yilmaz, A Badolato, AK Swan, BB Goldberg, A Imamoglu, and MS Ünlü. Strong extinction of a far-field laser beam by a single quantum dot. *Nano letters*, 7(9):2892–2896, 2007. 45

[92] JP Hadden, JP Harrison, AC Stanley-Clarke, L Marseglia, Y-LD Ho, BR Patton, JL OBrien, and JG Rarity. Strongly enhanced photon collection from diamond defect centers under microfabricated integrated solid immersion lenses. *Applied Physics Letters*, 97(24):241901–241901, 2010. 46

[93] Lucio Robledo, Lilian Childress, Hannes Bernien, Bas Hensen, Paul FA Alkemade, and Ronald Hanson. High-fidelity projective read-out of a solid-state spin quantum register. *Nature*, 477(7366):574–578, 2011. 46

[94] Tom D Milster. Chromatic correction of high-performance solid immersion lens systems. *Japanese journal of applied physics*, 38(part 1):1777–1779, 1999. 46

[95] Khaled Karrai and Richard J Warburton. Optical transmission and reflection spectroscopy of single quantum dots. *Superlattices and Microstructures*, 33(5):311–337, 2003. 50

[96] Benito Alén, Florian Bickel, Khaled Karrai, Richard J Warburton, and Pierre M Petroff. Stark-shift modulation absorption spectroscopy of single quantum dots. *Applied Physics Letters*, 83(11):2235–2237, 2003. 51

[97] Alexander Högele, Stefan Seidl, Martin Kroner, Khaled Karrai, Richard J Warburton, Brian D Gerardot, and Pierre M Petroff. Voltage-controlled optics of a quantum dot. *Physical Review Letters*, 93(21):217401, 2004. 51

[98] Jeremy L O'Brien and Jelena Vučkovi&cacute Akira Furusawa. Photonic quantum technologies. *Nature Photonics*, 3(12):687–695, 2009. 52, 73, 137

[99] F Schuda, CR Stroud Jr, and M Hercher. Observation of the resonant stark effect at optical frequencies. *Journal of Physics B: Atomic and Molecular Physics*, 7(7):L198, 1974. 52, 67

[100] RE Grove, FY Wu, and S Ezekiel. Measurement of the spectrum of resonance fluorescence from a two-level atom in an intense monochromatic field. *Physical Review A*, 15(1):227, 1977. 52

[101] HJ Kimble, M Dagenais, and L Mandel. Multiatom and transit-time effects on photon-correlation measurements in resonance fluorescence. *Physical Review A*, 18(1):201, 1978. 52, 73

[102] D Leibfried, R Blatt, C Monroe, and D Wineland. Quantum dynamics of single trapped ions. *Reviews of Modern Physics*, 75(1):281, 2003. 52

[103] Andreas Muller, Edward B Flagg, Pablo Bianucci, XY Wang, Dennis G Deppe, Wenquan Ma, Jiayu Zhang, GJ Salamo, Min Xiao, and Chih-Kang Shih. Resonance fluorescence from a coherently driven semiconductor quantum dot in a cavity. *Physical Review Letters*, 99(18):187402, 2007. 52, 67

[104] EB Flagg, Andreas Muller, JW Robertson, Sebastien Founta, DG Deppe, Min Xiao, Wenquan Ma, GJ Salamo, and Chih-Kang Shih. Resonantly driven coherent oscillations in a solid-state quantum emitter. *Nature Physics*, 5(3):203–207, 2009. 52, 67, 73, 75

[105] R Melet, Valia Voliotis, A Enderlin, D Roditchev, XL Wang, Thierry Guillet, and R Grousson. Resonant excitonic emission of a single quantum dot in the rabi regime. *Physical Review B*, 78(7):073301, 2008. 52, 67

[106] A.N. Vamivakas, Y. Zhao, C.Y. Lu, and M. Atatüre. Spin-resolved quantum-dot resonance fluorescence. *Nature Physics*, 5(3):198–202, 2009. 52, 67

[107] AH Myerson, DJ Szwer, SC Webster, DTC Allcock, MJ Curtis, G Imreh, JA Sherman, DN Stacey, AM Steane, and DM Lucas. High-fidelity readout of trapped-ion qubits. *Physical Review Letters*, 100(20):200502, 2008. 52, 166

[108] S Ates, SM Ulrich, S Reitzenstein, A Löffler, A Forchel, and P Michler. Post-selected indistinguishable photons from the resonance fluorescence of a single quantum dot in a microcavity. *Physical Review Letters*, 103(16): 167402, 2009. 53

[109] P Fallahi, ST Yılmaz, and A Imamoğlu. Measurement of a heavy-hole hyperfine interaction in ingaas quantum dots using resonance fluorescence. *Physical Review Letters*, 105(25):257402, 2010. 53, 101

[110] SM Ulrich, S Ates, S Reitzenstein, A Löffler, A Forchel, and P Michler. Dephasing of triplet-sideband optical emission of a resonantly driven inas/gaas quantum dot inside a microcavity. *Physical Review Letters*, 106(24):247402, 2011. 53, 64, 91, 92, 95

[111] AN Vamivakas, C-Y Lu, C Matthiesen, Y Zhao, S Fält, A Badolato, and M Atatüre. Observation of spin-dependent quantum jumps via quantum dot resonance fluorescence. *Nature*, 467(7313):297–300, 2010. 53, 139

[112] R Hanbury Brown and RQ Twiss. A test of a new type of stellar interferometer on sirius. *Nature*, 178(4541):1046–1048, 1956. 58

[113] S Felekyan, R Kuhnemuth, V Kudryavtsev, C Sandhagen, W Becker, and CAM Seidel. Full correlation from picoseconds to seconds by time-resolved and time-correlated single photon detection. *Review of Scientific Instruments*, 76(8):083104–083104, 2005. 59

[114] C. Matthiesen, A. N. Vamivakas, and M. Atatüre. Subnatural linewidth single photons from a quantum dot. *Physical Review Letters*, 108(9):093602, 2012. 61

[115] AJ Ramsay, Achanta Venu Gopal, EM Gauger, A Nazir, BW Lovett, AM Fox, and MS Skolnick. Damping of exciton rabi rotations by acoustic phonons in optically excited ingaas/gaas quantum dots. *Physical Review Letters*, 104(1):017402, 2010. 64, 91, 92, 95

[116] AJ Ramsay, TM Godden, SJ Boyle, Erik M Gauger, Ahsan Nazir, Brendon W Lovett, AM Fox, and MS Skolnick. Phonon-induced rabi-frequency renormalization of optically driven single ingaas/gaas quantum dots. *Physical Review Letters*, 105(17):177402, 2010. 64, 91, 92, 95

[117] H Stolz. Resonance rayleigh scattering from low dimensional semiconductors: What is still to come. *physica status solidi (b)*, 234(1):107–114, 2002. 67

[118] HJ Kimble and L Mandel. Theory of resonance fluorescence. *Physical Review A*, 13(6):2123, 1976. 73

[119] HJ Kimble, M Dagenais, and L Mandel. Photon antibunching in resonance fluorescence. *Physical Review Letters*, 39(11):691–695, 1977. 73

[120] Pieter Kok, William J Munro, Kae Nemoto, Timothy C Ralph, Jonathan P Dowling, and GJ Milburn. Linear optical quantum computing with photonic qubits. *Reviews of Modern Physics*, 79(1):135, 2007. 73, 137

[121] P Michler, A Kiraz, C Becher, WV Schoenfeld, PM Petroff, Lidong Zhang, E Hu, and A Imamoglu. A quantum dot single-photon turnstile device. *Science*, 290(5500):2282–2285, 2000. 73

[122] J Kim, O Benson, H Kan, and Y Yamamoto. A single-photon turnstile device. *Nature*, 397(6719):500–503, 1999. 73

[123] Stefan Strauf, Nick G Stoltz, Matthew T Rakher, Larry A Coldren, Pierre M Petroff, and Dirk Bouwmeester. High-frequency single-photon source with polarization control. *Nature Photonics*, 1(12):704–708, 2007. 73

[124] H.-S. Nguyen, G. Sallen, C. Voisin, Ph. Roussignol, C. Diederichs, and G. Cassabois. Ultra-coherent single photon source. *Applied Physics Letters*, 99(26):261904–261904, 2011. 75

[125] K Konthasinghe, J Walker, M Peiris, CK Shih, Y Yu, MF Li, JF He, LJ Wang, HQ Ni, ZC Niu, et al. Coherent versus incoherent light scattering from a quantum dot. *Physical Review B*, 85(23):235315, 2012. 76, 91

[126] Hai Son Nguyen, Gregory Sallen, Marco Abbarchi, Robson Ferreira, Christophe Voisin, Philippe Roussignol, Guillaume Cassabois, and Carole Diederichs. Photoneutralization and slow capture of carriers in quantum dots probed by resonant excitation spectroscopy. *Physical Review B*, 87 (11):115305, 2013. 76

[127] Andreas V Kuhlmann, Julien Houel, Arne Ludwig, Lukas Greuter, Dirk Reuter, Andreas D Wieck, Martino Poggio, and Richard J Warburton. Charge noise and spin noise in a semiconductor quantum device. *arXiv preprint arXiv:1301.6381*, 2013. 76, 79, 117

[128] U Bockelmann and G Bastard. Phonon scattering and energy relaxation in two-, one-, and zero-dimensional electron gases. *Physical Review B*, 42(14): 8947, 1990. 87

[129] H Benisty. Reduced electron-phonon relaxation rates in quantum-box systems: Theoretical analysis. *Physical Review B*, 51(19):13281, 1995. 87

[130] L Besombes, K Kheng, L Marsal, and H Mariette. Acoustic phonon broadening mechanism in single quantum dot emission. *Physical Review B*, 63 (15):155307, 2001. 87, 91, 111

[131] Paola Borri, Wolfgang Langbein, Stephan Schneider, Ulrike Woggon, Roman L Sellin, Dongxun Ouyang, and Dieter Bimberg. Ultralong dephasing time in ingaas quantum dots. *Physical Review Letters*, 87(15):157401, 2001. 87, 91, 111

[132] I Favero, Guillaume Cassabois, R Ferreira, D Darson, C Voisin, J Tignon, C Delalande, G Bastard, Ph Roussignol, and JM Gérard. Acoustic phonon sidebands in the emission line of single inas/gaas quantum dots. *Physical Review B*, 68(23):233301, 2003. 87

[133] B Urbaszek, EJ McGhee, M Krüger, Richard J Warburton, Khaled Karrai, T Amand, BD Gerardot, Pierre M Petroff, and Jorge M Garcia. Temperature-dependent linewidth of charged excitons in semiconductor quantum dots: Strongly broadened ground state transitions due to acoustic phonon scattering. *Physical Review B*, 69(3):035304, 2004. 87

[134] B Krummheuer, VM Axt, and T Kuhn. Theory of pure dephasing and the resulting absorption line shape in semiconductor quantum dots. *Physical Review B*, 65(19):195313, 2002. 87, 88, 91

[135] AV Uskov, Antti-Pekka Jauho, Bjarne Tromborg, Jesper Mørk, and R Lang. Dephasing times in quantum dots due to elastic lo phonon-carrier collisions. *Physical Review Letters*, 85(7):1516–1519, 2000. 87

[136] EA Muljarov and R Zimmermann. Dephasing in quantum dots: Quadratic coupling to acoustic phonons. *Physical Review Letters*, 93(23):237401, 2004. 87, 91

[137] Peter Y Yu and Manuel Cardona. *Fundamentals of semiconductors: physics and materials properties*. Springer Berlin etc, 1999. 88

[138] Toshihide Takagahara. Theory of exciton dephasing in semiconductor quantum dots. *Physical Review B*, 60(4):2638, 1999. 88

[139] Erik Stock, Matthias-Rene Dachner, Till Warming, Andrei Schliwa, Anatol Lochmann, Axel Hoffmann, Aleksandr I Toropov, Askhat K Bakarov, Ilya A Derebezov, Marten Richter, et al. Acoustic and optical phonon scattering in a single in (ga) as quantum dot. *Physical Review B*, 83(4):041304, 2011. 91

[140] S Michaelis De Vasconcellos, S Gordon, M Bichler, T Meier, and A Zrenner. Coherent control of a single exciton qubit by optoelectronic manipulation. *Nature Photonics*, 4(8):545–548, 2010. 91

[141] Dara PS McCutcheon and Ahsan Nazir. Quantum dot rabi rotations beyond the weak exciton–phonon coupling regime. *New Journal of Physics*, 12(11): 113042, 2010. 92

[142] M Glässl, MD Croitoru, A Vagov, VM Axt, and T Kuhn. Influence of the pulse shape and the dot size on the decay and reappearance of rabi rotations in laser driven quantum dots. *Physical Review B*, 84(12):125304, 2011. 92

[143] Jasper Chan, TP Mayer Alegre, Amir H Safavi-Naeini, Jeff T Hill, Alex Krause, Simon Gröblacher, Markus Aspelmeyer, and Oskar Painter. Laser cooling of a nanomechanical oscillator into its quantum ground state. *Nature*, 478(7367):89–92, 2011. 96

[144] Jack Hansom, Carsten H. H. Schulte, Claire Le Gall, Clemens Matthiesen, Jake Taylor, and Mete Atature. Nuclear-spin enabled electron spin qubits in the absence of external field. *in preparation*, 2013. 99, 101

[145] EA Chekhovich, AB Krysa, MS Skolnick, and AI Tartakovskii. Direct measurement of the hole-nuclear spin interaction in single inp/gainp quantum dots using photoluminescence spectroscopy. *Physical Review Letters*, 106 (2):027402, 2011. 101

[146] A. Ulhaq, S. Weiler, S. M. Ulrich, R. Roßbach, M. Jetter, and P. Michler. Cascaded single-photon emission from the mollow triplet sidebands of a quantum dot. *Nature Photonics*, 6(4):238–242, 2012. 104

[147] YP Varshni. Temperature dependence of the energy gap in semiconductors. *Physica*, 34(1):149–154, 1967. 110

[148] R Heitz, I Mukhametzhanov, A Madhukar, A Hoffmann, and D Bimberg. Temperature dependent optical properties of self-organized inas/gaas quantum dots. *Journal of electronic materials*, 28(5):520–527, 1999. 110

[149] G Ortner, M Schwab, M Bayer, R Pässler, S Fafard, Zbigniew Wasilewski, Pawel Hawrylak, and A Forchel. Temperature dependence of the excitonic band gap in in_ {x} ga_ {1- x} as/ gaas self-assembled quantum dots. *Physical Review B*, 72(8):085328, 2005. 111

[150] M Kroner, KM Weiss, S Seidl, RJ Warburton, A Badolato, PM Petroff, and K Karrai. Temperature dependent high resolution resonant spectroscopy on a charged quantum dot. *physica status solidi (b)*, 246(4):795–798, 2009. 111

[151] Private communication with C.-Y. Lu. 111

[152] Daniel Jaque and Fiorenzo Vetrone. Luminescence nanothermometry. *Nanoscale*, 4(15):4301–4326, 2012. 116

[153] DL Moehring, P Maunz, S Olmschenk, KC Younge, DN Matsukevich, L-M Duan, and C Monroe. Entanglement of single-atom quantum bits at a distance. *Nature*, 449(7158):68–71, 2007. 125, 171

[154] L. Slodička, G. Hétet, N. Röck, P. Schindler, M. Hennrich, and R. Blatt. Atom-atom entanglement by single-photon detection. *Physical Review Letters*, 110:083603, Feb 2013. 125

[155] H Bernien, B Hensen, W Pfaff, G Koolstra, MS Blok, L Robledo, TH Taminiau, M Markham, DJ Twitchen, L Childress, et al. Heralded entanglement between solid-state qubits separated by three metres. *Nature*, 497(7447):86–90, 2013. 125

[156] C Cabrillo, JI Cirac, P Garcia-Fernandez, and P Zoller. Creation of entangled states of distant atoms by interference. *Physical Review A*, 59(2):1025, 1999. 125, 137, 171

[157] L.-M. Duan, M. J. Madsen, D. L. Moehring, P. Maunz, R. N. Kohn, and C. Monroe. Probabilistic quantum gates between remote atoms through interference of optical frequency qubits. *Physical Review A*, 73:062324, Jun 2006. 125, 137, 171

[158] Clemens Matthiesen, Martin Geller, Carsten HH Schulte, Claire Le Gall, Jack Hansom, Zhengyong Li, Maxime Hugues, Edmund Clarke, and Mete Atatüre. Phase-locked indistinguishable photons with synthesized waveforms from a solid-state source. *Nature Communications*, 4:1600, 2013. 126

[159] Charles Santori, Jelena Vučkovi&cacute David Fattal, Glenn S Solomon, and Yoshihisa Yamamoto. Indistinguishable photons from a single-photon device. *Nature*, 419(6907):594–597, 2002. 126, 136

[160] Stefanie Weiler, Ata Ulhaq, Sven M Ulrich, Stephan Reitzenstein, Andreas Löffler, Alfred Forchel, and Peter Michler. Highly indistinguishable photons from a quantum dot in a microcavity. *physica status solidi (b)*, 248(4):867–871, 2011. 126

[161] Edward B Flagg, Andreas Muller, Sergey V Polyakov, Alex Ling, Alan Migdall, and Glenn S Solomon. Interference of single photons from two separate semiconductor quantum dots. *Physical Review Letters*, 104(13): 137401, 2010. 127, 132, 137

[162] L Childress, JM Taylor, Anders Søndberg Sørensen, and MD Lukin. Fault-tolerant quantum repeaters with minimal physical resources and implemen-

tations based on single-photon emitters. *Physical Review A*, 72(5):052330, 2005. 127, 137

[163] JT Höffges, HW Baldauf, W Lange, and H Walther. Heterodyne measurement of the resonance fluorescence of a single ion. *Journal of Modern Optics*, 44(10):1999–2010, 1997. 127

[164] PS Jessen, C Gerz, PD Lett, WD Phillips, SL Rolston, RJC Spreeuw, and CI Westbrook. Observation of quantized motion of rb atoms in an optical field. *Physical Review Letters*, 69(1):49–52, 1992. 127

[165] Ch Raab, J Eschner, J Bolle, H Oberst, F Schmidt-Kaler, and R Blatt. Motional sidebands and direct measurement of the cooling rate in the resonance fluorescence of a single trapped ion. *Physical Review Letters*, 85(3): 538–541, 2000. 127

[166] Sergey V Polyakov, Andreas Muller, Edward B Flagg, Alex Ling, Natalia Borjemscaia, Edward Van Keuren, Alan Migdall, and Glenn S Solomon. Coalescence of single photons emitted by disparate single-photon sources: the example of inas quantum dots and parametric down-conversion sources. *Physical Review Letters*, 107(15):157402, 2011. 129

[167] HP Specht, J Bochmann, M Mücke, B Weber, E Figueroa, DL Moehring, and G Rempe. Phase shaping of single-photon wave packets. *Nature Photonics*, 3(8):469–472, 2009. 129

[168] Pavel Kolchin, Chinmay Belthangady, Shengwang Du, GY Yin, and SE Harris. Electro-optic modulation of single photons. *Physical Review Letters*, 101(10):103601, 2008. 129

[169] Matthew T Rakher and Kartik Srinivasan. Subnanosecond electro-optic modulation of triggered single photons from a quantum dot. *Applied Physics Letters*, 98(21):211103–211103, 2011. 129

[170] J McKeever, A Boca, AD Boozer, R Miller, JR Buck, A Kuzmich, and HJ Kimble. Deterministic generation of single photons from one atom trapped in a cavity. *Science*, 303(5666):1992–1994, 2004. 129

[171] Matthias Keller, Birgit Lange, Kazuhiro Hayasaka, Wolfgang Lange, and Herbert Walther. Continuous generation of single photons with controlled waveform in an ion-trap cavity system. *Nature*, 431(7012):1075–1078, 2004. 129

[172] Atature Kiraz, M Atatüre, and A Imamoğlu. Quantum-dot single-photon sources: Prospects for applications in linear optics quantum-information processing. *Physical Review A*, 69(3):032305, 2004. 132

[173] Raj B Patel, Anthony J Bennett, Ian Farrer, Christine A Nicoll, David A Ritchie, and Andrew J Shields. Two-photon interference of the emission from electrically tunable remote quantum dots. *Nature Photonics*, 4(9): 632–635, 2010. 132, 137

[174] CK Hong, ZY Ou, and LEONARD Mandel. Measurement of subpicosecond time intervals between two photons by interference. *Physical Review Letters*, 59(18):2044–2046, 1987. 132

[175] Syed Abdullah Aljunid, Gleb Maslennikov, Yimin Wang, Dao Hoang Lan, Valerio Scarani, and Christian Kurtsiefer. Excitation of a single atom with exponentially rising light pulses. *arXiv preprint arXiv:1304.3761*, 2013. 134

[176] RB Patel, AJ Bennett, K Cooper, P Atkinson, CA Nicoll, DA Ritchie, and AJ Shields. Postselective two-photon interference from a continuous nonclassical stream of photons emitted by a quantum dot. *Physical Review Letters*, 100(20):207405, 2008. 136

[177] Yu-Ming He, Yu He, Yu-Jia Wei, Dian Wu, Mete Atatüre, Christian Schneider, Sven Höfling, Martin Kamp, Chao-Yang Lu, and Jian-Wei Pan. On-demand semiconductor single-photon source with near-unity indistinguishability. *Nature Nanotechnology*, 2013. 137

[178] L-M Duan and R Raussendorf. Efficient quantum computation with probabilistic quantum gates. *Physical Review Letters*, 95(8):080503, 2005. 137

[179] K. Konthasinghe, M. Peiris, Y. Yu, M. F. Li, J. F. He, L. J. Wang, H. Q. Ni, Z. C. Niu, C. K. Shih, and A. Muller. Field-field and photon-photon

correlations of light scattered by two remote two-level inas quantum dots on the same substrate. *Physical Review Letters*, 109(26):267402, 2012. 138

[180] Danny Kim, Sophia E. Economou, Ştefan C. Bădescu, Michael Scheibner, Allan S. Bracker, Mark Bashkansky, Thomas L. Reinecke, and Daniel Gammon. Optical spin initialization and nondestructive measurement in a quantum dot molecule. *Physical Review Letters*, 101(23):236804, Dec 2008. 140, 147, 153

[181] Warren Nagourney, Jon Sandberg, and Hans Dehmelt. Shelved optical electron amplifier: Observation of quantum jumps. *Physical Review Letters*, 56(26):2797–2799, Jun 1986. 141

[182] Th. Sauter, W. Neuhauser, R. Blatt, and P. E. Toschek. Observation of quantum jumps. *Physical Review Letters*, 57(14):1696–1698, Oct 1986. 141

[183] J. C. Bergquist, Randall G. Hulet, Wayne M. Itano, and D. J. Wineland. Observation of quantum jumps in a single atom. *Physical Review Letters*, 57(14):1699–1702, Oct 1986. 141

[184] T. Basche, S. Kummer, and C. Brauchle. Direct spectroscopic observation of quantum jumps of a single molecule. *Nature*, 373:132–134, January 1995. 141

[185] Eric A. Stinaff, Michael Scheibner, Allan S. Bracker, Ilya V. Ponomarev, Vladimir L. Korenev, Morgan E. Ware, Matt F. Doty, Thomas L. Reinecke, and Dan Gammon. Optical Signatures of Coupled Quantum Dots. *Science*, page 1121189, 2006. 142, 146, 147

[186] M. Scheibner, M. F. Doty, I. V. Ponomarev, A. S. Bracker, E. A. Stinaff, V. L. Korenev, T. L. Reinecke, and D. Gammon. Spin fine structure of optically excited quantum dot molecules. *Physical Review B*, 75(24):245318, Jun 2007. 142

[187] M. F. Doty, M. Scheibner, A. S. Bracker, I. V. Ponomarev, T. L. Reinecke, and D. Gammon. Optical spectra of doubly charged quantum dot molecules

in electric and magnetic fields. *Physical Review B*, 78(11):115316, Sep 2008. 142, 146, 158

[188] R. J. Warburton, B. T. Miller, C. S. Dürr, C. Bödefeld, K. Karrai, J. P. Kotthaus, G. Medeiros-Ribeiro, P. M. Petroff, and S. Huant. Coulomb interactions in small charge-tunable quantum dots: A simple model. *Physical Review B*, 58:16–221, 1998. 146

[189] M. Scheibner, A. S. Bracker, D. Kim, and D. Gammon. Essential concepts in the optical properties of quantum dot molecules. *Solid State Communications*, 149(35):1427–1435, 2009. 146

[190] X.-W. Chen, S. Götzinger, and V. Sandoghdar. 99% efficiency in collecting photons from a single emitter. *Optics letters*, 36(18):3545–3547, 2011. 170

[191] G. De Lange, Z. H. Wang, D. Riste, V. V. Dobrovitski, and R. Hanson. Universal dynamical decoupling of a single solid-state spin from a spin bath. *Science*, 330(6000):60–63, 2010. 171